

# LEGIBILITY NOTICE

A major purpose of the Technical Information Center is to provide the broadest dissemination possible of information contained in DOE's Research and Development Reports to business, industry, the academic community, and federal, state and local governments.

Although a small portion of this report is not reproducible, it is being made available to expedite the availability of information on the research discussed herein.



**PROCEEDINGS**  
**JUNE 23, 1988 SESSIONS**

**MASTER**

DISTRIBUTION STATEMENT

**DISCLAIMER**

Report was prepared as an account of work sponsored by an agency of the United States Government. Neither the United States Government nor any agency thereof, nor any of their employees, makes any warranty, express or implied, or assumes any legal liability or responsibility for the accuracy, completeness, or usefulness of any information, apparatus, product, or process disclosed, or represents that its use would not infringe privately owned rights. Reference herein to any specific commercial product, process, or service by trade name, trademark, manufacturer, or otherwise does not necessarily constitute or imply its endorsement, recommendation, or favoring by the United States Government or any agency thereof. The views and opinions of authors expressed herein do not necessarily state or reflect those of the United States Government or any agency thereof.

**PROCEEDINGS  
JUNE 23, 1988 SESSIONS**

LA-UR--89-200

DE89 006526

SIXTH TARGET FABRICATION  
SPECIALISTS MEETING

DO NOT WRITE

6TH TARGET FABRICATION SPECIALISTS' MEETING  
 J. ROBERT OPPENHEIMER STUDY CENTER  
 LOS ALAMOS NATIONAL LABORATORY  
 JUNE 20-24, 1988  
 THURSDAY (UNCLASSIFIED), JUNE 23, 1988

Thursday Morning Oral Session, June 23, 1988

Chairperson: Hyo-Gun Kim, Laboratory for Laser Energetics

PRESENTER	TITLE	PAGE
Loretta Shirey Naval Research Lab	Laser Target Fabrication at the Naval Research Laboratory	5
David Stopin Los Alamos	High-Sensitivity Radiography Detects Very Small Defects in Laser Fusion Targets	12
Hyo-Gun Kim LLE	Ablation Layer Coating on Inertial Fusion Targets at Laboratory for Laser Energetics	24
Hyo-Gun Kim LLE	X-Ray Microscopy of Inertial Fusion Targets Using A Laser Produced Plasma As An X-Ray Source	27
Richard Crawley KMS Fusion, Inc.	A Study of Factors Affecting The Deposition of Smooth Plasma Polymers	32
Alice Nyitray Los Alamos	Composite Foams	42
Fung-Ming Kong LLNL	Low-Density Resorcinol-Form- aldehyde Foams for Direct- Drive Laser ICF Targets	55
Blanca Haendler LLNL	Low-Density Polystyrene Foams For Direct-Drive Laser ICF Targets	63
Stevan Letts LLNL	Characterization of Low Density Materials and Their Precursors	71
Clifford Price LLNL	Low Voltage Scanning Electron Microscopy of Target Materials	79

Thursday Afternoon Oral Session, June 23, 1988

Chairperson: Glen Rambach, Lawrence Livermore National Laboratory

PRESENTER	TITLE	PAGE
Wayne Miller KMS Fusion, Inc.	Recent Results in Glass Shell Fabrication	90
Matt Ebner KMS Fusion, Inc.	Evaluation of Tensile Strength in Alkali Silicate Shells	101
John Grenz LLNL	The Filling and Leakage of Multilayer Polymer Fuel Capsules	112
Peter Gobby Los Alamos	Measurement of Argon Content in GMBs Using Neutron Activation	120
S. R. Murrell KMS Fusion, Inc.	The Fabrication of "Gaussian Bumps" on Small Spherical Substrates	129
Ravindra Upadhye LLNL	An Integrated Model for Sputter Coating Uniformity	137

Poster Session #4

Chairperson: Alfred Martin, KMS Fusion, Inc.

PRESENTER	TITLE	PAGE
Matt Ebner KMS Fusion, Inc.	The Reactivity of The Residual Blowing Gases in Glass Shells	144
R. Schneggenburger KMS Fusion, Inc.	Measurement of Glass Shell Buckling Strength Using a Piezoelectric Film Sensor	149
Clarence Thomas LLNL	Cryogenic Mechanical Charac- terization of Low-Density Polymeric Foams Being Developed for Direct-Drive Laser ICF Targets	152
George Overturff, III LLNL	Drying Studies on Inverse- Emulsion Polystyrene Foams	158
Kenneth King LLNL	Current Developments in PVA Coating of Polymer Microshells	165
Marita Spragge LLNL	Metrology Advancements in Target Assembly	173
Kyekyoon Kim Univ. of Ill.	Formation of Spherical-Shell SiO <sub>2</sub> Aerogel Pellets By A Sol-Gel Method	179
Chuck Chen LLNL	Low-Density Cellulose Acetate Foams for Direct-Drive Laser ICF Targets	189
Steven Buckley LLNL	Thermal Analysis of Low- Density Foams for Direct-Drive Laser ICF Targets	198
Harold Kramer LLNL	Development of a Die System For Molding Target Parts From Polystyrene	210

# LASER TARGET FABRICATION AT THE NAVAL RESEARCH LABORATORY

by

Loretta Mengel Shirey

Naval Research Laboratory  
Microelectronics Processing Facility  
4555 Overlook Ave. S.W.  
Washington DC. 20375-5000

## INTRODUCTION

Three years ago the Microelectronics Processing Facility (MPF), part of the electronics science and technology division at the Naval Research Laboratory (NRL), expanded its functions to include production of microstructures. The main interest was to design and fabricate laser targets for experiments on the NRL Laser Plasma lab's 1.5KJ, Nd-glass Pharos III laser and other lasers used by the Space Science and Plasma Physics Divisions. This paper will include a description of the MPF and its capabilities, some examples of successfully produced targets, details of the fabrication of one particular target, and a brief discussion of some of the new processes and samples that are being developed.

## MICROELECTRONICS PROCESSING FACILITY

The MPF was originally set up to fabricate experimental electronic structures and integrated circuits for the various labs at NRL. Additional functions now include: making Si and GaAs test devices for reliability studies, modelling devices, and studying the effects of hostile environments, such as radiation effects, on device performance. The MPF is organized into sections for:

- VAX based CAD combined with VALID and GPN workstations
- E Beam writing using Cambridge EBWF 6.5 and JEOL JBX 5DH nanowriters
- photolithography using both negative and positive resists

- electroplating of metals
- chemical vapor deposition
- GaAs Processing
- evaporation and metallization using filament, E-beam, and inductively heated sources, and sputtering systems
- device modelling
- oxidation and diffusion
- measurement and testing including an SEM and electrical test equipment
- assembly and bonding, including sawing, scribing, and packaging

The existence of these processing capabilities allowed the MPF to expand its operation into the production of microstructures. A lab dedicated to microstructure assembly was set up with very little need for additional equipment. Most of the microstructures fabricated to date have been laser targets.

In addition to in-house capabilities, the MPF also has access to some testing and production equipment located in other divisions at NRL. Some materials or jobs are obtained from or contracted out to outside companies for various reasons, for instance, materials that are readily available from a manufacturer or materials that involve a safety hazard which the MPF is not equipped to handle, e.g., making Be foils.

### EXAMPLES OF TARGETS

The Laser Plasma Lab at NRL engages in basic research to study the implosion of inertial confinement fusion pellets. The surface of a pellet is modelled using planar targets rather than spherical ones because the physics of the results is easier to interpret. A description of some of these targets, grouped by experiment, is given below.



### Inertial Confinement Fusion (ICF) experiments :

#### A) Rayleigh/Taylor instabilities in thin shells:

- milled structures in thin C foils
- Al tracer dots on plastic foil
- thin (6 - 25 $\mu m$ ) plastic and C planar foils and double foils (parallel) with fixed separation distances
- thin (6 - 12 $\mu m$ ) plastic foils with periodic perturbations whose amplitude and wave length can be varied, e.g., sine waves (spun on mandrils made by Rocky Flats), square waves and multiple waves.
- Au and CsI cathodes for X-ray streak camera

#### B) Laser plasma interaction studies (e.g., Raman backscattering and stimulated Brillouin scattering):

- thick (200 $\mu m$ ), flat polystyrene strips, and plastic disks on glass stalks

#### C) Uniform target acceleration studies in ICF targets:

- single and double carbon foils (5-10 $\mu m$ )
- Li foils (which don't emit X-rays)

### HANE (High Altitude Nuclear Effects) Experiments :

- 2 - 10 $\mu m$  Al and Bi disks and squares on 15 - 35 $\mu m$  diameter glass stalks
- Al, Au, rare earth element foils
- Rayleigh/Taylor targets

### Laser pumped X-ray laser studies :

- Cu (1000Å) coated formvar films (1200Å) over slits
- 1 $\mu m$  Cu foil with 100 $\mu m$  slit
- special geometry targets
- planar plastic film targets

### Spectroscopy studies of high Z elements :

- spherical glass beads ( $200\mu m$ ) on glass stalks (some with metals deposited on them, e.g., InSb, Nd, Pr, CsI)

### Transmittance studies of metals and sarans in the deep UV spectral region :

- formvar or saran films over circular openings (some with centered metal dots)

### X -- ray spectroscopy studies :

- metal dots on polystyrene foils

### AN EXAMPLE OF TARGET PROCESS FLOW

The following section describes the process flow for one of the more interesting targets. This particular target involves the production of Cu-coated formvar films used for laser-pumped X-ray studies. The target holder (called a stadium) is highly polished Al with a  $0.3mm$  or a  $0.5mm$  slit.

To make this target the following steps are employed:

- 1) Cast a  $1200\text{\AA}$  formvar film on a glass slide and measure the thickness on a Dektak, this is usually the crucial step because it is difficult to cast an even film, and difficult to measure the thickness because of its softness.
- 2) Cut the film to size and float it off onto water.
- 3) Pick up the film from the water surface onto a stadium so that the film is correctly positioned over the slit, and allow it to air dry.
- 4) Vacuum evaporate  $1000\text{\AA}$  Cu over the formvar film. This can be a problem because heat from the evaporation can cause holes in the formvar.

This target was used to demonstrate soft X ray lasing in Cu for the first time. During the experiment, the laser beam hits the target from the top direction and then produces a high temperature, high density plasma with an electron temperature of  $300\text{ev}$  and a

density of a few times  $10^{20}$  electrons/cc. The X-ray pinhole photograph shows that this is not an exploding foil plasma and but an ablating foil plasma, where high density occurs instead of expansion because the time scale is so minute. The camera is placed  $90^\circ$  to the laser beam and the line of focus is end-on straight down the cylindrical plasma. This is a time integrated photograph, i.e., the image on the front surface forms first and the rest forms later after breakthrough. Lasing is thought to occur on the front side of the target between  $200\mu m$  and  $300\mu m$  from its surface. The underneath portion represents the breakthrough plasma. The X-ray lasing occurs at a wavelength of about  $270 \text{ \AA}$ .

### DEVELOPMENTAL AREAS

The following are either new targets being developed or ongoing projects that have offered a particular challenge:

- determination of surface contamination
- spreading plastic films over large areas without developing pinholes or tears
- prevention of the oxidation causing peeling and flaking on evaporated films
- keeping split foils flat and with a constant width
- embedding tracers into materials
- spinning plastic sine waves with a planarized back
- casting thin films of saran and other materials to study transmission in the deep UV region

The following are areas where there is interest in future development, but no work has been started:

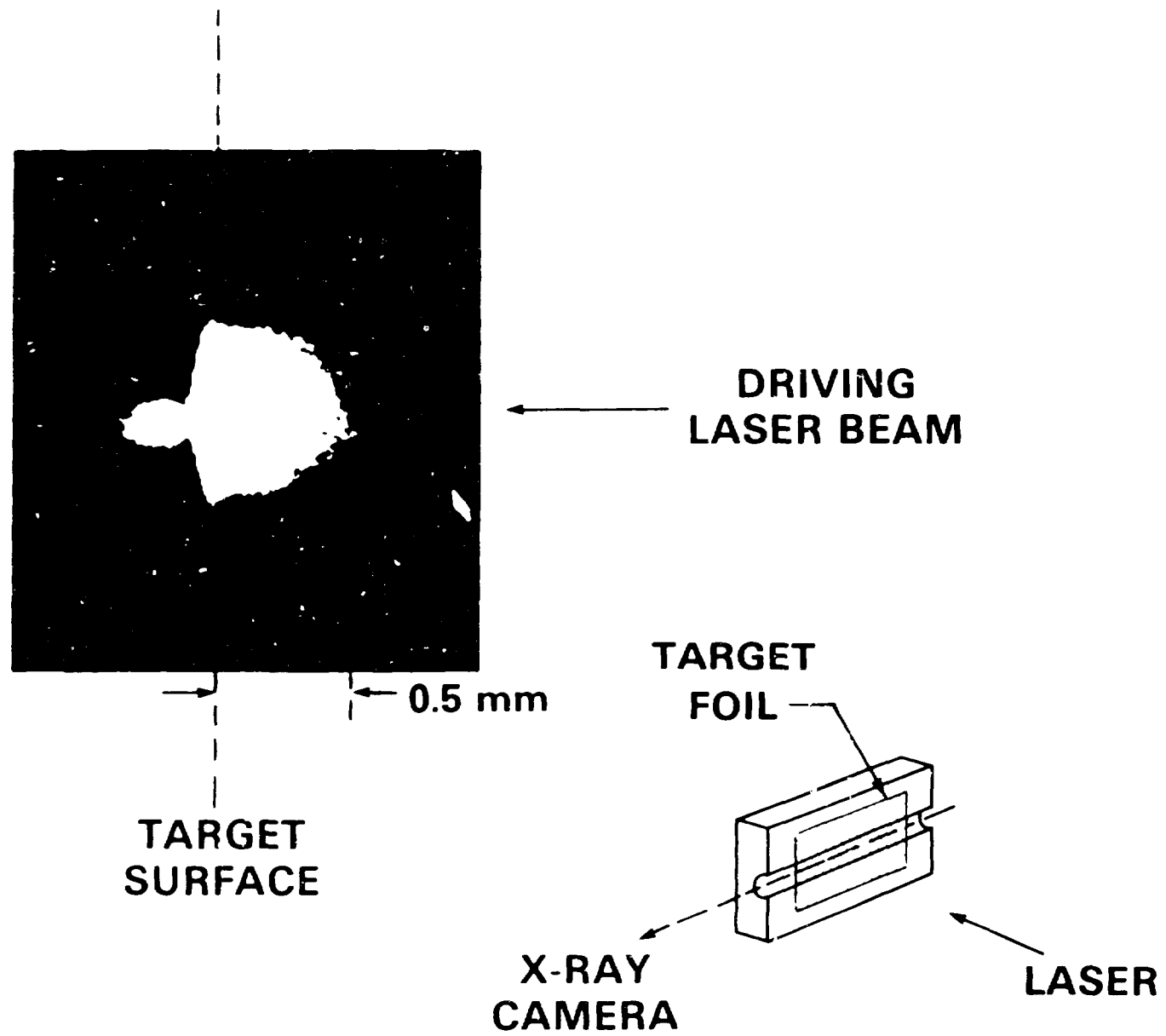
- low density foams
- thin, self supporting foils
- special geometry targets in three dimensions for lasing from multiple directions
- cryogenic targets, e.g., foam with deuterium

## CONCLUSION

This paper has briefly described the Microelectronics Processing Facility at the Naval Research Laboratory. Using existing equipment and techniques for microelectronics processing, target fabrication for plasma physics experiments involving high-energy lasers has been developed and is routinely carried out.

## ACKNOWLEDGEMENTS

I would like to thank the staff of MPF for cooperation in these projects, particularly John Kosakowski who helped set up the microstructure lab and Jack Taylor who helps design target processes.



# HIGH-SENSITIVITY RADIOGRAPHY DETECTS VERY SMALL DEFECTS IN LASER FUSION TARGETS

by

David M. Stupin  
Materials Science and Technology Division  
Los Alamos National Laboratory  
Los Alamos, NM 87545

Digital subtraction radiography is a near-real-time technique that can detect extremely small variations in thickness or density. I used this technique with a microfocus x-ray source having a nominal 10- $\mu\text{m}$ -diam focal spot to image 2- $\mu\text{m}$ -diam tungsten wires and thickness variations as small as 0.1%<sup>1-3</sup> measured over large areas. Although these samples were flat, experiments using positioning techniques common to the target fabrication community should yield similar sensitivities on spherical inertial confinement fusion (ICF) targets. These tests were limited to 17-keV x rays, a useful energy for our targets. I hope to eventually expand the technique to other energies as well.

The technique needs to be improved to detect 0.1% thickness variations occurring within areas as small as 10  $\mu\text{m}$  in diam to meet the needs of ICF target characterization. Such improvements are possible with devices that are either described in the literature or available commercially.

This method is fast and readily adapted to ICF-target-characterization techniques. To reduce noise, I average 128 video frames in both a background and a foreground image, and then subtract one from the other to reveal the defects. This image processing takes less than 30 s on equipment that costs less than \$10,000. Radiographing ICF targets in three orthogonal positions easily provides background and foreground images; any one of these orthogonal views can serve as the background image for the other two.

## DIGITAL SUBTRACTION RADIOGRAPHY

Digital subtraction radiography serves angiography<sup>4</sup> and other medical applications successfully to extract minute x-ray signals from noisy backgrounds. Verhoeven<sup>5</sup> demonstrated that detecting surprisingly small changes in x-ray absorption makes this technique useful for industrial applications as well. For flaw detection, an x-ray image of a perfect part (the background image) is subtracted from the image of the flawed part (the foreground image), leaving an image of only the flaw. For example, in digital subtraction angiography an x-ray image of a body is subtracted from an image of the same body that has an x-ray-opaque solution injected into the blood stream, producing an image of the blood vessels. Both body images are stored digitally before subtraction. This latter technique can be a near-real-time process if the background image is stored in memory and subtracted from the foreground image as it becomes available. Images can be extracted from very complex backgrounds.

In ICF target characterization, the foreground and background images are orthogonal views of the target. Usually three orthogonal views of each target are used to completely characterize its coating. Any one of these views can serve as the background for the other two. Furthermore, it is not essential that the view selected for the background be flawless, because, in the processed-subtracted image, defects in the background image appear as the negative of similar defects in the foreground image.

Areal density is the product  $\rho x$ , where  $\rho$  is the material density and  $x$  is the material thickness. Hence, an areal density change is caused by a variation in thickness or density. Small areal density changes cause small changes in x-ray absorption. The noise in the image limits detection of very small changes in x-ray absorption because the defect must be distinguishable from the noise. However, averaging video frames allows the detection of the smallest x-ray absorption changes by improving the signal-to-noise ratio of a digitized image. In addition, digitally subtracting an averaged background image from an averaged foreground image removes fixed-pattern noise from the image. Such fixed-pattern noise may be caused by defects in the imaging device. Hence, averaging and digital subtraction reduce two components of noise in the image. Video image processors costing \$10,000 can average a video signal and subtract it from a stored background image in a just a few seconds more than the time needed to average the video frames.

Furthermore, the recent introduction of several commercial microfocus x-ray sources makes real-time and digital subtraction radiography practicable for detecting small defects. Exceedingly small changes in x-ray absorption can be detected in near real time with a spatial resolution approaching that of x-ray film.

## OPTIMAL X-RAY ABSORPTION

To detect such small changes in x-ray absorption, it is advantageous to use an x-ray energy for which the  $\mu\rho x$  product is 1 to 3, where  $\mu$  is the x-ray mass attenuation coefficient ( $\text{cm}^2/\text{g}$ ).<sup>6</sup> An anode with characteristic K-lines in the energy region below 25 keV can produce x-ray fluxes higher than those from the conventional tungsten anode.<sup>7,8</sup> For example, the x-ray flux from a molybdenum anode bombarded with 45-kV electrons is about three times more intense than the flux from a tungsten anode. Furthermore, nearly all x rays have the energies of the molybdenum K-lines between 17 and 20 keV. Therefore, very intense, nearly monochromatic sources can be generated. The 17-keV x rays from molybdenum and the 22-keV x rays from silver are very sensitive to absorption changes in my phantom, described below, because  $\mu\rho x$  is 1.35 and 0.7, respectively, for these energies.

### The Phantom

To demonstrate the usefulness of the technique just described, I constructed a phantom composed of three materials: stacked polyethylene sheets totaling 0.38 cm in thickness, 0.025-cm-thick aluminum, and 0.05-cm-thick silicon. Figure 1 shows the  $\mu\rho x$  product for the constituents of the phantom to demonstrate their x-ray absorptions.

To detect very small absorption changes, I placed an aluminum step wedge over the phantom. Each step is 1  $\mu\text{m}$  high; the step thicknesses range from 1 to 12  $\mu\text{m}$ . One micrometer of aluminum has 0.05% of the areal density in the phantom and absorbs 0.14% of 17-keV x rays. Radiographers call x-ray attenuation subject contrast. The subject contrast of the phantom is 73% at 17 keV. Figure 1 exaggerates the thickness of the step wedge for clarity.

### Image Subtraction

The resultant images are formed by the method shown in Fig. 2. A 3-mA, 45-kV electron beam bombards a special water-cooled molybdenum anode in a microfocus x-ray source\* to produce x rays that illuminate the sample phantom and step wedge. Producing the molybdenum anode included depositing molybdenum<sup>9,10</sup> on a copper anode the same size as the tungsten anode supplied by the manufacturer. In addition to the copper construction, boring out the inside of the anode and inserting a water-cooling line improved the anode's heat-dissipating characteristics.

\* Scanray MF-160 TFI Corporation, P.O. Box 1611, New Haven, CT 06506



The x-ray image of the sample, magnified by  $2\times$  geometric projection, is cast onto a special x-ray television camera, which emits a signal that is digitized and averaged by a 512-by-512 pixel, 8-bit video digitizer.\*\* The special x-ray television camera is a phosphor-coated fiber optic train butted to a silicon-intensifier-target (SIT) television camera (Fig. 3). A  $\text{Gd}_2\text{O}_2\text{S:Tb}$  coating  $150\text{ }\mu\text{m}$  thick covers a removable fiber optic faceplate 40 mm in diameter. Optical grease physically couples this faceplate to a tapered fiber optic with ends 40 and 18 mm in diameter. The 18-mm end joins to the bare front face of a SIT tube† mounted in a standard SIT camera. The fiber optic train and the shielding protect the camera's electronics from front-illuminating x rays with energies up to 50 keV. The removable, coated faceplate facilitates changing x-ray phosphors.

The 128-frame averages travel to a computer†† (not shown) through an IEEE-488 interface. The computer subtracts the 128-frame average of the phantom image from the 128-frame average of the phantom-and-step image. Although averaging 128 video frames improves the signal-to-noise ratio in the image, camera-caused fixed-pattern noise and shading errors remain. Moreover, diminishing these errors by forming the difference of two average images does not eliminate all residuals.

The resultant image is transferred back to the frame grabber and displayed on a video monitor. This entire process takes a few minutes, but alternative ways to perform the same process in a few seconds are available.

In the step wedge image stored in computer memory, the step wedge does not become visible until the background is subtracted. An example of the digital subtraction appears later in this paper.

## DETECTION OF SMALL AREAL DENSITY VARIATION

Photographs of the television monitor show difference images of the phantom and step wedge and of the crossed  $2\text{-}\mu\text{m}$ -diam tungsten wires (Figs. 4, 5, and 6). Figure 4 is the step wedge image at  $2\times$  magnification and a map of the image. The stretched contrast in Fig. 4 clearly shows the image of the first step as it emerges from the background noise. Aluminum steps are vertical with the thinnest step on the left and the thickest step on the right. Two pointers at the top and bottom mark the  $1\text{-}\mu\text{m}$ -thick edge of the step wedge. By chance, a  $2\text{-}\mu\text{m}$ -diam wire in the subtracted background image coincides exactly with the pointers. Therefore, I estimate that the second step, which is a 0.1% areal density change,

\*\* Quantex DS-20. Quantex Corporation, 252 N. Wolfe Road, Sunnyvale, CA 94086.

† RCA #4804HP2. Burle Industries, Lancaster, PA 17604.

†† PDP-11/23. Digital Equipment Corp., Maynard, MA 01754.

is detected from the background. Subsequent experiments have substantiated detection of only the second step. I estimate that this image has 4-mm spatial resolution at the 0.5% contrast of the steps; hence, the individual 0.4-mm-wide steps are not resolved. Two horizontal black lines at the top of the image are 20- and 30- $\mu$ m-diam tungsten wires. The 12- $\mu$ m-thick area of the step wedge is slightly darker at the top than at the bottom because image subtraction has not removed all of the x-ray camera's shading characteristics and the nonuniformities of the x-ray flux. Line (a-a) shows the position of the video trace in Fig. 5.

Figure 5 shows the detection of the step wedge as it emerges from the background. It is a video trace across line (a-a) in the previous figure. Arrows (a) mark the beginning of the step wedge, that is, the location of the 1- $\mu$ m-thick step of aluminum. The step wedge is 12  $\mu$ m thick between arrows (b) and (c). The dip in the trace at arrows (a) is due to the wire in the subtracted image. The dashed line drawn through the data is an estimate of the noise-averaged signal and shows the detection of the 0.1% areal density change (the second step) in the sample. The slope of this estimate to the left of (a) and to the right of (c) is caused by residuals from the image subtraction that did not completely remove the camera's shading characteristics and the nonuniformities of the x-ray flux.

In Fig. 6 a map explains a photograph of crossed 2- $\mu$ m-diam tungsten wires that overlie the phantom. These two wires are faint; however, the 6- $\mu$ m-diam wires are clearly visible. Five horizontal wires with diameters of 30, 20, 12, 6, and 2  $\mu$ m and four vertical wires with diameters of 20, 12, 6, and 2  $\mu$ m appear in the figure. Aluminum foils 20 and 12  $\mu$ m thick cover the lower right corner. This corner is cluttered because contrast stretching, used to clarify the smallest wire, has destroyed both the shading of the foils and the detection of the wires over the foils. Tungsten 2  $\mu$ m thick attenuates about 30% of 17-keV x rays; hence, 2- $\mu$ m-wide lines with 30% absorption can be detected when overlying the phantom, which has 73% subject contrast.

In the sample image of Figs. 4 and 6, the step wedge or the smallest diameter wires are not visible until the background image is subtracted. This process is shown schematically in Fig. 7 where the wedge is not visible in the 128-frame average of the step wedge on the phantom (top left); only the two pointers and the larger diameter wires appear. The background image is a 128-frame average of the phantom by itself (top right). Because the phantom has no structure, the phantom image has no visible structure. When the two images are differenced, however, the step wedge becomes visible. For the crossed wire image, the 2- $\mu$ m-diam wires are not visible until the background is subtracted.

## HIGH SENSITIVITY AND THE ADVANTAGES OF REAL TIME

A distinction must be made between the detection sensitivity and the resolving powers of a detector system. Although crossed 2- $\mu$ m-diam wires are detected in one image, the spatial resolution is not 2  $\mu$ m. If two parallel wires of this diameter were separated by their diameter, they would not be resolved in these images. However, their presence would be detected. (Feldkamp<sup>11</sup> notes a similar result.)

Currently, digital subtraction radiography detects 0.1% variations in the areal density--that is, a variation in thickness or density--on flat samples. Hence, 0.1% areal density variations can be detected in near real time. For these tiny variations, spatial resolutions as small as 1 mm are typical. However, linear features as narrow as 2  $\mu$ m with 30% attenuation can be detected but not resolved over a background that attenuates 70% of the x rays.

Detecting 0.1% defects with diameters of 10  $\mu$ m in ICF targets requires an improvement in spatial resolution. Such improvements will be realized by using integrating charge-coupled device cameras and 1- $\mu$ m-spatial-resolution phosphors described by Flannery et. al.<sup>12</sup>

The sensitivities described in this work can be obtained with samples that have an optimal x-ray examination energy of 1 to 20 keV (2 to 50 kV) by changing the anode material to select an appropriate K-line. This energy range is optimal for a wide variety of manufactured plastic and ceramic parts, such as 0.001- to 7-cm-thick samples of polystyrene or polyethylene. Furthermore, the work of Verhoeven at 75 kV suggests that similar results occur at energies above 50 kV with commercial x-ray image intensifiers.

## ACKNOWLEDGMENTS

I thank Grant H. Stokes for many useful discussions and experiments; Norman E. Elliott for writing the software for the image processing; and Lutz Dahlke of Sandia National Laboratories, Livermore, California, for many helpful discussions and for suggesting several important references. I also thank Gary Reeves for fabricating the aluminum step wedge, Elfino Armijo for fabricating the anode and other parts, P. Roger Lagasse for designing many of the components used in this experiment, Veronica Gomez for fabricating the wire-resolution targets, John Ben Cole for his help in the laboratory, and Brian Thompson for editing the paper.

## FIGURE CAPTIONS

Fig. 1. X-ray absorption in the phantom, composed of plastic, aluminum, and silicon. Absorption of the first step of the step wedge (not shown to scale) is about 0.05% of the phantom.

Fig. 2. Digital subtraction radiography. The difference of two 128-frame averages produces images of objects with changes in thickness or density as small as 0.1% and of 2- $\mu$ m-diam wires with larger absorption.

Fig. 3. The x-ray television camera. The device is a phosphor-coated, fiber optic faceplate optically coupled to a tapered fiber optic faceplate that is, in turn, coupled to a SIT television tube. Shielding on the front of the camera and the faceplate protects the camera electronics from low-energy x rays.

Fig. 4. Left: A contrast-stretched image of a step wedge showing the detection of a 0.1% areal density change over the integrated-circuit phantom. Right: A map showing the location of the wedge and other objects. Two pointers indicate the edge of the 1- $\mu$ m step. Line (a-a) locates the video trace in Fig. 5.

Fig. 5. A video trace across the step wedge (line a-a in Fig. 4) showing the detection of the second step. Arrows (a) mark the beginning of the first (1- $\mu$ m) step. Arrows (b) mark the 12- $\mu$ m step. The region between (b) and (c) is 12  $\mu$ m thick. The image of a 2- $\mu$ m-diam wire in the subtracted background image coincides exactly with arrows (a). The dashed line is an estimate of the noise-averaged signal to guide the eye.

Fig. 6. Left: Crossed 2- $\mu$ m-diam tungsten wires (black lines) detected over the phantom. Right: A map of the wires and other objects. In addition to the 2- $\mu$ m wires, the figure shows crossed wires 6, 12, and 20  $\mu$ m in diameter.

Fig. 7. Digital subtraction radiography does not show the aluminum step wedge until the sample image (step wedge on phantom) is subtracted from the background image (phantom). In this schematic representation, only the pointers and the thick wires appear in the 128-frame average of the step wedge on the phantom (top left), and no detail is seen in the average of the phantom image (top right). The step wedge is visible once the two averaged images are differenced (bottom).

## REFERENCES

1. D. M. Stupin, "Filmless Radiographic Detection of Microscopic Wires and Very Small Areal Density Variations," *Materials Evaluation* **45**, 1315-1319 (1987).
2. D. M. Stupin, "Near-Real-Time Radiography Detects 0.1% Changes in X-Ray Absorption with 2-mm Spatial Resolution," in *Review of Progress in Quantitative Nondestructive Evaluation*, Vol. 7B, D. O. Thompson and D. E. Chimenti, Eds. (Plenum Publishing, New York, 1987), pp. 1723-1730.
3. D. M. Stupin, G. H. Stokes, and J. H. Steven-Setchell, "Near-Real-Time Radiography Detects Very Small Wires and Thickness Variations," in *International Advances in Non-destructive Testing*, W. J. McGonnagle, Ed. (Gordon and Breach Science Publishers, New York, in press).
4. M. Paul Capp, Sol Nudelman, Donald Fisher, Theron W. Ovitt, Gerald D. Pond, Meryl M. Frost, Hans Roehrig, Joachim Seeger, and Donald Oimette, "Photoelectronic Radiology Department," in *Digital Radiography*, William R. Brody, Ed. (SPIE, Bellingham, Washington, 1981), Vol. 314, pp. 2-8.
5. Leon Verhoeven, "Comparison of Enhancement Capabilities of Film Subtraction and Digital Subtraction Methods," in *Digital Radiography*, William R. Brody, Ed. (SPIE, Bellingham, Washington, 1981), Vol. 314, pp. 114-120.
6. Robin P. Gardner and Ralph L. Ely, Jr., *Radioisotope Measurement Applications in Engineering* (Reinhold Publishing Corporation, New York, 1967), p. 282.
7. J. V. Gilfrich, "Spectral Distribution of X-Ray Tubes," in *Handbook of Spectroscopy*, J. W. Robinson, Ed. (CRC Press, Boca Raton, Florida, 1974), Vol. 1, pp. 232-237.
8. D. B. Brown and J. V. Gilfrich, "Measurement and Calculation of Absolute X-Ray Intensities," *J. Appl. Phys.* **42** (10), 4044-4046 (1971).
9. D. W. Carroll and W. J. McCreary, "Fabrication of Thin-Wall, Freestanding Inertial Confinement Fusion Targets by Chemical Vapor Deposition," *J. Vac. Sci. Technol.* **20** (4), 1087-1090 (1982).

10. W. J. McCreary and D. W. Carroll, "CVD Techniques Applied to Energy Problems," in *Proceedings of the Eighth International Conference on Chemical Vapor Deposition, CVD-III*, Gouviex, France, September 15-18, 1981 (The Electrochemical Society, Pennington, New Jersey, 1981), Vol. 81-7, pp. 769-781.
11. L. A. Feldkamp, Ford Motor Co., Dearborn, MI 48121, private communication, June 1987.
12. B. P. Flannery, H. W. Deckman, W. G. Roberge, and K. A. D'Amico, "Three Dimensional X-Ray Microtomography," *Science* **237**, 1439-1444 (1987).

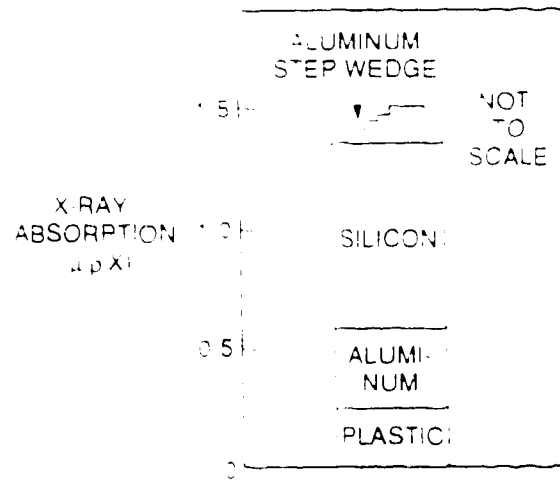


FIG. 1

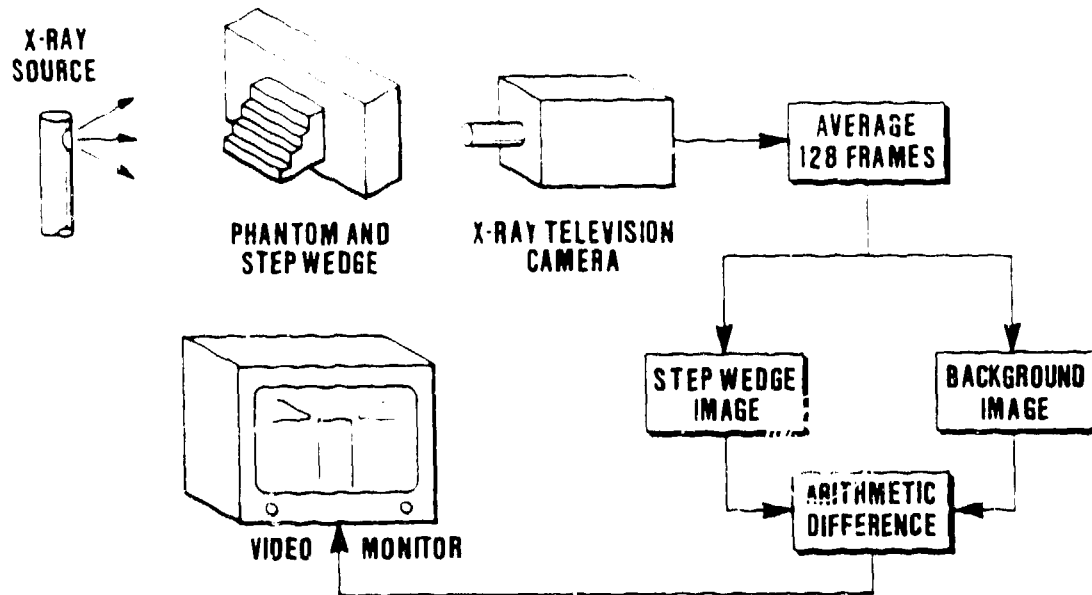


FIG. 2

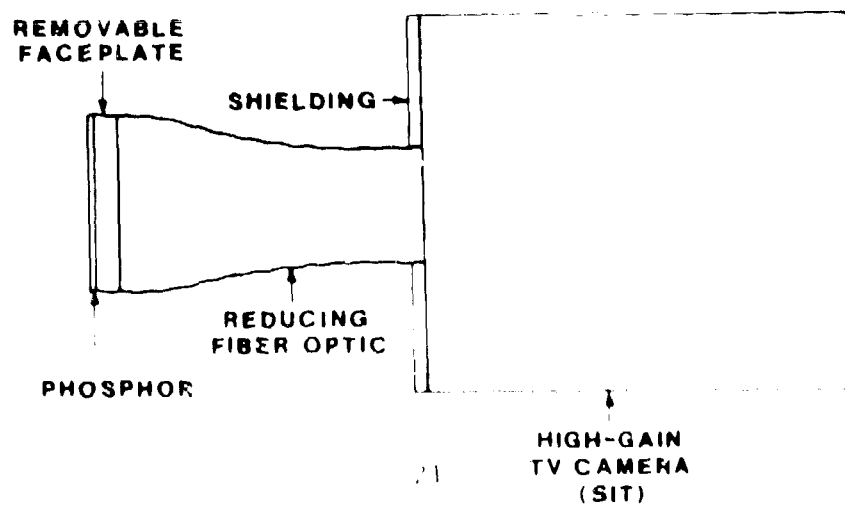


FIG. 3

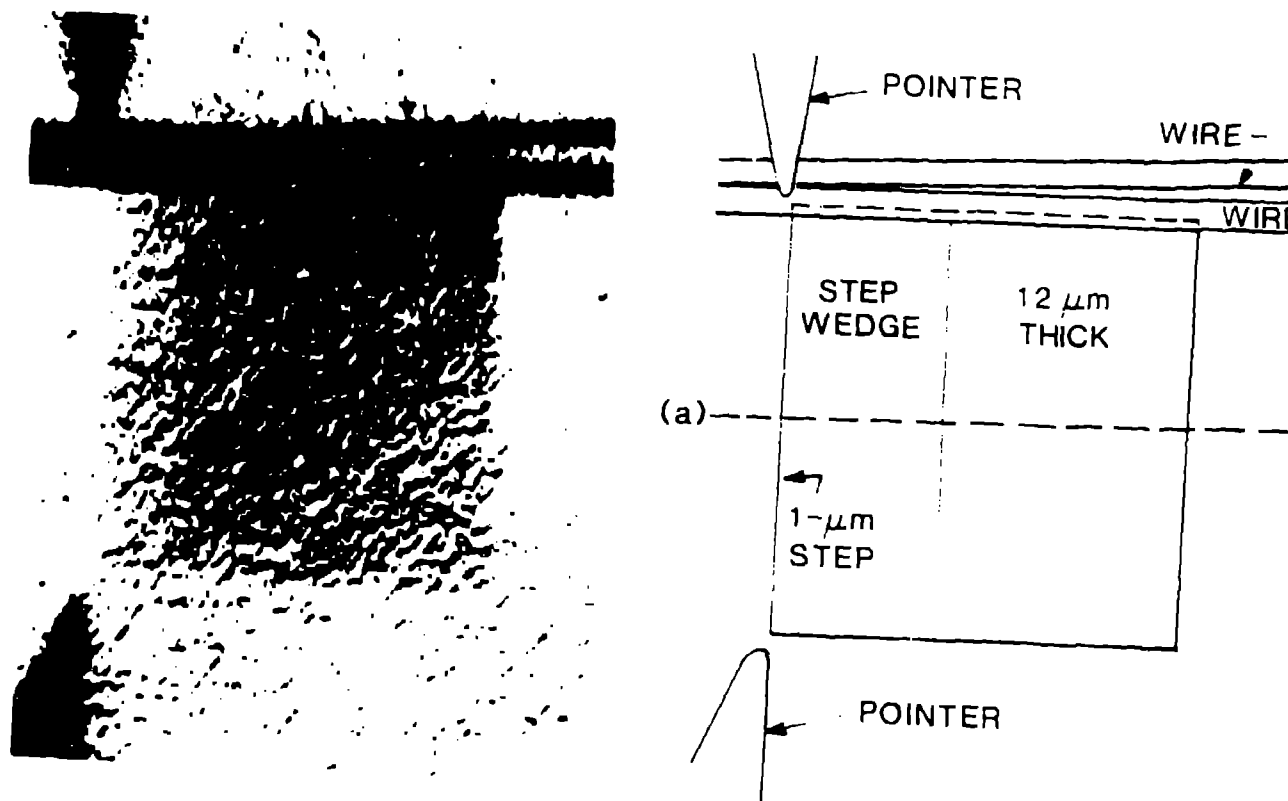


FIG. 4

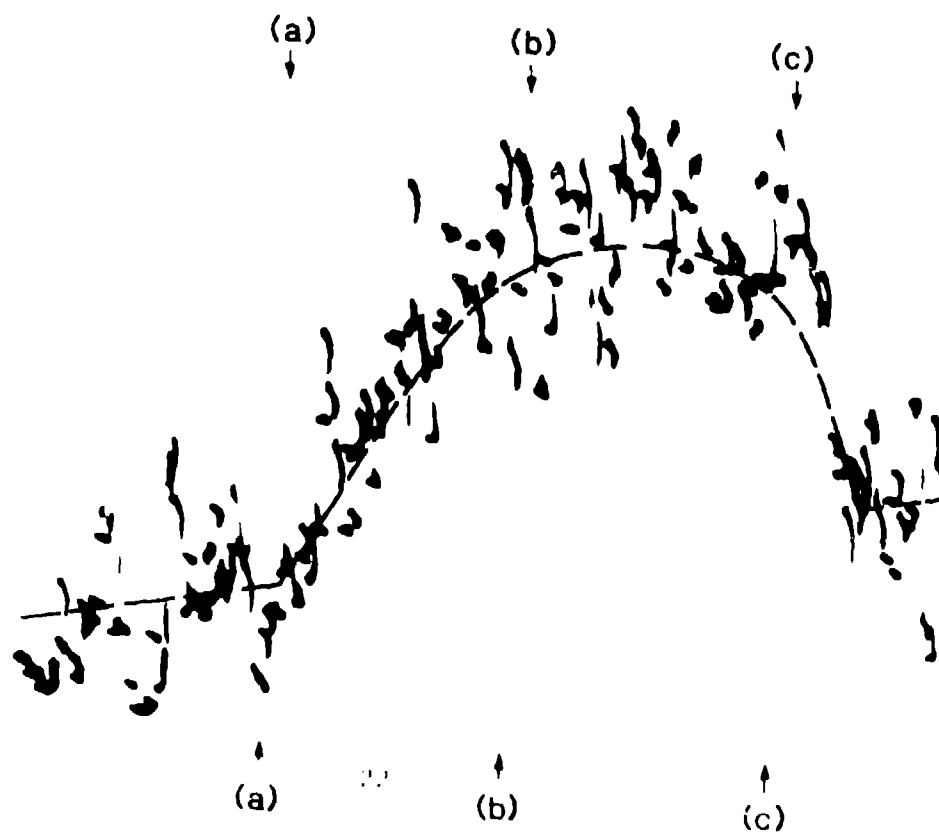


FIG. 5



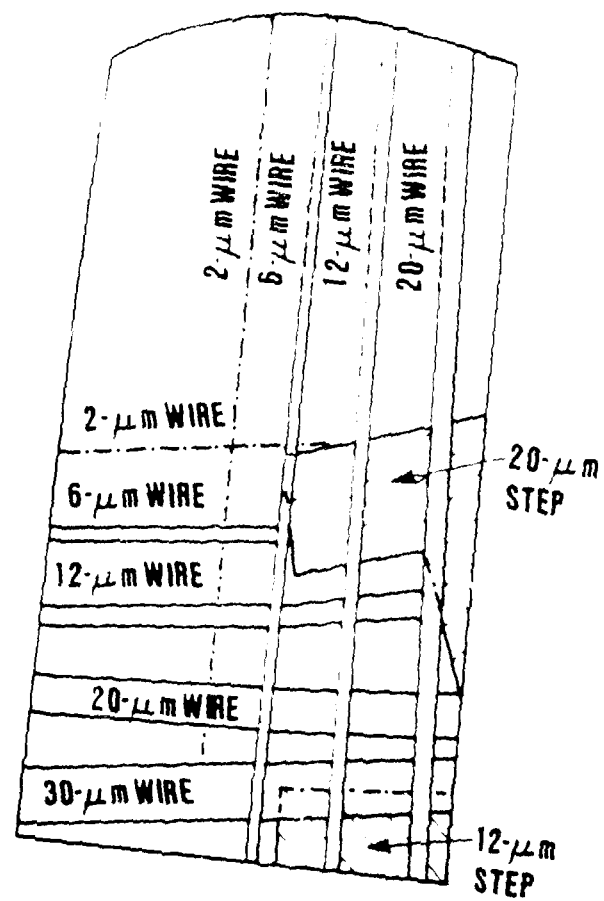


FIG. 6

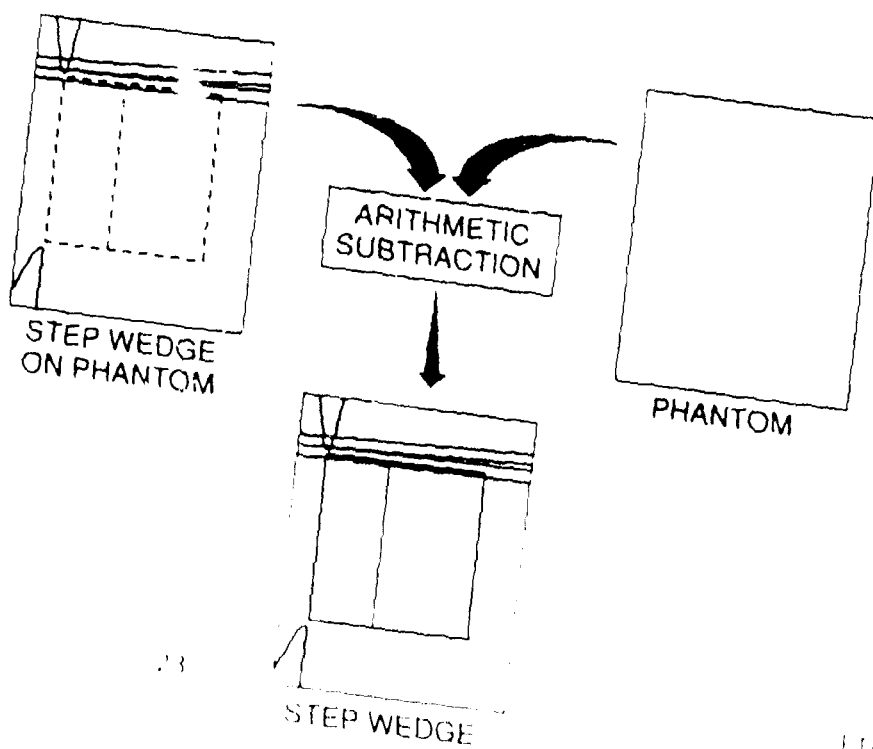


FIG. 7

**ABLATION LAYER COATING ON INERTIAL FUSION TARGETS AT  
UNIVERSITY OF ROCHESTER'S  
LABORATORY FOR LASER ENERGETICS**

Hyo-gun Kim, Roger Q. Gram, and John M. Soures  
LABORATORY FOR LASER ENERGETICS  
University of Rochester  
250 East River Road  
Rochester, NY 14623-1299

At University of Rochester's Laboratory for Laser Energetics (LLE), ablation layers are deposited on DT filled glass microballoon targets or unfilled polymer shell targets by a parylene coating scheme. The parylene process is material specific and works only for the di-para-xylylene and its derivatives. Polymerization of 2,2-paracyclophane results in a slightly rough surface finish caused by crystalline texture of the parylene film, which is approximately 60% by volume crystalline. Transforming crystalline parylene into an amorphous structure will cause the resulting film to be smoother. This transformation is accomplished by increasing the complexity and bulky nature of the monomer materials. In order to limit the composition of the ablation layer to hydrocarbons, 2,2-paracyclophane was modified with the alkyl group only.<sup>1</sup> Alkylation of di-para-xylylene introduces significant changes in the properties and structure of the resulting polymers. Crystallinity, melting temperature ( $T_m$ ), and glass transition temperature ( $T_g$ ) of the pure polymer decrease when modified. X-ray diffraction studies<sup>2</sup> indicate that alkyl modification does not alter the monoclinic unit cell structure. The lengths of the a-axis and c-axis remain constant but the length of the b-axis increases with the size of the pendant group. Since the c-axis lies along the chain direction and is parallel to the layer surface, the alkylated monomer is believed to form a polymer with the alkyl pendant group aligned perpendicularly to the layer surface.

X-ray diffraction experiments show ethyl parylene to consist of finely dispersed crystallites. The diminished crystallinity achieved with our alkyl modification serves a dual purpose. The surface roughness arising from crystalline texture is greatly diminished and the ablation layer surface smoothness is better than 1000 Å. In addition, density fluctuations within the layer are minimized.

The accurate and precise control of parylene coating thickness is performed by a laser reflectometer developed at LLE.<sup>3</sup> This reflectometer monitors the sinusoidal modulation of the reflectivity of a witness substrate during the coating. The functional relationship between the

reflectivity and optical thickness of the coating allows the measurement of film thickness during coating. The accuracy of the reflectometer can be as good as within a few hundred angstroms provided that the index of refraction is precisely known. In general, an accuracy of less than 1000 Å is routinely achieved.

If targets are supported using glass fibers or films, these constitute a significant perturbation to the sphericity and can contribute to hydrodynamic instability growth during the implosion process. An alternate target support scheme which was developed at LLE utilizes spider webs to minimize the target mass perturbation. Such a mounting scheme produces a thousand-fold reduction in the effective target support mass. This improvement is defeated, however, if a target with a low mass support is coated with an additional material that also coats and thickens the diameter of the support stalk. It would be desirable to coat the target while it is mechanically unsupported, before mounting on the low mass support. Such coating is accomplished at LLE by bouncing the targets on the surface of a mechanical resonator while the targets are coated by a modified parylene process.<sup>4</sup> Optimum bouncing is achieved with the resonator surface moving with a peak vertical velocity of ~3 cm/s at a frequency much greater than the bounce frequency of the targets. The resonator, a solid cylinder of high-Q material, uses a longitudinal mode of vibration motion, which is uniform over its surface. A flexural mode of the cylinder is used for dislodging targets which have become stuck. In their natural state, the targets become charged triboelectrically and by the beta emission from the tritium decay. The adhesion of these charged targets is eliminated by creating a low power plasma in the bouncing region.

The low power plasma required to prevent targets from sticking to each other and to the vibrating surface increases the deposition rate by a factor of 2 to 4. Careful control of plasma conditions is required to maintain bouncing while avoiding overly rapid polymerization, defect growth, embrittlement, and other adverse effects in the parylene layers.

The tensile strength achieved in bounce-coated parylene layers allows high fuel pressures in polymer shell targets. To measure the tensile strengths,<sup>5</sup> a set of polymer shells made by Lawrence Livermore National Laboratory (LLNL) was coated with various thicknesses of parylene, up to 12 µm. By permeating these shells with helium gas and quickly releasing the pressure, the highest attainable internal pressure was found for these shells. The tensile strength, 36 MPa, is comparable to values listed for nonplasma parylene.

Bounce-coated parylene layers have useful barrier properties for argon and gases with larger atomic radii. To measure the permeability to argon, bounce-coated polymer shells were permeated with argon, and the volume of gas permeating back out was measured as a function of

time. The permeability found for argon,  $3.3 \times 10^{-17}$  mol/ms Pa at 23°C, allows targets to be fabricated with time constants of several hours for argon retention.

#### ACKNOWLEDGMENT

This work was supported by the U.S. Department of Energy Office of Inertial Fusion under agreement No. DE-FC08-85DP40200 and by the Laser Fusion Feasibility Project at the Laboratory for Laser Energetics which has the following sponsors: Empire State Electric Energy Research Corporation, New York State Energy Research and Development Authority, Ontario Hydro, and the University of Rochester. Such support does not imply endorsement of the content by any of the above parties.

#### REFERENCES

1. LLE Review, University of Rochester, Vol. 9, 21 (1981).
2. N. S. Murthy and H. Kim, Polymer **25**, 1093 (1984).
3. H. Kim, T. Powers and J. Mason, J. Vac. Sci. Technol. **21**, 900 (1982).
4. R. Q. Gram, H. Kim, J. F. Mason and M. Wittman, J. Vac. Sci. Technol. **A4**, 1145 (1986).
5. R. Q. Gram, C. K. Immesoete, H. Kim, and L. Forsiey, J. Vac. Sci. Technol. **A**, to be published.

# **X-RAY MICROSCOPY OF INERTIAL FUSION TARGETS USING A LASER PRODUCED PLASMA AS AN X-RAY SOURCE**

by

Hyo-gun Kim and Mark D. Wittman  
LABORATORY FOR LASER ENERGETICS

University of Rochester  
250 East River Road  
Rochester, NY 14623-1299

## **ABSTRACT**

With the advent of an ablative layer coating technology for mechanically nonsupported ICF targets, the conventional optical interferometric technique for the characterization of these targets is no longer feasible since the batch process of this bounce coating technique makes it difficult to account for individual targets. A soft x-ray contact microradiography method which was developed for this purpose is limited in resolution by the  $0.5\text{-}\mu\text{m}$  grain size of the photographic medium used. Utilization of an x-ray sensitive photoresist extends the resolution to as low as  $50\text{ \AA}$ . The use of a laser-generated x-ray source for x-ray microscopy appears to require much less energy than published photoresist sensitivity data. A single-shot exposure of 100 J,  $0.527\text{-}\mu\text{m}$  wavelength and 1-ns laser shot suffices for image formation. The resulting x-ray micrographs show a higher spatial resolution than the images obtained by previous radiography techniques. The resolution of  $0.2\text{ }\mu\text{m}$  in the present study is due to the finite size of the x-ray source.

## **SUMMARY**

The successful implosion of direct drive inertial fusion (IF) targets requires high spherical symmetry, extremely uniform coatings, and a smooth surface finish. By replacing the glass capillary on which IF targets have been mounted in the past with submicron mounting schemes involving spider web filaments, this major mass perturbation has been substantially reduced. This requires that the targets be coated with plastic layers while they are not mechanically supported, but are bouncing within the pan shaped end of a mechanical resonator.

This bouncing process is basically a batch process in which all of the targets are mixed, thus losing the identity of the individual targets. Optical interferometry requires information before and after ablation layer coating to determine the coating thickness; and, therefore, cannot be used for targets coated using this process. X-ray contact microradiography is best suited for this purpose because it is a batch process which can characterize a large number of targets in a single exposure and can be used to examine multilayered opaque targets.

The resolution limit of x-ray contact microradiography is due to the grain size of the photographic emulsion utilized in the process. The grain size of the emulsion is at best on the order of  $0.5\text{ }\mu\text{m}$ ; thus, the minimum discernible feature size would have to be as large as several grains, i.e.,  $1\text{--}2\text{ }\mu\text{m}$ . The resolution can be improved if the emulsion is replaced by an x-ray sensitive polymer, which, in general, has a resolution of several hundred angstroms. This technique, termed x-ray contact microscopy, originally developed for morphological characterization of biological cells, is a hybrid of x-ray contact microradiography and x-ray lithography. We have adapted this technique for target characterization using a laser produced plasma as an x-ray source. When a high-power laser pulse is focused onto a foil target (e.g., Al, Ti, Zn) with a typical focal spot diameter of  $100\text{ }\mu\text{m}$ , an extremely hot plasma of small dimensions is formed, which in turn emits an intense pulse of x-rays.

A schematic of the experimental configuration is given in Fig. 1. The frequency doubled GDL Nd:glass laser, operating with 1-ns pulses at a wavelength of  $0.527\text{ }\mu\text{m}$  and 100 J of energy, is focused to a spot of  $\sim 100\text{ }\mu\text{m}$  in diameter on a flat target. The target chamber which includes the ICF targets and resist is evacuated to a pressure of  $\sim 10^{-6}$  Torr. The distance from the x-ray source to the ICF target is 10 cm, at which the penumbral blurring due to the finite source size is  $0.2\text{ }\mu\text{m}$ .

The photoresist coated Si wafer was held in intimate contact with the CH coated IF targets, which were supported between two tensioned  $2\text{ }\mu\text{m}$ -thick polyester films. A  $2\text{ }\mu\text{m}$  thick polyester film coated with  $1000\text{ }\text{\AA}$  of aluminum was placed between this assembly and the plasma x ray source to eliminate the portion of the electromagnetic spectrum emitted by the plasma with wavelengths longer than those of soft x rays.

The photoresist used is poly (butene 1 sulfone) (PBS) and it was used as received. The resist was spin coated onto a silicon wafer to a thickness of  $0.5\text{ }\mu\text{m}$ . Upon exposure, the resist was developed using a 70/30 mixture of methyl isoamyl ketone/2-pentanone followed by rinsing in a 60/40 mixture of methyl isoamyl ketone/isopropyl alcohol. The image was then examined under a differential interference contrast microscope. Postbaking of the photoresist at  $120^{\circ}\text{C}$  for 30 minutes increased the contrast.

The image shown in Fig. 2 is typical of those produced using this technique. It was produced by two successive laser shots of nearly equal energy which total 265 J on a Mo foil. Clearly visible in Fig. 2 is the 6- $\mu\text{m}$ -thick CH coating on the solid glass sphere. The variation in contrast about the perimeter of the image is a function of the optics used to view it and should be ignored.

When viewing images of submicron coatings using an interference contrast microscope, there are no distinct lines delineating the plastic-glass and image-background interfaces. Instead, these regions are bordered by a ring of finite width. This is predominantly caused by penumbral blurring in the image itself due to the finite extent of the source, and from the ultimate resolution of the microscope optics used to view and enlarge it. Penumbral blurring of the image can be reduced by increasing the source to sample distance; however, this blurring decreased linearly with increased distance while the x-ray irradiance on the imaging medium falls off quadratically. Also, scanning electron microscopy can be used to view the resultant image with better spatial resolution; but, because PBS was designed to be an electron beam resist, damage to the image occurs immediately upon examination. Certain replication techniques and subsequent viewing with a transmission electron microscope have been developed to alleviate this problem.

The penumbral blurring present in the images was determined experimentally to be  $\sim 0.2\ \mu\text{m}$ . This figure is in good agreement with the penumbral blurring as calculated from the previously stated geometric conditions; and it is also on the order of the resolution limit of an optical microscope. Therefore, using this technique under the present conditions, material coating thicknesses cannot be determined that under  $0.4\ \mu\text{m}$  in thickness.

As discussed above, we have shown that contact x ray microscopy is capable of characterizing inertial fusion targets with submicron resolution. The finite resolution of  $0.2\ \mu\text{m}$  in these experiments is due to the  $100\ \mu\text{m}$  diameter size of the laser produced x ray source, but not due to the resolution of the imaging medium, the photoresist. The resolution can be improved by making the source smaller and/or increasing the distance between the source and the ICF targets.

#### ACKNOWLEDGMENT

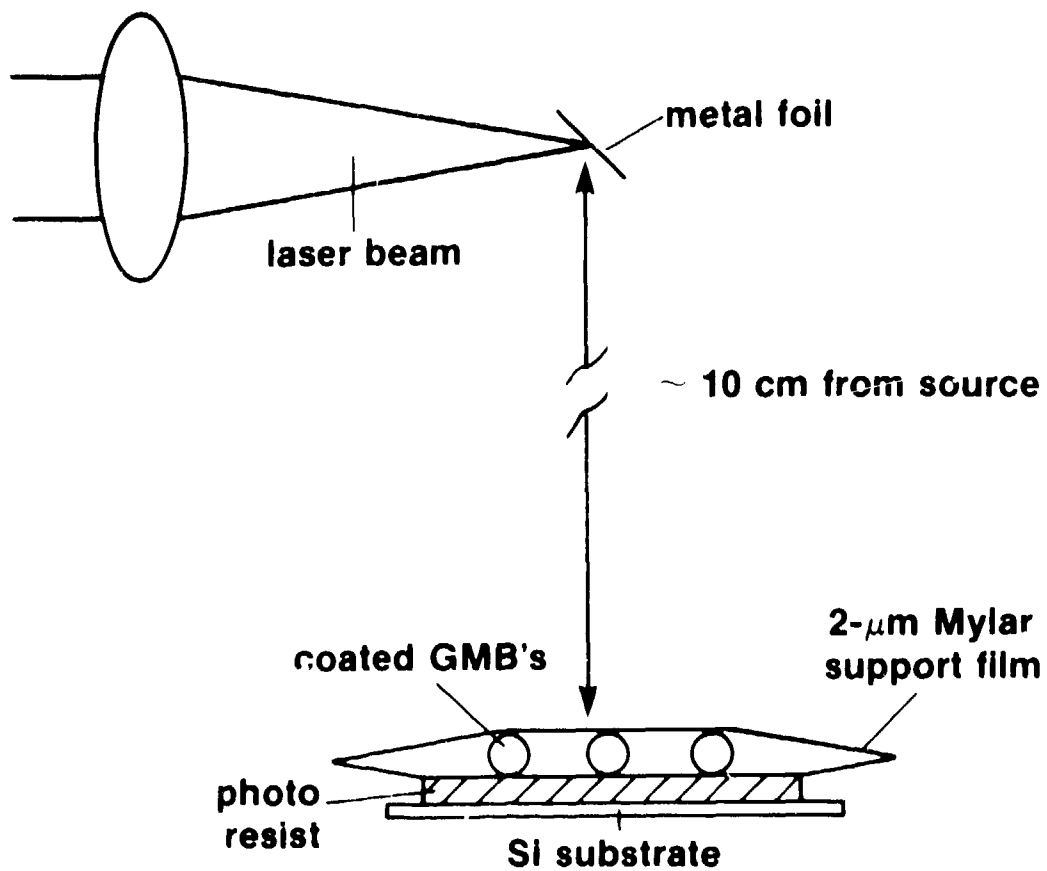
This work was supported by the U.S. Department of Energy Office of Inertial Fusion under agreement No. DE-FC08-85DP40200 and by the Laser Fusion Feasibility Project at the Laboratory for Laser Energetics which has the following sponsors: Empire State Electric Energy Research Corporation, New York State Energy Research and Development Authority, Ontario Hydro, and the University of Rochester. Such support does not imply endorsement of the content by any of the above parties.

## FIGURE CAPTIONS

Figure 1      Experimental configuration of x-ray microscopy using a laser-produced plasma as an x-ray source.

Figure 2      X-ray micrograph of a glass microballoon coated with a 6- $\mu\text{m}$  -thick parylene layer.





T822



100  $\mu\text{m}$

# A STUDY OF FACTORS AFFECTING THE DEPOSITION OF SMOOTH PLASMA POLYMERS

by

Richard L. Crawley, John C. Daukas, and Steven R. Murrell  
KMS Fusion, Inc.  
3621 South State Road  
Ann Arbor, Michigan 48106

## INTRODUCTION

We have been working to develop smooth CH coatings on glass and polymer spherical fuel capsules. Last year we were requested to dramatically improve the surface finish of the glow discharge polymer (GDP) coatings. This report summarizes the development carried out to accomplish this task and the results obtained along the way. We wish to acknowledge the support of LLNL personnel in this effort, including Bill Hatcher, Steve Letts, and Larry Witt.

## BACKGROUND

A typical surface finish of our previous standard GDP coatings is shown in Fig. 1. The surface can be seen to consist of a background surface texture which resembles cauliflower and a superimposed set of mound-like structures. The size of these features on the coated shells is dependent on many known as well as unknown parameters, including deposition chamber geometry, gas composition and flow rates, reaction pressure, and R-F power and input configuration.

Workers at LLNL have reported on the production of coatings with ultrasmooth surface finishes using the helical resonator plasma generator GDP system. We took a sample of uncoated shells to LLNL and in collaboration with LLNL scientists had them coated using the helical resonator. [This allowed us to make direct comparisons of surface finish on similar fuel capsules with similar cleaning and handling procedures.] We found that under a narrow range of operating conditions the helical resonator system did indeed produce GDP coatings with no discernible surface features. This not only suggested that glass shell surface cleanliness was adequate but that certain operating conditions lead to a lack of surface mounds and 'cauliflower' type background.

## DEVELOPMENT AND RESULTS

It was decided to bring up a developmental system at KMSF (GDP system #3) able to run under similar conditions to the helical resonator. As better surfaces were made, these operating changes could be incorporated in our production coaters (GDP #'s 1 and 2) with the least amount of production down time.

The initial deposition configuration is shown schematically in Fig. 2. The shells are rolled-bounced on a PZT driven bouncer pan (courtesy of LLNL) under the glow of a tapered plasma tube (with ideal PZT driver conditions the shells appear to remain very near the pan surface, rolling in spiral patterns without significant departures from the pan surface). The gas is introduced at the top, typically a mixture of hydrogen and butadiene at a flow rate of 10 sccm to 0.4 sccm, respectively. Maximum R-F power was limited to 7.5 watts (at 13.56 MHz) by the onset of flaking of the coating off the walls of the plasma tube and the bouncer cup.

An SEM photomicrograph of a typical GDP coating on a 350  $\mu$ m glass shell is shown in Fig. 3. Here it can be seen that the basic 'cauliflower' type background and mound-like structures are still there, but at reduced severity. Looking closely at the higher magnification image one sees a small piece of 'debris' highlighted against the background due to electron charging. We feel this 'debris' represents gas phase nucleated polymer which has dropped onto the surface of the shell and is in the process of being incorporated into the growing surface by continued deposition.

Moreover, we feel the deposition of gas phase nucleated polymer particulates leads to the moundlike structures seen on the GDP coatings. Ray Leiping et al. of LANL reported on conditions leading to the formation of gas phase polymer particles in a bell jar type plasma deposition system.<sup>2</sup> Bernie Brinker has seen a cloud of gas phase particulates hovering above their bounce coated shells in a microwave driven vertical plasma tube.<sup>3</sup> Steve Letts of LANL has worked with pulsed R F plasmas as a means of 'flushing out' the gas phase particulates before they could grow to a size where the coated shells would be effected.<sup>4</sup>

The gas phase nucleated polymer particulates appear to 'hang up' in the plasma for a period of time, growing in size, before dropping down to coat

the shells. It may be that electron charging of the particulate allows it to 'ride' the magnetic field produced by the R-F electric field. Gas flow conditions could also affect the residence time of the particulates in the plasma. We added a 'skirt' below the plasma tube in order to divert the gas flow directly onto the bounce-rolling shells. Figure 4 shows a schematic of the plasma tube system with the skirt. Note that the skirt extends the gas flow right down into the cup, perhaps significantly changing the flow pattern of the gas in this trans-molecular flow-viscous flow pressure regime (typically 75-150 mtorr in this location).

Figure 5 shows typical GDP coatings on glass shells produced using this deposition configuration. It can be seen that there is a complete absence of mound-like structures on the surface. This dramatic reduction in features suggests that gas phase particulates are not affecting the growing surface coating on the shells. It also reaffirms the belief that the initial raw shell stock is adequately clean and free of debris. We feel that the use of a skirt below the plasma tube changed the flow characteristics of the gas such that gas nucleated particulates could not ride the magnetic field long enough to grow to significant sizes.

However, the background surface texture remained to be addressed. It could be surmised that the surface is made up of a myriad of small scale gas phase particulates impinging on the growing surface to be incorporated into the film. But as yet there is no direct evidence to support this hypothesis. Moreover, this process could not be reasonably used to describe the ultra-smooth surfaces obtained using the helical resonator, where no discernible 'cauliflower' type structure is found even at very high magnification. Alternately, the surface could be produced by a combination of deposition processes occurring simultaneously, including deposition of polymer forming radicals which undergo 'normal' addition polymerization and deposition of small fragments of molecules which impinge on the surface and quickly become crosslinked into the surface. Operating parameters could determine which process dominates the coating deposition.

The onset of stress induces flaking of coating material off the walls of the tube and bouncer pan prevented us from raising the R F power intensity above 7.5 watts. The addition of water and/or forced air cooling of the

plasma tube reduced the risk of flaking and resulted in smoother coatings. Figure 6 shows an SEM photomicrograph of a typical shell coated with an air/water cooled plasma tube (with skirt). It can be seen that the background 'cauliflower' texture has been reduced significantly, apparently by the cooling of the tube. The LLNL helical resonator uses a water jacket with pressurized air blowby which appears much more effective at cooling the plasma tube than our muffin fan blower. This allows them to run at 20 watts of R-F power. LLNL lent us one of their helical resonators which was installed on our production GDP coater system #1. With this composite system, GDP coatings were produced with featureless surfaces (see Fig. 7). However, reducing the cooling air pressure, we could not run at higher power levels without severe flaking off the plasma tube. And attempts to run at reduced power levels with the helical resonator composite system led to a reoccurrence of a 'cauliflower' type background surface finish (see Fig. 8).

#### CONCLUSIONS

We conclude that mound-like growth structures in GDP coatings can be reduced by adjusting gas flow conditions to deter the growth of gas phase nucleated particulates. Also, the background 'cauliflower' type surface finish appears to be effected by plasma parameters including R-F power. This may be due to a change in dominance of normal surface addition polymerization versus crosslinking as the primary deposition mechanism. However, more work is needed in this area to elucidate what mechanism is responsible for the reduction of the 'cauliflower' surface texture.

#### REFERENCES

1. S. A. Letts, D. W. Myers, L. A. Witt, "Ultrasooth Plasma Polymerized Coatings for Laser Fusion Targets," UCRL 84475, August, 1980.
2. R. Leipins and K. Sakaoku, J. Appl. Polym. Sci., **16**, p. 2633, 1972.
3. B. A. Brinker, LLE, Private Communicatio at 29th National AVS Symposium, October, 1982.

4. S. A. Letts, "Hydrocarbon Coatings," in LLNL 1979 Laser Program Annual Report, UCRL #50021-79, p. 4-10.

## FIGURE CAPTIONS

- Figure 1. SEM micrographs of 350  $\mu\text{m}$  diameter glass Microshell<sup>R</sup> fuel capsule coated with 20  $\mu\text{ms}$  of glow discharge polymer (GDP) CH (GDP #1, 6/25/88).
- Figure 2. Schematic of initial reconfiguration of KMSF GDP coating system.
- Figure 3. SEM micrographs of Microshell<sup>R</sup> capsule coated with 17.5  $\mu\text{ms}$  GDP using reconfigured system at 76 mtorr pressure, 0.3 sccm butadiene, 7.0 sccm hydrogen, 7.5 watts 13.56 MHz R-F, at an apparent rate of 0.41  $\mu\text{m/hr}$  (GDP #3, 9/29/88)
- Figure 4. Schematic of KMSF GDP coating system with 'skirt' added below the plasma tube.
- Figure 5. SEM micrographs of Microshell<sup>R</sup> capsule coated with 39  $\mu\text{ms}$  GDP using plasma tube with skirt and 75 mtorr pressure, 0.3 sccm butadiene, 7.0 sccm hydrogen, 7.5 watts 13.56 MHz R-F, at an apparent rate of 0.6  $\mu\text{m/hr}$  (GDP #3, 10/20/88).
- Figure 6. SEM micrograph of Microshell<sup>R</sup> capsule coated with 23  $\mu\text{ms}$  GDP using cooled plasma tube and 75 mtorr pressure, 0.3 sccm butadiene, 7.0 sccm hydrogen, 7.5 watts 13.56 MHz R-F, at an apparent rate of 0.41  $\mu\text{m/hr}$  (GDP #1, 10/22/88).
- Figure 7. SEM micrograph of Microshell<sup>R</sup> capsule coated with 30  $\mu\text{ms}$  GDP using composite helical resonator KMSF GDP coating system #1 operating at 72 mtorr pressure, 0.4 sccm trans-2-butene, 10.0 sccm hydrogen, 20 watts 42 MHz R-F, at an apparent rate of 0.57  $\mu\text{m/hr}$  (GDP #1, 12/18/87).
- Figure 8. SEM micrograph of Microshell<sup>R</sup> Capsule coated with 15.3  $\mu\text{m}$  GDP using composite GDP system #1 operating at 75 mtorr pressure, 0.4 sccm trans-2-butene, 10.0 sccm hydrogen, with 7.5 watts 42.5 MHz R-F, with an apparent rate of 0.57  $\mu\text{m/hr}$  (GDP #1, 5/31/88).



Figure 1. SEM micrographs of 350  $\mu\text{m}$  diameter glass microshell<sup>®</sup> fuel capsule coated with 20  $\mu\text{m}$ s of glow discharge polymer (GDP) CH (GDP #1, 6/25/88).

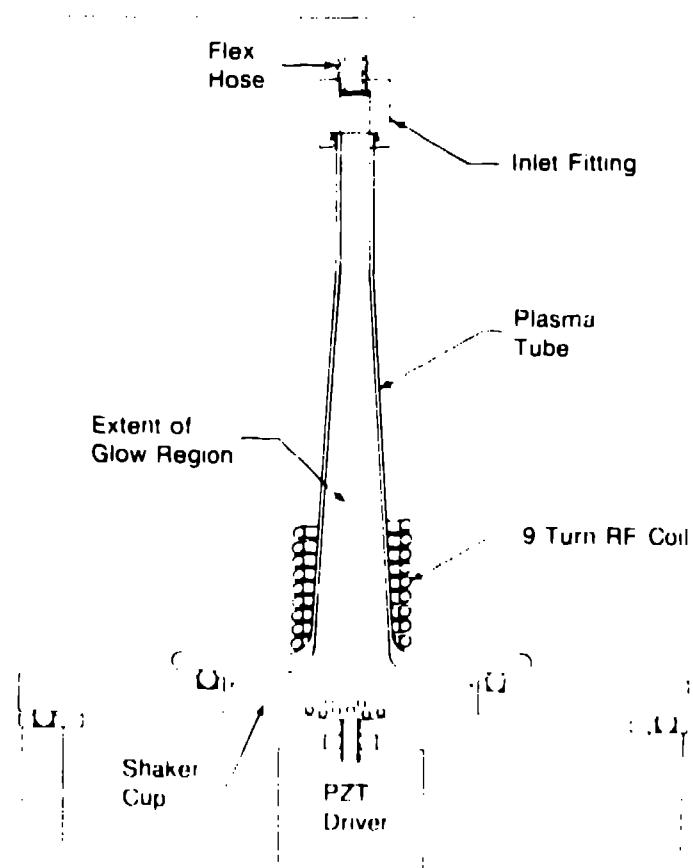


Figure 2 Schematic of initial reconfiguration of KMSF GDP coating system





Figure 3. SEM micrographs of microshell<sup>®</sup> capsule coated with 39  $\mu\text{ms}$  GDP using reconfigured system at 76 mtorr pressure, 0.3 sccm butadiene, 7.0 sccm hydrogen, 7.5 watts of 13.56 MHz R-F power, at an apparent rate of 0.41  $\mu\text{m/hr}$  (GDP #3, 9/29/87).

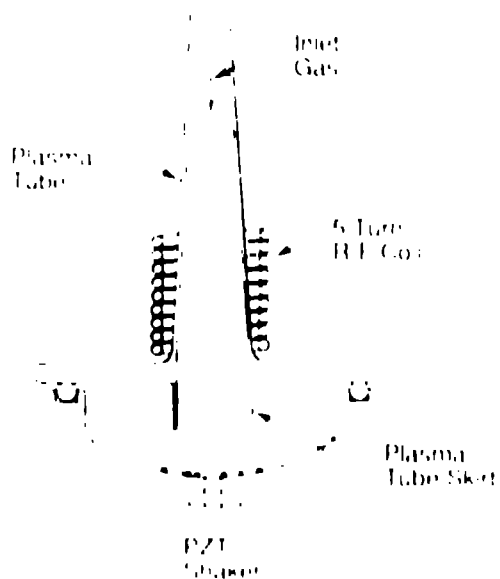


Figure 4 Schematic of KMSF GDP coating system with 'skirt' added below the plasma tube

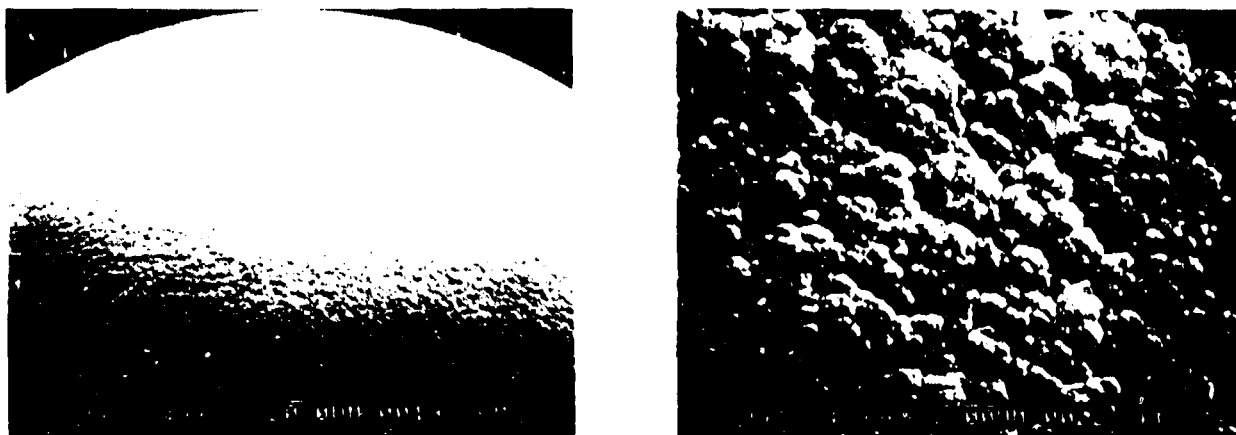


Figure 5. SEM micrographs of microshell® capsule coated with 39  $\mu\text{ms}$  GDP using plasma tube with skirt and 75 mtorr pressure, 0.3 sccm butadiene, 7.0 sccm hydrogen, 7.5 watts 13.56 MHz R-F, at an apparent rate of 0.6  $\mu\text{m/hr}$  (GDP #3, 10/20/87).



Figure 6. SEM micrograph of microshell® capsule coated with 23  $\mu\text{ms}$  GDP using cooled plasma tube and 75 mtorr pressure, 0.3 sccm butadiene, 7.0 sccm hydrogen, 7.5 watts 13.56 MHz R-F, at an apparent rate of 0.41  $\mu\text{m/hr}$  (GDP #1, 10/22/87)

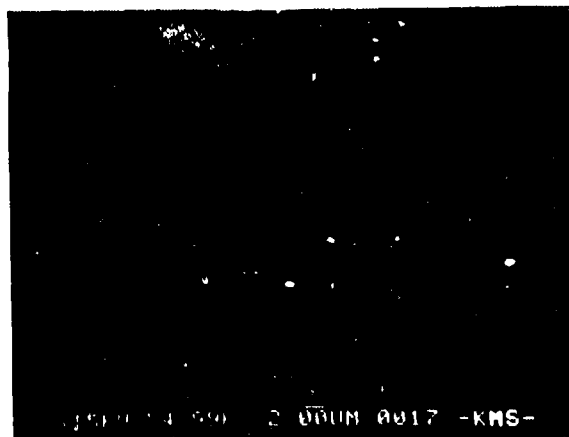


Figure 7. SEM micrograph of microshell<sup>®</sup> capsule coated with 30  $\mu\text{m}$  GDP using composite helical resonator KMSF GDP coating system #1 operating at 72 mtorr pressure, 0.4 sccm trans-2-butene, 10.0 sccm hydrogen, 20 watts 42 MHz R-F, at an apparent rate of 0.57  $\mu\text{m/hr}$  (GDP #1, 12/18/87).

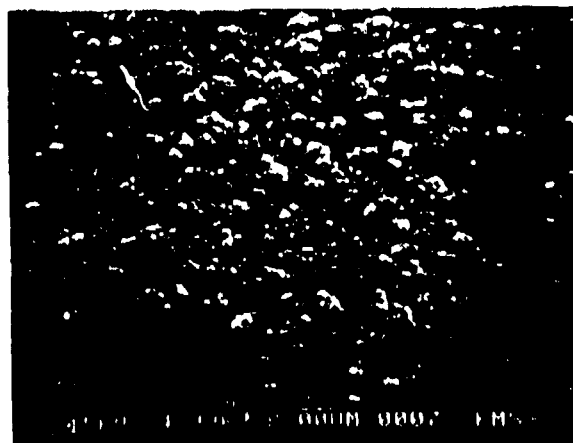
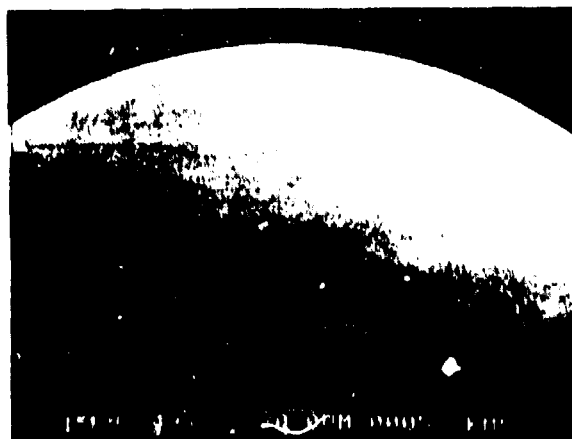


Figure 8. SEM micrograph of microshell<sup>®</sup> capsule coated with 15.3  $\mu\text{m}$  GDP using composite GDP system #1 operating at 75 mtorr pressure, 0.4 sccm trans-2-butene, 10.0 sccm hydrogen, with 7.5 watts 42.5 MHz R-F, with an apparent rate of 0.57  $\mu\text{m/hr}$  (GDP #1, 5/31/88)

## COMPOSITE FOAMS

Alice M. Nytray, Joel Williams and Mark Wilkerson  
Los Alamos National Laboratory  
Materials Science and Technology Division  
Los Alamos, New Mexico

### Introduction

Composite foams have been prepared which incorporate the best attributes of two materials. Polystyrene emulsion foams prepared by the Unilever method<sup>1</sup>, Si aerogel, and resole foams have been studied for use in laser fusion targets<sup>2</sup>. Foams for this application need to be strong enough to withstand machining operations and handling, yet they also require small pore/cell sizes because they must hold liquid DT against gravitational forces. These attributes are difficult to achieve in a single foam. The polystyrene emulsion foams have the advantages that they can be prepared easily over a wide range of densities (0.015 g/cc to 0.20g/cc) and are easy to handle and machine; however, the small cell sizes needed for good wicking of the DT liquid fuel are difficult to achieve. On the other hand, Si aerogel and resole foams have the desired small cell size ( $< 0.1 \mu\text{m}$ ), but the materials are mechanically weak making them difficult to handle and machine. Using a backfilling process, we have been able to make binary composite foams in which the cells of the polystyrene emulsion foam have been filled with aerogel or resole foam. These materials have the small cell sizes needed for good wicking of the liquid DT fuel and are rugged and easy to machine.

Figure 1 shows the typical open cell structure of a polystyrene emulsion foam (0.1 g/cc) with a cell size of about 30  $\mu\text{m}$ . Figure 2 shows the same foam backfilled with Si aerogel at several different concentrations. The aerogel concentrations, of

around 25mg/cc. At 10 mg/cc there was insufficient Si aerogel to complete fill the polystyrene foam.

Figure 4 and 5 show the resole foams prepared from resorcinol-formaldehyde and phloroglucinol-formaldehyde respectively. Although these materials filled the cells, the composite foams tended to shrink somewhat upon extraction especially at the higher densities of resorcinol-formaldehyde. These same characteristics were reported earlier for the resole foams<sup>2</sup>. The phloroglucinol-formaldehyde filled composite foams showed less shrinkage and could be successfully filled to lower concentrations.

Deuterium wicking experiments were performed at the National Bureau of Standards on several of the composite foams (Figure 6). The data (Fig. 7,8 ) indicates that the aerogel filled composite foam as well as the low density P/F filled foam wicked the liquid deuterium better than any of the individual materials.<sup>3</sup>

Compression tests indicate that the strength of the composite foam as well as its machinability is determined solely by the strength of the polystyrene foam.

At the present time, we are working to broaden the range of composite foam densities and to determine both the chemical and physical properties of these new materials.

## **Experimental Section**

### Preparation of the silica aerogel filled polystyrene emulsion foams.

Two stock solutions were prepared: a 250 ml stock solution containing 130.4g of tetramethyloxosilicate in anhydrous methanol and a 200 ml stock solution containing 48g of water in methanol. Equal amounts of solution of the stock solutions were mixed and diluted with additional methanol (or methanol and toluene) to give the desired density of filler. For example, 100 mg/cm<sup>3</sup> silica filler (Figure 1) was prepared by mixing 20 ml of each stock solutions with 10 ml of toluene. The polystyrene foam was immersed in the solution and trapped air was removed from the foam by drawing a vacuum over the solution. After the foam was saturated with the solution, three drops of catalyst (either fluoroboric acid or concentrated ammonium hydroxide) were added to the solution to initiate the polymerization. Generally, the gelation occurred within 24h. The

excess gel was removed from the surface of the foam; and, the foam was placed in a Polston to remove the solvents from the gel network. After a week of liquid CO<sub>2</sub> extraction, the carbon dioxide was supercritically extracted by raising the temperature of the Polaron to 40C and 1400psi. The CO<sub>2</sub> gas was then vented slowly overnight.

#### Preparation of Resorcinol-formaldehyde filled polystyrene emulsion foam.

To make a 6 wt% resorcinol-formaldehyde foam, 3.25 g resorcinol and 0.05g sodium carbonate were dissolved in 50g of distilled water. While stirring, 25 ml of isopropyl alcohol and 4.80g of 37% formaldehyde were added. The solution was placed into a bottle. The polystyrene foam was immersed in the solution and trapped air was removed from the foam by drawing a vacuum over the solution. The bottle was capped and placed in a 70C oven for a week to cure. The reddish amber gel was removed from the exterior of the foam and the solvent exchange process was begun. First, the filled foam was placed in a 5% acetic acid solution at 50C for 24h. The acid solution was then replaced by methanol. The methanol was replaced with fresh methanol every day for at least one week. The foam was placed in a Polaron to remove the solvents from the gel network. After a week of liquid CO<sub>2</sub> extraction, the carbon dioxide was supercritically extracted by raising the temperature of the Polaron to 40C and 1400psi. The CO<sub>2</sub> gas was then vented slowly overnight.

#### Phloroglucinol formaldehyde filled polystyrene emulsion foam.

The phloroglucinol formaldehyde filled foams were prepared in the same manner as the resorcinol formaldehyde foams except phloroglucinol was used in place of resorcinol.

## References

1. Unilever Research Laboratory, *Emulsion Process for Making Foams*, European Patent 60138 (Sept 3, 1982).
2. Progress Report 1986, *Low-Density Hydrocarbon Foams for Laser Fusion Targets*, Lawrence Livermore National Laboratory, Livermore, Calif., UCID-21080-86.
3. Proceedings of the Fifth Target Fabrication Specialist Meeting, 1986, Las Vegas, Nevada, Conf-860330, Vol.1, p. 159.

## **List of Figures**

- Figure 1. SEMS of Polystyrene Emulsion Foam
- Figure 2. SEMS of Si Aerogel/Polystyrene Composite Foam
- Figure 3. SEMS of Si Aerogel/Polystyrene Composite Foam
- Figure 4. SEMS of Resorcinol-Formaldehyde/Polystyrene Composite Foams
- Figure 5. SEMS of Phloroglucinol-Formaldehyde/Polystyrene Composite Foams
- Figure 6. Liquid Deuterium wicking data
- Figure 7. Liquid Deuterium wicking data
- Figure 8. Liquid Deuterium wicking data



# Polystyrene Emulsion Foam

Density = 0.1g/cc

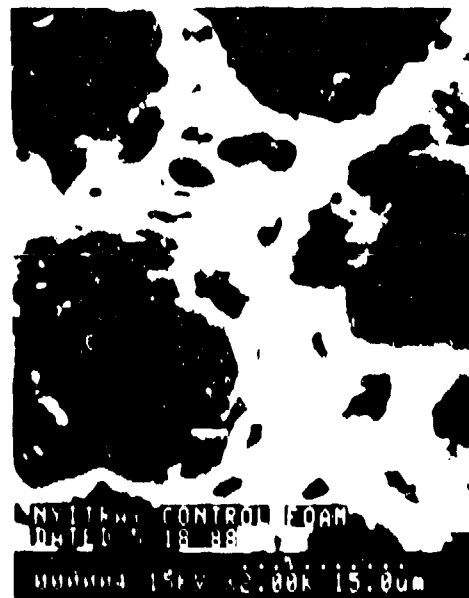
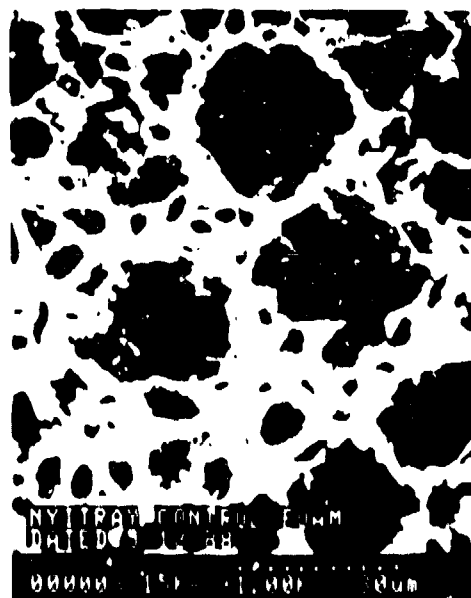
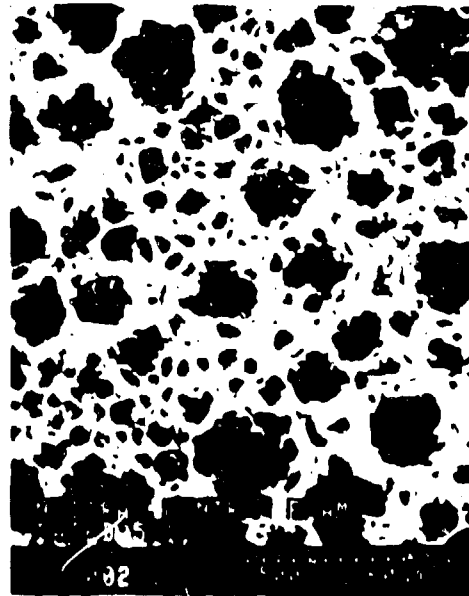
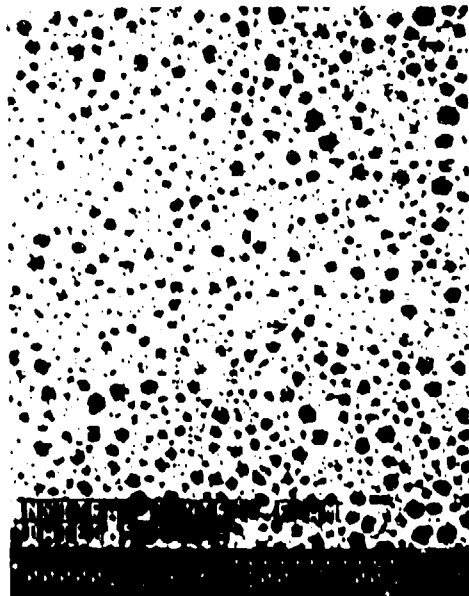
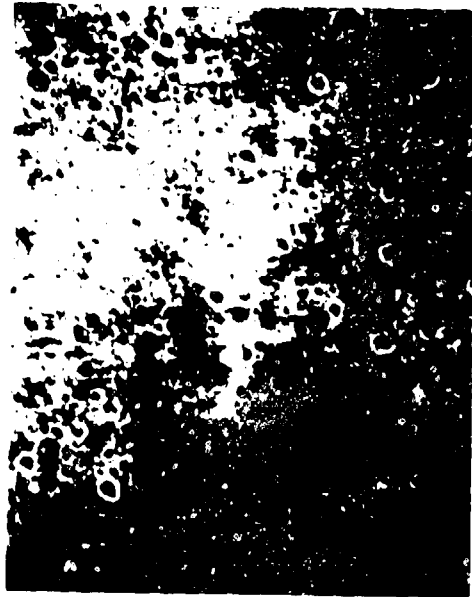


Figure 1

## Si Aerogel Foam in Polystyrene Foam

100 mg/cc SiO foam  
in 0.1 g/cc PS foam



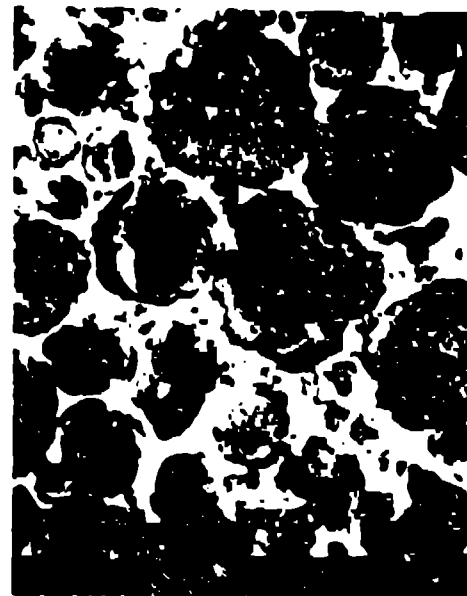
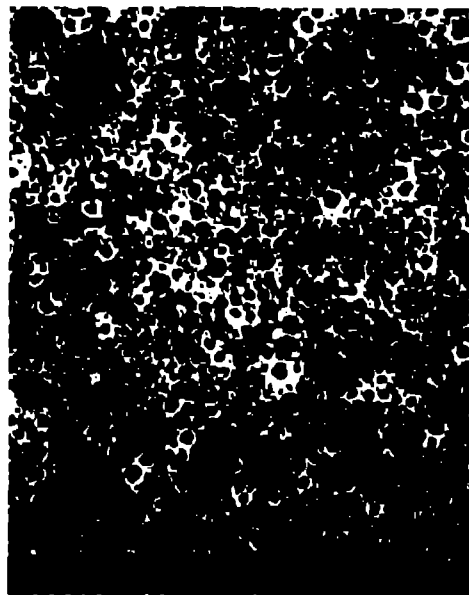
50 mg/cc SiO foam  
in 0.1 g/cc PS foam



Figure 2

## Si Aerogel Foam in Polystyrene Foam

25 mg/cc SiO foam  
in 0.1 g/cc PS foam



10 mg/cc SiO foam  
in 0.1 g/cc PS foam

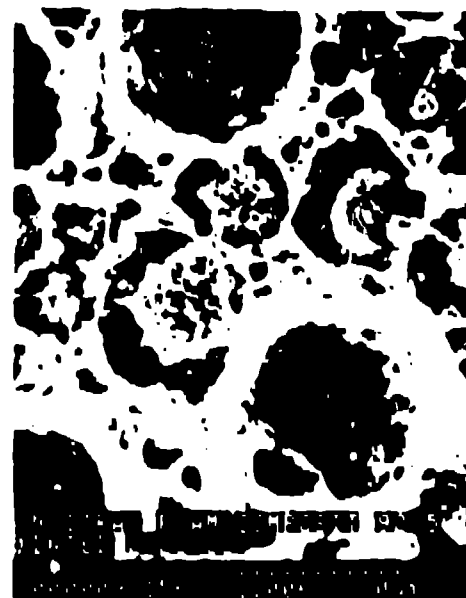
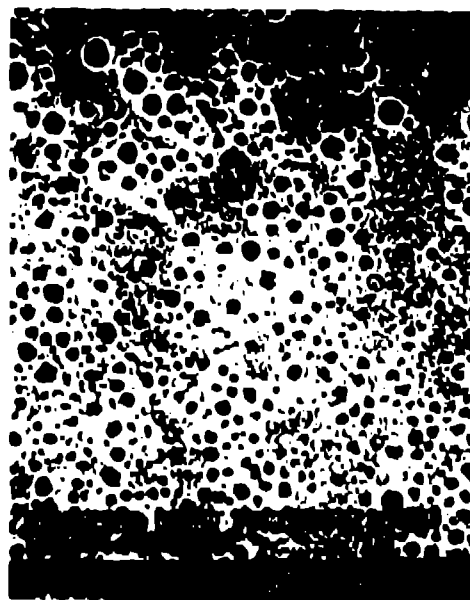
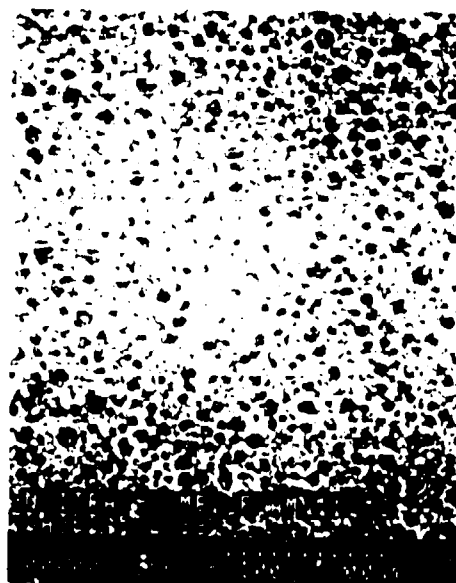


Figure 3

## Resorcinol-Formaldehyde Foam in Polystyrene Foam

6 wt% R/F foam  
in 0.1 g/cc PS foam



4 wt% R/F foam  
in 0.1 g/cc PS foam

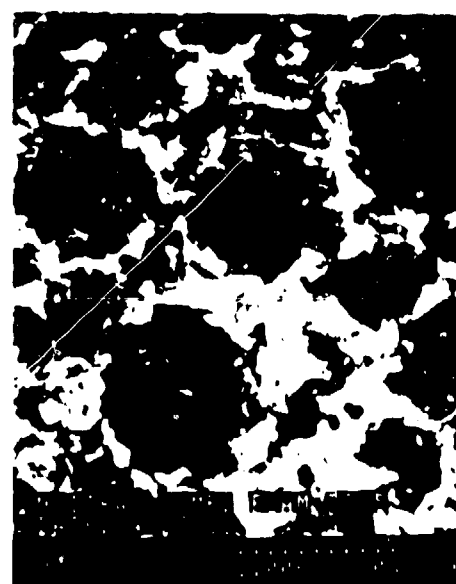
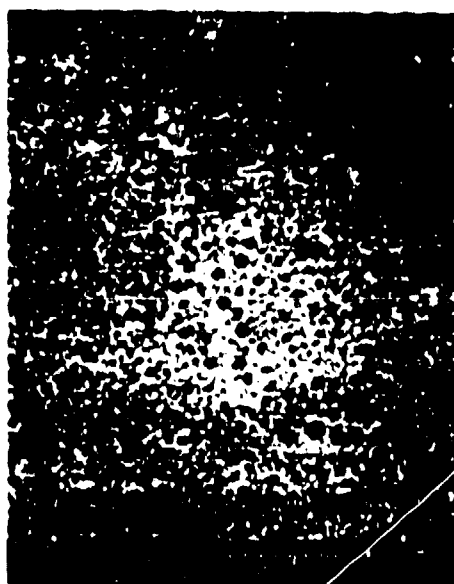
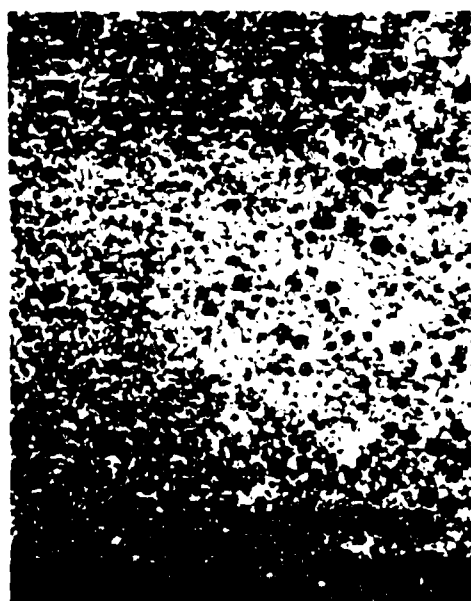


Figure 4

## Phloroglucinol-Formaldehyde Foam in Polystyrene Foam

7 wt% P/F foam  
in 0.1 g/cc PS foam



2 wt% P/F foam  
in 0.1 g/cc PS foam

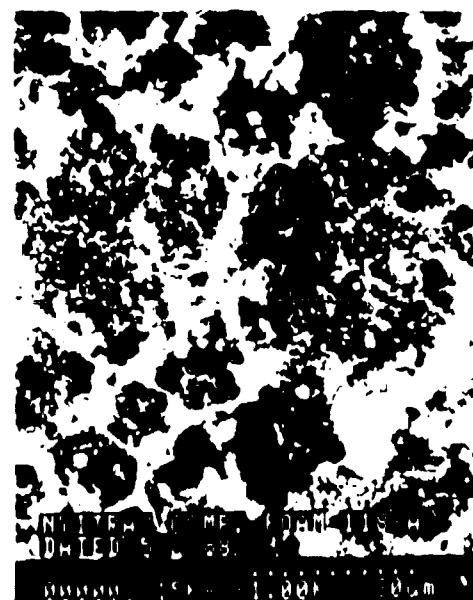
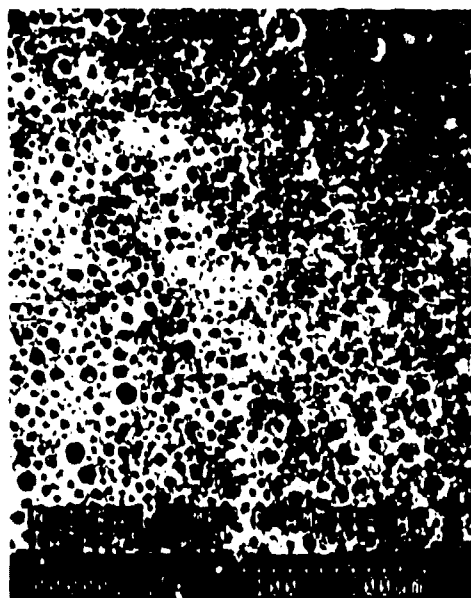


Figure 5

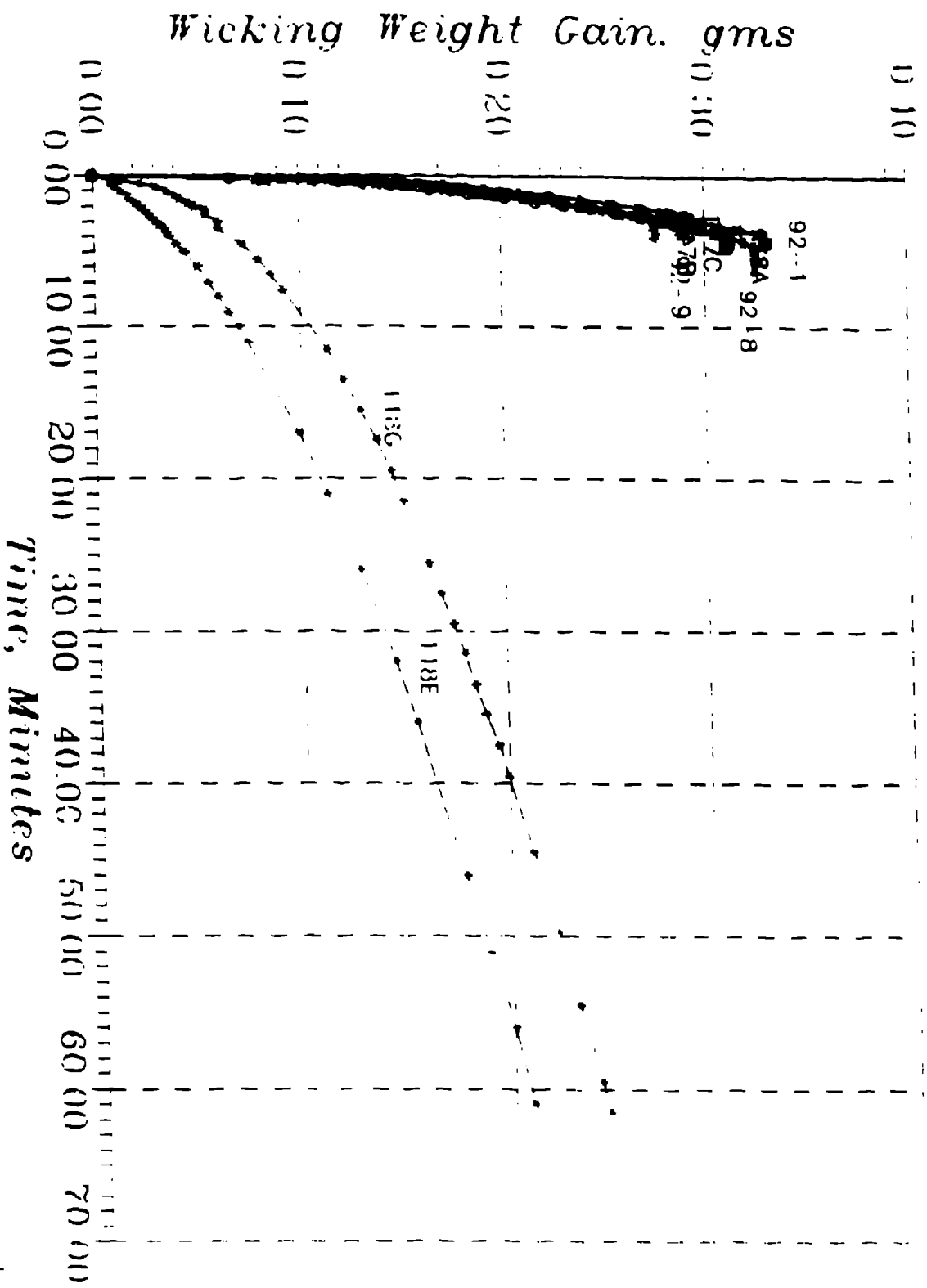


Figure 6

- 92-1 Aerogel (100mg/cc) PS
- 92-8 Aerogel (50mg/cc)-PS
- 92-9 Aerogel (25mg/cc) PS
- 118A Phloroglucinol/Formaldehyde(2 wt%)-PS
- 117B Phloroglucinol/Formaldehyde(6 wt%)-PS
- 117C Phloroglucinol/Formaldehyde(4 wt%)-PS
- 118G Resorcinol/Formaldehyde(4 wt%)-PS
- 118F Resorcinol/Formaldehyde(5 wt%)-PS

Latent Heat of Fusion (J/g)

Sample	Latent Heat of Fusion (J/g)
92-1	10.4
92-8	10.4
92-9	10.4
118A	10.4
117B	10.4
117C	10.4
118G	10.4
118F	10.4



Figure 8

Composite Foam	Foam Density (g/cc)	D2 (g)	D2 (cc)	Porosity %
Aerogel/PS (100mg/cc)	0.1121 (0.235/2.096)	0.312	1.818	86.73
Aerogel/PS (50mg/cc)	0.1203 (0.248/2.061)	0.320	1.864	90.46
Aerogel/PS (25mg/cc)	0.0996 (0.185/1.857)	0.270	1.573	84.70
6wt% PF/PS	0.1681 (0.311/1.850)	0.262	1.523	82.34
4 wt% PF/PS	0.1407 (0.264/1.876)	0.271	1.579	84.16
2 wt% PF/PS	0.1199 (0.237/1.977)	0.293	1.707	86.35
5 wt% RF/PS	0.1444 (0.288/1.995)	0.296	1.724	86.44
4 wt% RF/PS	0.1514 (0.308/2.037)	0.271	1.576	87.78



## LOW-DENSITY RESORCINOL-FORMALDEHYDE FOAMS FOR DIRECT-DRIVE LASER ICF TARGETS\*(UNC)

Fung-Ming Kong, Steve Buckley, Len Caley, Blanca Haendler,  
Lucy Hair, and Steve Letts

University of California  
Lawrence Livermore National Laboratory  
P. O. Box 5508, Livermore, CA 94550

### INTRODUCTION

Target design for a direct-drive, high gain ICF target<sup>1</sup> calls for the use of a low-density, low-atomic-number foam to define and stabilize liquid DT in a spherical shell configuration. For the purpose of high gain, the density of the foam should be as low as possible, and definitely not larger than  $70 \text{ mg/cm}^3$ . To fulfill other target physics and wetting stability requirements, the foam should have a cell size of less than  $4 \mu\text{m}$  with a density and cell size variation of not more than 1% in  $30 \mu\text{m}$  diameter cores through the foam. It should be wettable by liquid DT and stable to radioactive DT decay, machinable or moldable to parts with less than  $5 \mu\text{m}$  average peak-to-valley surface finish, and have a thermal expansion coefficient no larger than that of the ablator material.

The development of low-density foam materials from resorcinol-formaldehyde (RF) system was initiated by R.W. Pekala at LLNL.<sup>2,3</sup> The foams are promising as target materials because of their very small cell size, estimated to be about  $0.1 \mu\text{m}$ , which offers potentially great DT-fill stability. The synthesis of RF foams involves the condensation reaction of the monomers resorcinol and formaldehyde to form a sol-gel in a slightly basic aqueous solution at elevated temperature. After curing, the gel is treated with an acid to allow more crosslinking between molecules with hydroxymethyl groups, and then by supercritical extraction from liquid carbon dioxide to form a foam. The properties of the resultant

\*Work performed under the auspices of the U. S. Department of Energy by the Lawrence Livermore National Laboratory under contract number W 7405-ENG-48.

foam depend on the degree of crosslinking and the morphology of the porous structure, which is controlled by the stoichiometric ratio of the monomers and the process conditions. We have investigated the effects of formulation and curing on foam properties. We have also utilized carbonization as one way to increase the mechanical strength of RF foams. In this paper, results from the formulation and curing studies, and the properties of RF and carbonized RF (CRF) foams will be discussed as related to design specifications.

#### PREPARATION AND PROPERTIES OF RF AND CRF FOAMS

Foam properties depend on a vast number of chemical and process variables. In order to increase the efficiency of experimental development, we applied the principles of statistical design to the development of RF foams. This approach helped us to identify key variables with a minimum number of experiments, and provided a means of optimizing the system with respect to those variables. The first step was a screening test which identified the factors that suppress foam shrinkage were low % sodium carbonate initiator, high % reactants, high molar ratio of formaldehyde to resorcinol (F:R), and long curing times. The effects of these factors on foam properties were then investigated in more detail to understand their significance.

For the formulation study, we applied a three-variable Box-Behnken response surface methodology (RSM) design. We varied the % reactants from 4 to 8%, F:R from 1.6:1 to 2:1, and the concentration of  $\text{Na}_2\text{CO}_3$  from 0.025 to 0.08wt%. The foams were prepared in random order. First, the reactants were mixed and stirred at 70°C for 2 hours. Then they were cured at 70°C for 7 days inside sealed ampules before washing in 5% acetic acid at 50°C for 1 day. The gels then went through a series of solvent exchange steps. They were put into methanol, amyl acetate, and then liquid carbon dioxide for 7 days each. The  $\text{CO}_2$  was taken above its critical temperature and was bled off slowly to avoid passing a liquid meniscus through the material. The densities of these foams are shown in Fig. 1. It is apparent that  $\text{Na}_2\text{CO}_3$  plays a dominant role in controlling foam shrinkage. For a fixed amount of reactants added, all foams having the lowest density were obtained

from formulations with the lowest concentration of  $\text{Na}_2\text{CO}_3$ . The effect of F:R, on the other hand, appears less significant. The lowest density obtained from this study was  $57 \text{ mg/cm}^3$ . However, this foam fractured easily when being cut or touched.

In the curing study, we fixed the formulation at 6wt% reactants, F:R at 2:1, and  $\text{Na}_2\text{CO}_3$  at 0.05wt%. We cured the mixtures at 70, 90, and 110°C for 7 to 14 days. We found that foam density is affected only by the curing temperature and is independent of time. The densities were in the range of  $90 \text{ mg/cm}^3$  after curing at 70°C, and  $80 \text{ mg/cm}^3$  after curing at 90 and 110°C. The compressive modulus of the foam is affected by both curing temperature and time. All moduli were measured by compressing  $1 \times 1 \times 1 \text{ cm}$  cubes to a maximum of 10% strain at 0.1 mm/min. By comparing their moduli in the elastic region, we found that they are between 1 and 2 MPa when cured at 70°C and 90°C. Foams cured at 110°C, had many cracks, and the moduli decrease as the curing time increases. Since we were more concerned about lowering the density, as long as the foam had enough structural integrity to sustain machining and tritium radiation at cryogenic temperatures, we selected 90°C and 9 days as the optimum curing conditions. To reinforce these results, we cured the formulation with the lowest density ( $57 \text{ mg/cm}^3$ ) from the formulation study at 90°C for 9 days. The density was lowered to  $48 \text{ mg/cm}^3$ , and the foam was not as fragile as before. It could be vibrotomed into blocks with smooth surfaces.

Key findings from the above studies have enabled us to produce foams of very low density. By lowering the  $\text{Na}_2\text{CO}_3$  concentration to 0.0125 wt% and using the optimum curing conditions, RF foams with densities in the range of 20 to  $80 \text{ mg/cm}^3$  are consistently produced. While their low densities are attractive from the point of view that they would allow a lower target ignition temperature, they sometimes fracture easily during handling and machining. One method we have tried to greatly improve the mechanical strength of RF foams is carbonization.

Carbonization is a process in which polymers are heated in an inert atmosphere to temperatures above 300°C. In carbonizing RF, we heat the foams in argon from room temperature to 1050°C in 12 hours, maintaining 1050°C for 4 hours, and then cooling down to room temperature in 24 hours.

We discovered that RF generally retains the same shape after carbonization, but its shrinkage is greater than its weight loss, which results in an increase in density. Figure 2 shows the change in foam density before and after carbonization. It is interesting to observe that when the initiator concentration is fixed at 0.0125wt%, all foam density increases approximately by 20 mg/cm<sup>3</sup>, or between the range of 130% to 20%, for the entire range which we investigated. Elemental analysis reveals that RF has a conversion efficiency of 80%. Since the oxygen content also diminishes, carbonization helps to lower the average atomic number of RF. The most striking result of carbonization is a tremendous increase in mechanical properties. Preliminary mechanical tests indicated that the compressive modulus and compressive strength of the RF foams increase by more than 20 times after carbonization. In another study, we learned that higher initiator concentration would lead to a greater increase in foam density when subjected to carbonization. The effect of initiator concentration on the properties of CRF foams are being investigated.

In an effort to identify the basic structures of RF and CRF, we have performed transmission electron microscopy (TEM). TEM results reveal that both RF and CRF are composed of interconnected beads as in the case of silica aerogel. The bead size is on the order of 100 Å, and the largest cell size is roughly ten times larger. Furthermore, electron diffraction reveals that RF forms glassy carbon after carbonization which is totally amorphous and does not exhibit the crystalline peaks of graphite. The cell structure and electron diffraction pattern of CRF are shown in Fig. 3. X-ray radiography shows that good density uniformity can be achieved in these foams. Currently we are trying to develop techniques to verify that the foams meet the 1% variation requirement.

To explore the dimensional and wetting stabilities of RF and CRF foams in liquid DT, we performed a number of preliminary experiments for the bulk materials. By measuring their thermal expansion coefficients at cryogenic temperatures, RF was found to shrink by 0.55%, and CRF expanded by 0.15%. Both were found to be wetted by liquid DT without significant dimensional changes after exposure for one day. Encouraging results were also obtained from machining tests. Both RF and CRF foams are machinable. The ground

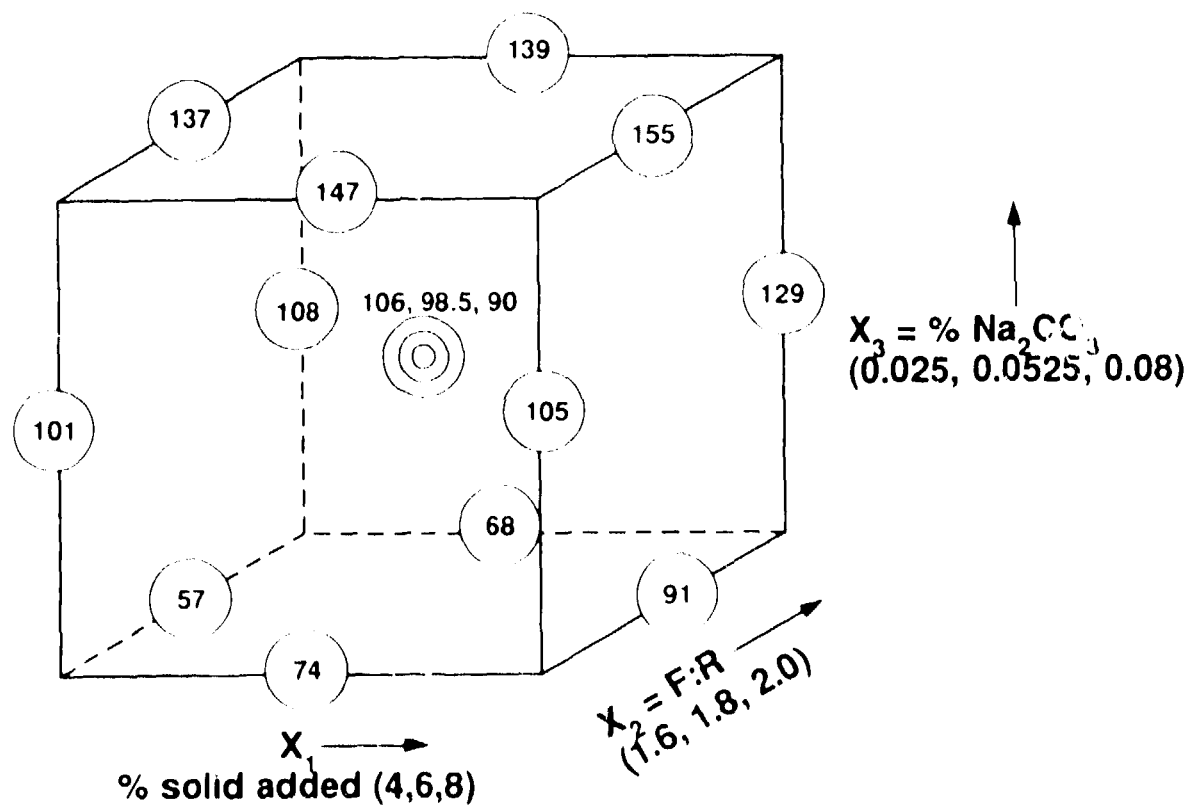
finish of CRF can be as low as 3-4  $\mu\text{m}$ ; that of RF is yet to be found.

### CONCLUSIONS

We have investigated the effects of formulation and process variables on the properties of RF foams. Low initiator concentrations and long curing time at 90°C are the key to suppressing foam shrinkage and achieving density close to the theoretical value. To produce foams with densities less than 70  $\text{mg}/\text{cm}^3$  but good mechanical strength, one needs to utilize carbonization. When the initiator concentration and F:R are fixed at 0.0125wt% and 2:1 respectively, carbonization would increase the foam density by 20  $\text{mg}/\text{cm}^3$  and the compressive modulus and strength by more than 20 times. Both the RF and CRF foams appear to have uniform density distribution and cell sizes of less than 0.1  $\mu\text{m}$ , are wettable by liquid DT without significant dimensional changes and are machinable. Based on all the information collected, RF and CRF foams appear to be promising materials for direct-drive laser ICF targets.

### REFERENCES

1. R.A. Sacks and D.H. Darling, "Direct Drive Cryogenic ICF Capsules Employing DT Wetted Foam," Nucl. Fusion, 27(3),447,(1987).
2. L.M. Hair, R.W. Pekala, R.E. Stone, Chuck Chen, and S.R. Buckley, "Low Density Resorcinol-Formaldehyde Aerogels for Direct-Drive Laser ICF Targets," J. Am. Vac. Soc., in press. Also available as Lawrence Livermore National Laboratory, Livermore, Calif., UCRL-96641.
3. R.W. Pekala and R.E. Stone, "Low Density Resorcinol-Formaldehyde Foams," Polym. Prepr., 29,204,(1988).



\* Numbers inside circles are foam density in  $\text{mg}/\text{cm}^3$

Figure 1. Effect of formulations on foam density

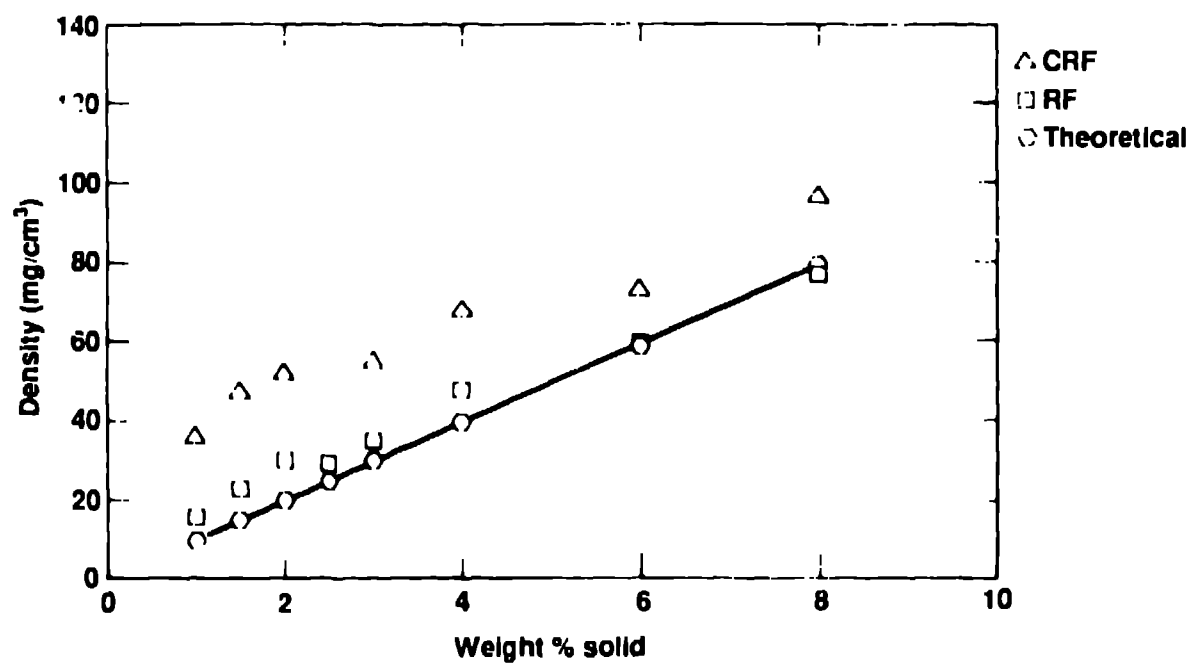


Figure 2. Effect of carbonization on foam density

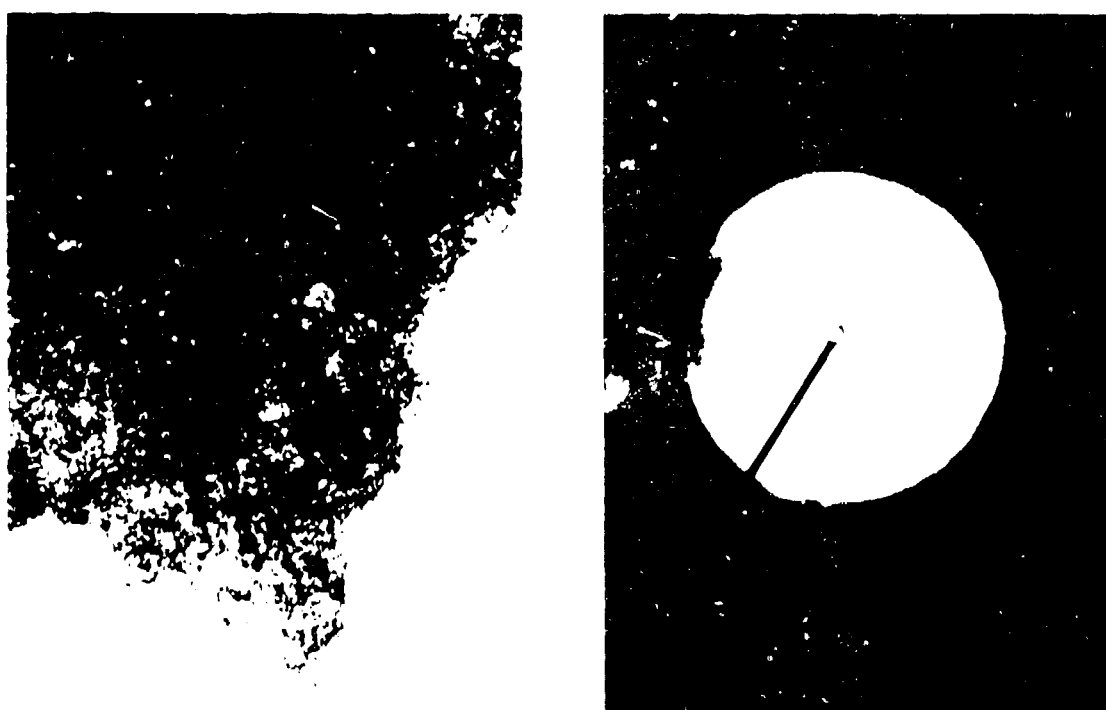


Figure 3 Transmission electron micrograph  
and electron diffraction pattern of  
carbonized resorcinol-formaldehyde.  
Magnification = 50 KX.



## LOW-DENSITY POLYSTYRENE FOAMS FOR DIRECT-DRIVE LASER ICF TARGETS\*(UNC)

Blanca L. Haendler, Robert C. Cook, D. Lynn James,  
Fung-Ming Kong, Stephan A. Letts, Steven C. Mance,  
George E. Overturf III, Dan L. Schumann,  
and Clarence Thomas, Jr.

University of California  
Lawrence Livermore National Laboratory  
P. O. Box 5508, Livermore, CA 94550

### INTRODUCTION

We are developing foams for the direct-drive, high-gain ICF target that is described in the 1985 Laser Program Report<sup>1</sup> and in a paper by R. A. Sacks and D. H. Darling.<sup>2</sup> This target design calls for a spherical shell of foam that can be wetted with liquid DT. The liquid DT is both fuel and ablator: the foam holds the DT in a spherical-shell configuration that is compressed to high density and ignited by the laser energy. The foam should have a density of 50 mg/cm<sup>3</sup> or less and be composed mainly of carbon, hydrogen, and oxygen; less than 1% of the material can be elements of higher Z than silicon. In addition, the foam should have a cell size of less than 4  $\mu$ m to meet uniformity requirements and a pore size of less than 1  $\mu$ m to stably hold the liquid DT. The foam must tolerate exposure to the radiation environment of tritium and to cryogenic temperatures without changing dimensions during the time needed for the target to fill and stabilize before a shot. The foam must be machinable or moldable to the required spherical-shell configuration and tolerances. Also, some target designs will require a foam with an overcoat of approximately 5  $\mu$ m of a hydrocarbon (CH) or other low-Z material.

One of the candidate materials for these targets is low-density polystyrene (PS) foam. The process we use for making these foams is based on an inverse-emulsion system developed by Unilever Research Laboratory<sup>3</sup> and also reported by Litt and coworkers.<sup>4</sup> A water phase containing sodium

\*Work performed under the auspices of the U. S. Department of Energy by the Lawrence Livermore National Laboratory under contract number W 7405 ENG 48.

persulfate as a polymerization initiator is added to an oil phase which is a mixture of two monomers, styrene and divinylbenzene, and an oil-soluble surfactant. The surfactant is sorbitan monooleate manufactured by ICI Americas Inc. under the tradename Span 80. The divinylbenzene is used as a crosslinking agent which should increase the mechanical strength of the foams. The water phase constitutes from 92-95% of the total material, so that upon addition the two phases form a high-internal-phase emulsion (HIPE) with the water as the internal phase. This emulsion is mixed (a variety of devices can be used), and then polymerized at 50°C in a water bath or oven, and the resulting foam dried in a vacuum oven between room temperature and 40°C until all the water is removed. The result is a foam of density 50-80 mg/cm<sup>3</sup> depending on the amount of water phase used. The details of the process for making the foams are described in Ref. 5, and additional information about foam structure and properties is given in Ref. 6.

#### FOAM PREPARATION AND CHEMISTRY

We investigated emulsion stability and foam characteristics in terms of the chemistry and processing of the PS system, and we have used statistically designed experiments to optimize the properties of the foam. We continue to use Span 80 as our surfactant, since it has proven superior to the others we have tested. Although sodium persulfate acts effectively as a polymerization initiator in this system, it would be desirable to replace it with a material of lower atomic number. We tested a variety of organic polymerization initiators, and we also tried some polymerizable surfactants, but they produced foams of low mechanical strength that have large cells with nodular walls. It seems likely that it is necessary to have a water-soluble rather than an oil-soluble initiator to ensure that the polymerization occurs at the interface rather than within the oil phase. Therefore, we continue to use sodium persulfate and are investigating the possibility of removing it from the foam after polymerization and drying.

We have looked at the molecular weight of the foams, and we found the inverse square root dependence of the degree of polymerization on initiator concentration which is expected for a free-radical mechanism. We have also

investigated the rate of polymerization by optical microscopy and by viscometry. The agreement between the two methods was good: the onset of polymerization occurs at approximately 1-2h at 50°C. We also carried out studies of the rate of drying of the foams under different conditions, and we investigated different mixing devices. Currently, our best foams are made in a syringe-pump mixing apparatus.

We also performed a statistically designed three-variable Box-Behnken response surface methodology (RSM) experiment designed to optimize foam properties with respect to the ratio of styrene to divinylbenzene, the concentration of surfactant in the oil phase, and the concentration of initiator in the water phase. The most important information obtained from this experiment was that the structures of the three center-point foams, as determined by SEM, were widely different. One foam had the expected 2-3  $\mu\text{m}$  cell size and was reasonably uniform, one had cells ranging up to 10  $\mu\text{m}$ , and the third had regions of apparent coalescence 100  $\mu\text{m}$  across and was very non-uniform. This was the first time that the reproducibility of the foam process had been checked in any systematic way, and the results indicated that it was very far from ideal. This experiment was done with foams of density 50  $\text{mg}/\text{cm}^3$ , and we have since concluded that reasonable quality foams require densities of 80-85  $\text{mg}/\text{cm}^3$ . Otherwise, there is too much water in the internal phase, and coalescence occurs.

Throughout our development of PS foams we have used x-ray radiography to assess foam uniformity. Often the radiographs show a pattern of dark concentric rings which can in some cases be eliminated by adjusting parameters on the mixing device or by taking extreme care with the purity of our materials. We have tried to identify the cause of the rings by exposing pieces of the foams to various solvents to see if they would wash out. We first tried a Soxhlet extraction with hexane because we thought it would remove any remaining surfactant. This treatment resulted in a weight loss which corresponded reasonably well with the amount of residual surfactant expected to remain in the foam. However, comparison of radiographs taken before and after extraction showed only minor changes. We then soaked the same sample in water, and obtained a weight loss corresponding approximately

to the amount of sodium sulfate remaining in the foam from decomposition of the initiator. This time the radiograph showed virtually complete removal of the rings. We repeated this entire procedure with another sample and got the same results. Thus we are reasonably confident that the rings consist primarily of sodium sulfate (or possibly sodium bisulfate) which, for reasons we have yet to determine, in some cases deposits unevenly throughout the foam, probably during the drying process. We have designed an experiment in which the foams and extract solutions will be analyzed to confirm the presence or absence of the species we expect. This will also determine whether the order of washing makes any difference and whether the washing harms the foam structure. We will use these results to develop the most efficient procedure for removing both the surfactant and the sulfate from the foams. Aside from improving our foam quality, these results are very important in that they point to a significant lowering of the density of PS foams.

#### TARGET-RELATED PROPERTIES

We have conducted a number of tests designed to assess the performance of PS foams as targets. We measured the low temperature coefficient of thermal expansion and found it to be 1.4% contraction to 15K. A capillary pressure test yielded a value of 0.75 psi with hydrogen, which should correspond to approximately 1.5 psi with DT. Hydrogen wetting results for PS foams are shown in Fig. 1 with other target materials for comparison. Quantitative data for DT wetting are just beginning to accumulate, but samples have been exposed for several days with no apparent dimensional changes or radiation damage, and the fill appears to be acceptable. PS foams have excellent mechanical properties: a sample with a density of 85 mg/cm<sup>3</sup> has a compressive modulus between 15 and 20 MPa. The foams are very easy to machine. Precision grinding gives our best surface finish thus far, which is approximately 5  $\mu$ m. Several hydrocarbon bonding agents are being investigated and look promising, most particularly a 1  $\mu$ m thick polystyrene butadiene film.

The specification for target density uniformity is somewhat ill defined at this time, but is generally given as uniformity of the projected or

radial density to within 1% between areas of 30  $\mu\text{m}$  diameter. X-ray radiography gives a qualitative assessment, but we need a quantitative technique to verify that the foams meet target specifications. We have developed a technique where a piece of foam is placed on a stepper-motor-driven stage on a microscope equipped with a light measuring photometer. The transmitted light intensity was scanned at 120  $\mu\text{m}$  intervals. A computer that controlled the stage motion and collected the photometric intensities. Figure 2 shows an automated scan through a step wedge of foam. The step heights are 0.6, 0.8, 1.0, 1.2, and 1.5 mm. On the second step from the left, two small density increases are apparent as depressions in the intensity. This technique does not give us the resolution we ultimately need, but it is useful as a first step.

In addition to our work on experimental measurement techniques, we have also developed a well-defined computer model that closely resembles the features of PS foams. The objective here is to study the relationships among cell size, cell-size distribution, foam density, and radial density uniformity. This model allows calculation of the Fourier transform of radial density as a function of distance and the  $k$  vector. Ultimately this should give us guidance in developing specifications for density uniformity.

## CONCLUSION

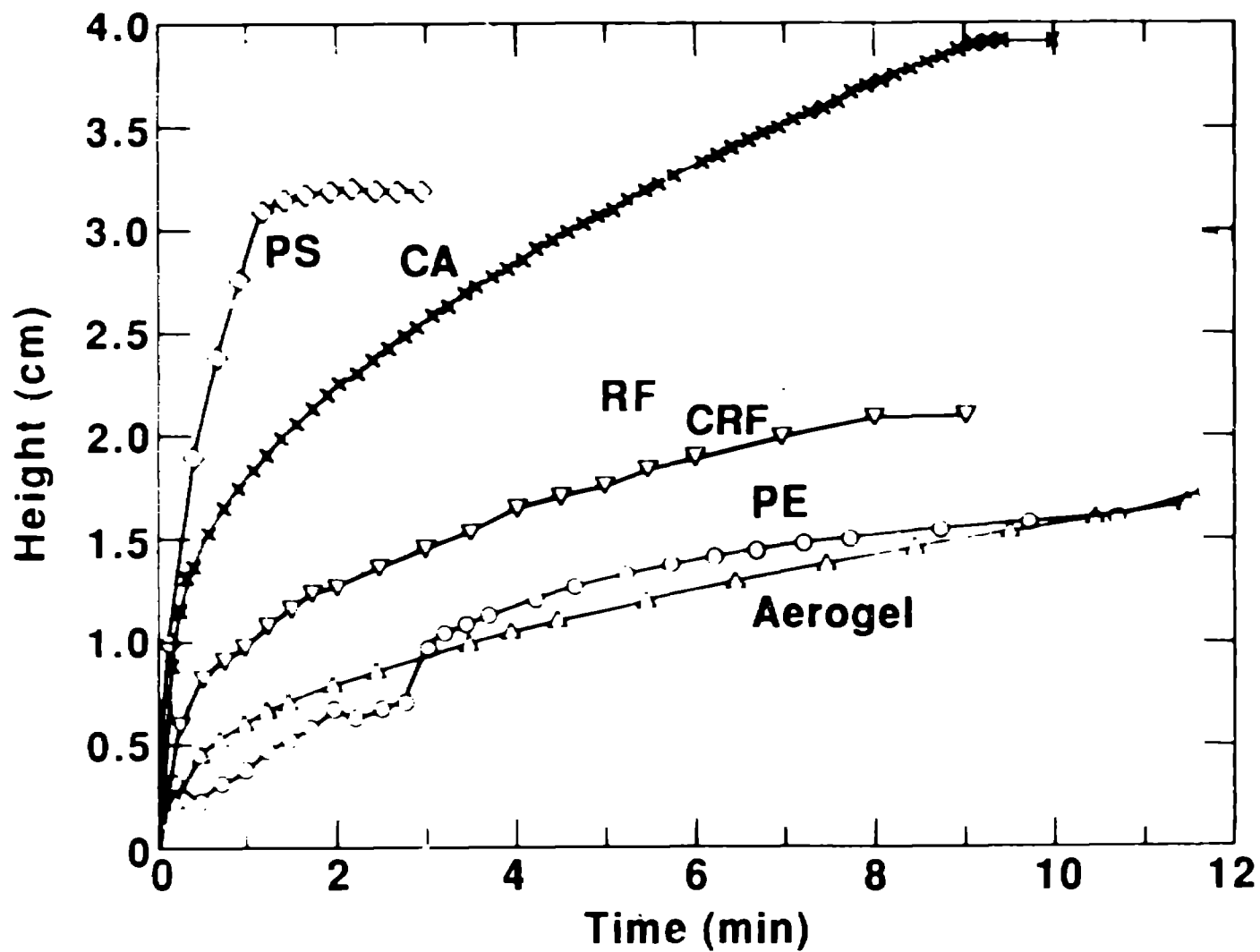
We have made good progress in developing PS foams for direct-drive Laser ICF targets. The advantages of PS foams over other foam candidates lie in their superior mechanical strength and ease of machinability. Their disadvantages lie in their relatively large cell size and coefficient of thermal expansion and in their lack of easy reproducibility, which may be a problem in terms of the as yet unassessed issue of density uniformity. To date, however, the foams have given acceptable results on all the target-related tests which have been performed.

## REFERENCES

1. Laser Program Annual Report 85, Lawrence Livermore National Laboratory, Livermore, Calif., UCRL 50021-85 (1986), pp.3-2 to 3-3.
2. R. A. Sacks and D. H. Darling, Nucl. Fusion 27,447, (1987).

3. Unilever Research Laboratory, Emulsion Process for Making Foams, European Patent 60138 (Sept. 3, 1982).
4. M. H. Litt, et. al., J. Coll. Inter. Sci., 115,312, (1987).
5. Laser Program Annual Report 85, Lawrence Livermore National Laboratory, Livermore, Calif., UCRL-50021-85 (1986), pp.3-18 to 3-21.
6. Laser Program Annual Report 86, Lawrence Livermore National Laboratory, Livermore, Calif., UCRL-50021-86 (1987), pp.5-2 to 5-15.

## Foams were compared for hydrogen wicking rate

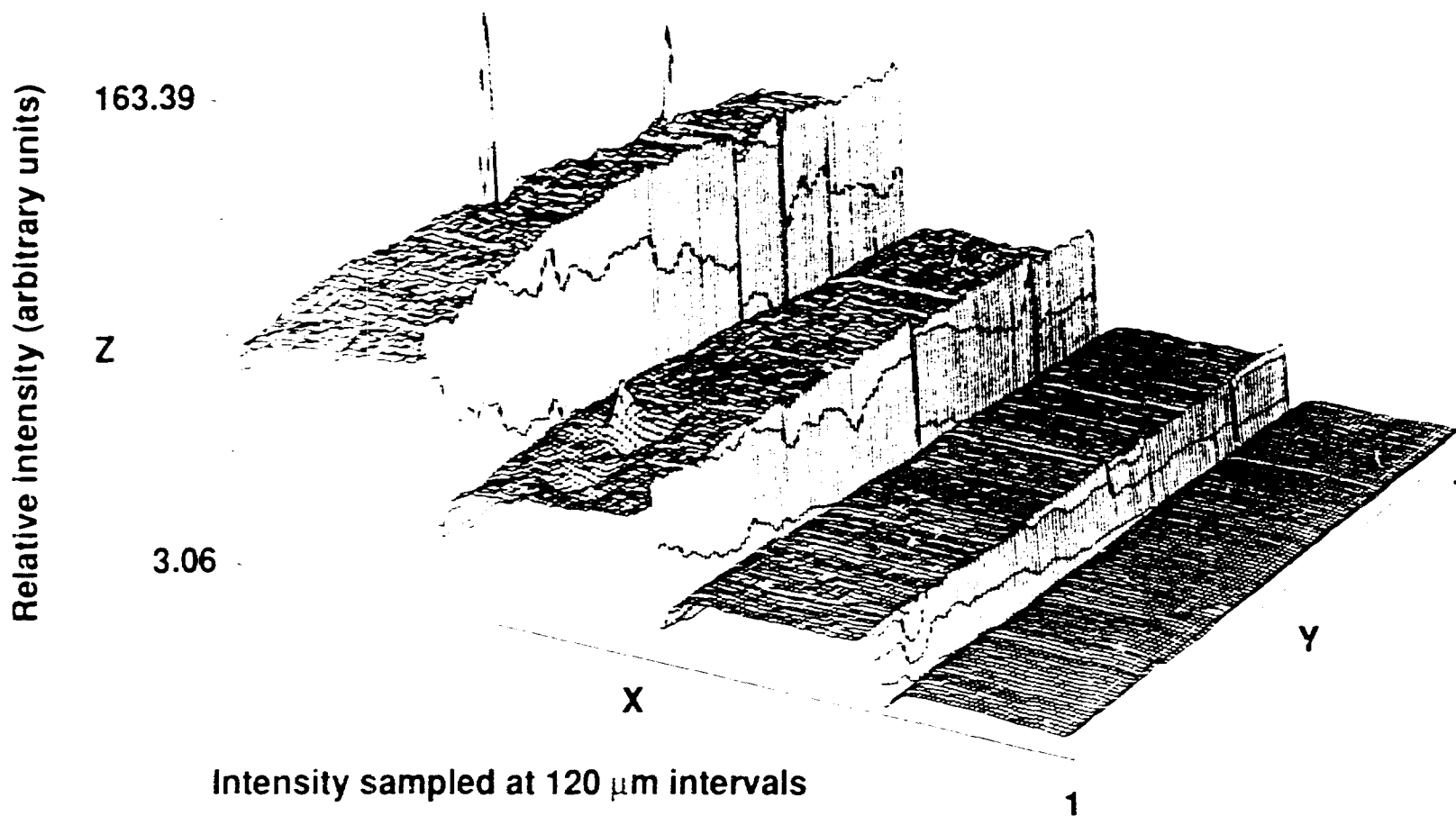


10-05-1067-2299A

288

Figure 1 - Hydrogen wetting rates of low-density foam materials

# A photometric scan of a PS foam step-wedge helps assess density uniformity



02-32-0588-1302

REV. 10/21/01-7264-2

Figure 2 - A photometric scan of a PS foam step-wedge



## CHARACTERIZATION OF LOW-DENSITY MATERIALS AND THEIR PRECURSERS\*(UNC)

Steven A. Letts, Steven R. Buckley, Chuck Chen, Andy R. Cook,  
Robert Cook, Blanca L. Haendler, Brooks C. Johnston,  
Fung-Ming Kong, Steven C. Mance, George E. Overturf III  
and Clarence Thomas, Jr.

University of California  
Lawrence Livermore National Laboratory  
P. O. Box 5508, Livermore, CA 94550

We are currently developing low-density polymer foam materials for the direct-drive laser ICF targets.<sup>1</sup> Acceptance of the material for target use requires evaluation of many physical properties of the foam. We have developed techniques for characterizing the foams for cell size, uniformity, density, thermal contraction, elastic modulus, liquid wetting, and radiation stability. In addition, to understand and control the processes used to prepare the foams to achieve better reproducibility, we have developed techniques for studying the foam starting materials. The starting materials, either emulsions or gels, were studied for rheology, thermal properties, optical properties, and reaction rates.

One foam preparation route uses high-internal-phase emulsions of water in styrene and divinylbenzene which are polymerized and then dried to produce polystyrene foams. We have used surface, rheological and optical characterization to determine the effect of formulation on emulsion stability. Emulsions are sheared to reduce the droplet size to 2-3  $\mu\text{m}$ . We have found that the emulsion viscosity rises with the time and intensity of mixing. Figure 1 shows the shear modulus of an emulsion as a function of the number of passes through a mixing orifice. Increased mixing raises the shear modulus. The mixed emulsion was then measured for viscosity over a range of shear rates for a period of 1 h. The viscosity was found to drop as a function of time due to coalescence.

To minimize coalescence it is desirable to polymerize the emulsion

\*Work performed under the auspices of the U. S. Department of Energy by the Lawrence Livermore National Laboratory under contract number W-7405-ENG-48.

rapidly. The polymerization rate can be increased by raising the temperature, but this also accelerates coalescence. To optimize the polymerization conditions, we studied the effect of cure temperature and initiator concentration was studied on the rate of polymerization and the morphology of the resulting foam. Figure 2 shows the effect of cure temperature on foam structure. As the cure temperature increases the foam pore size increases. Thus, cure conditions provide a potential means of controlling porosity. Measurements of polymerized foam molecular weight show that increasing the rate of polymerization reduces the molecular weight. We have found that below a molecular weight of 20,000 low-density foam materials have low strength and tend to crumble.

Condensation polymerization of resorcinol and formaldehyde in dilute solutions results in formation of rigid gels that can be solvent exchanged and then supercritically dried to low-density materials. Foams made by this technique have densities down to  $18 \text{ mg/cm}^3$  with cell sizes of less than  $0.1 \mu\text{m}$ . Dynamic mechanical spectroscopy was used to follow the polymerization of the RF system. In this experiment we used a rheometer equipped with a couette (concentric cylinder) viscometer. The inner cylinder is sinusoidally oscillated at a constant frequency and amplitude while the magnitude and phase angle of the force transmitted to the outer cylinder is recorded as a function of time as the polymerization reaction proceeds. We were able to determine the shear modulus, as the gel polymerized. Figure 3 shows the shear modulus as a function of time for four RF gels polymerizing at temperatures ranging from  $59.2$  to  $81.7^\circ\text{C}$ . Increased temperature accelerated the rate of polymerization as evidenced by the earlier increase in modulus of the gels approached a limiting value independent of cure temperature. This indicates that the degree of crosslinking is the same for all cure temperatures.

All foams were characterized for thermal contraction from room temperature to  $15 \text{ K}$ . Figure 4 summarizes the deformation. Over this temperature range polystyrene foam shrinks by  $1.5\%$ , cellulose acetate  $0.6\%$ , resorcinol-formaldehyde  $0.55\%$ , and carbonized RF expands  $0.15\%$ .

The hydrogen wetting properties of foams were measured by dipping cooled foams into liquid hydrogen. Figure 5 shows the height of liquid hydrogen

infoams as a function of time. We have found that smaller-cell-sized foams wick liquid hydrogen at a slower rate because of greater viscous drag forces.

We have investigated three foams for use in wetted foam targets. We have found that each has particular strengths. Polystyrene foams are robust and machinable, but have the largest cell size. Cellulose acetate and resorcinol-formaldehyde foams have submicron cell size and low thermal contraction, but are more fragile and difficult to machine.

#### REFERENCE

1. R.A. Sacks and D.H. Darling, "Direct Drive Cryogenic ICF Capsules Employing DT Wetted Foam," Nucl. Fusion, 27(3), 447(1987).

# Fluids Spectroscopy was used to follow the effect of mixing on Emulsion Viscosity

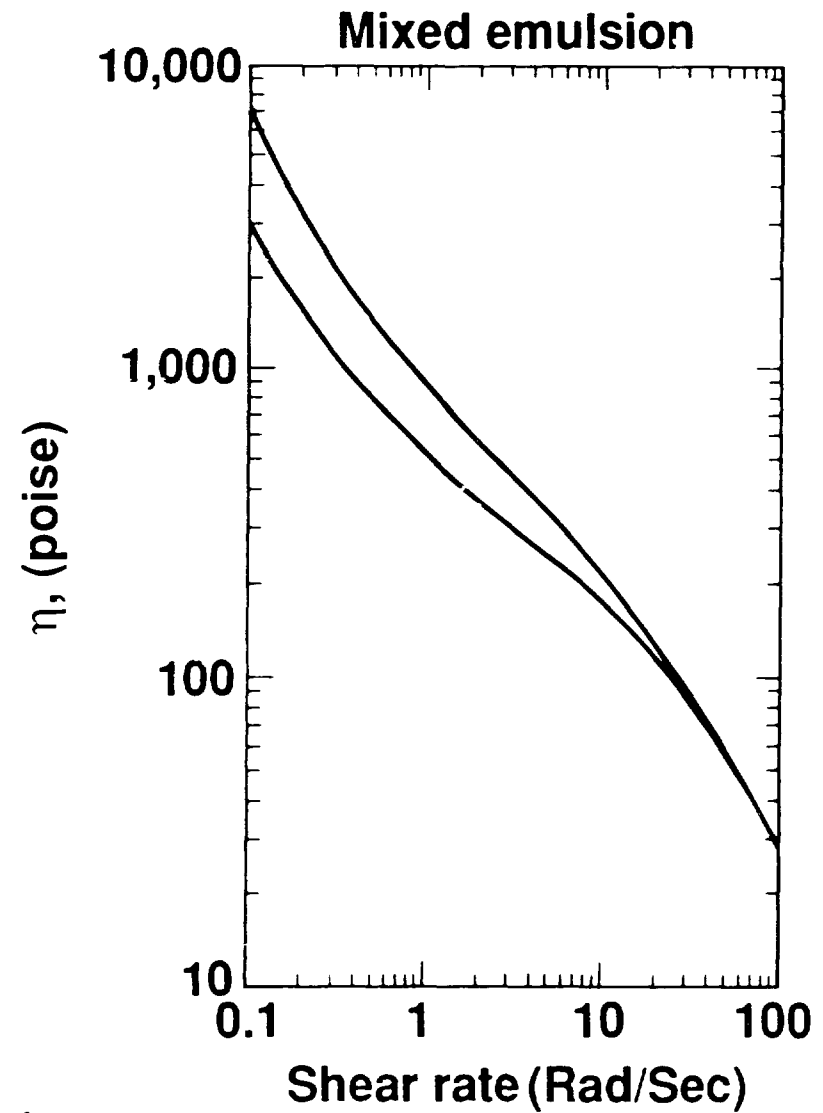
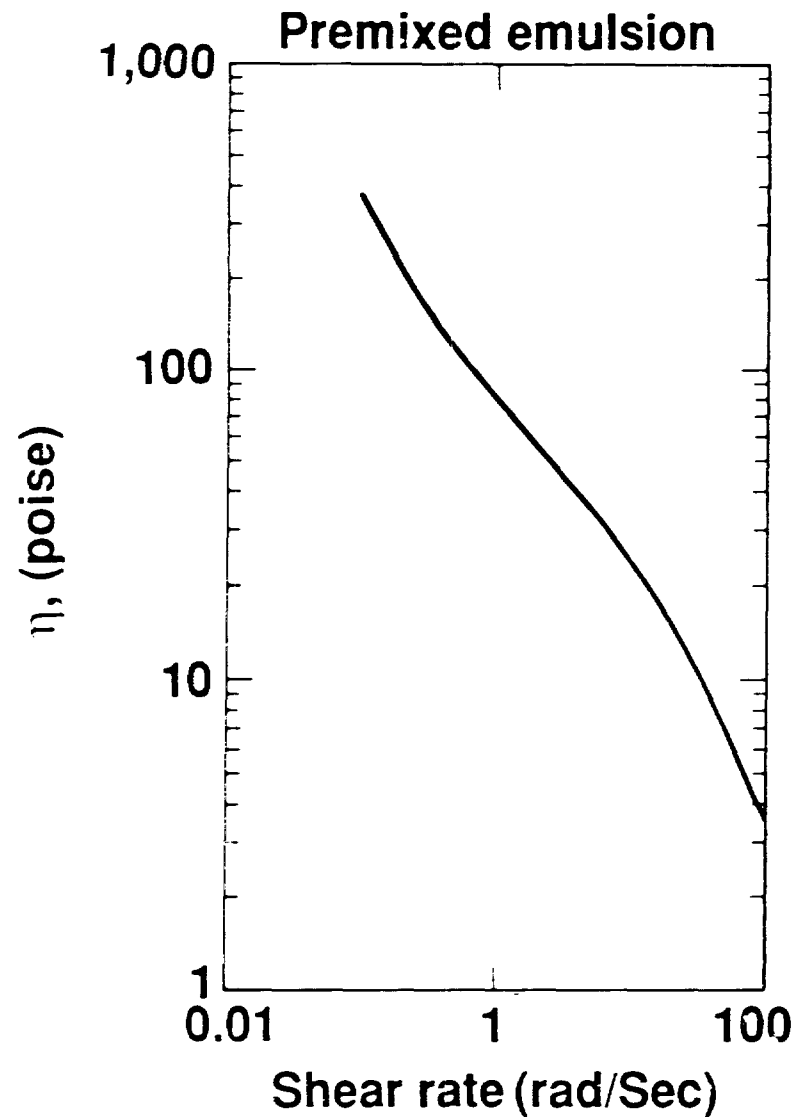
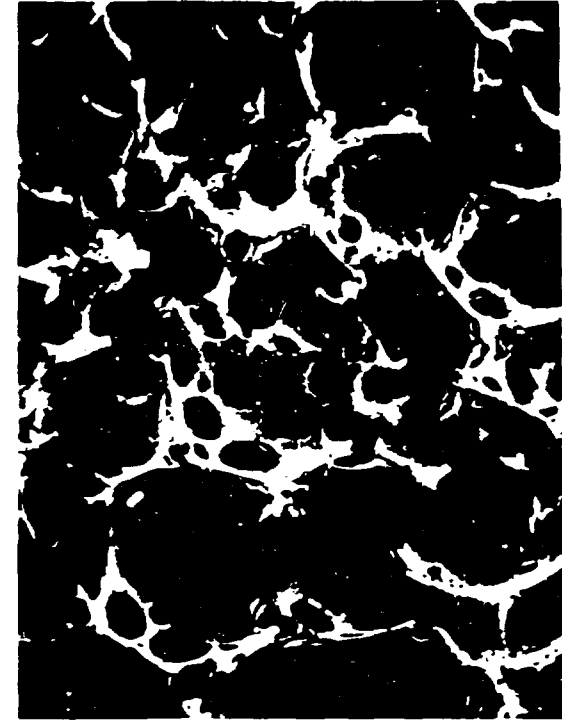
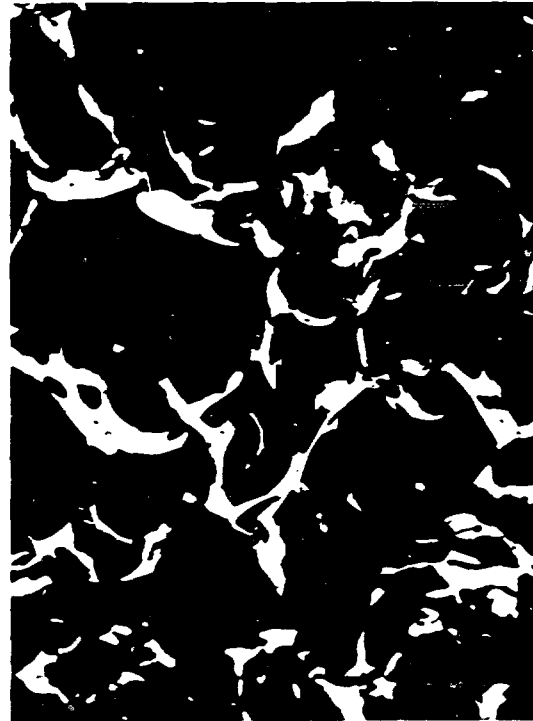
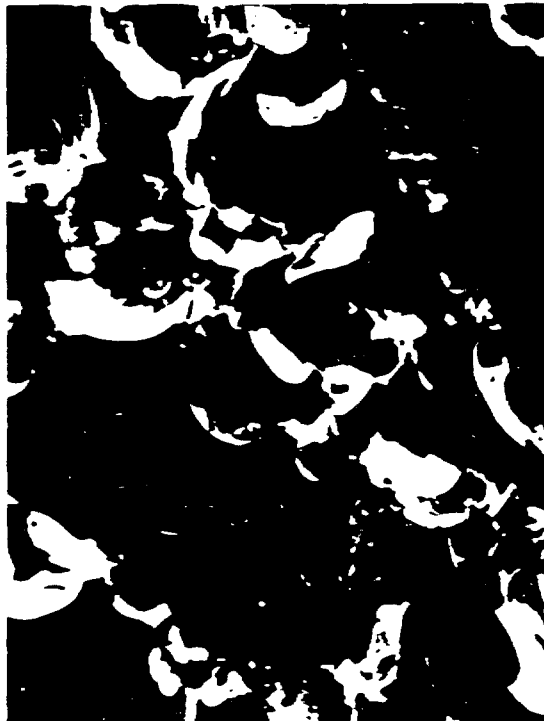


Figure 1

# Polymerization temperature and initiator concentration strongly affect foam cell and pore structure



15  $\mu$

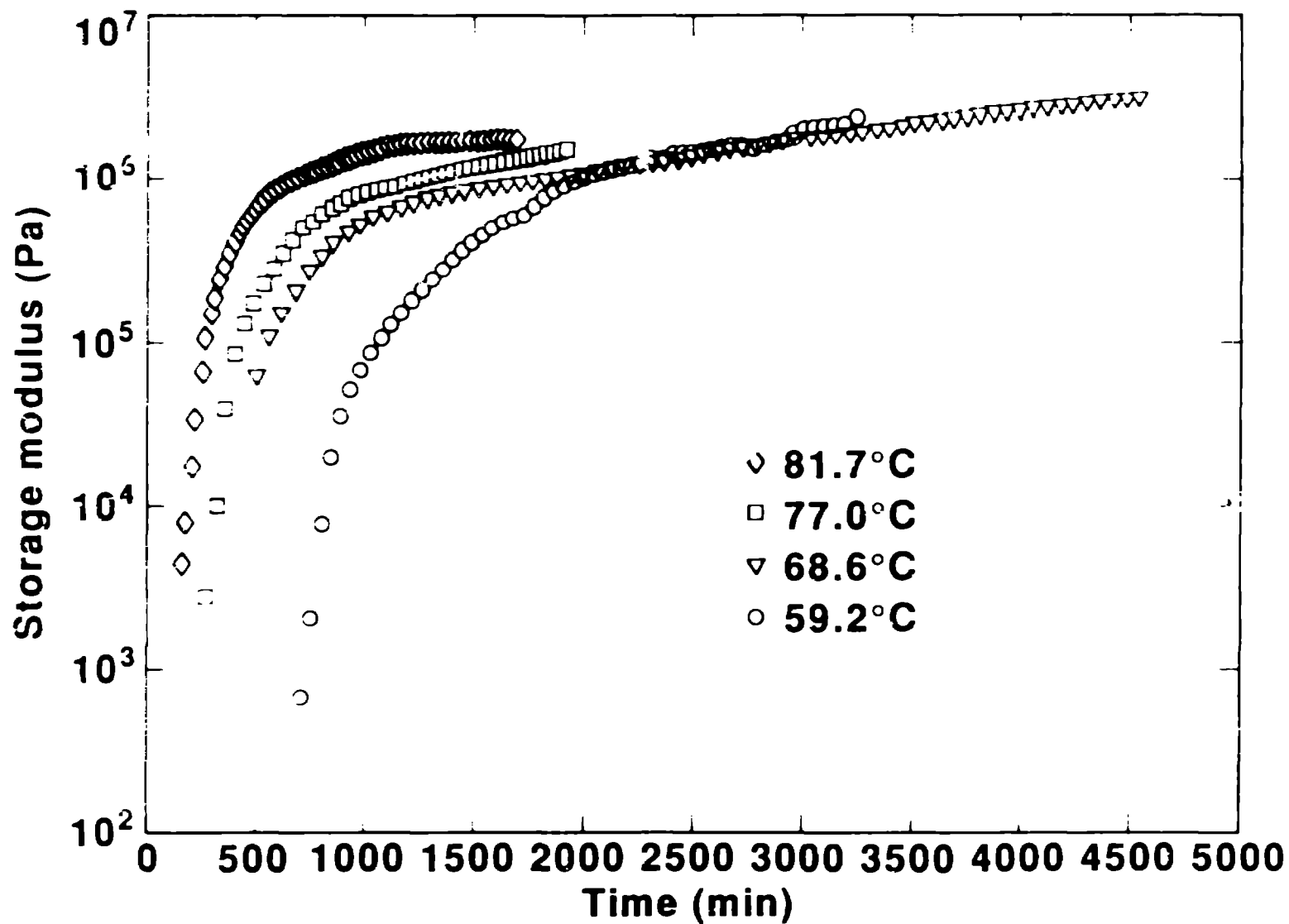
6.2 g/L initiator  
50°C

11.9 g/L initiator  
50°C

6.2 g/L initiator  
70°C

Figure 2

## RF gels reach a modulus that is independent of temperature



10-05-1087-2304

Figure 3

# Thermal contraction measurements of foams

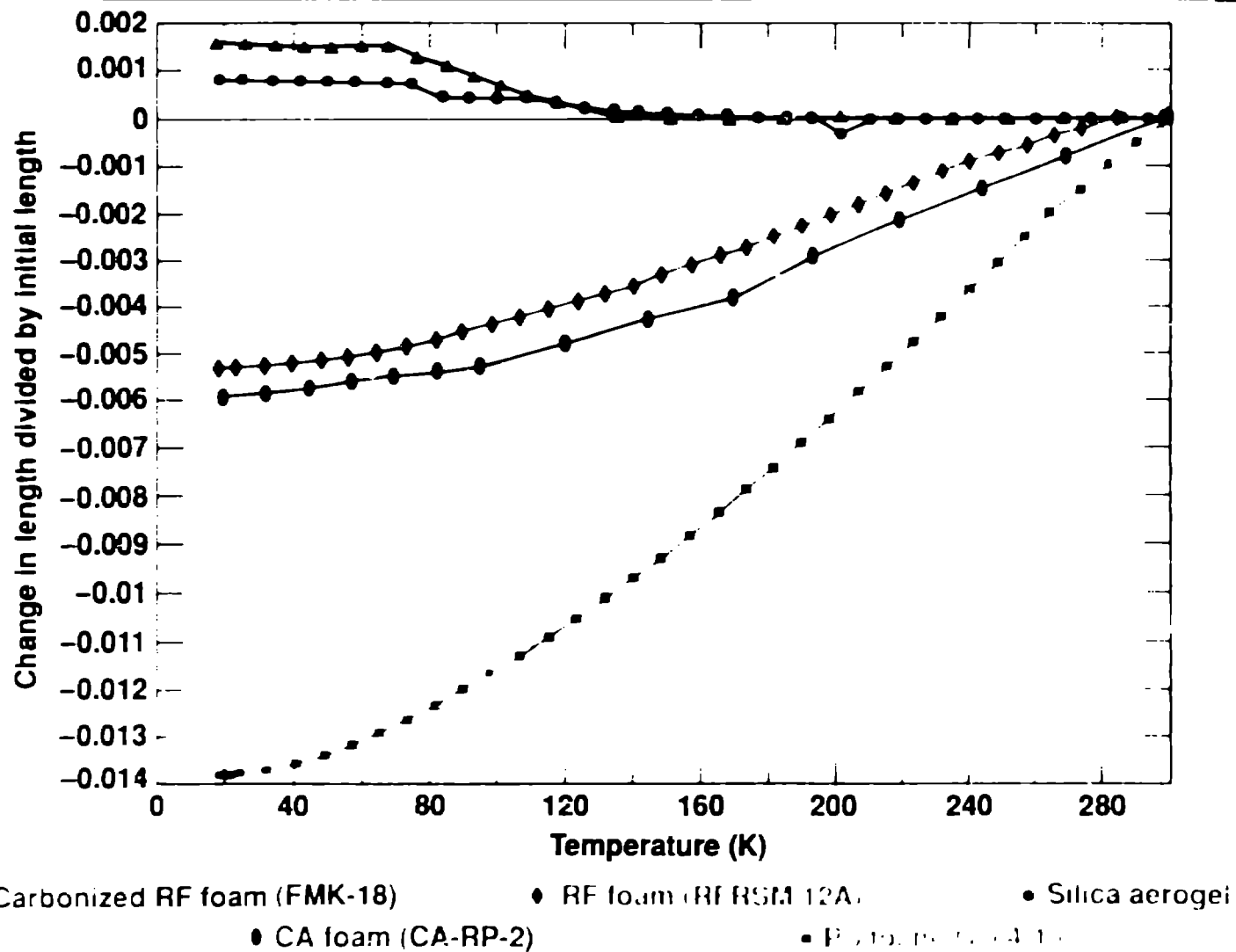


Figure 4

## Foams were compared for hydrogen wicking rate

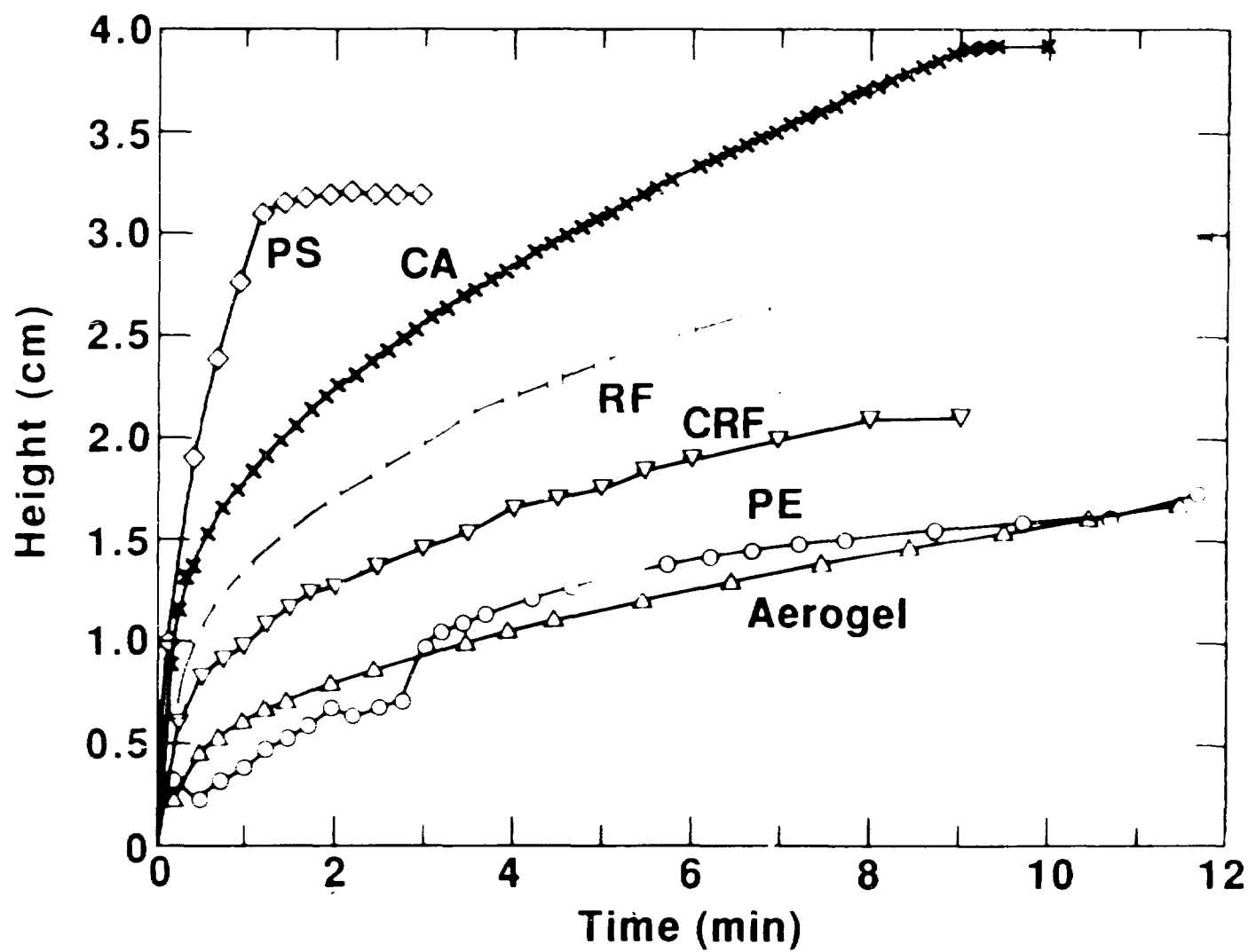


Figure 5



## LOW-VOLTAGE SCANNING ELECTRON MICROSCOPY OF TARGET MATERIALS\*(UNC)

Clifford W. Price

Lawrence Livermore National Laboratory  
P. O. Box 5508, Livermore, CA 94550

Paul L. McCarthy

Hewlett-Packard  
P. O. Box 39, Boise, ID 83707

### INTRODUCTION

The improved resolution of a SEM equipped with a field-emission gun (FESEM) at low-voltage is highly beneficial for the examination of many types of low-density materials.<sup>1</sup> Low-density materials frequently have fine, delicate microstructures that are highly susceptible to distortion and damage and are difficult to analyze and in a conventional SEM. Specimens previously examined in a conventional SEM required conductive coatings to eliminate charging and achieve high-resolution. However, cell structures in low-density polymer foams can be severely distorted by coatings, and much of the fine structural detail can be obliterated.<sup>2</sup> In extreme cases, coatings can form artifact structures<sup>3</sup> that are unrelated to the actual structure. Thin membranes that form cell walls in some polymer foams also are extremely susceptible to electron-beam damage. This paper will demonstrate the severity of these problems in ICF materials, show that they can be substantially reduced by low-voltage scanning electron microscopy (LVSEM), and demonstrate that the resolution of the FESEM at low voltage is adequate to resolve much of the fine structural detail in these materials.

### EXPERIMENTAL PROCEDURE

The simplest technique to examine microstructures in low-density materials is to fracture specimens and examine the fracture surface. The fracture surfaces may not be entirely representative of the structure in

\*Work performed under the auspices of the U. S. Department of Energy by the Lawrence Livermore National Laboratory under contract number W-7405-ENG-48.

these materials,<sup>4</sup> but they are reproducible and contain essential structural features that are characteristic of these materials. Therefore, fracture surfaces were examined for this study. Polystyrene foams and aerogel were fractured in air; cellulose acetate foams were equilibrated in liquid nitrogen before fracturing. The LVSEM was performed on an Hitachi S-800 FESEM equipped with a cryogenic pumping system.

## RESULTS

Polystyrene Foam: Cell structures in low-density polystyrene foams vary with density. Two foams with a nominal density of  $0.05 \text{ g/cm}^3$  were examined. One foam had a duplex cell structure composed of agglomerations of fine cells interspersed between large cells; it also had a low density of pores in the cell walls. The other foam was synthesized with a higher concentration of surfactant and had a more uniform cell size with a high density of pores in the cell walls.

Figures 1a through 1c show typical cell structure found in the low-porosity foam with the duplex structure. Figure 1a, obtained from a carbon-coated specimen at 20 kV, shows evidence of subsurface cell structure from excessive electron-beam penetration at high voltage. Structural detail is not apparent on the cell walls in Fig. 1a but is apparent at 2kV in Fig. 1b, which is the same field. The fine cell structure in an uncoated specimen obtained at 1.5 kV is shown in Fig. 1c. Carbon coating does tend to obliterate some of the fine structural details, but this problem is not readily apparent in Fig. 1. Fig. 1c shows a contrast effect that is sensitive to voltage and disappears at 0.5 kV.(2) The light and dark contrast regions form at points of contact between adjacent cells.

The uncoated specimen did charge at 1.5 kV, and the charging became more severe at the slow recording rate of 40 s/frame and 2048 lines/frame. Although charging subsided at 0.5 kV, loss of resolution became noticeable. Therefore, Fig. 1c was recorded by using multiple sweeps of the conventional viewing raster at 0.5 s/frame and 512 lines/frame. An internal switch was used to activate the camera shutter, and the image was recorded with about 40 to 50 frames. This multiple-frame exposure technique is roughly equivalent to using frame grabbing and averaging techniques available in

computerized image-analysis instruments, but it does leave observable scan lines. Use of rapid scanning to minimize charging and electron-beam damage is an established technique<sup>5</sup> that can be conducted and perhaps even enhanced with high-quality image-analysis systems currently available for the SEM.

Coating distorted and wrinkled the larger cell surfaces in the low-porosity foam. Figure 2a was obtained from a coated specimen at 2 kV; Fig. 2b was obtained from an uncoated specimen at 0.5 kV with the multiple-frame exposure technique. These figures demonstrate that coating damage can be eliminated by LVSEM examinations of uncoated polystyrene specimens. Although coating damage obviously is undesirable and can be serious, it does not significantly affect the observed cell size because of the constraint of the underlying material. Consequently, cell-size measurements made on coated specimens are reasonable and useful for relative comparisons. Furthermore, examination of the subsurface cell structure at high voltage does provide important information on three-dimensional cell geometry. Therefore, examination of coated polystyrene foams can provide useful information in spite of coating damage, but the type and extent of damage must be determined.

Subtle modifications caused by coating distortion often are difficult to recognize. Such modification occurred at the edges of pores in the high-porosity polystyrene foam with the uniform cell size. Figure 3a is a stereo pair from a coated specimen taken at 1.5 kV; the edges around the pores are severely puckered. Figure 3b is a stereo pair from the uncoated material taken at 1.5 kV with the multiple-frame exposure technique; it shows slightly less puckering than in the coated specimen. This difference is subtle but real, and it was consistently observed throughout each specimen. Because it is slight, it does not impair relative comparisons, but again, the extent of coating damage must be determined to assess its relevance.

**Cellulose Acetate:** Low-density cellulose acetate foams are susceptible to both electron-beam damage and coating damage. They also tend to charge severely even at low voltage in the FESEM. In fact, the charging and instability of the cellulose acetate were sufficiently great that the multiple-frame exposure technique was ineffective. The instability at 0.8

kV is demonstrated in Fig. 4. Figure 4a is regarded to be an acceptable structure of low-density cellulose acetate foam with a nominal density of  $0.05 \text{ g/cm}^3$ . It was obtained by focusing in one area, then quickly traversing to the area to be photographed and immediately initiating the exposure. Only minimal beam damage is suspected to have occurred. Figure 4b was taken after approximately 30 s additional exposure. Figures 4a and 4b are mounted as a pseudo-stereo pair<sup>6</sup> to emphasize the deterioration. Since the specimen tilt was not changed, the three-dimensional structure evident in the pseudo-stereo pair results from the surface damage induced by the electron-beam. Some areas in Fig. 4 are too severely distorted to be viewed in stereo.

Figures 5a and 5b show extensive electron-beam damage that formed after a 2-minute exposure at 2 kV. The extent of beam damage is evident at low magnification in Figure 5b. A large void formed during the exposure, and noticeable coagulation occurred along some ridges in the fracture surface. The apparent cell size also is smaller than in the relatively undamaged material in Fig. 4a, indicating that some shrinkage occurred.

Damage in low-density cellulose acetate foam caused by carbon coating is shown in Fig. 6. Figure 6a shows considerable modification by a light coating of about 2.5 nm; Fig. 6b shows even more extensive damage by a slightly heavier coating of about 5 nm. A carbon coating of about 10 nm, which is normal for most materials, can completely obliterate the structure in this material.

**Silica Aerogel:** Silica aerogel is an extremely delicate material that must be examined in a FESEM at low voltage without coating to properly observe the structure.<sup>3</sup> Early TEM studies revealed the structure to be composed of fibrous chains of globular particles.<sup>7</sup> Iler<sup>8</sup> showed that measurements of specific surface area obtained by the Brunauer-Emmett-Teller (BET) technique correlated reasonably well with calculations based on the surface area of spheres that used the average particle diameter revealed by TEM. Specific surface area measurements based on data generated by small-angle x-ray scattering (SAXS) using synchrotron radiation also correlate well with BET measurements.<sup>9,10</sup> The delicate structure of silica aerogel is highly susceptible to electron-beam damage in the TEM, so

even the TEM observations are subject to uncertainty. However, agreement among surface-area estimates based on TEM particle-size measurements, BET specific surface-area measurements, and SAXS surface-area measurements supports the TEM observations. Unfortunately, similar agreement could not be obtained with conventional SEM examinations of coated silica aerogel specimens.

Examples of coated and uncoated silica aerogel structures are shown in Figs. 7a and 7b, respectively. The silica aerogel study was obtained from Airglass AB, Sjöbo, Sweden; it had a nominal density of  $0.1 \text{ g/cm}^3$ . Figure 7a is from a gold-coated specimen that was examined at 20 kV. The globular structure in Fig. 7a is typical of both gold- and carbon-coated specimens with sufficiently thick coatings to prevent adverse electron charging effects. Figure 7b is an uncoated specimen examined in the FESEM at 2 kV. It shows a fibrous structure that correlates reasonably well with the TEM results. Obviously, the globular structure in Fig. 7a is an artifact structure that is not related to the fibrous structure in Fig. 7b.

## SUMMARY

Coating damage, artifact structures induced by coating, and electron-beam damage are severe problems when delicate microstructures in many low-density materials are examined by conventional SEM techniques. Low-density polystyrene foam is representative of materials that can be distorted by applications of conductive coatings. The distortion is not always severe, and some useful results can be obtained from coated specimens. However, proper examination of undistorted structures in polystyrene foams does require LVSEM in the uncoated state. Cellulose acetate foam is representative of materials that are extremely susceptible to both coating and electron-beam damage even at low voltage. Obviously, cellulose acetate can only be examined by LVSEM in the uncoated state. Silica aerogel is representative of a class of materials that apparently nucleate artifact structures when they are coated. These artifact structures may bear no resemblance to the actual structure, as was the case for silica aerogel, and they can be extremely confusing. The FESEM can image the fibrous structure of silica aerogel in uncoated specimens at low

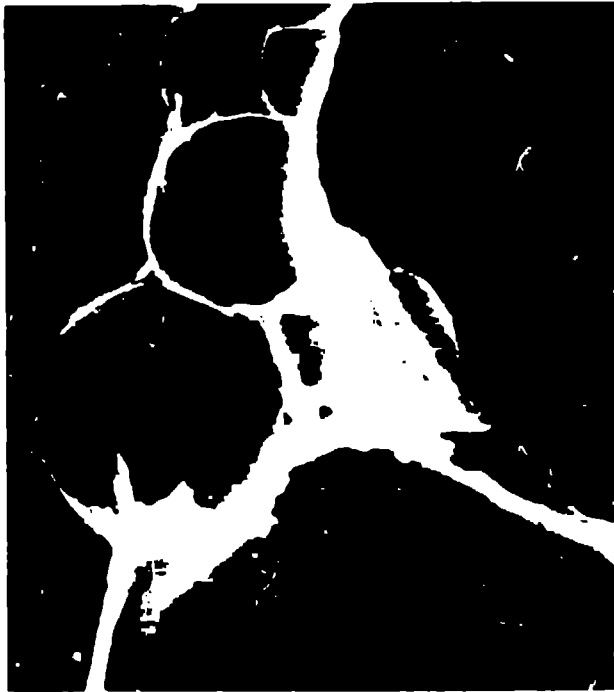
voltage, but the structure obviously is approaching the resolution limit of the Hitachi S-800 at 2 kV. Fortunately, most of these problems can be either significantly reduced or eliminated by LVSEM examinations of uncoated specimens. Furthermore, techniques such as ion-beam coating<sup>11,12</sup> and computerized image processing are expected to be beneficial for most of these materials and will be explored in the near future.

#### ACKNOWLEDGMENTS

B. L. Haendler, F. M. Kong, and S. A. Letts synthesized the materials, provided technical advice, and reviewed the manuscript. This paper was extracted from a paper that appeared in Scanning, 10, 29 (1988).

#### REFERENCES

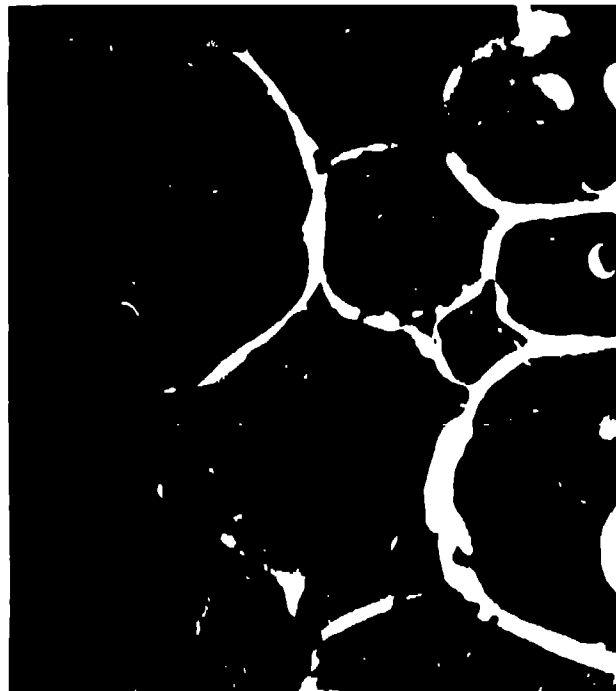
1. L. M. Welter and V. J. Coates, Scanning Electron Microscopy 1974, IITRI, Chicago, pp 60-66.
2. C. W. Price and P. L. McCarthy, Proc. 45th Annual Mtg Electron Microscopy Soc Am, San Francisco Press, Inc., San Francisco, California, 1987, pp. 390-391.
3. C. W. Price and P. L. McCarthy, Proc. 45th Annual Mtg Electron Microscopy Soc Am, San Francisco Press, Inc., San Francisco, California, 1987, pp. 206-207.
4. C. W. Price and P. L. McCarthy, Proc. 44th Annual Mtg Electron Microscopy Soc Am, San Francisco Press, Inc., San Francisco, California, 1986, pp. 880-881.
5. L. M. Welter and A. N. McKee, Scanning Electron Microscopy 1972, IITRI, Chicago, pp 162-168.
6. J. B. Pawley, Scanning 9, 134-136 (1987).
7. I. Sugar and F. Guba, Acta Chim. Acad. Hung., 7, 233 (1955).
8. R. W. Iler, The Chemistry of Silica, John Wiley and Sons, New York, 1979, p. 469.
9. D. W. Schaefer and K. D. Keefer, Phys. Rev. Lett., 56, 2199 (1986).
10. S. S. Laderman and J. B. Mitchell, unpublished research, 1984.
11. A. C. Evans and J. Frank, Scanning, 4, 169 (1981).
12. B. H. Kemmenoe and G. R. Bullock, J. Microsc., 132, Pt. 2, 153 (Nov 1983).



(a)

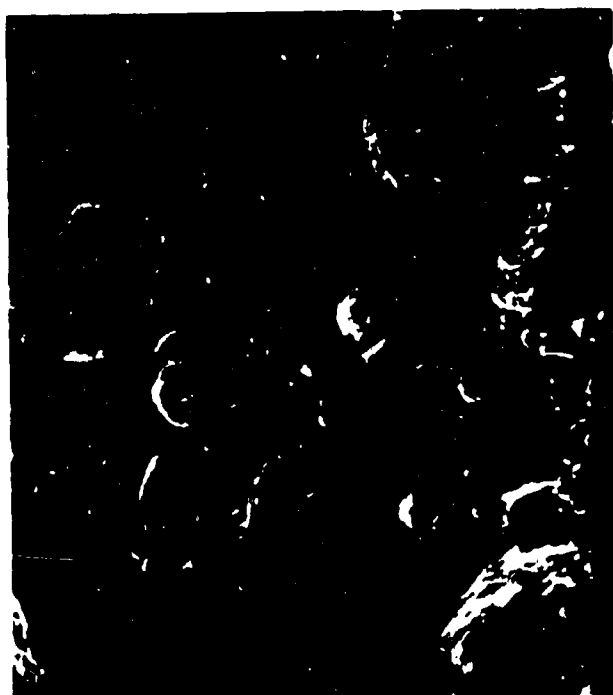


(b)

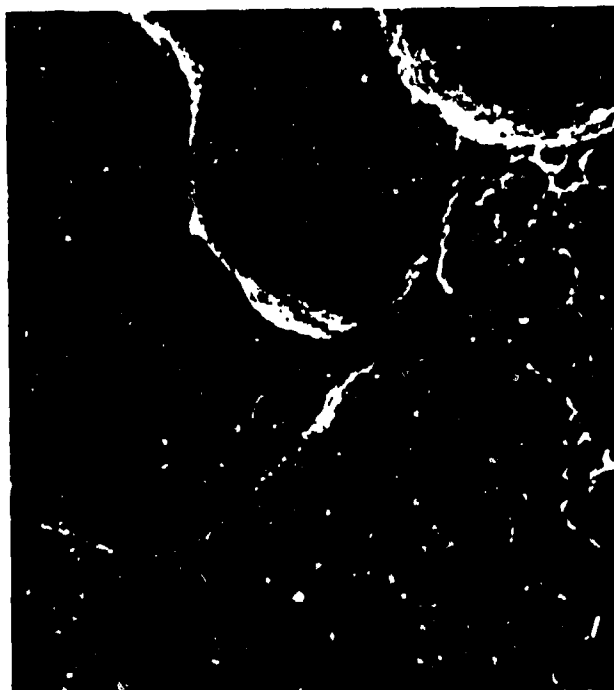


(c)

Fig. 1 - Comparison of the fine cell structure in the low-porosity polystyrene foam with the duplex cell structure; (a) carbon-coated at 20 kV, (b) carbon-coated at 2 kV, and (c) uncoated at 1.5 kV. Horizontal image width = 80  $\mu\text{m}$ .



(a)



(b)

**Fig. 2 - Comparison of coating damage in the large cell structure of the low-porosity polystyrene foam with the duplex cell structure; (a) carbon-coated at 2 kV and (b) uncoated at 0.8 kV. Horizontal image width - 160  $\mu\text{m}$ .**



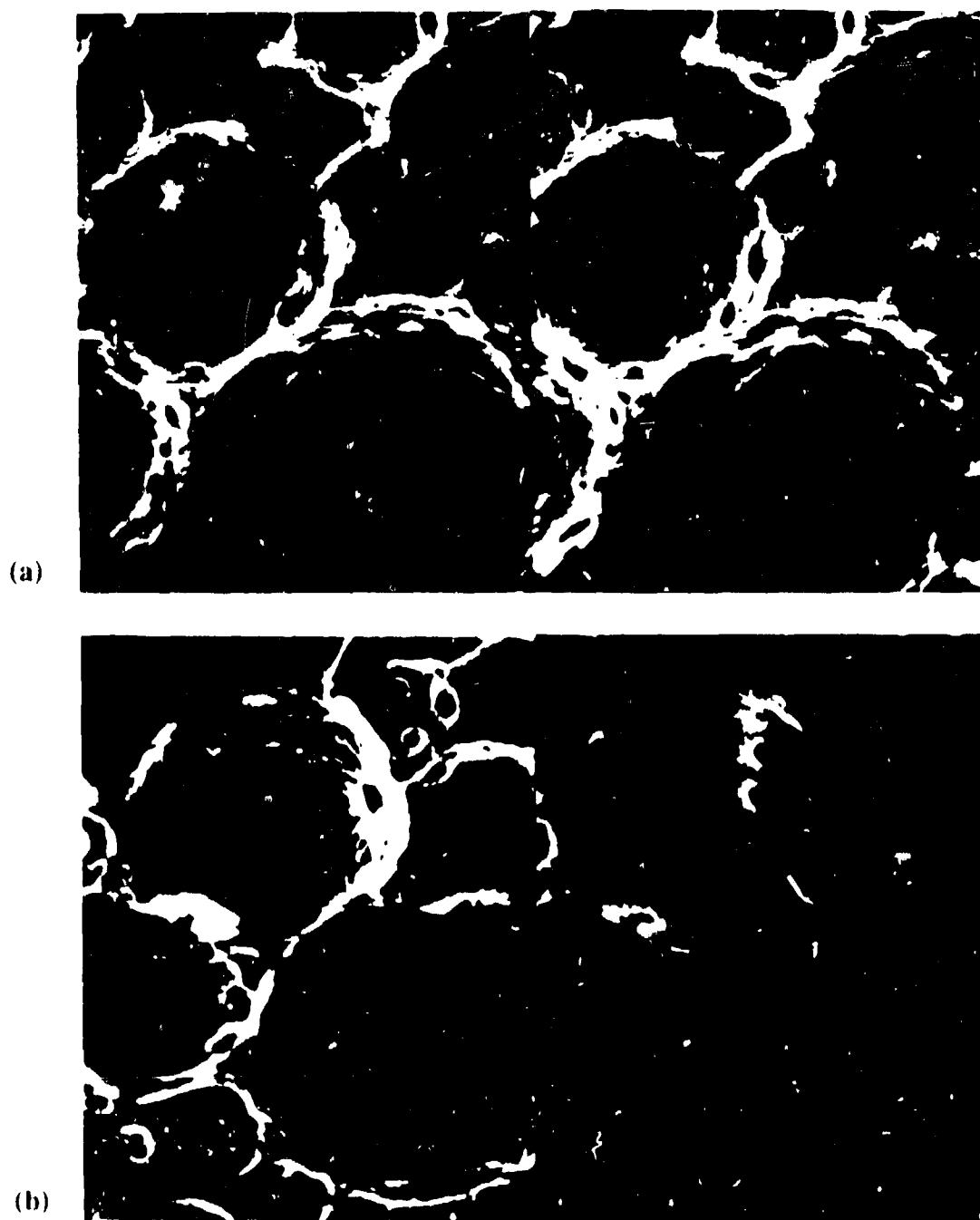


**Fig. 3 - Stereo pairs from the high-porosity polystyrene foam with the uniform cell structure showing the difference in distortion around pores in the cell walls; (a) a carbon-coated specimen at 2 kV and (b) an uncoated specimen at 0.5 kV. Horizontal image width = 26  $\mu$ m.**

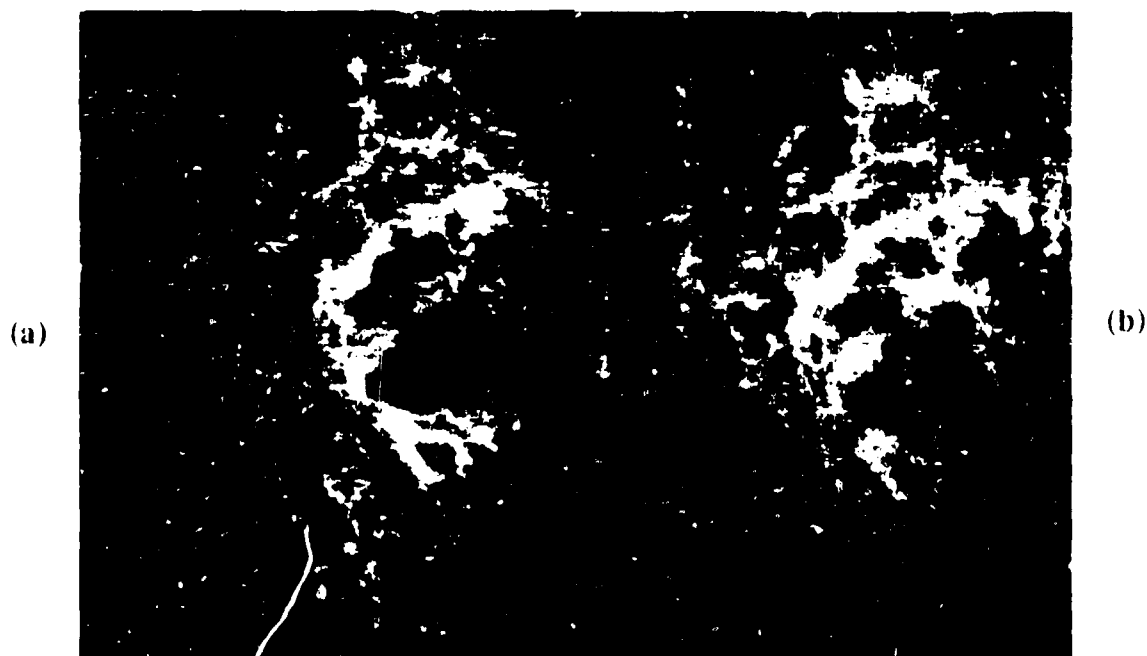
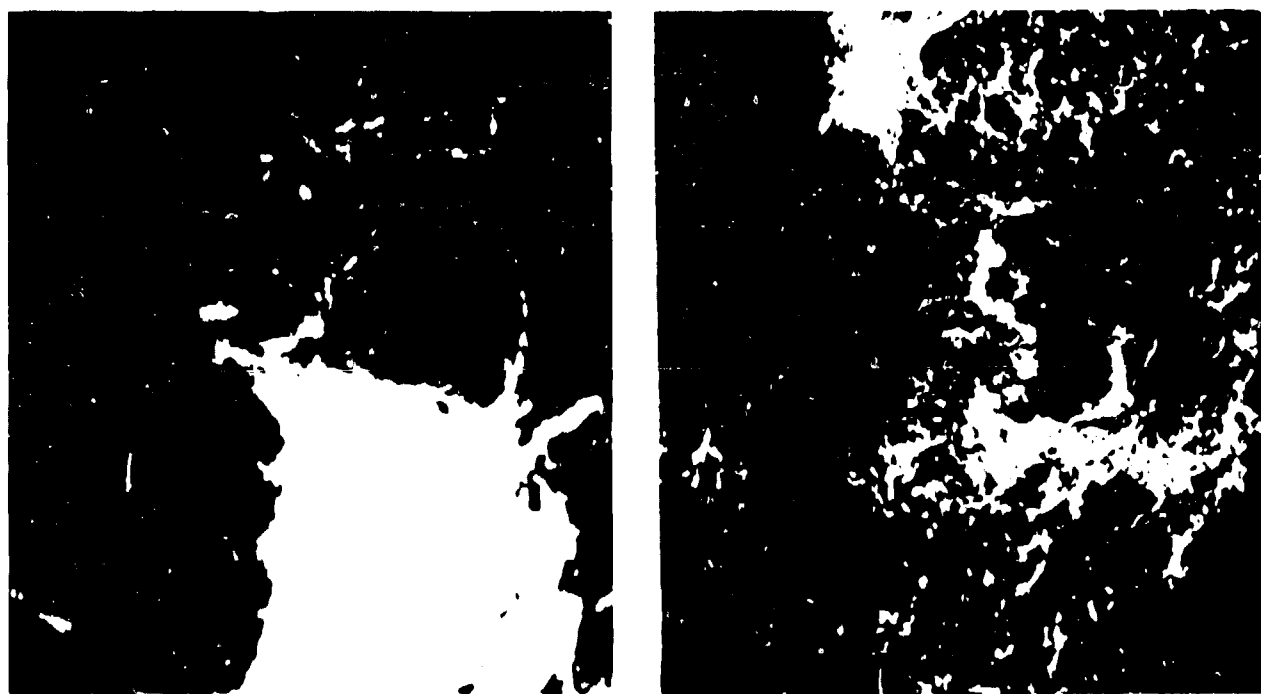
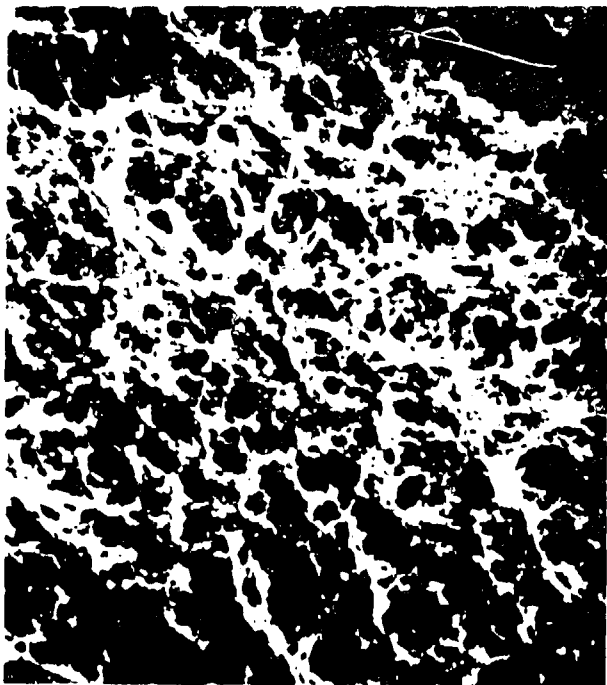


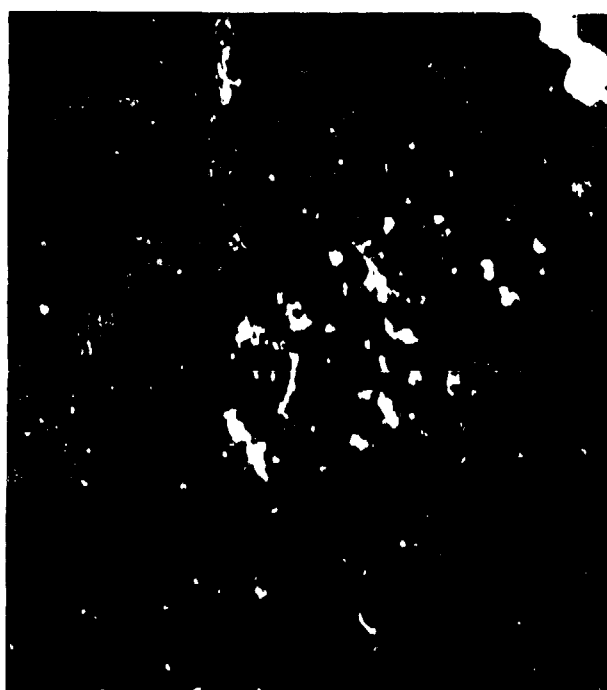
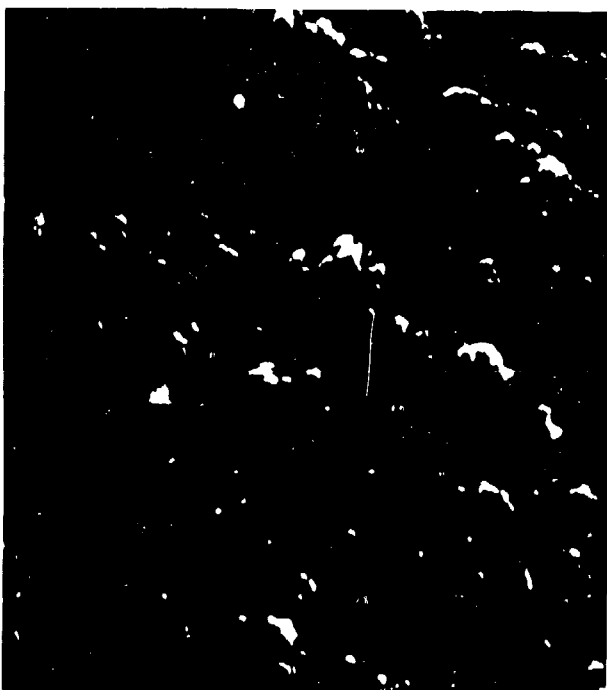
**Fig. 4 - Structure of 0.05 g/cm<sup>3</sup> cellulose acetate foam at 0.8 kV; (a) initial micrograph, left and (b) after 30-s exposure, right; mounted as a pseudo-stereo pair to accentuate the distortion. Horizontal width = 6.5  $\mu$ m.**



**(a) Fig. 5 - Electron-beam damage formed in 0.05 g/cm<sup>3</sup> cellulose acetate at 2 kV; (b) (a) the area exposed (b) area (a) at low magnification along with an adjacent area that was exposed for the same time. Horizontal image width: (a) = 8.0  $\mu$ m, (b) = 40  $\mu$ m.**



(a) Fig. 6 - Modification of the cell structure of  $0.05 \text{ g/cm}^3$  cellulose acetate foam by (b) (a) light carbon coating and (b) slightly heavier carbon coating. Horizontal image width =  $8.0 \text{ }\mu\text{m}$ .



(a) Fig. 7 - Structure of  $0.1 \text{ g/cm}^3$  silica aerogel; (a) coated at 20 kV and (b) uncoated (b) at 2 kV. Horizontal image width: (a)  $1.6 \text{ }\mu\text{m}$ , (b)  $2.0 \text{ }\mu\text{m}$ .

## RECENT RESULTS IN GLASS SHELL FABRICATION

by

Wayne J. Milier  
Raymond P. Belanger  
KMS Fusion, Inc.  
3621 State Road  
Ann Arbor, MI 48106-1567

As the ICF program advances, the energy delivered by drivers increases, requiring glass shell targets of larger diameters and wall thicknesses. Our glass shell fabrication goals then are to steadily increase the range of diameters and wall thicknesses we can make as well to increase the average wall uniformity over the entire size range.

Using our drop tower technology we are pursuing two approaches: to optimize the key experimental processing parameters, and to optimize the feed-stock gel composition. In the early 80's we emphasized the processing parameters, achieving greater control and reliability over the process as well as extending the shell size range. More recently we have concentrated on the gel feed-stock. In this paper we report significant increases in the shell size range and overall wall uniformity of our shells using optimal gel feed-stock. In addition we report on-going experiments (similar to those used in industry for quality assurance) designed to identify any significant processing parameters not found by our other methods.

### DETERMINING AN OPTIMAL ALKALI CONCE

At the last target fabrication we reported the results of experiments designed to determine the optimal alkali ratio in an alkali-borosilicate gel<sup>4,5</sup>. Keeping the alkali content (i.e., total oxide equivalent molar percentage) at 15% we systematically determined the optimal sodium to potassium to rubidium ratio to be 1:1:4.

Our next step was to find the optimal alkali content in the gel for the optimal alkali ratio. We examined gels ranging from 5% to 35% alkali oxide. Each gel was tested, by varying known processing parameters, under conditions to make smaller, thin-walled shells ( $\approx 100$ - $600\text{ }\mu\text{m}$  OD by  $\approx 0.5$ - $8\text{ }\mu\text{m}$  walls) and also under conditions to make larger, thick-walled shells ( $\approx 200$ - $800\text{ }\mu\text{m}$  OD by  $\approx 2$ - $14\text{ }\mu\text{m}$  walls). Five different shell runs were performed under each set of conditions with each gel. Since cesium was not included in the earlier experiments to determine optimal alkali ratios, we also examined a 15% cesium oxide gel.

Shell diameters slowly decreased and shell wall thicknesses increased as the alkali oxide content increased. The most important trend is shell wall uniformity, measured by the percentage of class A shells in a batch. A class A shell has less than 10% non-concentricity in a single-view interference photograph. As shown by figure 1, class A increases with gel alkali oxide content for the thinner, smaller shells, but attains its maximum at about 20% for the thicker-walled shells. Cesium did not improve wall uniformity in the 15% gels.

Since larger, thicker shells are of greater interest, the 20% gel was selected for further study.

#### MODELING THE 20% GEL

Further study of the 20% gel required the development of an empirical model quantitatively relating the key processing parameters to the resulting glass shell characteristics. Two sets of experiments were performed: "screening" experiments to identify the key processing parameters, and "response" surface experiments to quantitatively relate the key parameters to the resulting glass shell characteristics. This type of experimentation was previously discussed.<sup>1,2,5</sup>

The screening experiments examined eleven parameters composed of gel parameters and gel blowing parameters. The gel parameters were gel size, and

four gel pre-treatments by humidity exposure, autoclaving, vacuum oven drying, and pyrolysis. The gel-blowing parameters were tower temperature, shot size, shot interval, number of shots, water vapor pressure, and the use of a portal to partially close the top of the tower furnace tube. Of these, four were found to be key parameters worthy of further study: gel size, autoclaving, pyrolysis, and water vapor pressure.

Response surface experiments were completed for the four key parameters using a Box-Behnken experimental design. However the resulting polynomial equation did not reliably predict the results of shell batches run at the extreme values of the parameters. We added some extreme points to the design. The new polynomial equation is reliable.

The calculated response surfaces show that this gel produces good quality shells over a large shell size range. Figure 2 shows the response surface for diameter. The calculated overall size range goes to 1100  $\mu\text{m}$  OD and 14  $\mu\text{m}$  wall thickness, shown by figure 3.

#### LARGE SHELLS WITH THE 20% GEL

The response surface experiments were performed using gel sizes up to 425  $\mu\text{m}$ . In order to push the shell size range further, we examined shell fabrication using our largest gel sizes, 425-500  $\mu\text{m}$  and 500-600  $\mu\text{m}$ . We performed a pseudo-response surface design using gel size, tower temperature, and water vapor pressure as variables. The results were fit to a simple four-parameter polynomial. The calculated shell size range is shown in figure 4. Note that the tower furnace temperature has a strong effect on OD. We have not observed this trend with smaller gel sizes.

The percentage of class A shells is low in this size range, but the class B shell percentage is reasonably high. Class B shells have greater than 10% nonconcentricity in a single-view interference photograph, but do not have other defects (i.e. Class B shells have P1 defects but not P2 and

greater). However for direct-drive experiments, this level of nonconcentricity is acceptable.

#### SHEWHART EXPERIMENTS

We spent many years finding significant experimental parameters. However we still had anecdotal evidence that shell runs are not as repeatable as one would like. Although many pet theories "explained" the results, we did not even have clear evidence for significant non-repeatable runs.

As a result, over the past year, we have repeated five different shell runs weekly. The runs are very similar to Shewhart control chart runs used in industry to determine when a process is under control (i.e. repeatable) and when a process is out of control (i.e. due to uncontrolled process parameters). Shewhart experiments are statistically analyzed to clearly show whether our shell runs are varying by more than the expected random fluctuations of controlled parameters. The pooled standard deviation of all shell batches determines the expected standard deviation of the means of each sample. "Control" limits are set at  $\pm 3$  mean standard deviations around the overall mean of all the runs. If a process is under control, 99.7% of the sample averages fall within the control limits.

A Shewhart control chart for shell diameters is shown by figure 5. Although the control limits are broad, clearly less than 99.7% of the runs are within the limits. Thus our process is affected by unidentified, uncontrolled parameters. We have kept track of many environmental factors (e.g. inside and outside temperatures and humidities, etc.) but, unfortunately have not found a clear connection to uncontrolled variations. We are continuing the search.

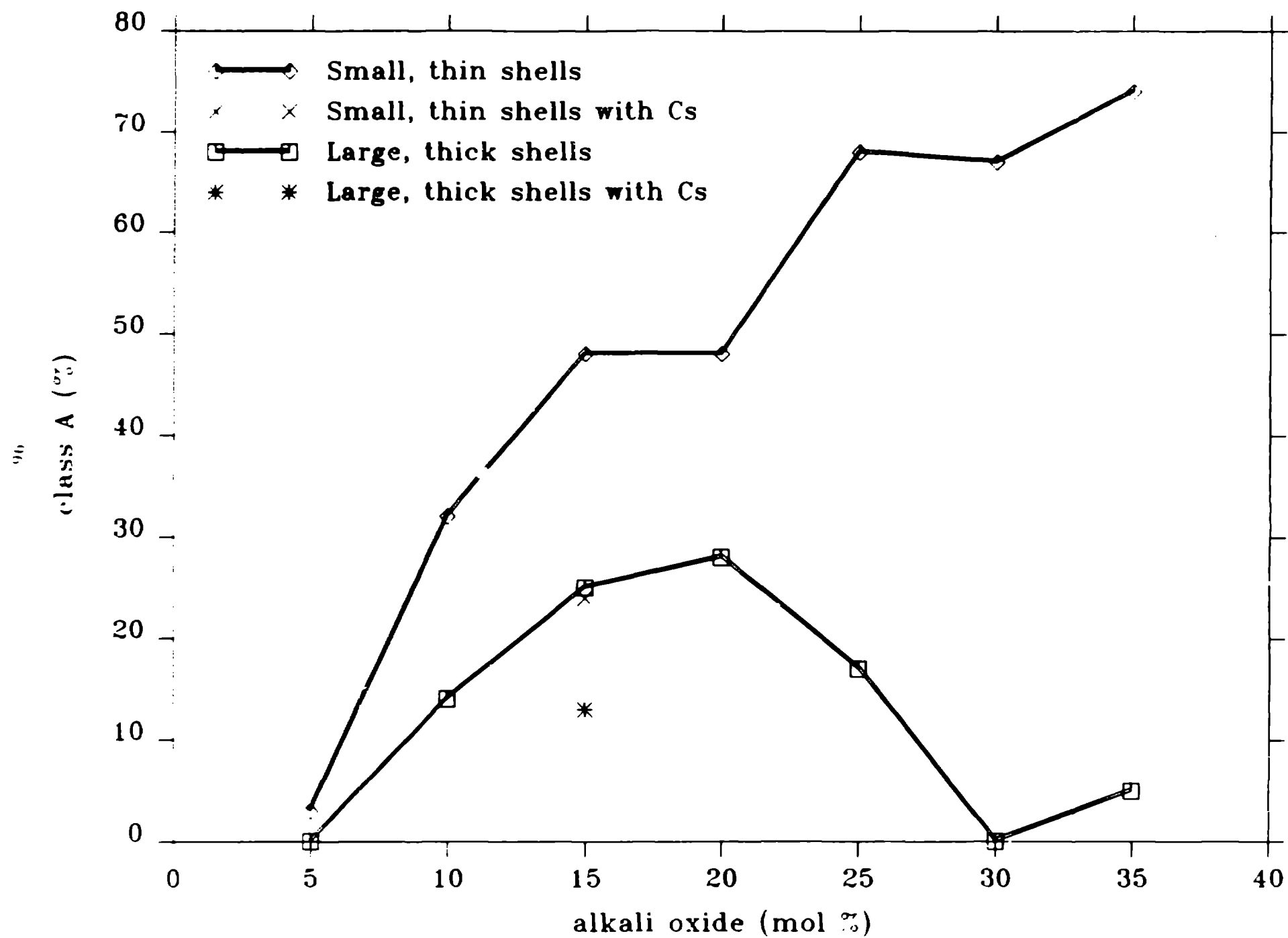
## CONCLUSIONS

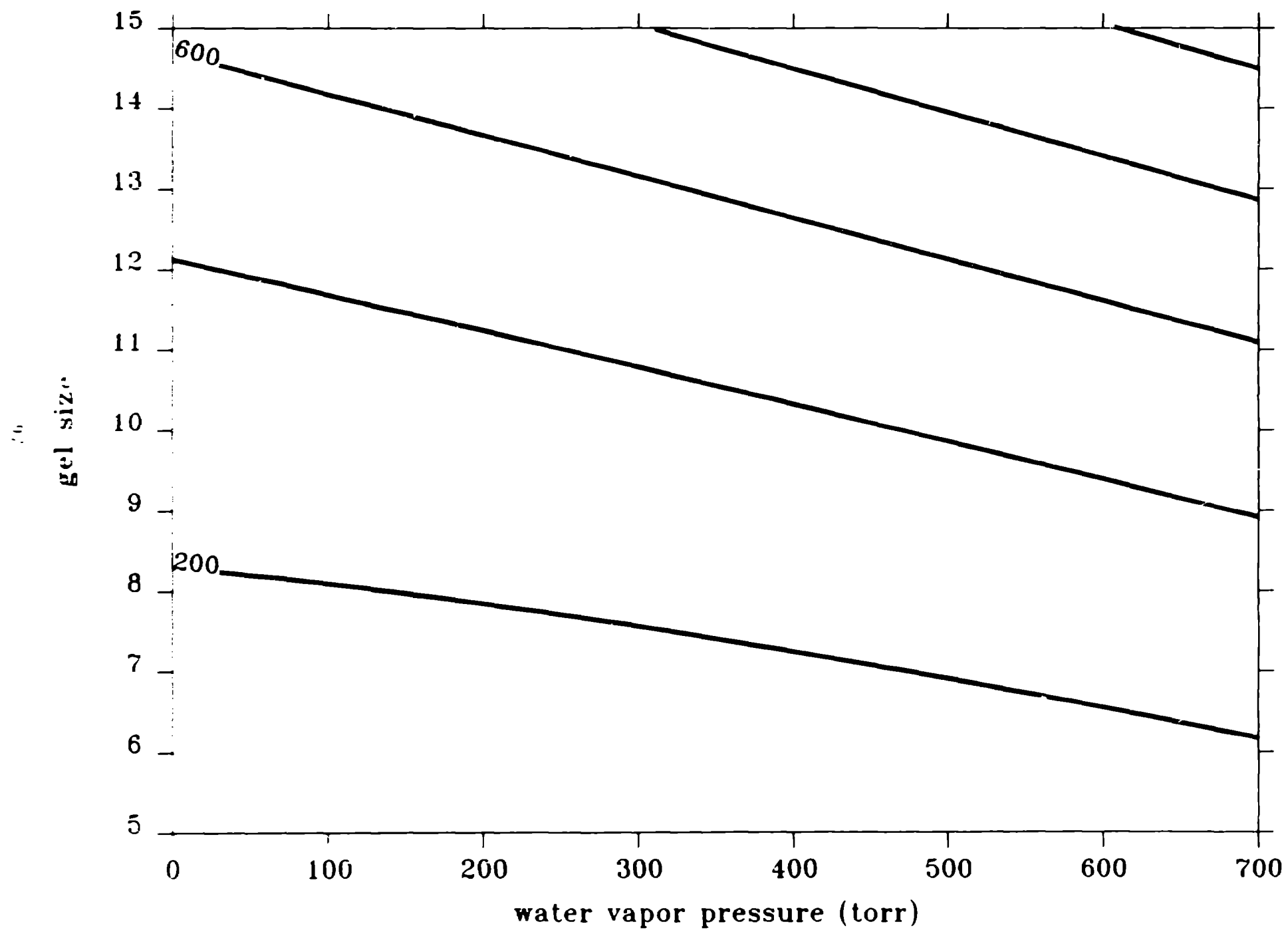
We are increasing the size range and wall uniformity of our glass shells. We have found and quantitatively explored a superior gel containing 20% alkali oxide in the ratio of Na:K:4Rb. The new gel produces shells over a large size range with very good wall uniformity. We are also continuing Shewhart experiments to identify and control parameters that have significant long term effects on shell synthesis reliability.

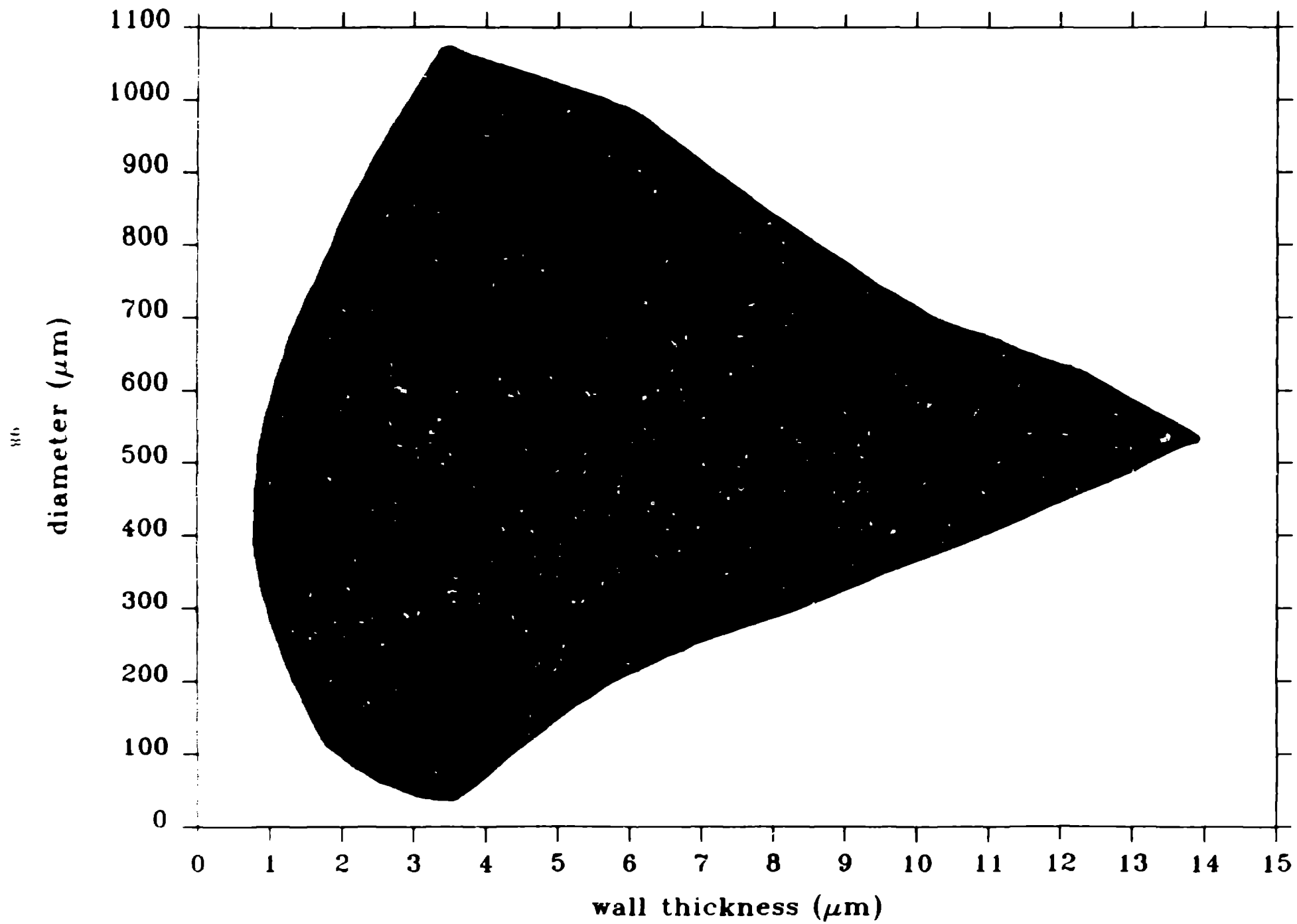
## REFERENCES

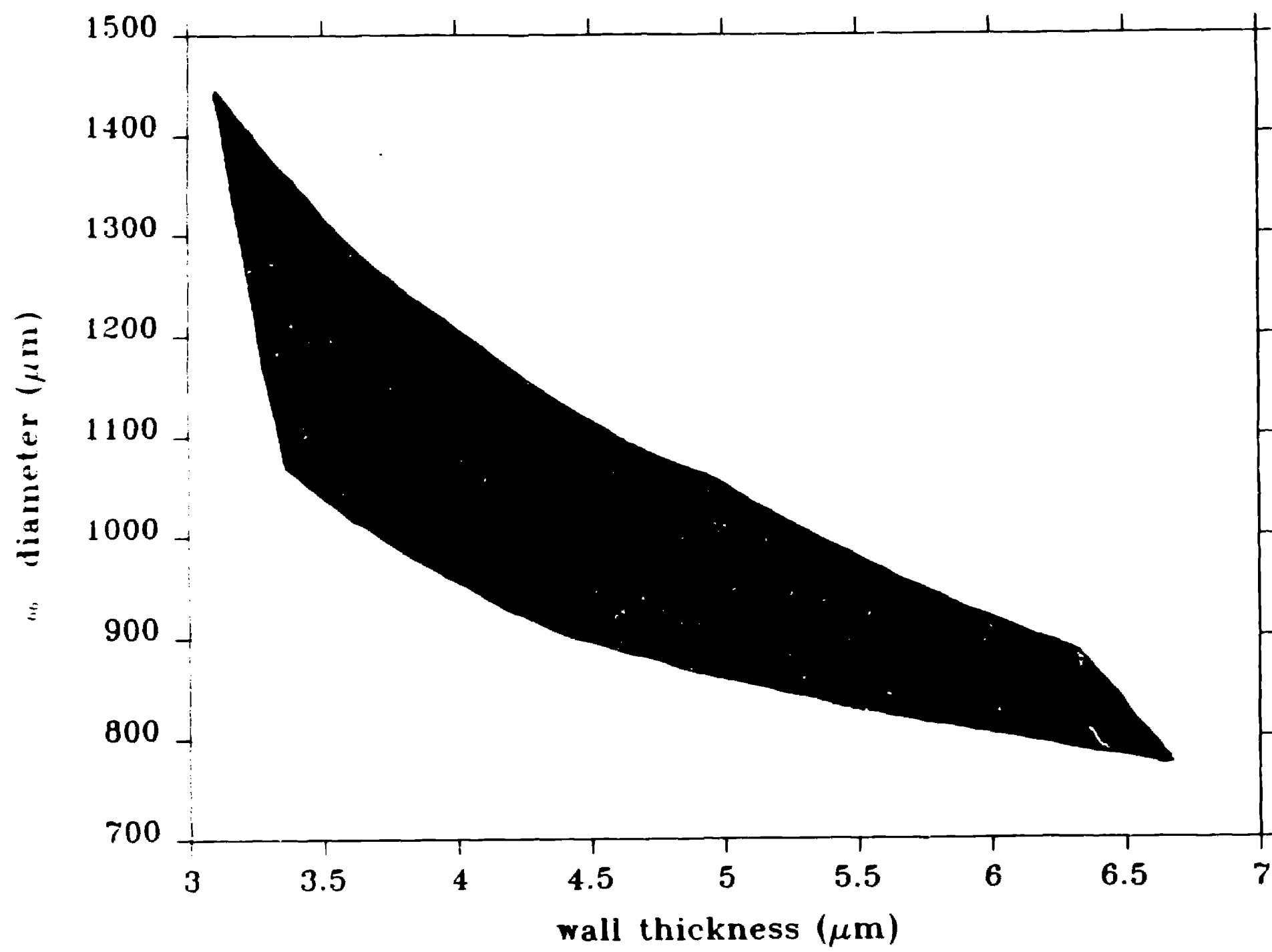
1. R. Belanger and W. J. Miller, "Glass Shell Preparation," J. Vac. Sci. Technol. A, 3, 1270 (1985).
2. W. J. Miller and R. Belanger, "Process Control of Hollow Glass Sphere Production," presented at the 2nd Annual Target Fabrication Specialists Meeting, Las Vegas, Nevada, March 29-31, 1983.
3. W. J. Miller and R. Belanger, "Reducing the Aspect Ratio of Hollow Glass Spheres," presented at the 2nd Annual Target Fabrication Specialists Meeting, Las Vegas, Nevada, March 29-31, 1983.
4. W. J. Miller and R. Belanger, "Optimum Alkali Ratios in Glass Shells," presented at the 5th Annual Target Fabrication Specialists Meeting, Las Vegas, Nevada, March 24-27, 1986.
5. R. Downs, M. Ebner, and W. J. Miller, "Hollow Glass Microspheres by Sol-Gel Technology", in Sol Gel Technology for Thin Films, Fibers, Preforms, Electronics, and Speciality Shapes, edited by Lisa C. Klein, Noyes Publications:Park Ridge, New Jersey, 1988; Chapter 16.

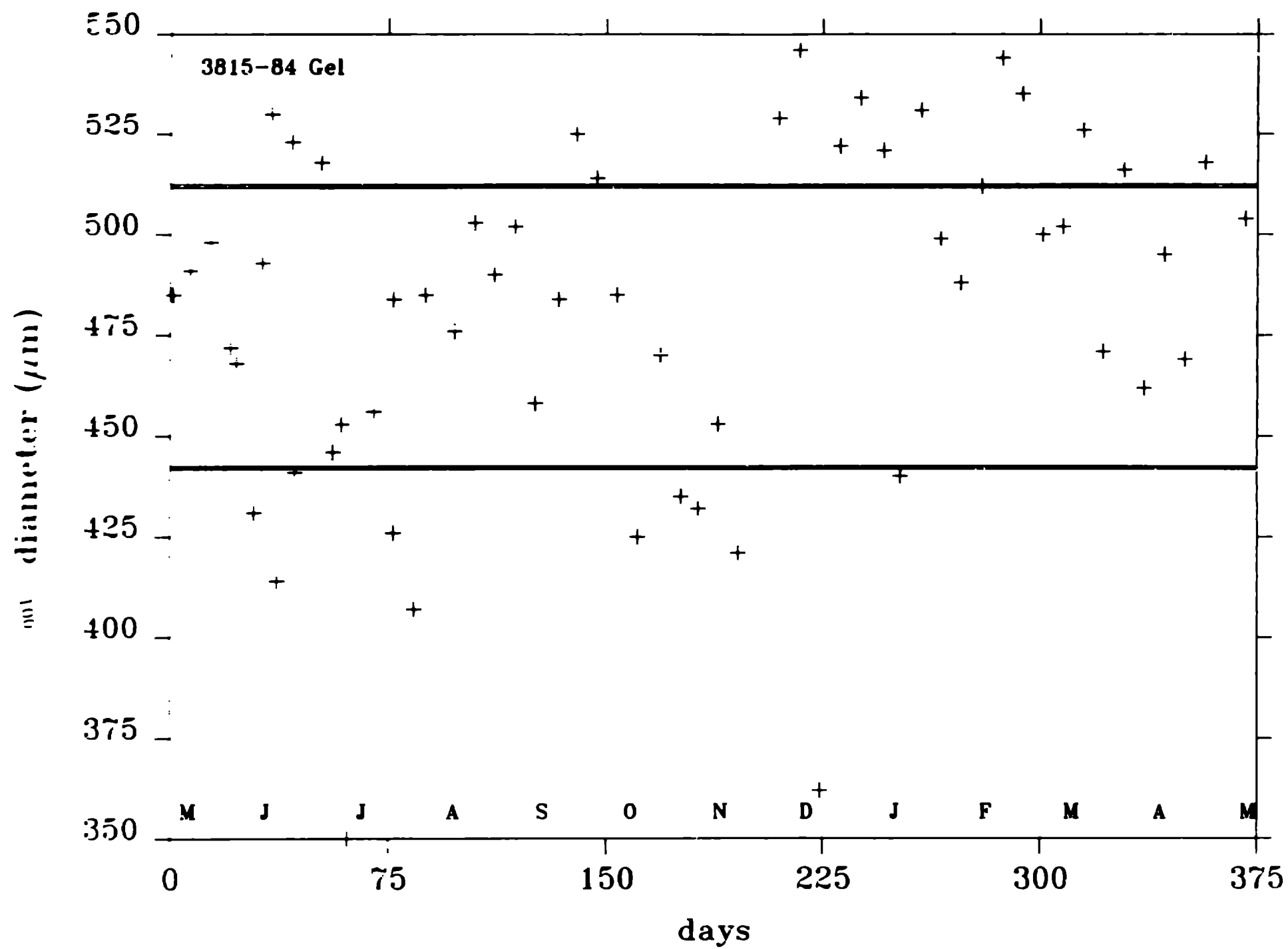












## EVALUATION OF TENSILE STRENGTH IN ALKALI SILICATE SHELLS

M. A. Ebner, W. J. Miller, and J. L. Evans  
KMS Fusion, Inc.  
3621 South State Road  
Ann Arbor, Michigan 48106

### INTRODUCTION

Glass shells used as ICF fuel containers must withstand extreme external and internal pressure. A shell's resistance to external pressure (compressive strength) determines how rapidly it can be filled with fuel by permeation; its resistance to internal pressure (tensile strength) determines how much gaseous fuel it can ultimately hold.

The compressive failure of glass shells has been identified as a buckling failure mode.<sup>1</sup> It is characterized by Young's modulus, which is dependent on composition. The buckling strength of glass shells has been determined for several compositions.<sup>2,3</sup>

Tensile strength data for glass shells are not as plentiful.<sup>4,5</sup> Tensile strength is difficult to study because it is a function of the history of the glass and does not have an inherent value. While the theoretical strength of glass is on the order of  $1.38$  to  $3.44 \times 10^{10}$  Pa, the actual strength of a particular glass object is usually several orders of magnitude lower, and is determined by the flaw population. Furthermore, tensile failure can occur either by stress intensification at the tips of surface flaws and defects, or by crack growth induced by stress corrosion (delayed failure or fatigue). Consequently, since flaws are generally produced on the surface of glass objects by handling and exposure to an abrasive or reactive environment, glass fracture is highly random in nature. These considerations have caused increasing concern in target fabrication as target sizes have increased and specifications become more stringent.

We seek to determine the effects on tensile strength of the permeant gas, and of the geometric characteristics, surface area, and glass volume of the shells. As the failures have become more costly, greater target reliability (or predictability) has become increasingly desirable. We have therefore resumed studies to determine the effective tensile strength of glass shells.

EXPERIMENTAL PROCEDURE. The shells used in these experiments were alkali silicate glass with a nominal 95 mol% silica composition. Randomly chosen shells were individually characterized for diameter and wall thickness by optical microscopy and interferometry. The diameters of the shells varied from 450 to 750  $\mu\text{m}$ , the wall thickness from 1.2 to 8.6  $\mu\text{m}$ , and the aspect ratio (o.d./wall) from 55 to 590. Between 160 and 250 shells were used in each experiment; the characterized shells were arrayed in aluminum or brass "egg crates" to preserve their identities during the experiment.

To ensure that buckling failure did not occur as the shells were filled with gas ( $\text{H}_2$  or He) in preparation for the tensile tests and obscure the tensile strength data, the crated shells were subjected to 30 atm buckling pressures prior to permeation. The permeant gas was added in stages ( $< 25$  atm, in a Parr bomb) to avoid the development of excessive buckling pressures. These stages generally involved repeated pressure increments of 20 atm at 260 to 360°C, with permeation times between pressure increments long enough to achieve  $> 90\%$  pressure equilibration.

Tensile strength was evaluated every 25 atm as the room-temperature pressure in the shells was increased stepwise from 25 to 285 atm (He) and 25 to 250 atm ( $\text{H}_2$ ). As described in the preceding paragraph, the shells were pressurized at elevated temperatures. The 20 atm (high temperature) pressure increases were repeated as many times as necessary for the room-temperature pressure to increase by 25 atm. Then the Parr bomb was cooled and vented, and failures aurally and visually inventoried.

The actual pressure in the shells at each step was verified only for  $\text{H}_2$ -filled shells because He permeated from the shells too rapidly at room temperature to yield reliable data. The  $\text{H}_2$  fill pressure was determined by breaking individual shells in an evacuated PVT volume fitted with a Baratron 10 Torr pressure transducer. The method yielded very good gas fill data with a very narrow pressure distribution, generally with a  $\sigma$  of 2%.

The final pressures were limited by the pressure and temperature limits of the Parr bomb and the permeation rates of the glass; to achieve these high pressures, the final permeation steps were conducted at reduced temperatures ( $< 360^\circ\text{C}$ ) to remain within the pressure limits of the Parr bomb. The

experiments were terminated when 90% (He) and 86% (H<sub>2</sub>) of the shells had failed.

DATA ANALYSIS. The fracture stress of the failed glass shells was calculated from the shell diameter, wall thickness, and fill pressure at failure, using the hoop stress equation,

$$\Delta P = 4S/AR,$$

where  $\Delta P$  is the tensile load on the glass wall,  $S$  is the fracture stress, and  $AR$  is the aspect ratio (o.d./wall) of the fractured shell. Because of the random nature of failure, these experiments produced failure stress data with very broad distributions.

If the distributions are normal, the characteristic failure stress (tensile strength) for the sample can readily be calculated from histograms, cumulative failure probability curves, or from the slope of a least-squares regression function fitting a scatter plot of the individual shell data (hoop stress format). We elected to use the Weibull statistical treatment, which is commonly used to describe the brittle failure of solids. It is a versatile method that can accommodate skewed distributions, and that can also be used to predict the probability of failure as a function of the applied stress and the shell geometry.

In the common form of the Weibull expression, failure probability is a function of applied stress<sup>6,7,8</sup>

$$F = 1 - \exp [-(S/S_0)^m],$$

and

$$F = n/(N + 1),$$

where  $F$  is the failure probability or the fraction of the sample that failed below the measured sample failure stress,  $S$ ;  $m$  is the Weibull modulus;  $S_0$  is a scaling factor or the characteristic strength;<sup>6</sup>  $n$  is the rank of the sample in order of increasing measured failure stress, and  $N$  is the total number of tested samples. The Weibull modulus  $m$  is an indication of the spread of the distribution. As  $m$  approaches zero, the spread of the failure stress distribution increases and the probability of failure at any stress  $S < S_0$  increases. As  $m$  increases, the spread of the data decreases, indicating greater homogeneity in the sample. The probability of failure is significant only



for  $S \approx S_0$  (Ref. 6). In addition, when  $m \approx 3$ , the sample distribution is considered to be a normal distribution.<sup>7</sup>

In practice, the data are plotted in the double logarithm form of the above equation,

$$\ln[-\ln(1 - F)] = m \ln S - m \ln S_0.$$

Since the Weibull expression is now a linear function, the Weibull modulus  $m$  and scaling factor  $S_0$  can be obtained from the slope and intercept of the least-squares regression fit to the data. The median failure stress  $S_m$  can be calculated from the relationship,  $S_m = S_0(0.693)^{1/m}$ .

The Weibull equation is also useful for predicting the probability of shell failure as a function of fill pressure and aspect ratio of the shells. Using the Weibull expression together with the hoop stress equation gives

$$P = (4S_0/AR)[-\ln(1 - F)]^{1/m}.$$

Consequently, for known values of  $S_0$  and  $m$ , one can plot failure probability,  $F$ , contours as a function of fill pressure and shell aspect ratio.

#### RESULTS AND DISCUSSION.

We expected to encounter brittle fracture of the stressed shells during the rapid venting of the (dry) gas from the Parr bomb. However, in none of the many fill-and-vent cycles could any bursting of shells in the dry gas atmosphere be detected through the walls of the Parr bomb with a stethoscope. Instead, upon opening the Parr bomb to the ambient air (at 75 to 85% relative humidity), there invariably commenced a staccato of bursting shells. Detectable bursting usually ceased within 30 min. The audible count of these bursting shells agreed to within 10% with the subsequent visual inventory; the discrepancy is probably due to the detection error (coincident bursts) in the audible count. Thus these losses must be attributable to failure by stress corrosion by the ambient moisture, rather than to brittle failure in the dry gas environment of the Parr bomb.

The distribution of the failure stress data for the He sample was broad and nearly normal, ranging from  $1.58 \times 10^8$  to  $2.04 \times 10^9$  Pa. The mean failure stress of the actual sample data were  $8.20 \times 10^8$  Pa ( $\sigma = 2.82 \times 10^8$  Pa). The Weibull modulus  $m$  and the median failure stress  $S_m$  were 3.31 (standard error = 0.043) and  $8.27 \times 10^8$  Pa, respectively. The contours for 5% and 50%

probability of failure for these shells, calculated as described above, are shown as a function of He fill pressure and shell aspect ratio in Fig. 2.

The distribution of the failure stress data for H<sub>2</sub> was broad and normal, similar to that of the He data, with failure stresses ranging from  $1.38 \times 10^8$  to  $1.23 \times 10^9$  Pa. The Weibull modulus  $m$  and the median failure stress  $S_m$ , calculated from the slope and intercept of the regression function, are 3.50 (standard error = 0.02) and  $6.82 \times 10^8$  Pa, respectively.

The comparison of the least-squares regression fits to the Weibull plots of the He and H<sub>2</sub> data in Fig. 1 shows only a slight difference in slope, indicative of a similarity in the shape of the data distributions, but a significant difference in intercept, indicative of a difference in median strength.

As shown in Table 1, the mean and median failure stress values for the H<sub>2</sub> sample population were both about 20% lower than the corresponding values of the He data. While the large  $\sigma$  values for the mean values of these broad data distributions would suggest otherwise, the difference between the two mean failure stress values is indeed statistically significant since the confidence intervals at the 95% level for the two means do not overlap. Furthermore, there is a 95% level of confidence that the means of the two data sets differ by  $1.55 \times 10^8 \pm 5.53 \times 10^7$  Pa (see Fig. 2).

This difference in median strengths has a significant effect on failure probability, as shown by the comparison of 5% and 50% failure probability conforms for He and H<sub>2</sub> in Fig. 2.

There are at least two mechanisms that may account for the reduction of glass strength by H<sub>2</sub>. Hydrogen may react with the glass, reducing the silica to form SiH and SiOH moieties<sup>9,10</sup> in the glass, or it may react with the residual CO<sub>2</sub> (a blowing gas) in the shell.<sup>11,12</sup> This reduction reaction could result in the production of as much as 0.2 atm water vapor pressure (at room temperature) in the shell. This water vapor could react with the inner glass surface to cause corrosion-induced flaws to form on the inside surface.

Spectroscopic evidence of the silica reduction reaction has been reported for reaction temperatures greater than 500°C.<sup>9,10</sup> Shelby<sup>9</sup> has also implied that the reaction may proceed at lower temperatures. If this is indeed so, then the extent of reaction and the reaction rate are expected to be highly

dependent on the gas pressure, temperature, and cumulative reaction time. Thus one would expect the average failure stress value to decrease steadily as the fill progressed, as a consequence of the increasing  $H_2$  pressure and reaction (fill) time.

An analysis of the failure data did not reveal such a trend. The failure stress data for  $H_2$  do not show any relationship to cumulative reaction time or to  $H_2$  pressure, as shown in the  $H_2$  scatter plot of Fig. 3. This is more readily apparent when only the median failure stress values for each data group at the various pressures are considered, as indicated by the arrows in the figure. The best straight-line fit to these median failure stress values has zero slope, indicating that there is no relationship of failure stress to fill time or  $H_2$  concentration.

The present data are more consistent with the residual  $CO_2$  reduction mechanism, which is thermodynamically more favored than the silica reduction. Furthermore, this reaction is expected to have a much higher reaction rate and is expected to go to completion rapidly because of the large excess of  $H_2$ . The total reaction time is expected to be considerably less than the cumulative fill times used in these experiments, and the effects of this reaction should manifest themselves early in the fill cycle. Preliminary evidence from residual gas reactions with  $D_2$  supports these speculations.<sup>12</sup>

As glass shell surface area increases (due to increasing shell diameter), the number of flaws per shell is likely to increase, as is the probability that a shell will have a fatal flaw. Therefore, one could expect the observed failure stress to decrease with increasing shell surface area. However, a detailed analysis of the two sets of failure data has shown no dependence of tensile strength on shell surface area.

There is, however, an apparent relationship between failure stress and glass volume. As shown in Fig. 4, plots of failure stress as a function of glass volume show a pattern of decreasing tensile strength with increasing glass volume, both in the  $H_2$  and the He data. A portion of this trend may be the result of error in experimental measurements of failure pressure and wall thickness. However, our error analysis reinforces our confidence in the validity of the relationship between glass volume and tensile strength.

In principle, if tensile strength were truly an intrinsic material property, one would expect the observed failure stress to remain constant, independent of glass volume. However, the original Weibull equation<sup>13</sup> postulates the relationship of increasing glass volume  $V$  to decreasing glass strength,

$$F = 1 - \exp [-V(S/S_0)^m].$$

As before,  $m$  and  $S_0$  can be obtained from the slope and intercept of the least-squares regression fit. The median failure stress now depends on  $m$ ,  $S_0$ , and  $V$ ,

$$S_m = S_0(0.693/V)^{1/m}.$$

Including the volume term in the Weibull equation results in a much better fit of the calculated probability contours to our data (see Fig. 5). However, further work is needed to clarify that volume, rather than wall thickness or inverse aspect ratio, is causing the decreased failure pressure.

**Table 1. Failure Stress Values for Gas-Filled Glass Shells**

Failure Stress from Sample Distribution ( $10^8$ Pa)				Weibull Characteristics		
Fill Gas	Pressure Median	Pressure Mean	$\sigma$	95% Confidence Interval	$m$	$S_m$ ( $10^8$ Pa)
He	7.99	8.20	2.82	7.72 - 8.68	3.3	8.27
H <sub>2</sub>	6.64	6.64	2.08	6.34 - 6.96	3.5	6.82
Difference between mean (95% confidence interval) =						$1.55 \times 10^8 + 5.53 \times 10^7$ Pa.

## REFERENCES

1. R. L. Downs, B. D. Homyk, and R. G. Schneggenbuger, Digest of Topical Meeting on Inertial Confinement Fusion, (Opt. Soc. Am., Washington, D.C. , 1980) paper THB18, p. 94/94.
2. W. J. Miller, R. L. Downs, L. A. Scott, and R. G. Schneggenburger, J. Vac. Sci. Technol., **18**, 1290 (1981).
3. J. V. Milewski, Rev. Sci. Instrum., **52**, 1647 (1981).
4. J. V. Milewski and R. G. Marsters, J. Vac. Sci. Technol., **18**, 1279 (1981).
5. R. G. Schneggenburger, unpublished results.
6. W. D. Kingery, H. K. Bowen, and D. R. Uhlmann, Introduction to Ceramics, 2nd ed. (John Wiley and Sons, Inc., NY, 1976) pp. 787-790.
7. R. H. Doremus, "Fracture and Fatigue of Glass," in Treatise on Materials Science and Technology, **22**, Glass III, edited by M. Tomozawa and R. H. Doremus (Academic Press, NY, 1982).
8. B. A. Kschinka, S. Perrella, H. Nguyen, and R. C. Bradt, J. Am. Cer. Soc., **69**, 467 (1986).
9. J. E. Shelby, J. Applied Phys., **51**, 2589 (1980).
10. R. H. Doremus, Glass Science, (John Wiley and Sons, NY, 1971) pp. 231-2.
11. R. L. Downs, M. A. Ebner, B. D. Homyk, and R. L. Nolen, J. Vac. Sci. Technol., **18**, 1272-75 (1981).
12. M. A. Ebner, W. J. Miller, L. T. Thompson, "Reactivity of the Residual Gases in Glass Shells," Sixth Target Fabrication Meeting, 1988.
13. J. Weibull, Ing. Vetenskaps Akad. Handl, Stockholm, No. 151, 1939.

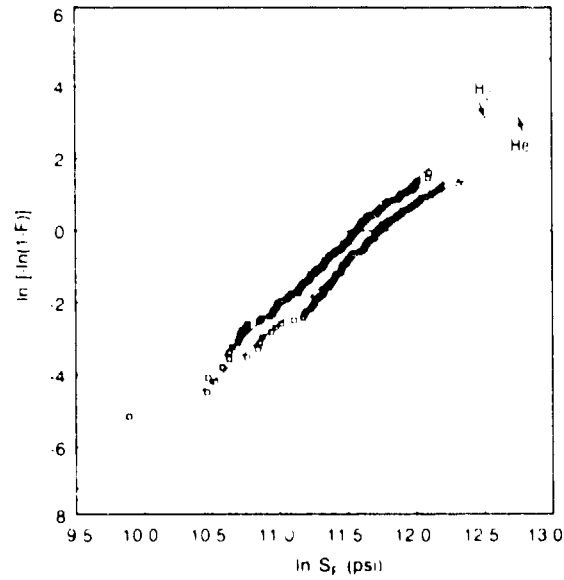


Figure 1. The Weibull distribution of tensile failure stress is shown for He-filled (lower line) and  $H_2$ -filled (upper line) glass. There is only a slight difference in the slope of the two lines, which indicates that the data distributions were similar in shape. However, there is a significant difference in intercept, which indicates a difference in the median strength.

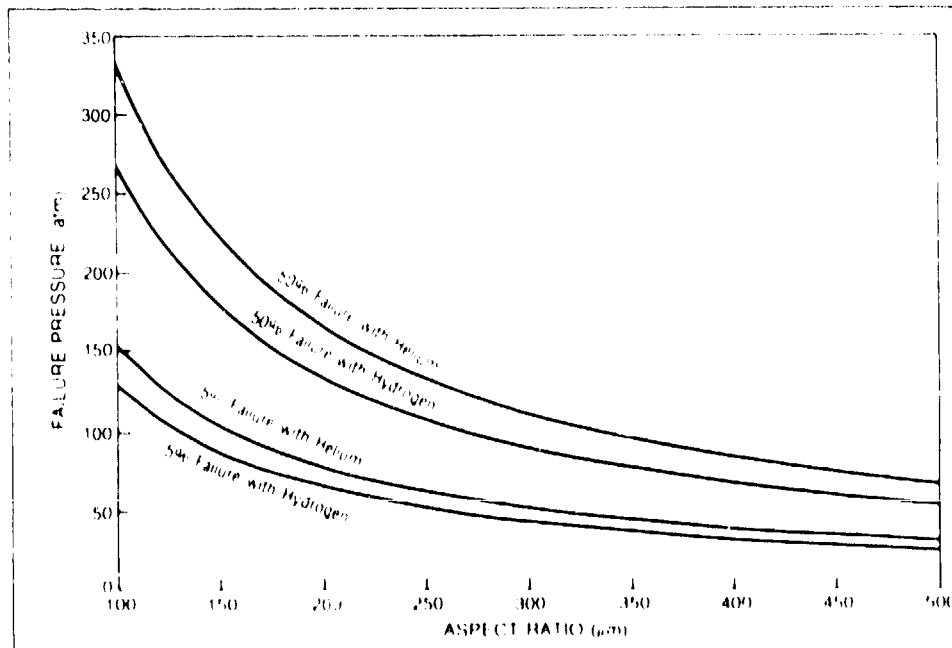


Figure 2. Contours for 5% and 50% probability of failure for hollow glass shells, calculated using Weibull parameters, are shown as a function of He (or  $H_2$ ) fill pressure and shell aspect ratio. The difference in the 50% failure probability contours is appreciable. There is a 95% level of confidence that the means of the two data sets differ by  $1.55 \times 10^8 \pm 5.53 \times 10^7$ .

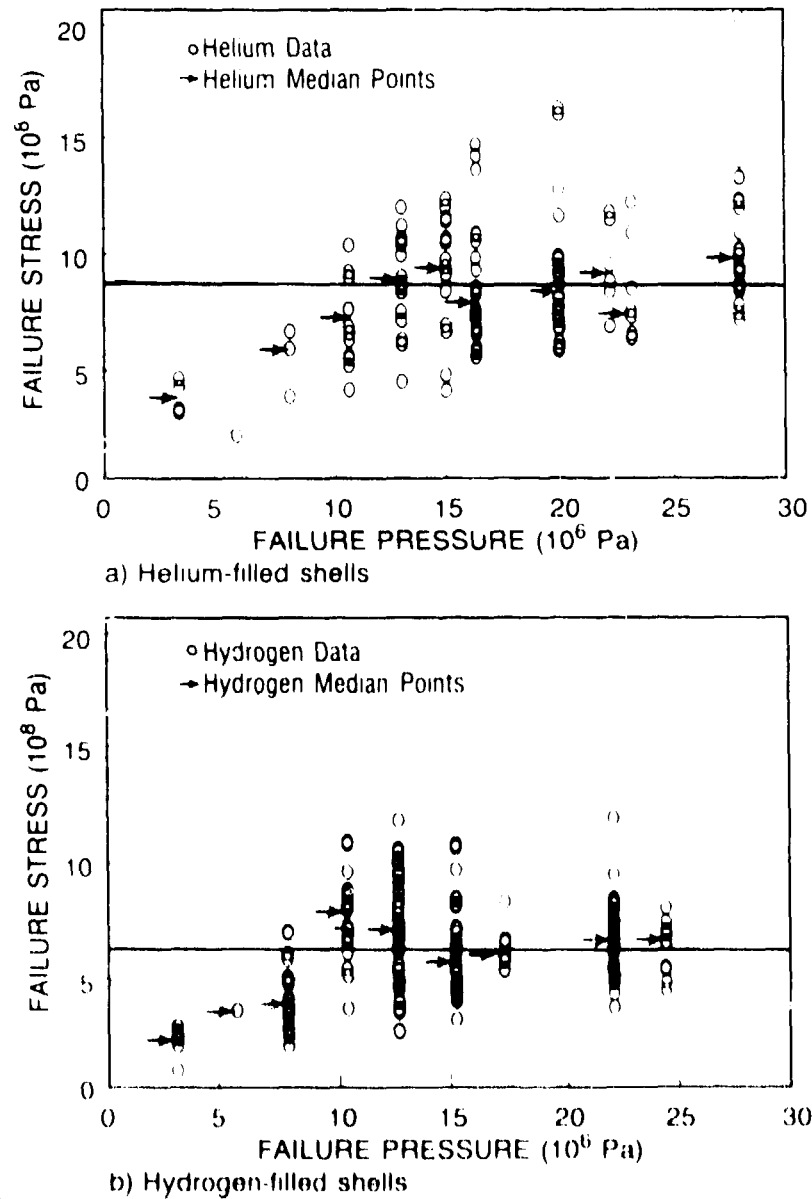


Figure 3 The failure stresses in a population of (a) He-filled and (b)  $H_2$ -filled glass shells are shown as a function of the gas concentration (i.e., fill pressure) at failure. Arrows indicate the median failure stress value in each data group. The line, equivalent to the mean failure stress, approximates the best fit to the data (the first three data groups at the lower pressures may have involved buckling failures and were not included in this analysis). The best fit to both data sets can also be approximated with a zero slope function, indicating that the median failure stress is not a function of fill time or gas concentration.

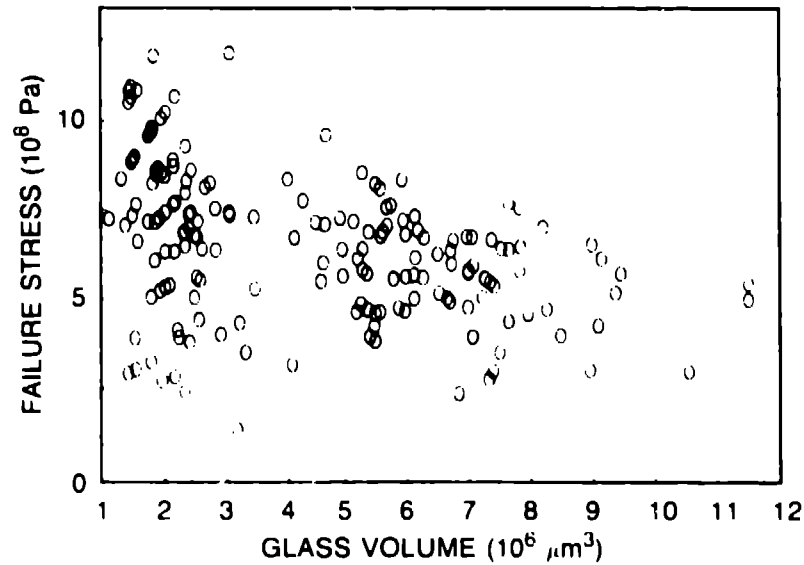


Figure 4 If tensile strength is an intrinsic material property, then the observed failure stress will remain constant, independent of glass volume. Our results, however, suggest that tensile strength decreases with increasing glass volume.

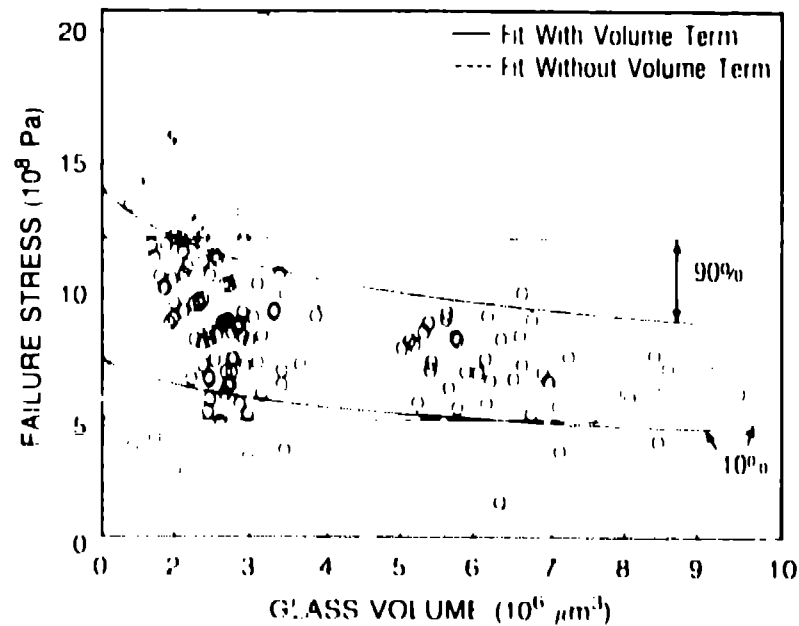


Figure 5 Calculated 10% and 90% failure probability curves are shown super-imposed on the helium data. The straight lines result from calculations in which the volume term was excluded from the Weibull treatment. The curves represent calculations in which the volume term was included, this results in a much better fit to our data, since the predicted failure stress decreases with glass volume.



## THE FILLING AND LEAKAGE OF MULTILAYER POLYMER FUEL CAPSULES\*

John Z. Grens and Eben M. Lilley

University of California  
Lawrence Livermore National Laboratory  
P. O. Box 5508, Livermore, CA 94550

### INTRODUCTION

Poly(vinyl alcohol) (PVA) coated polystyrene (PS) shells have been described by Burnham et al,<sup>1</sup> and are used in Nova laser targets. It is necessary to know both the fuel (deuterium) fill and the amount of other gas, such as argon, very accurately so that the experimental results can be properly interpreted. This paper describes briefly how the trace gas and fuel are added to the shells, how the resulting fill is measured and the leakage to be expected when the shell is removed from pressurized storage.

### TRACE GAS ADDITION

Neither the PS core nor the PVA coating provide any significant barrier to gas flow. The argon is concentrated in the PVA layer, the permeability is so low - half life in the one year at the argon must be added before the PVA coating is cured. The permeability is at odds with published data for films, but has been confirmed many times. The argon content of the shells changes only slowly after the PVA is cured.

We constructed the apparatus shown in Figs. 2 and 3 to allow us to remove the air from the shells which had previously been loaded into capillary tubes and then expose them to a partial pressure of argon. Usually this is .05 to 0.10 atmosphere. The shells are then brought to a total pressure of just under 1 atmosphere and PVA solution admitted from the heated reservoir in the base of the apparatus. The argon content

\*Work performed under the auspices of the U. S. Department of Energy by the Lawrence Livermore National Laboratory under contract number W-7405-ENG-48.

essentially does not change from this time onward - we have checked this by curing the PVA in an argon filled column and in a nitrogen filled column, and find no difference.

#### TRACE GAS MEASUREMENT

We independently confirm the fill of trace gas by X-ray fluorescence. This is not a particularly easy measurement due to the minute quantity of argon present and the interference of the Chlorine peak adjacent to it (fig. 4). The sample is mounted between two 300-400 Angstrom formvar films at a carefully located position in a 35 mm slide frame. About a 5 mm diameter spot is available in which the readings remain constant. The machine used is a Kevex 700, operated by Beam Lab Inc. of Livermore, CA.

Calibration has been accomplished in two ways. We prepared a dot of Potassium Chloride of accurately known mass, the K lines of which neatly bracket the argon K line. We also prepared 1 atmosphere and .01 atmosphere argon filled shells - two pressures we can get very accurately. The method gives a resolution of slightly better than .01 atm.

#### FUEL GAS FILL

After the shells have been PVA and CH coated, radiographed for size and layer thickness, had the trace gas determined by X-ray fluorescence and placed in individual glass capillary tubes, they are ready for deuterium fill.

The permeability of PVA to hydrogen is high enough in young capsules that they may be filled at room temperature in a reasonable length of time. The permeability of the PVA does change with time - decreases - but we have not made a detailed study of it. Very young capsules of the 400 micrometer size range have a 1/e leak rate of 10 hours or so, older ones - a month or two - may be in the 25 hour range. The capsules easily withstand a 10 atmosphere external pressure, and we use steps of this size to bring the pressure to the desired fill, usually 50 atmospheres. An appropriate partial pressure of argon is maintained during the fill process.

### FUEL GAS LEAKAGE

The filled capsules are heat treated at 60°C for 24 hours. This process extends the 1/e time for leakage (again, of a 400 micrometer capsule) to a nominal 100 hours. If we just aged them for a year or so, they would get near this number on their own, but the low temperature heat treatment is quicker.

Leakage is checked on selected capsules by placing them in capillary tubes with one end sealed and monitoring the motion of a small plug of Mercury placed in the tube. This is done either with consecutive photomicrographs or with the apparatus shown in Fig. 5, which monitors the change in resistance of a pair of fine wires as the location of the Mercury plug changes.

Capsules and completed targets are stored under pressure in quick opening autoclaves. The nominal time from when a target is removed from pressurized storage until it is shot at by the laser is about 2 hours - argon loss is nil and deuterium loss is about 1.5%.

### REFERENCES

1. Burnham, A. et al, J. Vac. Sci. Technol. A5 (6), Nov/Dec. 1987, p. 3417.

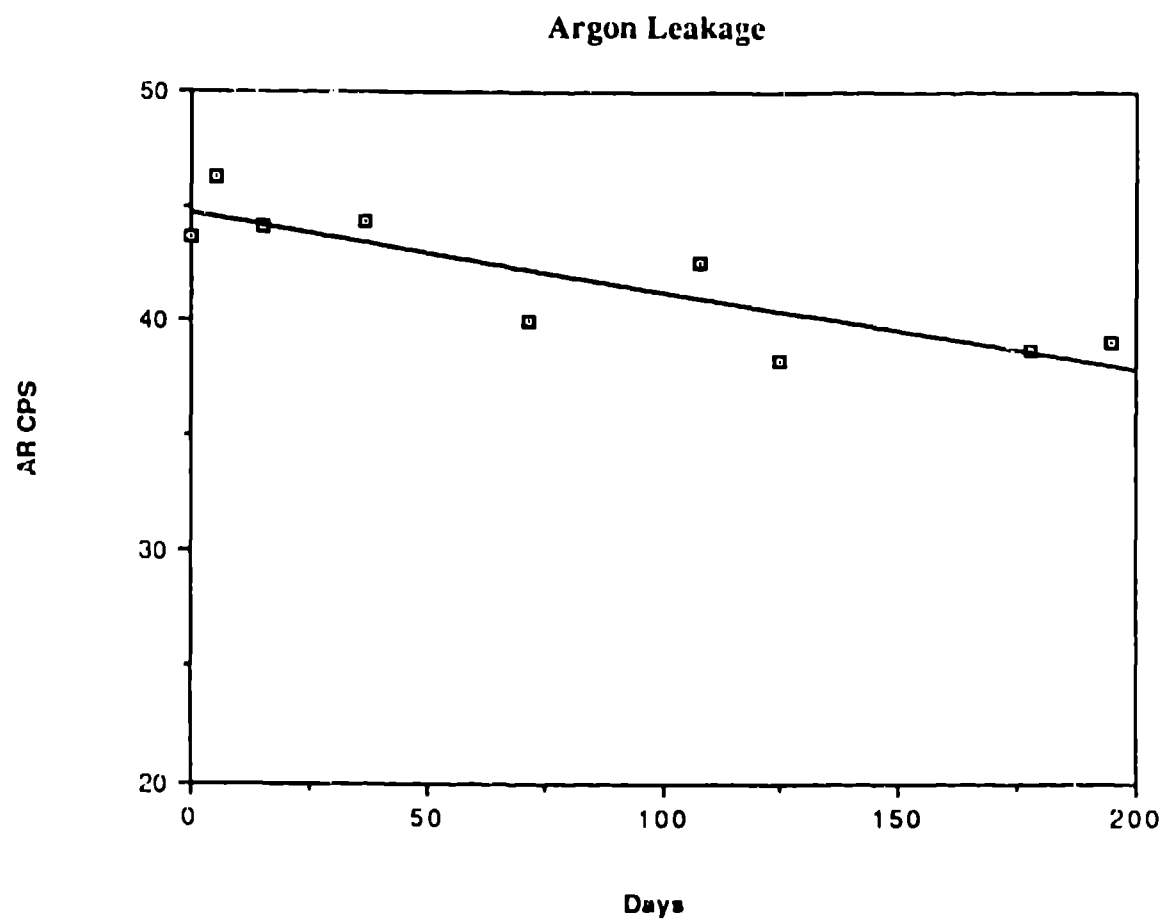


Figure 1. Argon loss vs. time

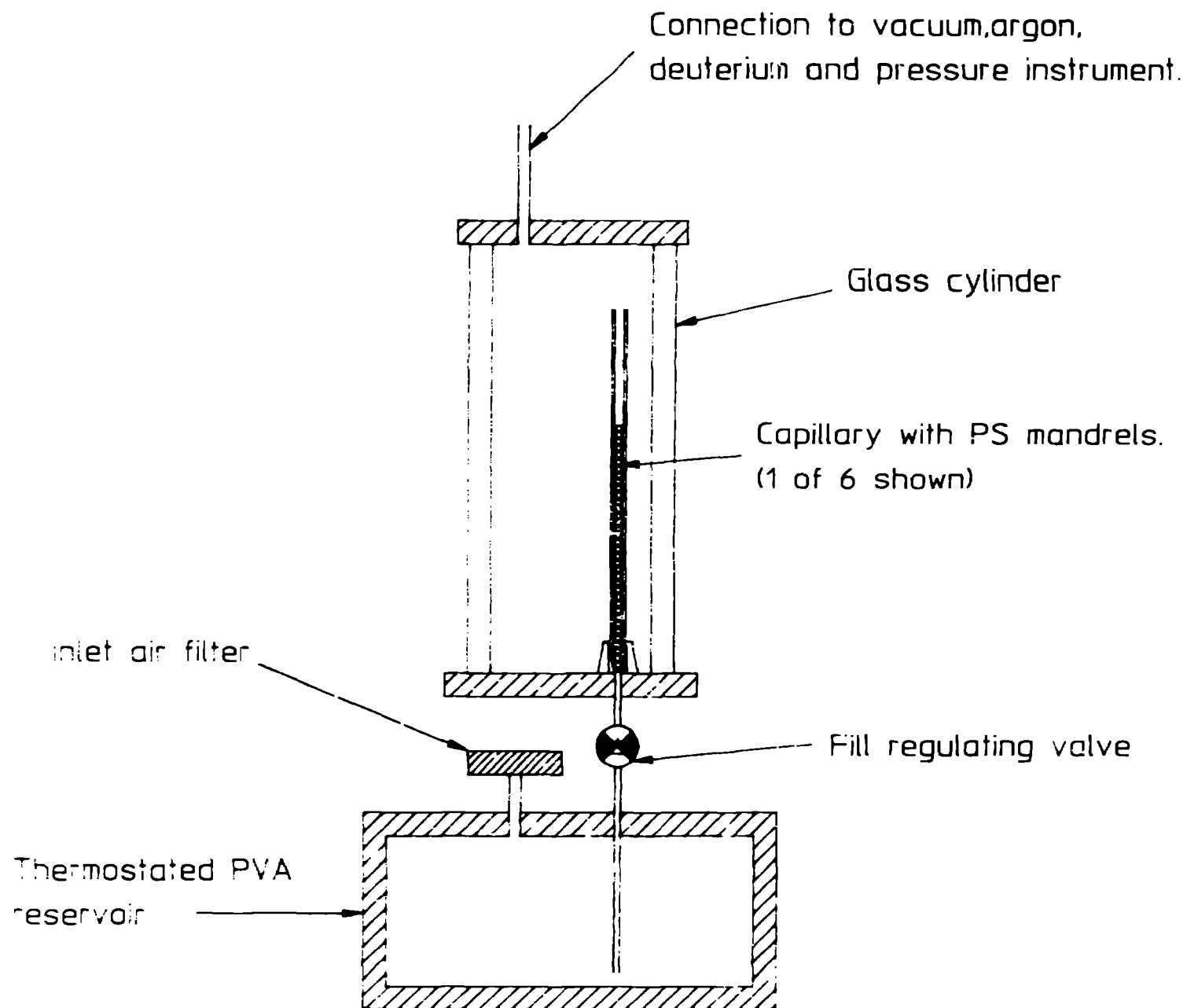
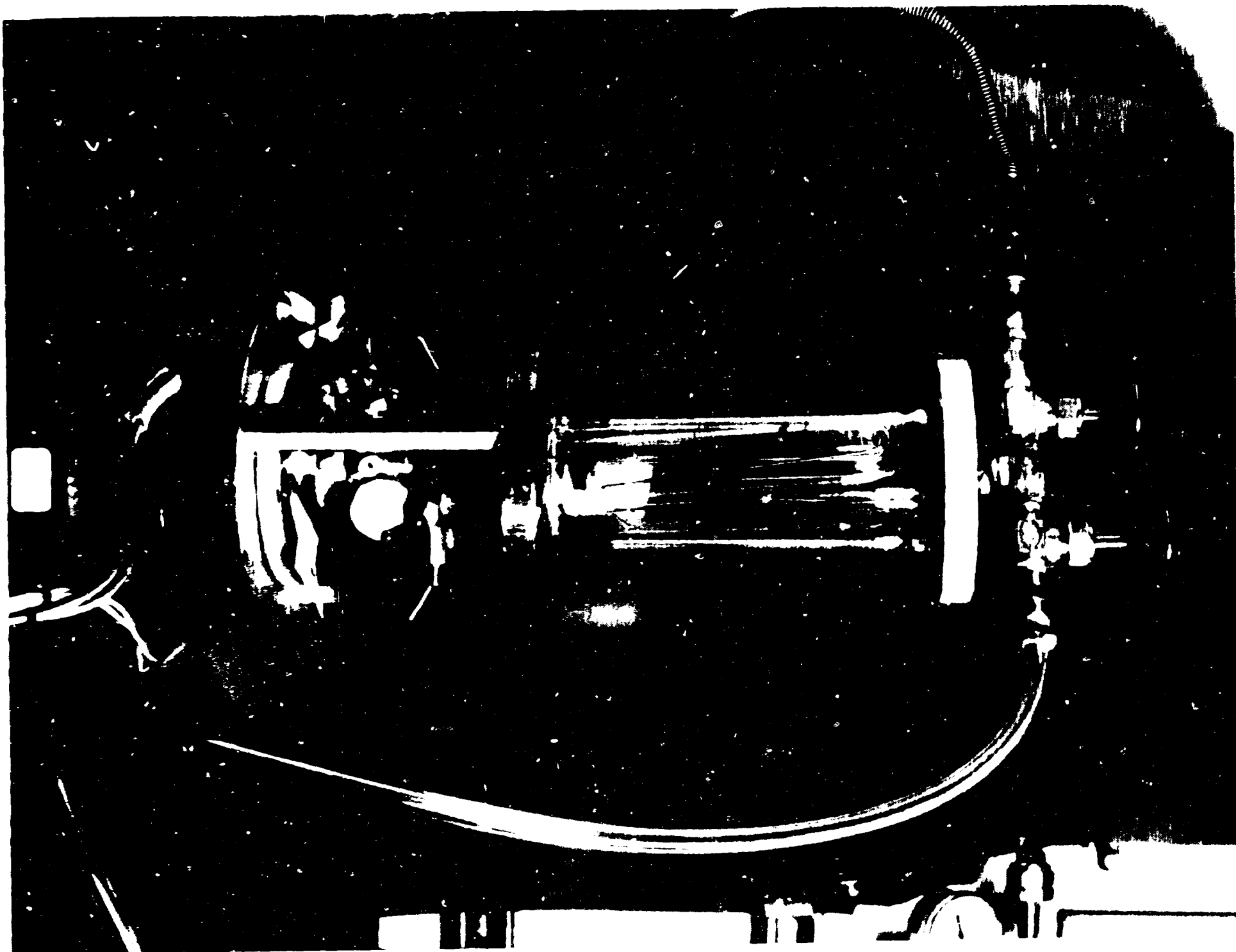


Figure 2. Apparatus for filling PS-PVA



871202428

300SEC

Counts

240-B E E M L A B 0 2 - 1 0 - 8 8

210-S O L I D 0 . 1 A T M A R B E A D N O 4 1 2 / 0 2

180-D C T T E D B L A N K F O R M V A R 1 2 / 0 2 / 8 7

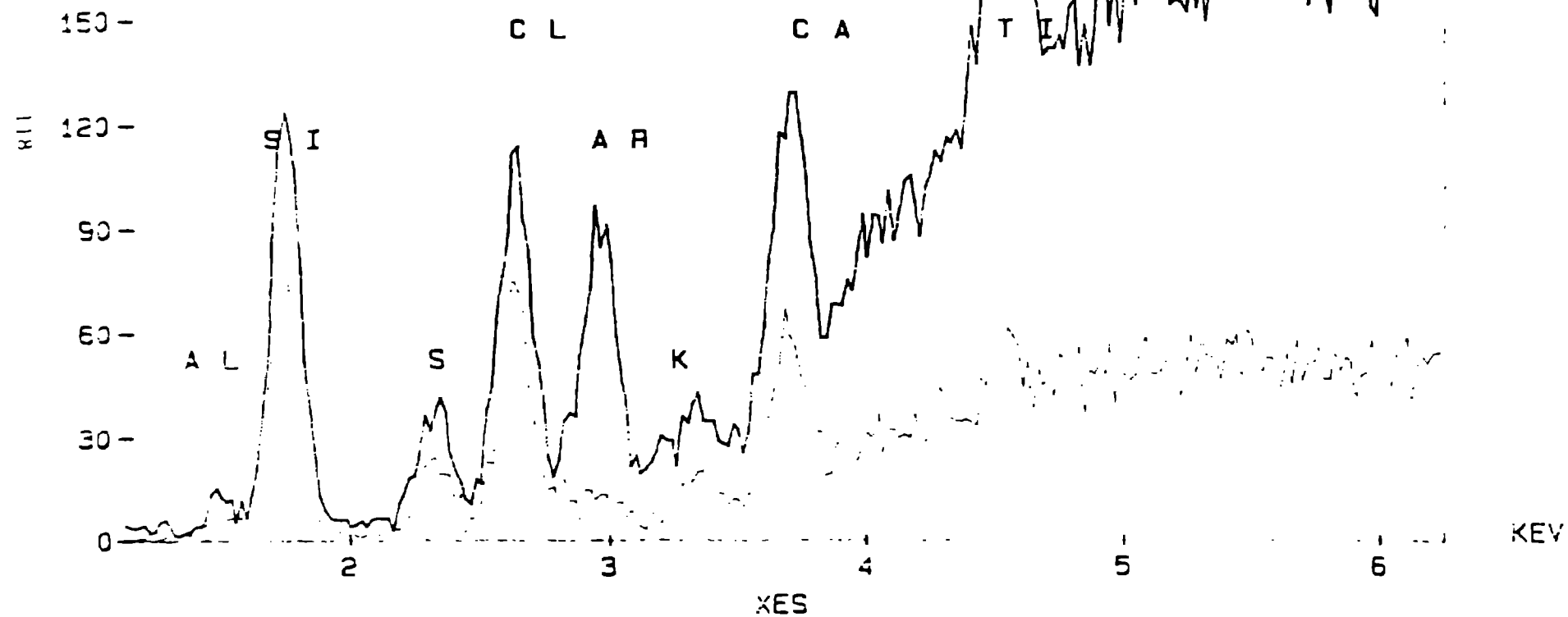


Figure 4. XRF Spectrum

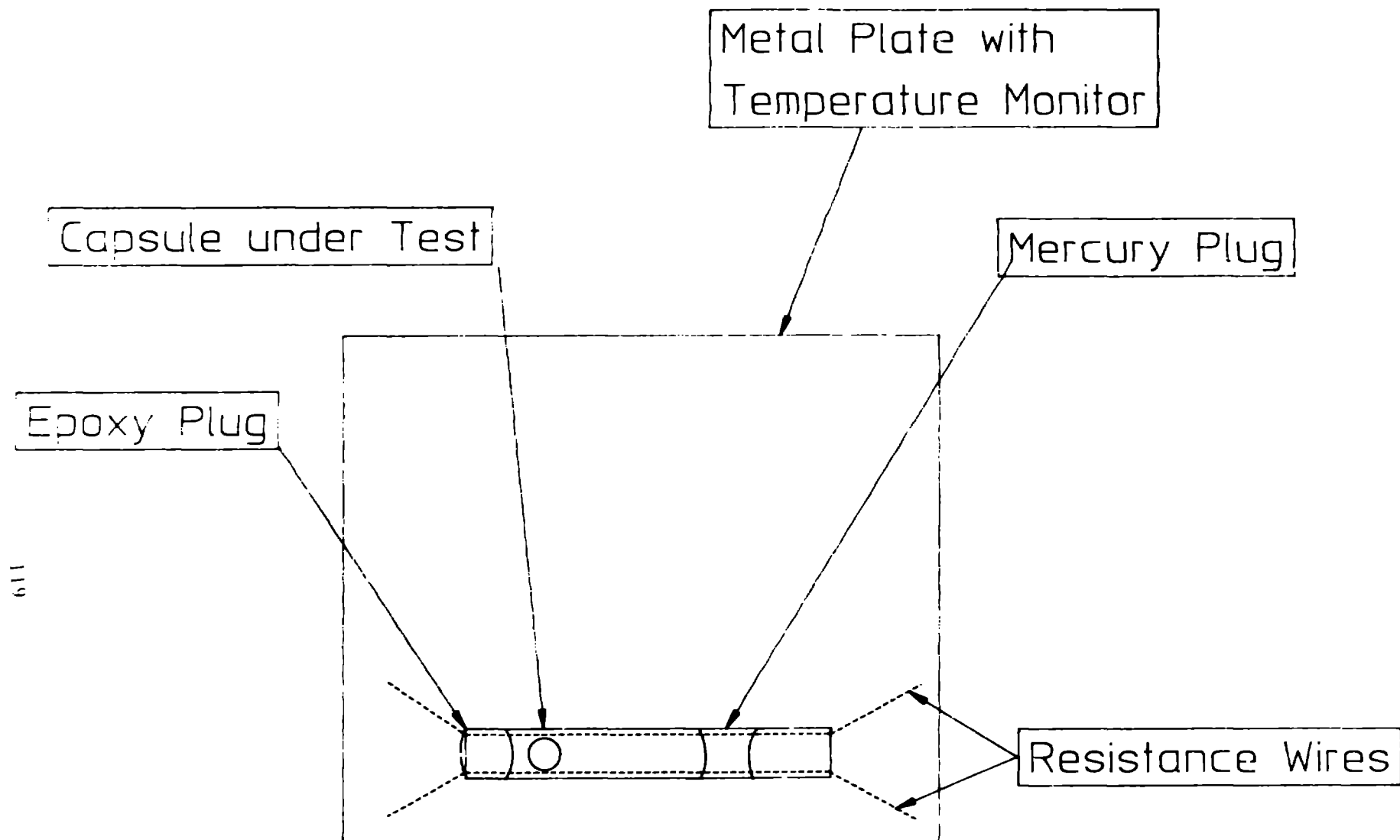


Figure 5. Apparatus for measuring capsule leakage.



MEASUREMENT OF ARGON CONTENT IN GMBS  
USING NEUTRON ACTIVATION

by

Peter L. Gobby  
Materials Science & Technology Division  
Los Alamos National Laboratory

and

Matt Hyre  
U.S. Army

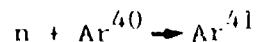
ABSTRACT

Neutron activation has been used to non-destructively determine the argon content of glass microballoons. A technique was developed using a standard which relieves the need for knowledge of the neutron flux and the detection efficiency of the gamma rays. Argon contents of approximately 20 nanograms were determined with an accuracy of about 35%.

INTRODUCTION

Argon is frequently used as a tracer in laser fusion experiments. The intensity of its 3 keV emission is a measure of density and temperature in the implosion of an argon filled glass microballoon (GM3). Since each target shot requires a considerable investment in time and money, it is important that the argon content is verified before firing the laser. We have chosen to investigate the utility of neutron activation in making this determination.

$\text{Ar}^{40}$  makes up 99.6% of naturally occurring argon, so the neutron capture reaction of interest is



The thermal neutron cross section for this reaction is 0.53 barn.  $\text{Ar}^{41}$  subsequently decays via  $\beta^-$  to  $\text{K}^{41}$  with a half life of 1.83 hour. A

gamma ray of energy 1.293 MeV is released concurrent with the  $\beta$ -decay. It is this gamma-ray which is detected in the neutron activation analysis.

#### MATHEMATICAL FORMULATION

In order to deduce the amount of argon present in a sample from the number of gamma rays detected, it is necessary to develop some equations describing the activation process and subsequent decay. In general, the rate equations describing these processes are

$$dN/dt = -NI\sigma \quad (1)$$

and

$$dN^*/dt = NI\sigma - \alpha N^*, \quad (2)$$

where  $N$  is the number of atoms of the species to be detected (in our case, argon),  $I$  is the thermal neutron flux,  $\sigma$  is the cross section,  $N^*$  is number of activated atoms and  $\alpha$  is the decay constant (the natural log of 2 divided by the half-life).

Equation (1) merely describes the conversion of the original species into the activated species. In principle, the original species is being "used up", but in practice the cross section and neutron flux are small enough that no significant portion of the original sample is converted to the activated species in an activation exposure less than many weeks. Consequently  $N$  is effectively a constant.

Equation (2) describes the rate of change of the activated species. Since the activated species is being created and destroyed (activation and radioactive decay), there are two terms that contribute to this rate of change.

These equations can be easily solved to yield

$$N_0 = \frac{\alpha \Sigma}{\eta \sigma I [\exp(\alpha t_1) - 1] [\exp(-\alpha t_2) - \exp(-\alpha t_3)]} \quad (3)$$

where  $N_0$  is the original number of atoms of the species of interest in the sample,  $\Sigma$  is the number of gammas detected,  $\eta$  is the detection efficiency,  $t_1$  is the activation time,  $t_2 - t_1$  is the time between removal of the sample from the reactor and the start of counting and  $t_3 - t_2$  is the counting time. The time between removal from the reactor and the start of counting allows the activity due to the short-lived oxygen and nitrogen isotopes to reduce significantly so the sample could be handled safely. It also helped reduce background count rates.

#### ARGON DETERMINATION

The samples of interest were 300  $\mu\text{m}$  GMBs filled with 0.8 atmosphere of argon (20 nanograms Ar). With such a small sample it was necessary to minimize the amount of material irradiated to reduce the background to a tolerable level. To this end, the GMB under test was mounted as shown in Fig. 1. The tantalum piece was first attached to the nylon fiber with RTV. The tantalum had been weighed beforehand and was used as a standard. After the RTV was cured the GMB could be attached. This provided a secure mounting, but also allowed subsequent removal of the GMB from the stalk for use as a laser target.

Once mounted the sample was placed in a polyethylene bottle and placed in the reactor for irradiation. After irradiation for one half to one hour, the bottle was removed from the reactor and placed in a lead shielded container until the activity reduced to a safe level. The stalk mounted GMB was then removed from the bottle and transferred to another similar bottle. This was necessary because air contains one percent argon, and the signal from the argon thus trapped in the bottle during irradiation would easily swamp the desired signal. The sample was then placed in front

of the detector for gamma counting. The detector was a standard germanium detector with a 1.9 keV FWHM resolution.

A gamma spectrum of an argon filled GMB is shown in Fig. 2. The large variety of peaks is due primarily to Ta. The peak shown as  $\beta^+$  is due to the 0.511 MeV gammas released when a positron annihilates with an electron. Positron-electron pairs are formed when gamma rays of 1.022 MeV or higher are absorbed near a heavy nucleus. There are also impurities in the nylon and RTV that show up in the spectrum. Manganese and indium are two such impurities whose gamma lines are identified in Fig. 2. A small amount of manganese poses no problem in the analysis for argon, but a very small amount of indium complicates matters somewhat.

Activated indium has a gamma line at 1.293 MeV, identical in energy to the argon line of interest. In addition, the cross section for  $\text{In}^{115}$  is 155 barns, about 300 times larger than that for argon. Consequently a very small indium contamination can easily bury the Ar gamma signal.

Fortunately, the indium contamination was small enough that it could be corrected for. The indium line at 1.097 MeV was used basically to determine the amount of indium present. Then the indium contribution to the 1.293 MeV peak could be determined and subtracted, leaving only the contribution due to the argon.

The tantalum piece placed adjacent to the GMB during radiation served to eliminate the need to know the precise neutron flux and the detection efficiency. Since the amount of tantalum was known, along with its half life and cross section, we could use equation (3) to calculate  $I\eta$ , the product of the neutron flux and detection efficiency. Since the tantalum was adjacent to the GMB, it saw the same neutron flux. Since a tantalum gamma line was near in energy to the argon line (1.289 MeV for Ta, 1.293 MeV for Ar), but resolvable, its detection efficiency would also be identical. (See Fig. 3.) In this way, it was not necessary to know either  $I$  or  $\eta$ .

## RESULTS AND CONCLUSION

Two samples were run to check out the technique. Both GMBs were 300  $\mu\text{m}$  diameter and were reported to contain 20 nanograms of argon.

Sample #1 was mounted with a 56  $\mu\text{g}$  Ta standard and was irradiated for one hour. It then rested for 22.75 minutes before counting began, which lasted 33 minutes. The argon mass determined from this data was 19.7 nanograms.

Sample #2 was mounted with a 89  $\mu\text{g}$  Ta standard and was irradiated for 30 minutes. Its rest period was only 13.7 minutes, and counting lasted 33 minutes. The argon mass for this sample was determined to be 16.6 nanograms.

The rather large uncertainty ( $\pm 35\%$ ) was due entirely to the uncertainty in the tantalum cross section. The argon and indium cross sections and all half-lives are known to much higher precision. Count rates were significantly large, so counting statistics also were not a factor in the ultimate precision.

The utility of neutron activation for the determination of argon content in Gmb's has thus been proven. Higher precision could be achieved by using a standard with a better known cross section. The requirements of such a standard would include a well-known cross section and half life, gamma energy in the range of 1.293 MeV but separable from it and negligible impurities that would conflict with the argon gamma signal (e.g., indium).

#### FIGURE CAPTIONS

1. Recoverable mounting system The tantalum piece is attached to the nylon stalk with the RTV. After the RTV is cured, the GMB was placed in the position shown. After irradiation and counting the GMB could be easily removed for remounting as a target.
2. Gamma-ray spectrum of neutron irradiated target with tantalum standard.
3. Expanded gamma-ray spectrum for energies above 1.24 MeV showing the indium peak coincident with the argon peak at 1.293 MeV as well as the tantalum peak at 1.289 MeV used to determine the product of neutron flux and detection efficiency.

300 $\mu$ m GMB (.8 atm Ar  $\Rightarrow$  20 ng)

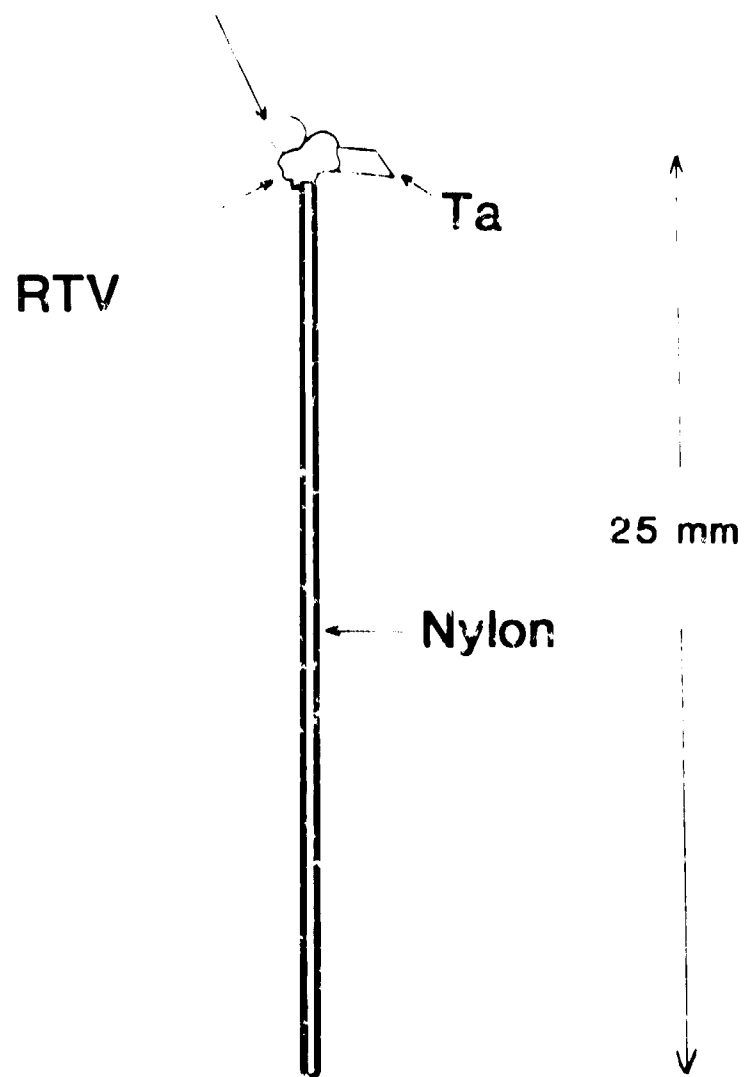


Figure 1

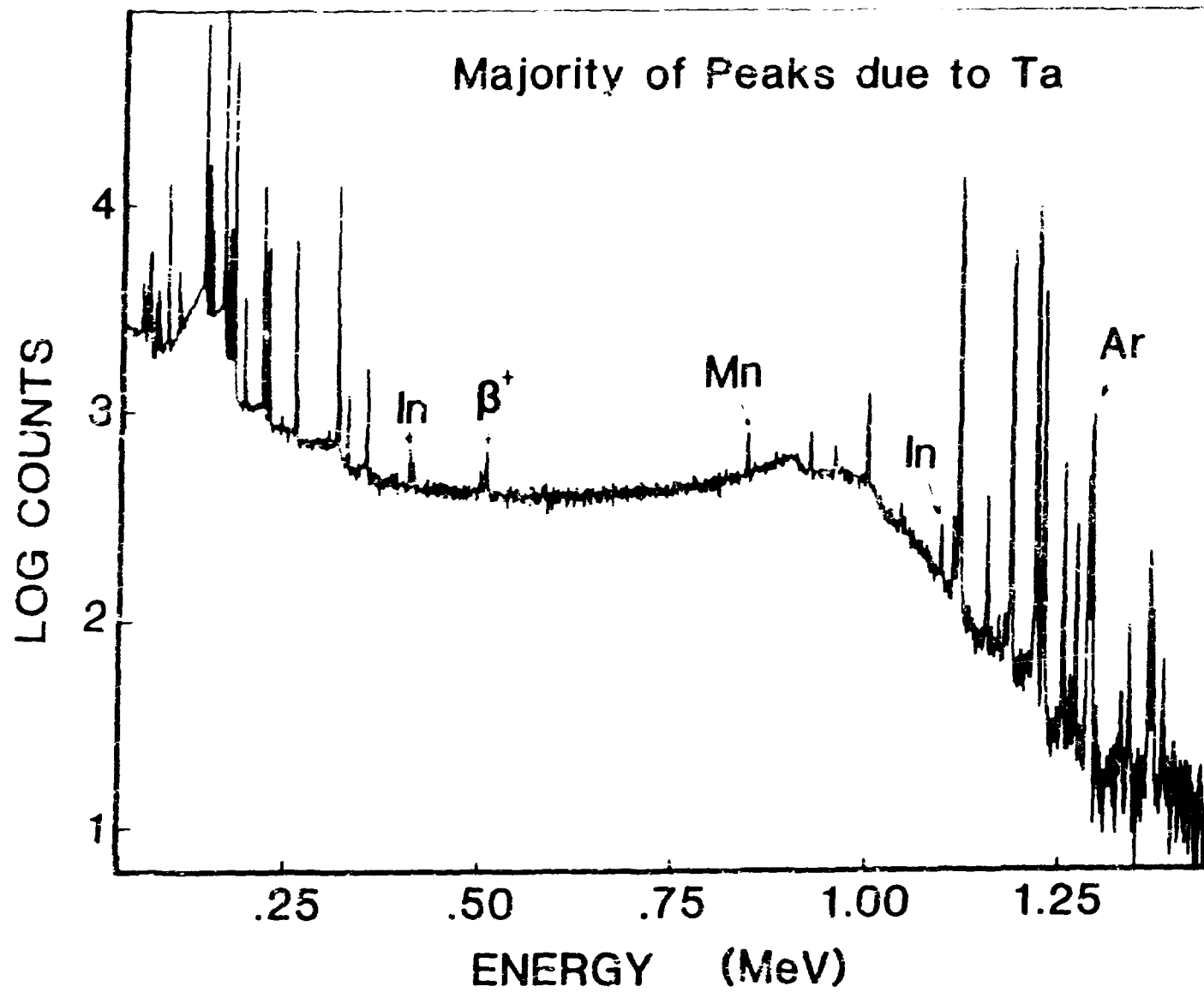


Figure 2



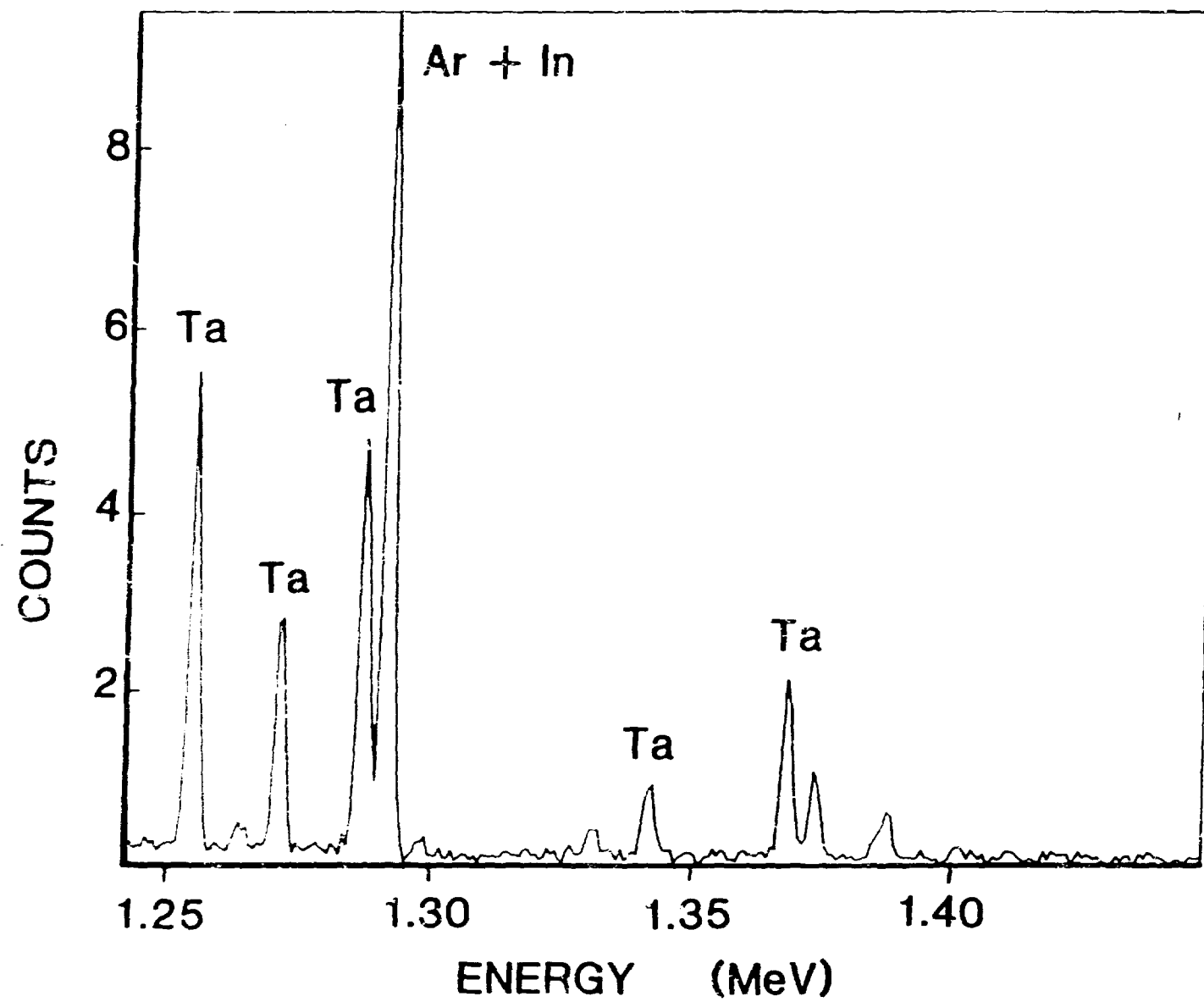


Figure 3

# THE FABRICATION OF "GAUSSIAN BUMPS" ON SMALL SPHERICAL SUBSTRATES

by

S. R. Murrell, G. B. DeMaggio, H. K. Lintz,  
J. A. Ruppe, A. R. Soltis, and J. C. Daukas  
KMS Fusion, Inc.  
3621 South State Rd.  
Ann Arbor, Michigan 48103

## INTRODUCTION

The objective of the reported work was to fabricate hollow microsphere targets containing well known wall non-uniformities and surface defects. These targets will be used to study the influence of known perturbations on implosion dynamics. The geometric characteristics were chosen such that the perturbation cross section is described by a Gaussian curve with a well defined height and full width half maximum (FWHM). Perturbations were to consist of both low-Z polymer (polystyrene) and Mid-Z material (aluminum). The application of the polystyrene bumps was accomplished by melting polystyrene beads onto the GDP coated surface of polymer targets. This report, however, limits the discussion to the preliminary studies for fabricating aluminum "Gaussian bumps" on glass microshell targets by means of evaporation through a pinhole aperture. Also discussed is a model developed in parallel which helped us to better understand the bump formation process and to optimize the deposition parameters.

## DESCRIPTION OF MODEL

It is assumed that deposition through a mask occurs only at those points on the substrate which are exposed by line of sight to the evaporant source. The rate of deposition for any exposed point is proportional to the area of the source "visible" through the aperture from that point. One can imagine a cone with its apex at a given point on the substrate, and with its angular extent confined by the pinhole. This cone is called the line of sight cone and subtends a solid angle determined by the diameter of the pinhole aperture and by the spacer distance (see Fig. 1). This line of sight cone projects a "disk" called the projection disk onto the plane of the source. The diameter of the projected disk is a function of the solid angle of the cone and the

distance between the source and the substrate. The source itself is represented mathematically by a disk which is located on the source plane.

The deposition rate at any given point on the substrate is dependent on the total area of overlap of the source disk and the projected disk. The point on the substrate which corresponds to the maximum overlapped area receives the highest deposition rate. The source disk and the projected disk corresponding to the center point on the substrate, for example, are concentric. Therefore, the overlap area is at its maximum value always at the center. This is the location of the maximum height of the bump. Further away from the center of the substrate, the center of the projected disk is a small distance away from the center of the source disk. The overlap area, then, decreases to only a certain percentage of the maximum. At points on the substrate beyond a certain distance the projected disk and the source disk will no longer overlap. This corresponds to a deposition rate of zero on the substrate at these points.

A histogram is calculated which gives values of the percentage of maximum overlap area as a function of distance from the center line through the substrate. An absolute value is then given for the maximum height of the modeled bump. Finally, the height of the bump at each point away from the center is simply the corresponding percentage of this maximum. The histogram, then, represents a true cross sectional view of the resulting "Gaussian Bump". The histogram is plotted in graph form and a direct comparison is made between the plot and an SEM micrograph of the actual fabricated bump.

#### EXPERIMENTAL

The pinhole mask is shown in Fig. 2. The aluminum vapor passes through the pinhole apertures which range in diameter from 20 to 40  $\mu\text{m}$ . The vapor transverses a distance dependent on the spacer distance. Finally, the aluminum deposits on the shell which is being held in place by a counter sunk hole in a small brass disk. The shell is forced against this disc by thin plastic wrap so that it will not change position as the deposition run proceeds.

The pinhole aperture assembly is then positioned directly above the aluminum evaporant source (see Fig. 3). The aluminum is evaporated by means of an electron beam gun. The electron gun is used because of its relatively low radiant temperature and high evaporation rate.

The first few bumps fabricated through a 25  $\mu\text{m}$  aperture proved to be a surprise. These bumps resembled cones rather than Gaussian curves. Upon inspection of the pinhole aperture it was discovered that the 25  $\mu\text{m}$  aperture closed completely during the run. The model was then altered to account for the closing aperture which was assumed to close linearly with time. After incorporating the closing aperture into the model, the bump and model were in close agreement as shown in Fig. 4.

In the model, a pinhole diameter of 35  $\mu\text{m}$  with a spacer distance of 203  $\mu\text{m}$  resulted in a bump with a full width half maximum of 34  $\mu\text{m}$ . The corresponding fabricated bump shown in Fig. 5 has a FWHM of 29  $\mu\text{m}$ . The value entered for the bump height in the model was 9.8  $\mu\text{m}$  just as is the height of the fabricated bump. Although the model describes the overall dimensions of the bump, it does not describe the shape of the bump exactly. These differences may be due to several factors that have not yet been incorporated into the model.

These factors may include: the flux of evaporant; the temperature of the aperture mask; possible variations in the directionality of the evaporant impinging on the aperture; imperfections in the shape of the aperture; uncertainties in experimental measurements such as: aperture diameter, spacer distance, fluctuating source diameter, source to substrate distance, and overall configuration alignment. These factors may have an effect not only on bump shape but on the morphology of the bump as well as the morphology of the film which is responsible for clogging the aperture (they are different). The above mentioned factors will be incorporated into the model in future work. The resulting effects will be weighted against each other and compared with corresponding fabricated bumps.

#### CONCLUSION

We have produced localized perturbations on small spherical substrates which, in cross section, resemble Gaussian curves. The overall dimensions of these "Gaussian Bumps" are closely predicted by a model which has been developed in parallel.

Further studies of the film growth process are required to account for the differences between the model and the fabricated bumps. Forced changes in the model to gain better agreement with experiments may translate to ac-

quired knowledge about the processes involved in the evaporation of aluminum through a pinhole mask. Perhaps the work may be generalized to study the deposition characteristics of various evaporants passed through masks of any shape and size.

#### FIGURE CAPTIONS

- Figure 1. Schematic diagram of substrate, pinhole aperture, and source disk. The line-of-sight cone projects a disk onto the source plane.  
Note: The center line extends from the center of the microshell substrate to the center of the source disk.
- Figure 2. Schematic diagram of pinhole aperture assembly. The spacer distance and the aperture size can be easily changed.
- Figure 3. Photograph of experimental arrangement. The aperture assembly is positioned over the source with an x-y micro-positioning stage. The viewing mirror helps the operator see the source.
- Figure 4. SEM micrograph of a bump fabricated using a 25  $\mu\text{m}$  aperture and a 53  $\mu\text{m}$  spacer. The aperture closed completely during the deposition run. The calculated bump is also shown for comparison between the model and the fabricated bump.
- Figure 5. SEM micrograph of a bump fabricated using a 35  $\mu\text{m}$  aperture and a 203  $\mu\text{m}$  spacer. The aperture closed to 30  $\mu\text{m}$  diameter during the run. The calculated bump is shown for comparison.

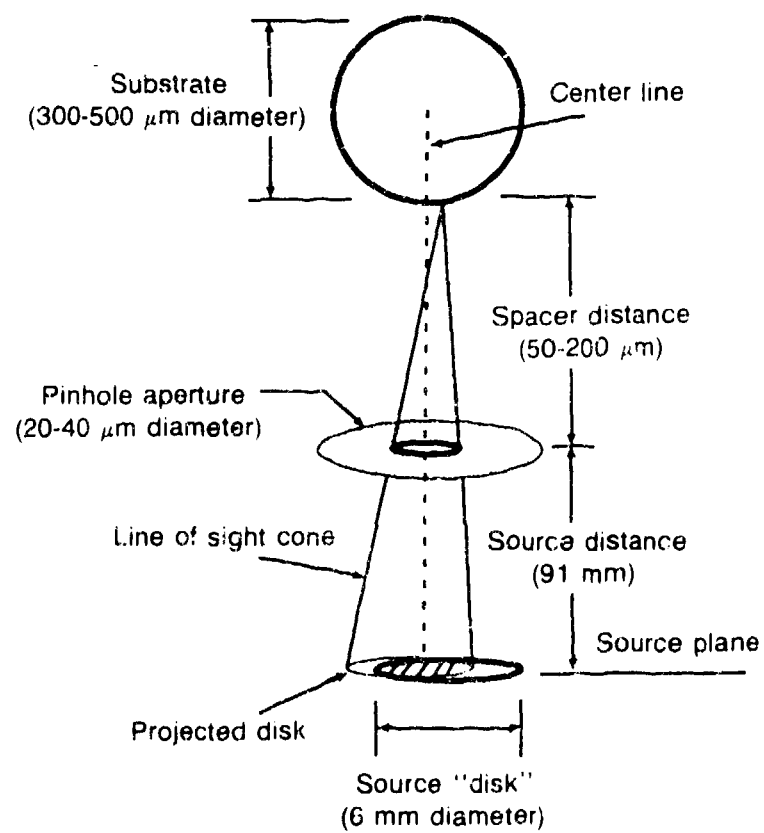


Figure 1. Schematic diagram of substrate pinhole aperture, and source disk. The line-of-sight cone projects a disk onto the source plane.

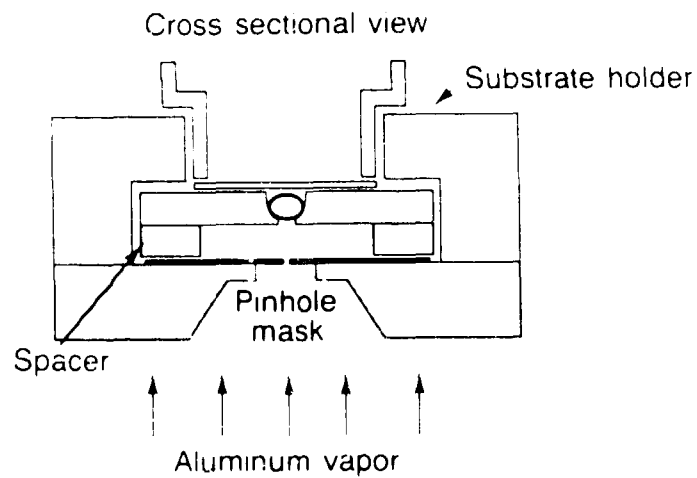


Figure 2. Schematic diagram of pinhole aperture assembly the spacer distance and the aperture size can be easily changed.

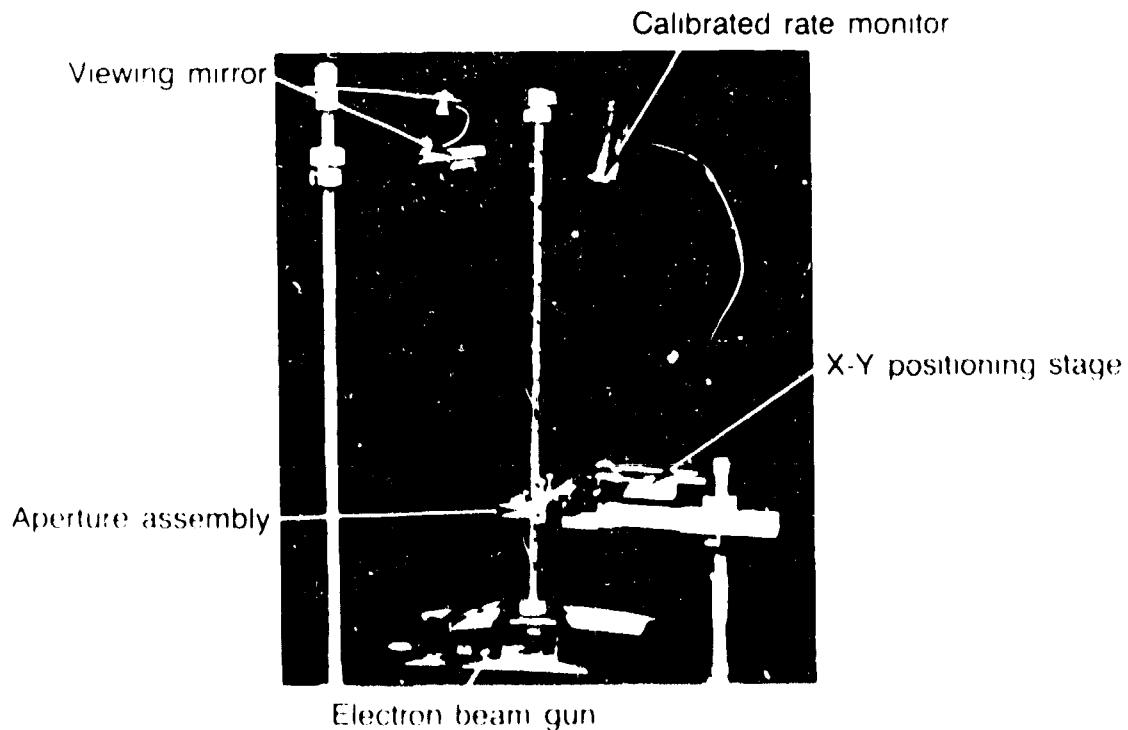


Figure 3 Photograph of experimental arrangement The aperture assembly is positioned over the source with an x-y micropositioning stage The viewing mirror helps the operator see the source



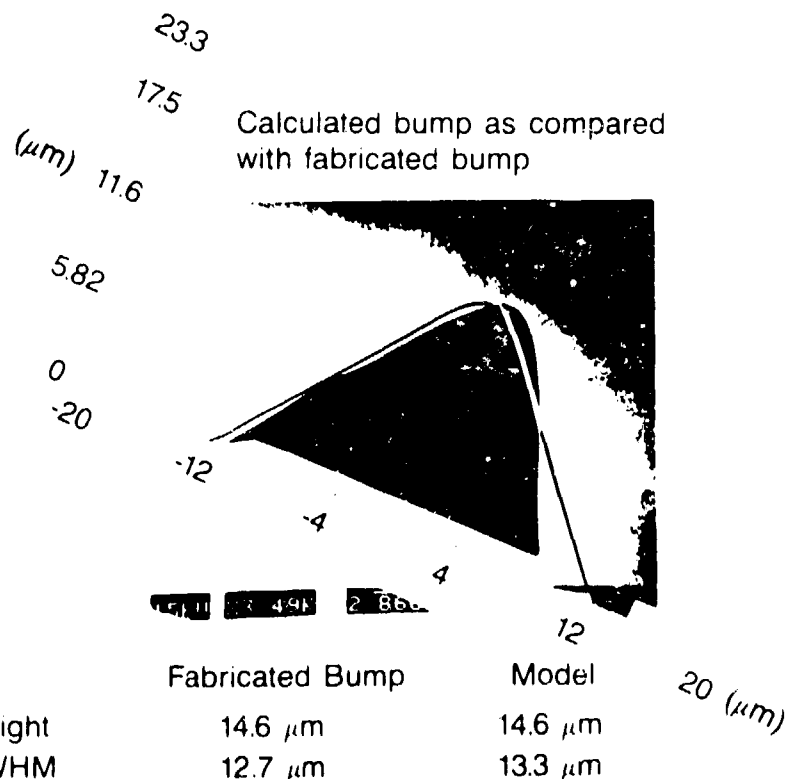


Figure 4. SEM micrograph of a bump fabricated using a 25  $\mu\text{m}$  aperture and a 53  $\mu\text{m}$  spacer. The aperture closed completely during the deposition run. The calculated bump is also shown for comparison between the model and the fabricated bump.

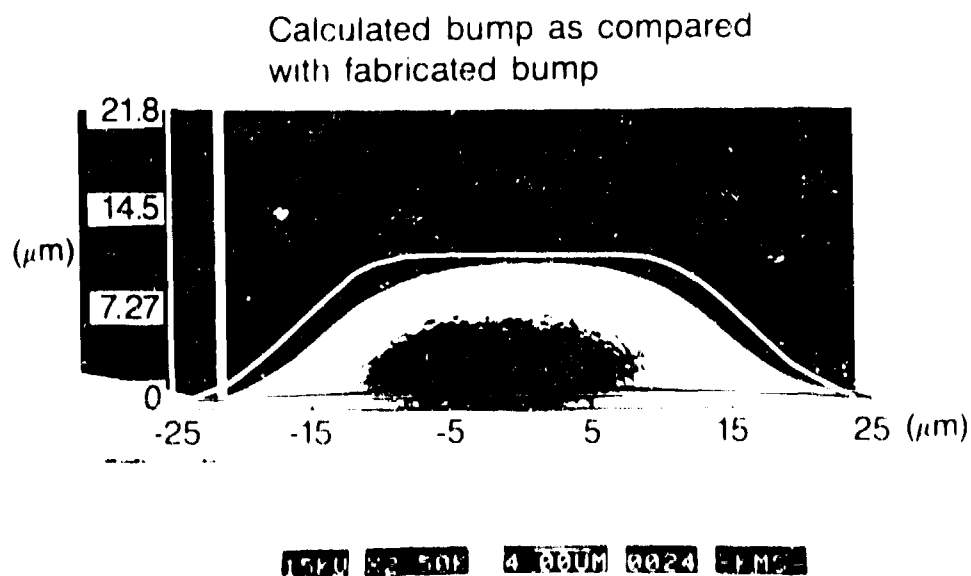


Figure 5. SEM micrograph of a bump fabricated using a 35  $\mu\text{m}$  aperture and a 203  $\mu\text{m}$  spacer. The aperture closed to 30  $\mu\text{m}$  diameter during the run. The calculated bump is shown for comparison.

## AN INTEGRATED MODEL FOR SPUTTER COATING UNIFORMITY\*

R. S. Upadhye, M. K. Kong, and E. J. Hsieh

University of California  
Lawrence Livermore National Laboratory  
P. O. Box 5508, Livermore, CA 94550

### INTRODUCTION

The coating flux received by substrates in a sputter coating process consists of two components: the diffusive flux, contributed by fully thermalized atoms, and the directed flux, contributed by atoms which have retained a major part of their original velocity. Following our earlier computer modeling work,<sup>1</sup> we have developed an integrated model of the process which assigns weights to the two mechanisms; the weighting factors are then related to the process and equipment parameters. Our modeling results will be compared to experimental data and available theoretical calculations from the literature.

### EXPERIMENTAL

A schematic of the experimental set-up is shown in Figure 1. The sputtering chamber has a maximum sputtering distance of 12". A Cu Sloan 3"-ring is used as the sputtering target. The gun is mounted off-center with the closest wall distance equal to 6". We used 1/8" glass rods as substrates. All depositions were made at 20 mtorr and room temperature. In our experiments, we varied the substrate to target distance ( $\ell$ ) while holding the ground plane to target distance ( $L$ ) at 12". After each experiment, we monitored film thicknesses at the glass rod.

### RESULTS

As expected, the flux rate ratio between locations 6 and 4 decreases as the substrate is moved down toward the ground plane. Both flux rates

\* Work performed under the auspices of the U. S. Department of Energy by the Lawrence Livermore National Laboratory under contract number W 7405 ENG 48.

drop as  $\ell/L$  is increased from the base value of 0.5. However, the ground plane has a stronger shadowing effect on location 6 than 4 because the latter depends exclusively on diffusional coating flux. Thus the flux rate ratio decreases also. As the substrate is moved closer to the source, thus decreasing the value of  $\ell/L$  below 0.5, the flux ratio decreases rapidly. The flux rate ratios are plotted in Figs. 2 and 3.

## DISCUSSION

The initial flux leaving the target is directional, where the sputtered atoms follow a straight line trajectory. In this state, their movements can be described by simple, line-of-sight models<sup>2</sup>. As the sputtered atoms undergo collisions with the sputtering gas (typically Ar) atoms, they become increasingly thermalized (i.e., acquire random velocity orientation). After a sufficient number of collisions, the target atoms are completely thermalized, and their net movement can be described by diffusion equations. The transition from the directed to the diffusional flux is gradual.

The proposed model takes into account the gradual shift from one mechanism to the other in a continuous manner. Using similar assumptions of our earlier work<sup>1</sup> we can write the following set of equations to define the diffusional transport part of our model:

$$\frac{d^2 C}{dz^2} + \left(\frac{1}{r}\right) \cdot \frac{d}{dr} \left(r \frac{dC}{dr}\right) = 0 \quad (1)$$

with the boundary conditions of a specified diffusional flux,  $f(r)$ , at the chamber entrance, and zero concentrations at all exposed surfaces. We solved these equations using the Topaz 2-D finite element program (which is a heat conduction code) using the analogy between heat conduction and diffusive mass transfer.<sup>3</sup> We have shown earlier that the coating uniformity on a small substrate is insensitive to the initial flux distribution.<sup>1</sup> For the purpose of this investigation, we imposed a uniform flux at the chamber entrance.

The calculations of the directed flux distribution are straightforward: the top of the substrate facing the target receives the full directed flux

(corrected for surface orientation), whereas the bottom part, being in the shadow, gets no flux.

Let  $\phi_z$  be the fraction of thermalized atoms at any position  $z$ . Let  $\lambda$  be the mean free path of the atoms at the chamber pressure and temperature, and  $n$  the expected number of collisions undergone by the metal atoms at the position  $z$ . Then, following the treatment given by Ecker et. al.,<sup>4</sup> and Townes,<sup>5</sup> we can write:

$$\phi_z = 1 - e^{-k \cdot n} = 1 - e^{-k (z/\lambda)} \quad (2)$$

Let  $f_0$  be the initial directed flux,  $f_d$  and  $f_t$  be the directed and thermalized flux contributions at position  $z$ , and  $f_n$  be the net flux at position  $z$ . Then, since the metal atom concentration is much smaller than that of the inert gas, we can write

$$f_n = (1 - \phi_z) \cdot f_d + \phi_z \cdot f_t \quad (3)$$

Equations 1, 2 and 3 completely define the model. The mean free path can be estimated using the kinetic theory of gases; for our specific case, we have calculated it to be .079 inch. We have estimated the decay constant  $k$ , defined in equation 2, from our data to be 0.006. We adjusted the value of  $k$  until we got a satisfactory fit between the data and the model calculations.

Figures 2 and 3 summarize the thermal and integrated model calculations and the data. The ratio of the minimum to maximum flux rates (namely, at locations 6 and 4 respectively) on the substrate surface is plotted on the y-axis. The experimental data points are shown as stars connected by a solid line, following the legend shown in the figures.

The integrated model predicts correct trends over its entire range. Also, the model predicts correct uniformity values for  $x/z$  between .125 and .75. As the flux decreases away from the target, and as the influence of the ground plane increases, the errors in the data as well as the diffusional model increase. This may explain the disagreement between the model and the data for  $x/z$  greater than 0.75.

## CONCLUSIONS

We have developed a simple, integrated, one parameter model to describe the flux uniformity in a sputter coating process. This model is valid for both the line-of-sight and diffusional mechanisms. It accounts for the gradual transition from the directed to the diffusional flux control, and is valid over the entire range.

## ACKNOWLEDGEMENTS

We thank E. L. Pierce for obtaining the experimental data.

## REFERENCES

1. Upadhye, R.S., M. K. Kong, and E. J. Hsieh, "Analysis of Sputter Coating Uniformity by Computer Modeling", Journal of Vacuum Science and Technology, Book 3,A,May-June 1988.
2. Holland, L., "Vacuum Deposition of Thin Films", Chapman and Hall Ltd., London, (1970).
3. Shapiro, Arthur B., "Topaz - A finite element heat conduction code for analyzing 2-D solids", Lawrence Livermore National Laboratory, UCID - 20045.
4. Ecker, G. and K. G. Emelius, "Cathode Sputtering in Glow Discharge", The Proceedings of the Physical Society, Section B, Volume 67, 546-552, 1954.
5. Townes, C. H., "Theory of Cathode Sputtering in Low Voltage Gaseous Discharge", Physical Review, Volume 65, 319-327, 1944.

2557M

# Idealized system schematic

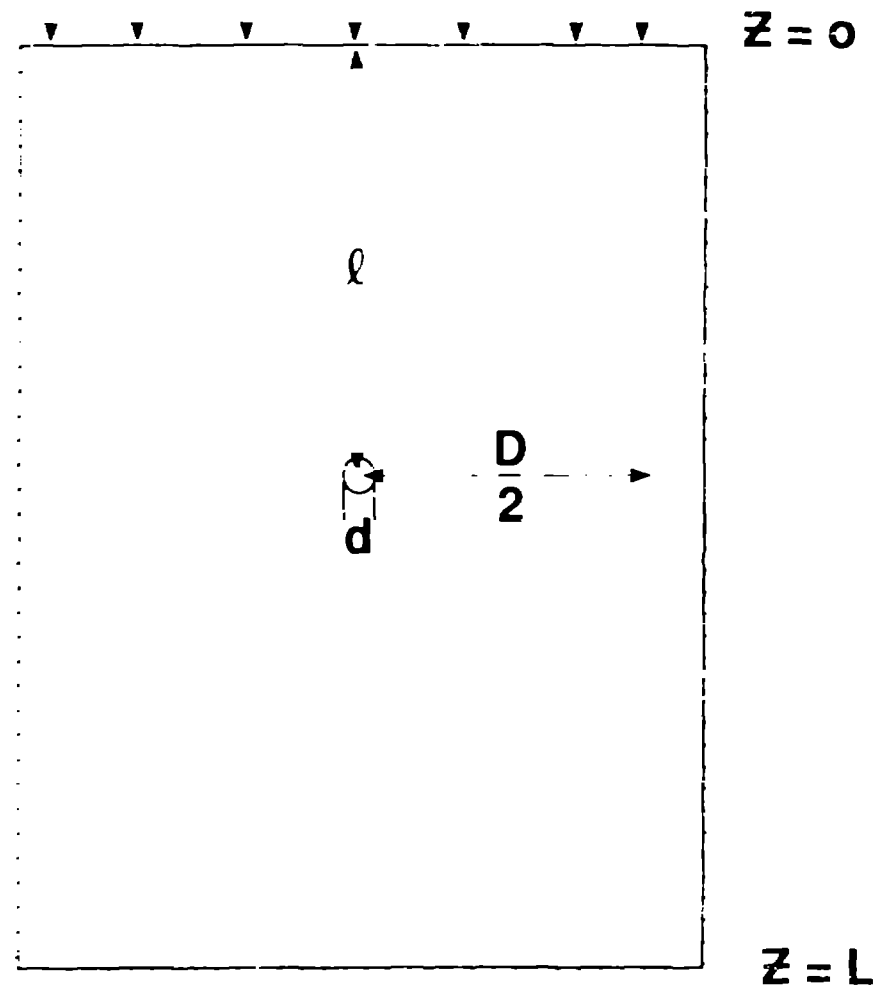


Figure 1

# Thermal model and data comparison

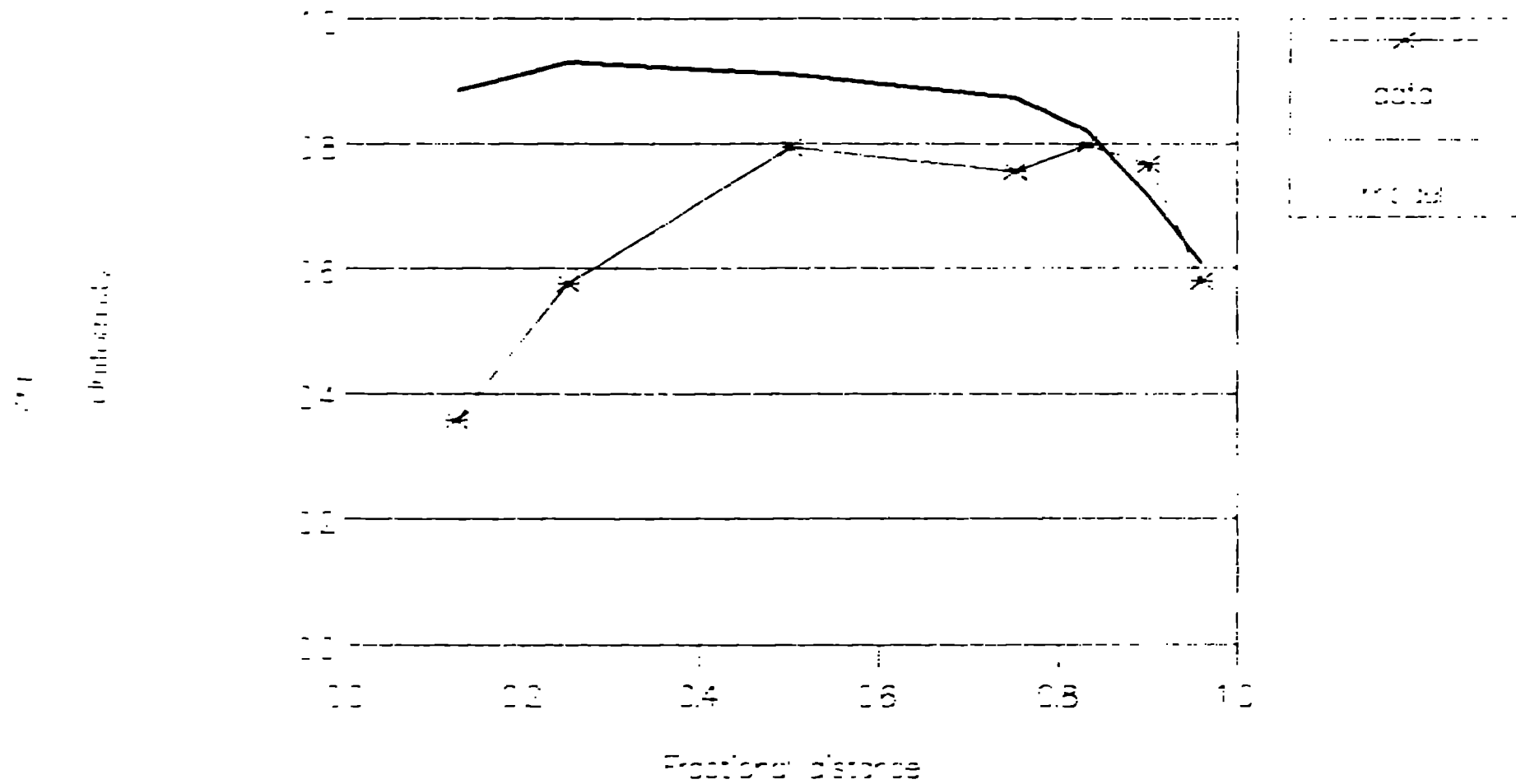


Figure 2

# Integrated model and data comparison

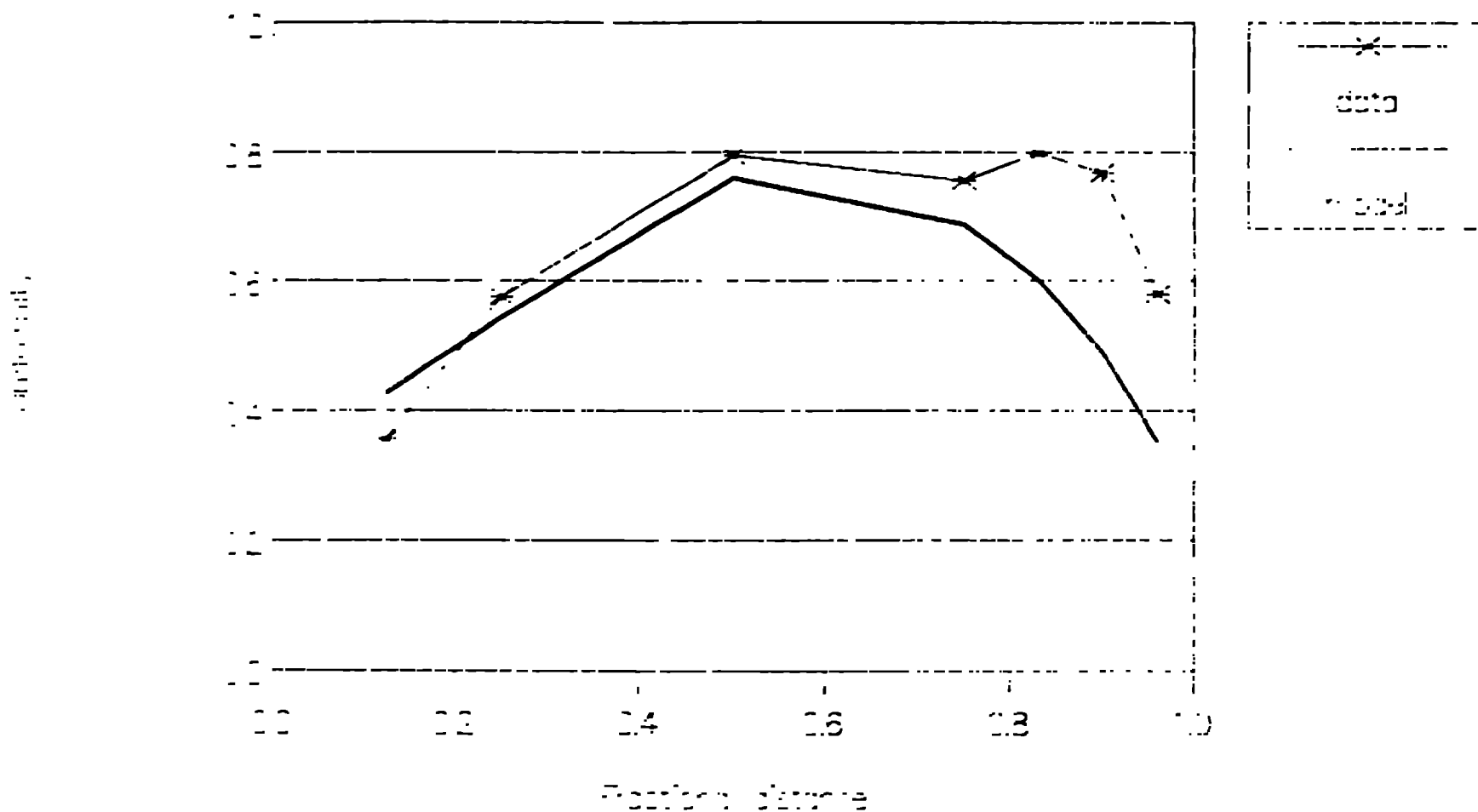


Figure 3



## THE REACTIVITY OF THE RESIDUAL BLOWING GASES IN GLASS SHELLS

by

Matthias A. Ebner, Wayne J. Miller, and Levi T. Thompson  
KMS Fusion, Inc.  
3621 South State Road  
Ann Arbor, Michigan

### INTRODUCTION

A major concern in Inertial Confinement Fusion (ICF) implosion experiments is the mixing of the fuel with electron-rich, high-Z species that may degrade the efficiency of the DD or DT fusion reaction. The shell material, normally glass, has been the focus of much of this concern. The residual blowing gases within the shell, which are intimately mixed with the fuel, have usually been ignored because of their negligible concentrations in high-pressure targets. Removing or reducing the levels of residual blowing gases becomes especially important in targets with a low pressure of fuel because they significantly dilute the fuel. We contend that it is feasible to reduce the amount of residual blowing gases in glass shells.

Glass shells made from xerogels usually contain residual blowing gases that include CO<sub>2</sub>, N<sub>2</sub>, O<sub>2</sub>, and H<sub>2</sub>O. The residual blowing gases are present at pressures up to 0.25 atm (at room temperature) and consist of 60-90% CO<sub>2</sub>.<sup>1</sup> Not only do residual blowing gases dilute the fuel, but CO<sub>2</sub> and H<sub>2</sub>O can corrode the interior surface of the glass shells by forming basic carbonates and eventually silicates. Corrosion features weaken the shell wall, i.e., lower the tensile strength, and may cause Rayleigh-Taylor instabilities during the implosion. This problem increases with shell size, because the mass of reactive residual gas increases geometrically with shell diameter and because high levels of water vapor must be used in making such shells.

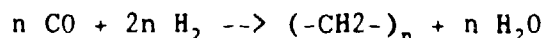
Carbon dioxide can be converted to CO and possibly to hydrocarbons, which have a lower average Z and are inert to glass. In principle, this conversion can be accomplished by the hydrogenation of CO<sub>2</sub>. Several of the important reactions are:

the reverse gas shift reaction,



the methanation reaction,

$\text{CO} + 3\text{H}_2 \rightarrow \text{CH}_4 + \text{H}_2\text{O} \quad \Delta G_{633} = -15.264 \text{ Kcal/mole}$   
and possibly the Fischer-Tropsch synthesis reaction,



Thus the net reaction is



While the methanation reaction is thermodynamically favored, the reverse shift reaction is not, as indicated by the estimated Gibb's free energies at 360°C (the usual permeation temperature for filling targets). Nevertheless, the enormous excess of hydrogen (usually 2 to 100 atm for ICF targets) is expected to favor the hydrogenation of  $\text{CO}_2$  to methane.

Despite the favorable thermodynamics, gas phase methanation has a significant kinetic barrier. Commercial practice requires the use of a catalyst to achieve acceptable methanation rates.<sup>2,3,4</sup> For example, a stoichiometric mixture of reactants at 1 atm will reach 90% of reaction equilibrium in 8 hours when catalyzed by nickel.<sup>3</sup> Without a catalyst, this reaction will not proceed to any measurable extent in the 72-120 hours that is usually required to fill a glass target, despite the large excess of hydrogen. Ionizing radiation can also activate reactions such as methanation by producing excited, more reactive intermediates from the reactants. We have studied the reactivity of the residual blowing gases in the presence of  $\text{D}_2$ , DT, and  $\text{T}_2$  (DT and  $\text{T}_2$  produce  $\beta$  particles). This note summarizes our preliminary results.

#### EXPERIMENTAL PROCEDURE

About 2 ml. of alkali silicate glass shells were filled with 20 atm of  $\text{D}_2$ , DT, or  $\text{T}_2$  at 360°C. The initial hydrogen isotope/ $\text{CO}_2$  mole ratio was greater than 65, and the permeation fill lasted 3 days. Subsequently, the shells were evacuated of hydrogen by permeation at the same temperature over a period of at least 2 days. Thus the minimum contact time at 360°C was 3 days. The residual gases in the shells were analyzed before and after the fill by mass spectrometry. The residual gases in as-made shells consisted of >95%  $\text{CO}_2$ , with the balance being  $\text{N}_2$ . Oxygen was presumed to be present in quantities similar to  $\text{N}_2$ , but could not be quantitatively determined by our mass spectrometer.

## DISCUSSION OF RESULTS

The results of the experiments are summarized in Table 1. Reaction with a large excess of  $D_2$  reduced more than 95% of the  $CO_2$  to CO; no methane or higher hydrocarbons were detected. Reaction with a similar quantity of DT yielded a similar extent of conversion of  $CO_2$ . In this case, however, the product mixture consisted of about 60% CO, 40% isotopically mixed methanes, and trace quantities of ethylene and ethane. Reaction with the same concentration of tritium, which produces twice the  $\beta$  flux as DT, yielded about 90% conversion of  $CO_2$ . In this case, the product distribution consisted of 40% CO, 53% methane, and 7% ethylene and ethane. No effort was made to analyze for polymer formation. Water, a major product of these reactions, was not detected in the final product mixtures in any of the reactions. The reaction temperatures and contact times were sufficient to permit all of the water to permeate out of the glass shells.

The nearly complete hydrogenation of  $CO_2$  to CO by  $D_2$  indicates that the reverse shift reaction is fast relative to the times required for permeation of  $D_2$  into the glass shells. The absence of any methane in the reaction product indicates that the methanation rate is slow in the absence of a catalyst or radiolysis, despite the large excess of hydrogen.

Carbon dioxide hydrogenation by DT and  $T_2$  was nearly complete, but produced mixtures of CO and hydrocarbons. Furthermore, when the  $\beta$  flux was doubled (by using  $T_2$  instead of DT) at constant hydrogen pressure, the hydrocarbon selectivity increased by almost 70%. The hydrocarbon selectivity can be defined as the moles of  $CO_2$  consumed in producing hydrocarbons. Doubling the  $\beta$  flux also increased the yield of ethane and ethylene, which are Fischer-Tropsch synthesis products, from <1% to 7%. The fast rate of the reverse shift reaction observed for  $D_2$  and the effect of  $\beta$  radiation on the methanation and Fischer-Tropsch synthesis reactions suggest that  $CO_2$  hydrogenation proceeds through a fast reverse shift step, followed by a rate limiting methanation step. Furthermore, the Fischer-Tropsch synthesis reaction appears to be favored by  $\beta$  radiation.

Beattie<sup>5,6</sup> and Douglas<sup>7</sup> also studied the effect of  $\beta$  radiation on carbon oxide hydrogenation. The kinetics were determined for reactant pressures less than 1 atm, and for  $T_2/CO_2$  ratios ranging from 15 to 100. For  $CO_2$  hy-

drogenation, Beattie reported that reaction equilibrium was reached in 2 to 4 weeks. Water and  $\text{CH}_4$  were the principal products with minor amounts of  $\text{CO}$  (2%),  $\text{C}_2\text{H}_4$  (3%), and a polymeric material that was probably a hydrocarbon.<sup>5</sup> The products of  $\text{CO}$  hydrogenation were  $\text{H}_2\text{O}$ ,  $\text{CH}_4$ ,  $\text{CO}_2$  and a polymer that was probably paraformaldehyde.<sup>6</sup> Studies by Douglas also identified  $\text{H}_2\text{O}$  and  $\text{CO}_2$ , along with acetaldehyde, glycol, glyoxal and paraformaldehyde as  $\text{CO}$  hydrogenation products.<sup>7</sup>

### CONCLUSIONS

The results of this work indicate that the residual  $\text{CO}_2$  in glass ICF targets can be hydrogenated to lower-Z species during the permeation filling of the glass shells. Deuterium reduces  $\text{CO}_2$  to  $\text{CO}$ , while  $\text{DT}$  or  $\text{T}_2$  reduce  $\text{CO}_2$  to a mixture of  $\text{CO}$  and hydrocarbons. Water, a major byproduct of these reactions, is lost by out permeation. Evidently,  $\beta$  radiation facilitates the complete hydrogenation of  $\text{CO}_2$ . Future work will determine the catalytic activity of the conventional ICF glass shell surfaces, and shell surfaces of glasses that have been doped with transition metals. In addition, we plan to determine the kinetics of these reactions and the effects of  $\beta$  (from both tritium and external sources), gamma, and possibly RF radiation on the reaction rates and product distributions.

Table 1. Residual  $\text{CO}_2$  in glass shells are completely reduced by  $\text{D}_2$  to  $\text{CO}$ ;  $\beta$  radiation facilitates the further reduction to hydrocarbons.

Extent of Reaction Fill Gas	Product Distribution of $\text{CO}_2$	$\text{CO}$	$\text{CH}_4$	$\text{C}_2\text{H}_4$
$\text{D}_2$	>95%	100%	0	0
$\text{DT}$	>95%	60%	40%	<1%
$\text{T}_2$	>90%	40%	53%	7%

NOTE: No  $\text{D}_2\text{O}$ ,  $\text{DTO}$ , or  $\text{T}_2\text{O}$  was found in above analysis. At the reaction temperatures of  $360^\circ\text{C}$ ,  $\text{H}_2\text{O}$  is expected to be lost by permeation through the glass.

## REFERENCES

1. R. L. Downs, M. A. Ebner, B. D. Homyk, and R. L. Nolen, J. Vac. Sci. Technol., **18** (3), 1272-1275 (1981).
2. D. S. Newsome, Catal. Rev.-Sci. Eng., **21** (2), 275-318 (1980).
3. R. F. Probststein and R. E. Hicks, Synthetic Fuels, McGraw-Hill, Inc., 1982.
4. H. H. Storch, N. Golumbic, R. B. Anderson, The Fischer-Tropsch and Related Syntheses, John Wiley & Sons, Inc., New York, 1952.
5. W. H. Beattie, 'The Radiolysis of Mixtures of Carbon Dioxide and Hydrogen', LA-4657, UC-4 Chemistry, TID-4500, Los Alamos Scientific Laboratory of the University of California, Los Alamos, New Mexico, June 1971.
6. W. H. Beattie, 'The Radiolysis of Mixtures of Carbon Monoxide and Hydrogen', LA-4658, UC-4 Chemistry, Los Alamos Scientific Laboratory of the University of California, Los Alamos, New Mexico, June 1971.
7. D. L. Douglas, J. Chem. Phys., **23**, 1558 (1955).

## MEASUREMENT OF GLASS SHELL BUCKLING STRENGTH USING A PIEZOELECTRIC FILM SENSOR

by

Roger G. Schneggenburger, Loretta A. Loughrey  
David A. Butkiewicz, and Kathlyn A. Bandy

The importance of glass shell strength becomes clear when one attempts to fill 100 carefully characterized, thin wall glass shells with a high pressure of fuel gas. Unless care is exercised in controlling the driving pressure, many of the shells will break, wasting the time and effort of characterization and losing valuable shells.

KMS Fusion has pursued shell strength studies for over ten years. We have learned that when glass shells fail from excess stress (both compressive and tensile), they emit a pressure pulse. Filled shells, for example, when removed from the pressurization chamber, can be heard popping from across a room, if filled to a pressure beyond the strength of the glass walls to contain it. This pressure pulse provides a signal for detecting failure during testing.

Recently Pennwalt Corporation has advertised a new piezo- and pyro-electric material it calls KYNAR<sup>®</sup>, a thin film made of polyvinylidene fluoride. This material has unusually high piezoelectric response, and seemed a good candidate sensor to detect the buckling collapse of glass shells.

### EXPERIMENTAL

A pressure chamber was constructed by welding high pressure flanges, with pressure feed-thrus to each end of a 9 cm x 2.5 cm (OD) piece of stainless steel tubing (see Fig. 1). Appropriate valves, tubing, and a pressure gauge were connected to one flange to bring nitrogen gas to the test chamber and to accurately read the pressure, up to 100 atm.

A small piece of KYNAR<sup>®</sup> film, 1 cm x 2 cm, was attached to the electric feed-thru in the other flange, to which were also attached leads to a digital storage oscilloscope. The steel pressure chamber was carefully grounded during experiments to prevent noise in the oscilloscope trace.

To run a strength test, one flange of the pressure chamber was removed and a metal slide, holding a glass shell for testing, was inserted into the chamber. The shell had been carefully characterized for OD and wall thick-

ness, and was held in place on a small piece of double sticky cellophane tape. The flange was replaced, and pressure in the chamber slowly increased until a sharp vertical line appeared in the oscilloscope trace, indicating the shell had collapsed. The system pressure was recorded, pressure vented, and the cycle repeated with another shell.

All tests were run at room temperature. Placement of the shells in the chamber was varied; the largest signal was produced when the shell was a short distance from the film. At least 50 shells were measured in this manner for each batch tested.

### RESULTS

For each shell collapse pressure was plotted against  $\left(\frac{w}{OD}\right)^2$  in accordance with the equation for buckling strength,

$$P = \frac{8E}{\sqrt{3(1-\nu^2)}} \cdot \left(\frac{w}{OD}\right)^2$$

where

P = pressure at which the shell collapses

E = Young's modulus

$\nu$  = Poisson's ratio (0.21 for glass)

w = shell wall thickness, in  $\mu\text{m}$

OD = shell outside diameter, in  $\mu\text{m}$

The slope of the best straight line through the data yielded a value of Young's modulus for the batch of shells tested, as shown in Fig. 2.

This data is much less scattered than previous data we have collected on buckling strength tests, due to the more precise measurement of breaking pressure. The KYNAR<sup>®</sup> sensor provides a strong signal, it is a strong, flexible material, easy to use, and is inexpensive. One disadvantage, however, is its low melting point ( $\sim 180^\circ\text{C}$ ), which prevents its use in strength tests at elevated temperatures.

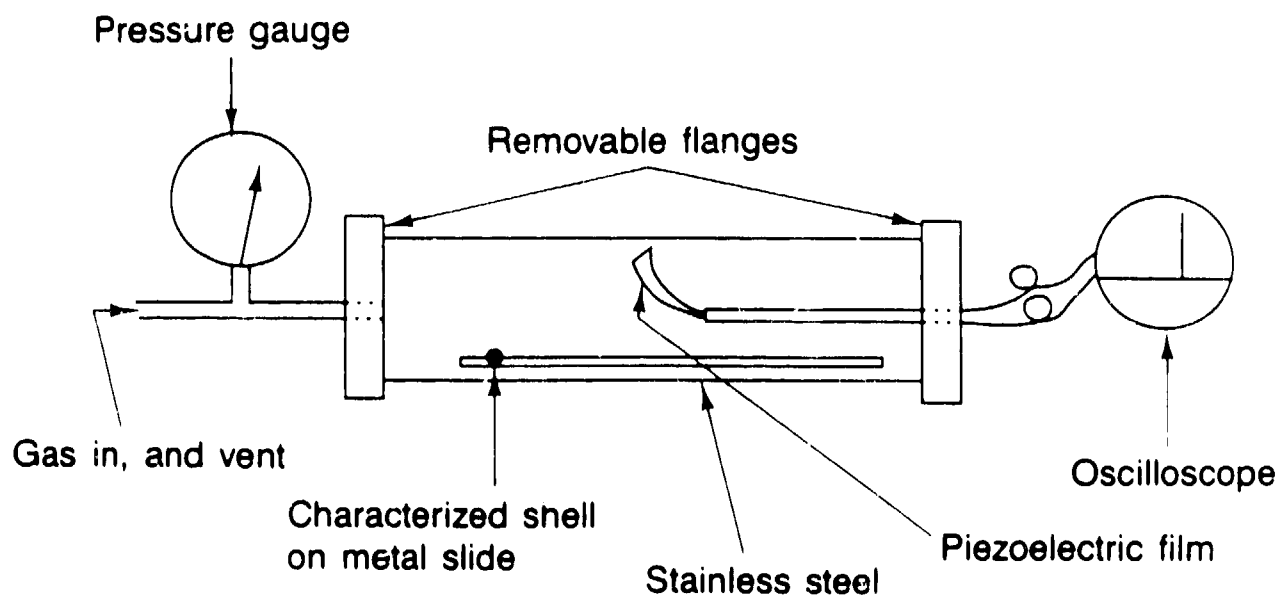


Figure 1. Experimental apparatus.

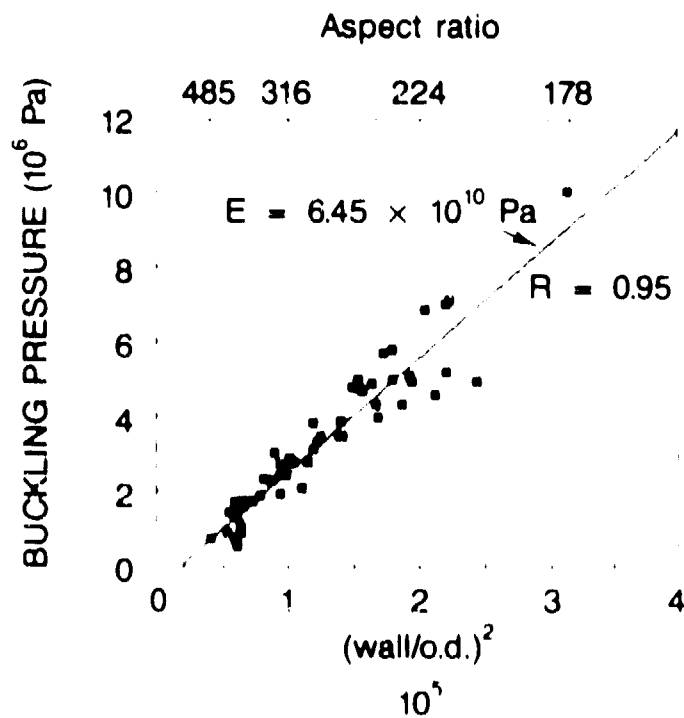


Figure 2. Buckling data from T4R492 (empty shells).



## CRYOGENIC MECHANICAL CHARACTERIZATION OF LOW-DENSITY POLYMERIC FOAMS BEING DEVELOPED FOR DIRECT-DRIVE LASER ICF TARGETS\*(UNC)

Clarence Thomas, Jr., D. Lynn James, Stephan A. Letts,  
and Steven C. Mance

University of California  
Lawrence Livermore National Laboratory  
P. O. Box 5508, Livermore, CA 94550

### INTRODUCTION

It is extremely important that we measure the Low Temperature Coefficient of Thermal Expansion (LTCTE) of various foams presently being developed for ICF targets. We must characterize the thermal expansion behavior of foam materials at cryogenic temperature because the foams will be prepared in a nominal room temperature environment and then cooled to approximately 20 K for filling with liquid DT.

### EXPERIMENTAL GOAL

Our goal was to characterize the dimensional change of foams over a range of 300 to 15 K. This experiment was accomplished by utilizing a Perkin-Elmer TMS-2 Thermomechanical Analysis System which was originally designed to operate from 400 to 90 K while observing the dynamic mechanical behavior of a test specimen as a function of temperature, frequency, and stress modulation. After modifying this system for lower temperature operation, we were able to characterize the absolute contraction or expansion of five foams. The dynamic mechanical behavior of foams as a function of cryogenic temperatures will not be included here.

### EXPERIMENTAL SYSTEM MODIFICATIONS

Our modifications to the existing system included extending the temperature range to 15 K, and installing a non-contact length-sensing transducer into the mechanical circuit which is approximately 100 times more

\*Work performed under the auspices of the U. S. Department of Energy by the Lawrence Livermore National Laboratory under contract number W 7405 ENG 48.

sensitive than the original system (see Fig. 1 for a photograph of the LTCTE System). The operating temperature of the system was extended to 15K by the design and fabrication of a new cryostat with feedback temperature and cryogen flow control capability (see Fig. 2 for a logic diagram of the improved system). The sensitivity of the length sensing transducer was improved by substituting an eddy current transducer for the existing LVDT. This new transducer was determined to have a sensitivity of 1 micron.

#### EXPERIMENTAL TEST SYSTEM

Specimen length changes and temperature are recorded on a x-y plotter as well as on a H.P. 9836 computer which incorporates a temperature measurement feedback loop and also controls the cryogen flow. This system can be operated in two different modes: static length measurement as a function of temperature, or dynamic mechanical spectroscopy. In the static measurement mode, a constant load force is applied to the sample specimen and the length changes are recorded as a function of temperature. In the dynamic range stress can be selectively imposed via a linear electromagnet and is driven by the control unit in either square-wave, or sinusoidal form with selectable modulation frequency usable in the ranges from 0.01 to 10.0 hertz for the observation of the dynamic mechanical behavior. These length changes are also recorded as a function of temperature.

#### EXPERIMENTAL DATA

Our first series of experiments involved measurements of the thermal contraction in the temperature range of 300 to 15 K. The foams were prepared by vibratoming samples into rectangular prisms with dimensions of 5x5x7.5 mm. The low-density foams tested were polystyrene (PS), resorcinol-formaldehyde (RF), carbonized resorcinol-formaldehyde (CRF), cellulose acetate (CA), and silica aerogel. The fractional dimensional change or percent of linear shrinkage or expansion as a function of temperature is shown in Fig. 3. The contraction of PS foam to 15 K was measured to be 1.4%. We measured exactly the same behavior on samples of full density PS which were used for initial calibration tests of the system. Literature values of the thermal contraction of PS are listed as

1.5%. CA and RF foams have very similar thermal contraction behavior with values of 0.6 and 0.55% respectively. Both silica aerogel and CRF expand on cooling by 0.1 and 0.15% respectively. The expansion of materials having a plate morphology, such as polyethylene, on cooling has been observed before. The overall volume of the material drops with temperature, however, the dimensions of the material do not change uniformly. The material contracts strongly in the thin dimension of the plate. This strong contraction causes the length dimension to actually increase.

#### OBSERVATIONS

We have noted contraction excursions in both the CRF and the aerogel foams during subsequent warm-ups after cooling to 15 K. These excursions appear to be caused by adsorption phenomena which we have eliminated by annealing the test specimen under ultrahigh vacuum at 120°C for 48 hours prior to LTCTE experiments. For the purpose of target construction it would be desirable to have no thermal contraction, however, having accurate measurements of the contraction/expansion allows us to predict the final dimensions. From these results, we can conclude that the CRF foams are potentially superior to PS in this respect. Targets can probably be successfully made from PS foams, but the larger thermal contraction may mean significant challenges for the target design.

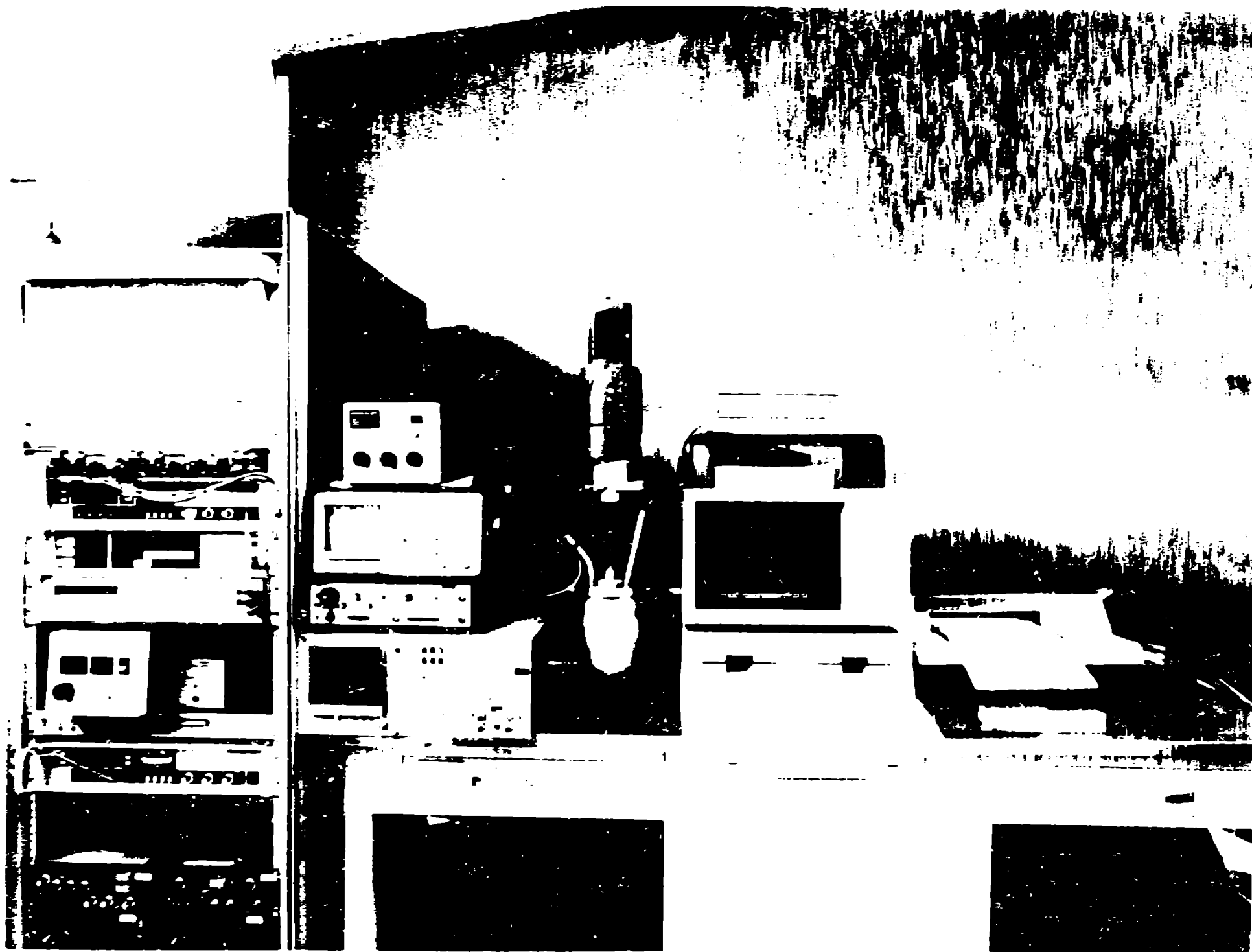


Figure 1 - Experimental System

# Thermomechanical measurement system Logic diagram

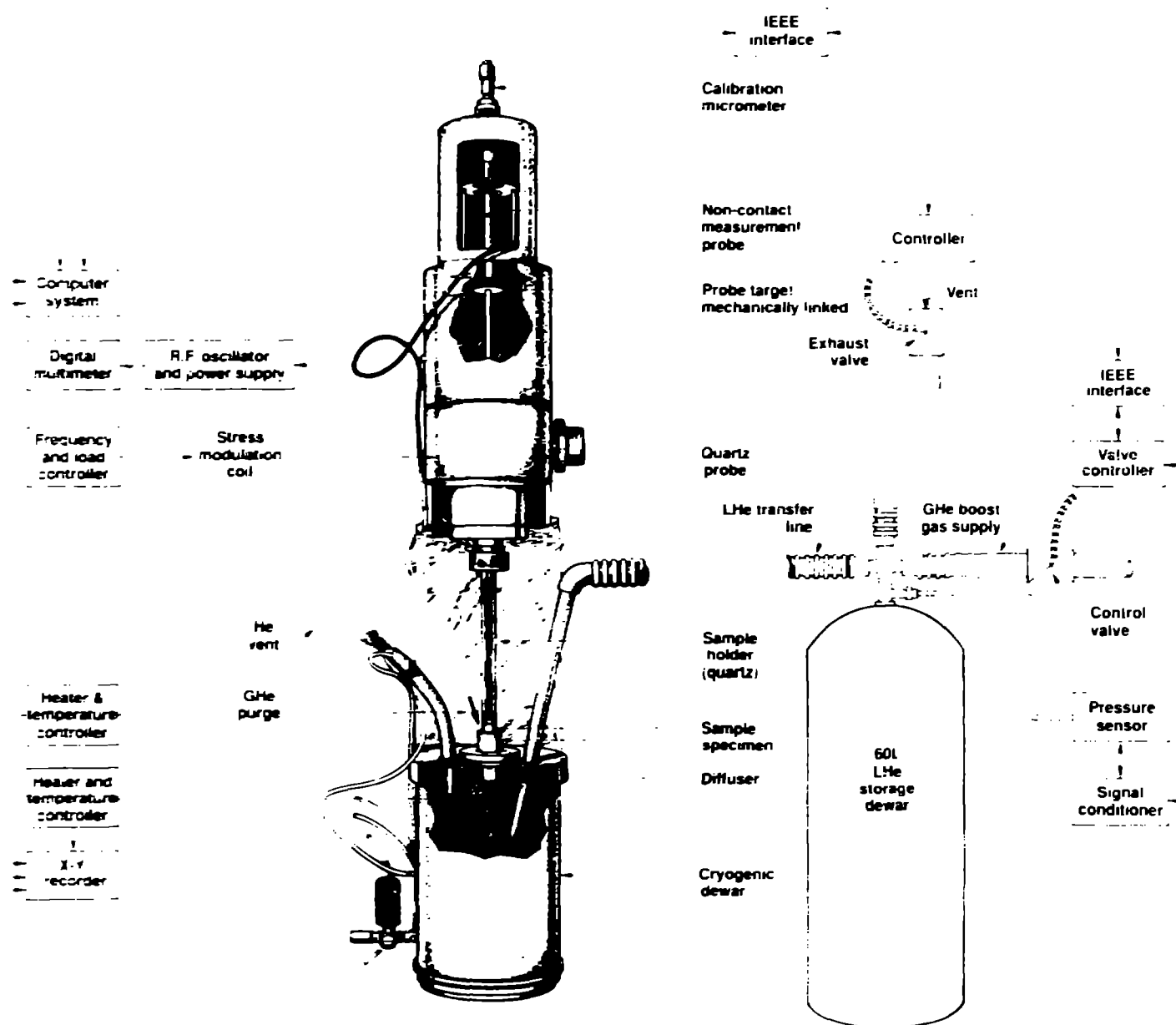
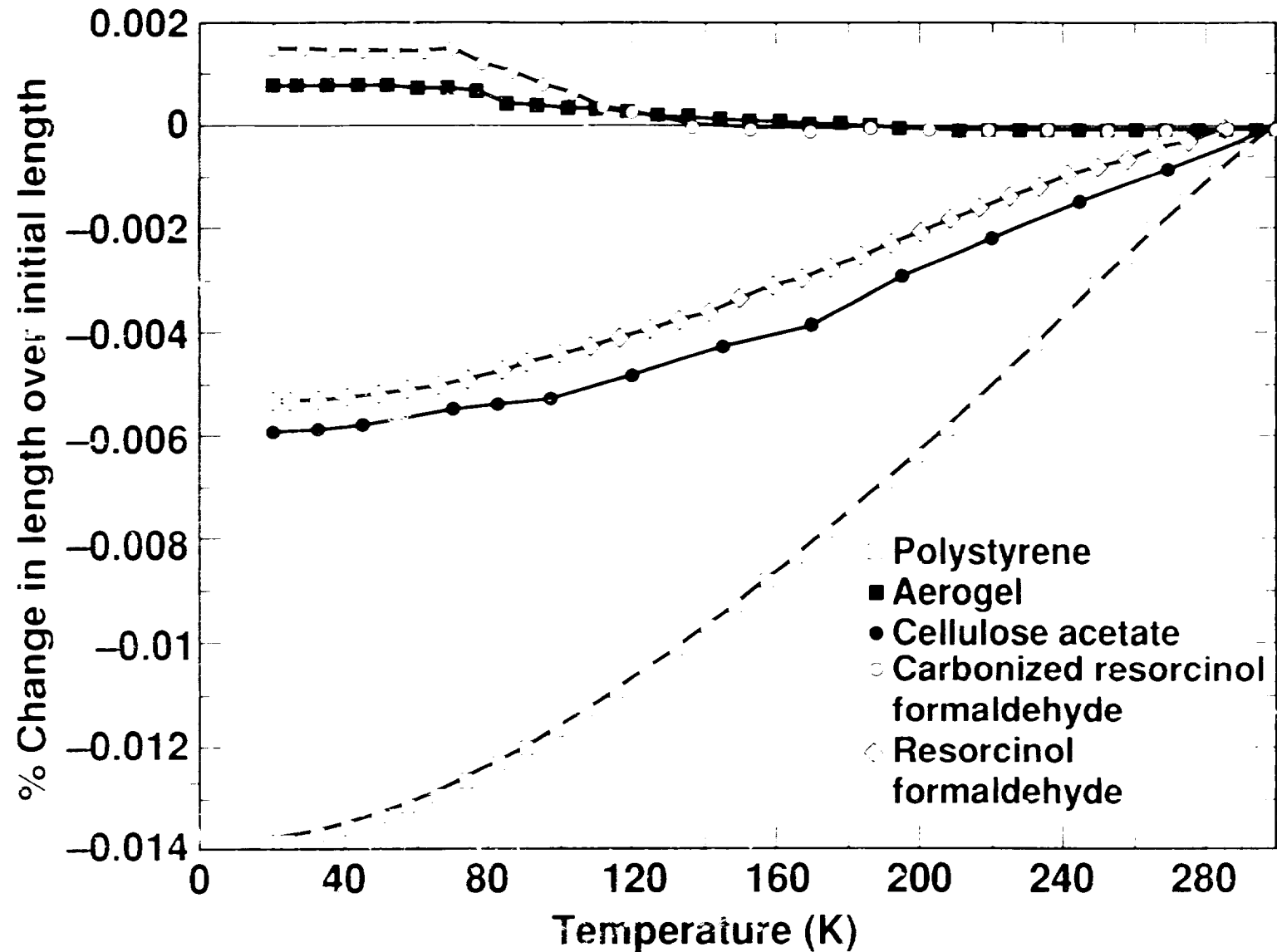


Figure 2 - Logic Diagram

# Experimental Data



## Contraction measurements of foams

Figure 3 - Experimental Data

## DRYING STUDIES ON INVERSE-EMULSION POLYSTYRENE FOAMS\*(UNC)

George F. Overturf III

University of California  
Lawrence Livermore National Laboratory  
P. O. Box 5508, Livermore, CA 94550

### INTRODUCTION

Polystyrene (PS) foams are being developed as candidate materials for direct-drive ICF targets. We are using an inverse-emulsion system originally developed by Unilever Research Laboratory.<sup>1</sup> A water-in-oil (w/o) high-internal-phase emulsion (HIPE) is made by using a surfactant such as sorbitan monooleate (Span 80) and a w/o ratio of 90/10 to 95/5. The oil phase is a 50:50 mixture of styrene and divinylbenzene (DVB) monomers, and the surfactant is usually 20wt% of the oil phase. The DVB is added to increase the strength of the foam through crosslinking. The water phase contains sodium persulfate as a thermal polymerization initiator.

Once a PS emulsion has polymerized, the water must be removed from the foam structure by drying in a vacuum oven to produce the void space within the foam. It is desirable to remove the water as rapidly as possible without damaging the foam. The drying rate may also reveal something about the structure of the foam. We have found that the water will rust out the mechanical vacuum pumps normally used on the ovens. To solve this problem, a new type of vacuum pump which works on a venturi principle was selected because it would pass the water without any harmful effects. The mechanical pumps would evacuate an empty chamber to a base pressure of approximately 50 mTorr, but the base pressure for the new pump was approximately 7 Torr. There was concern that the rate of drying would decrease, thus slowing the production rate of PS foams, but initial comparisons between the two pumps yielded similar drying rates. This prompted a study to determine the mechanisms of the drying process and to see if its efficiency could be

\*Work performed under the auspices of the U. S. Department of Energy by the Lawrence Livermore National Laboratory under contract number W-7405-ENG-48.

improved by changing the temperature and pressure.

In order to measure the rate of water removal with time, an electronic balance with a remote display unit was placed inside a vacuum oven. The remote display unit had an RS-232 output which was fed to a computer for data logging. Logging increments were typically 10 min.

The oil portion of the PS emulsions used for this experiment consisted of 42wt% styrene, 42wt% DVB, and 16wt% sorbitan monooleate. The samples were emulsified using a counter-rotating mixer. The densities were approximately  $80 \text{ mg/cm}^3$ . The emulsions were polymerized in a 50 ml plastic syringe. Polymerization was carried out in an oven at  $50^\circ\text{C}$  for 24 h. After polymerization, the container was sectioned using a band saw, leaving cylindrical sections which were 0.5 or 1.0 cm thick with the sides still enclosed in plastic. The samples were placed in the vacuum chamber on the zeroed balance, data logging was initiated, and the vacuum pump was activated.

Simply viewing the data as weight versus time yields a declining curve which yields little information on the mechanisms that drive the drying process, but one can determine the total amount of time it took to dry the sample. When looking at the rate of drying versus time, it becomes apparent that there is initially a sharp increase in the drying rate due to the evaporation of surface water. The balance of the drying process is relatively slow. The inconsistencies in producing the samples caused slight variations in length which do not affect the area through which evaporation occurs, but do increase the volume of water removed. Since this determines the amount of time to complete the drying process, and the purpose of the experiment was to compare the rates of drying, it was decided to normalize the volume of water by looking at the drying rate as a function of the ratio of the weight of water to that of dry foam. Since all of the samples were made to the same bulk density, the ratio of water to polystyrene foam is constant, and the drying rates can be compared. Figure 1 shows the results of three runs plotted in this manner.

The first run was made with the oven at ambient temperature and the venturi pump achieving a base pressure of 8 torr. The second run was also at ambient temperature but with a mechanical pump which achieved 200 mtorr.



There is very little difference in the two rates, and the total drying time for both was approximately 8 d. The third run was with the venturi pump but with the oven at 50°C. In this case, the rate of drying has roughly doubled, and the samples dried in about 4 d.

The increase in drying rate with temperature is to be expected, due to the increase in the rate of evaporation of water, but the lack of any pressure effect was somewhat surprising. In order to get more information about the process, the experimental set-up was modified. A vacuum transducer was attached to the oven so that pressure could also be logged with each weight reading. The internal temperature of the foam sample was measured and logged to determine the amount of temperature drop due to the heat loss from vaporization.

The emulsion formula and method of preparation were the same as for the previous experiments, but the emulsion was cast in a 250 ml Nalgene container with 30 gauge type J thermocouples arranged so that the junction was in the middle and the leads separately exited through small holes drilled on opposite sides of the container. Each sample had three thermocouples which were spaced top to bottom so that one was in the center and the other two were 0.5 cm and 1.0 cm in from their respective surfaces. Polymerization was performed as before, and the container was sectioned into a plastic-encapsulated cylinders roughly 3 cm long with two exposed faces 6 cm in diameter. The samples were placed in the vacuum chamber on the zeroed balance, and a fourth thermocouple was placed so that it touched the center of the surface of one end of the sample. Data logging was initiated and the vacuum pump was activated.

The results of three runs made with this system are shown in Fig. 2. It is clear that the shape of the curves has changed somewhat with these larger samples. The effect of increasing temperature is again observed. In order to test the effect of increasing the flow through the vacuum oven, a sample was run where a dry nitrogen gas feed was attached through a needle valve to the drying oven, which raised the base pressure from 8 Torr to 11 Torr. This did increase the drying rate, although not as much as increasing the temperature, and the sample dried in 2.5 d.

More information can be obtained when the sample core temperature is

observed versus moisture content as shown in Fig. 3. In the beginning the water/foam ratio is a little over eleven to one and still at a slightly elevated temperature from having just been taken out of the polymerization oven. After the vacuum pump is turned on and the water begins to evaporate, temperature throughout the sample drops sharply due to the loss of heat required to vaporize the water. The temperature remains depressed until nearly 80% of the water is removed, which occurs in only about half of the total drying time. At this point the temperature begins to rise from the outer regions of the sample towards the center.

In the case of the sample with the nitrogen purge, the internal temperatures dropped below 0°C, indicating that the water may have frozen. If this is the case, it will be necessary to determine whether this has any deleterious effects on foam structure. In a preliminary experiment on another vacuum oven system, SEM analysis showed no changes, but this needs to be confirmed.

These temperature measurements and preliminary X-ray radiography experiments on partially dried foams suggest that the water surface is moving from the outside of the foam to the center. Our next step is to develop a model of the drying process which explains all of this data.

#### REFERENCES

1. Unilever Research Laboratory, Emulsion Process for Making Foams, European Patent 60138 (Sept. 3, 1982).

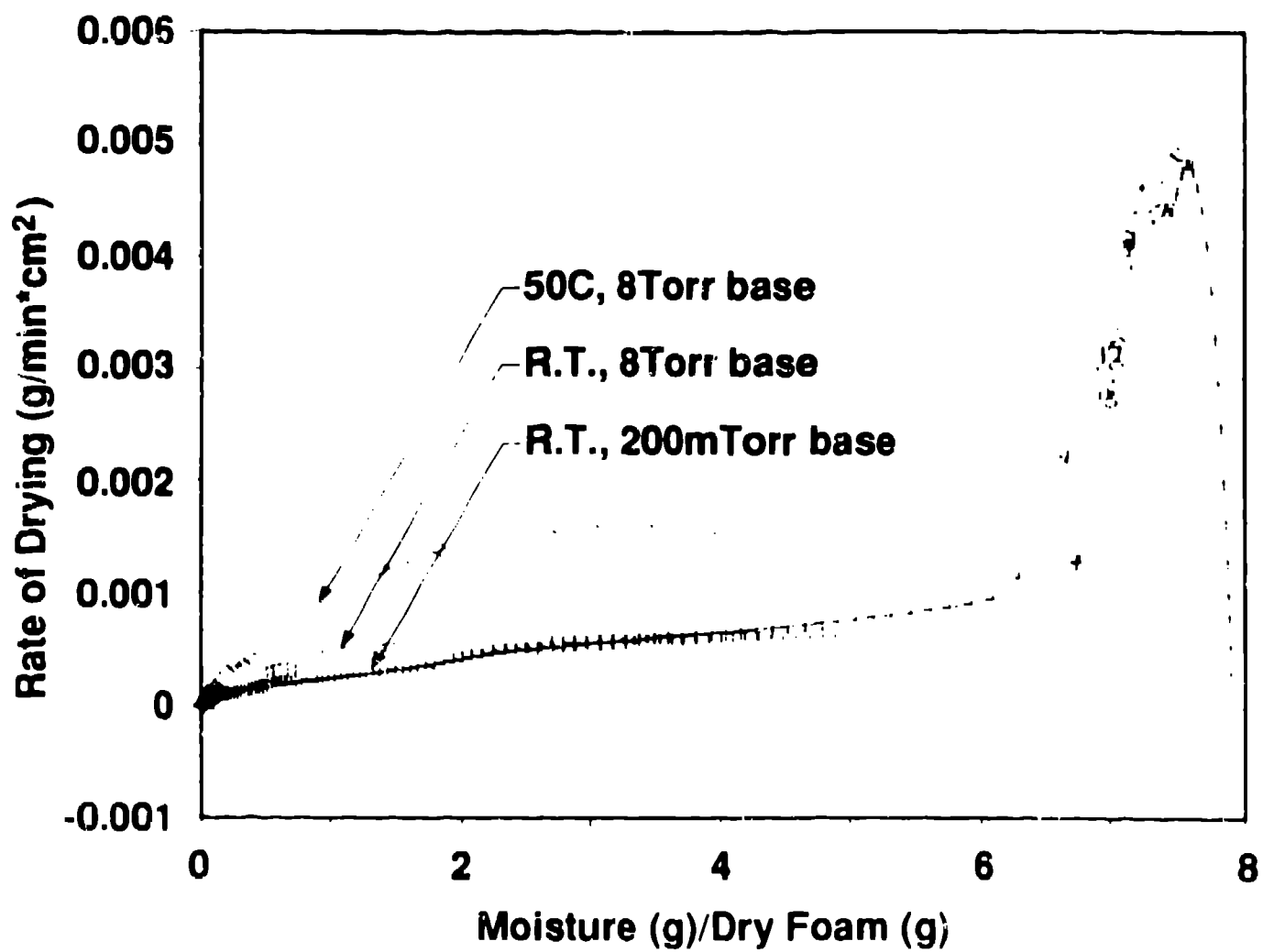
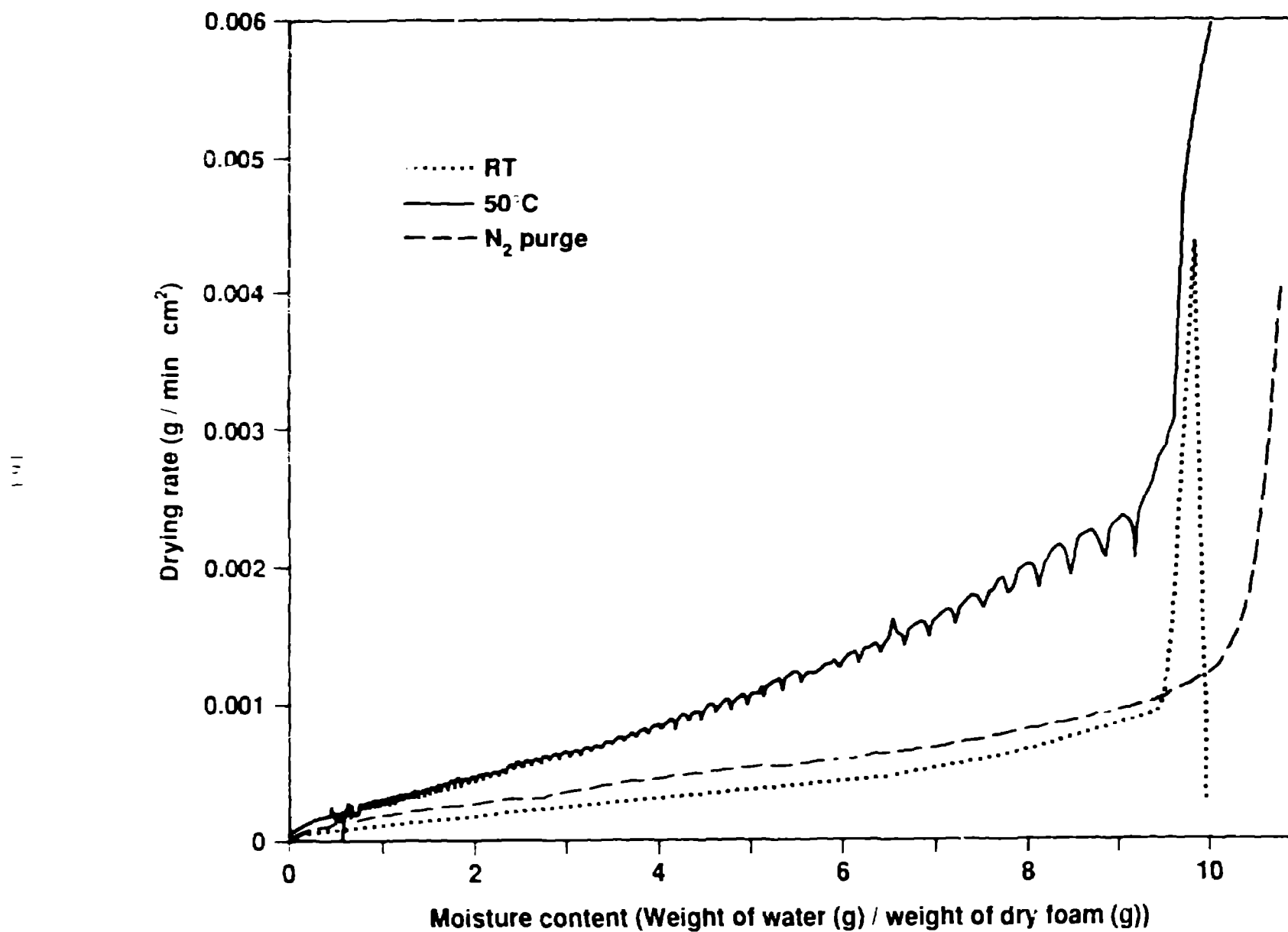


Figure 1 - Comparison of drying rates after varying temperature and pressure.



02-32-0588-1254

Figure 2 - Comparison of drying rates of the thermally monitored samples.

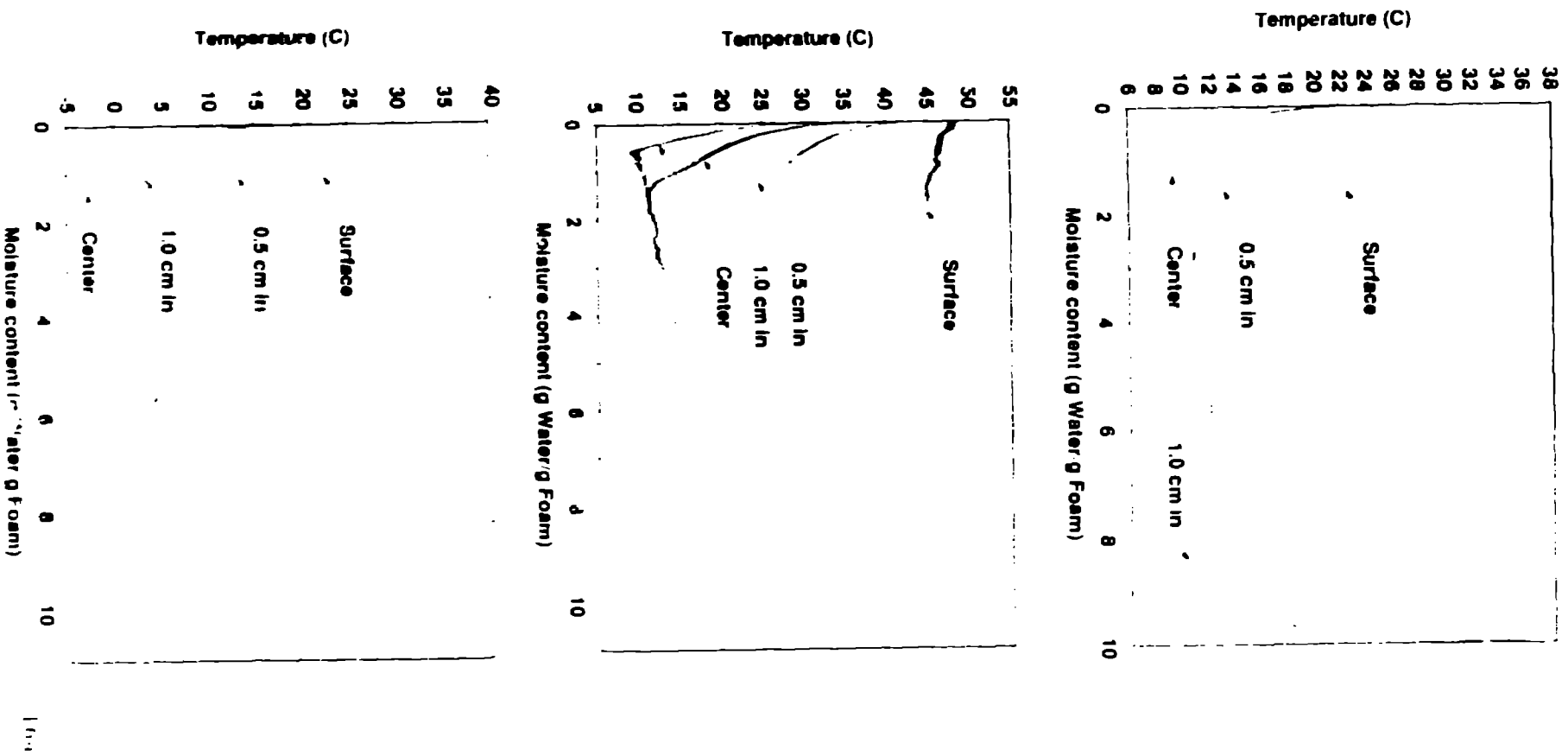


Figure 3 - Temperature profiles of drying polystyrene foams at room temperature (top),

## **CURRENT DEVELOPMENTS IN PVA COATING OF POLYMER MICROSHELLS**

**Kenneth J. King**

**University of California  
Lawrence Livermore National Laboratory  
P. O. Box 5508, Livermore, CA 94550**

### **ABSTRACT**

Some of the targets shot in the Nova Laser use a polymer microshell mandrel coated with a PVA (polyvinyl alcohol) gas retention layer and a CH ablator layer. The PVA coating is formed in a separate process from the CH coating. A number of design changes have been made to the existing PVA shell handling and coating equipment. These changes have resulted in simplified and faster shell handling; increased yields; proven versatility of the system; and, greater accuracy of trace gases in the coated shells.

### **INTRODUCTION**

New target specifications and research toward increased productivity have brought about changes in the original equipment developed for PVA coating of microshells.

### **SCOPE**

This paper is an introduction to the equipment in use for PVA coating of polymer microshells at LLNL. It is an abridged version of the poster session of the same title presented at the 1988 Target Specialists' Meeting in Los Alamos, New Mexico. For additional information about the PVA coating system in use at LLNL the following paper by this author is recommended for further reading: FABRICATION AND OPERATING OF A SYSTEM FOR THE PVA COATING OF POLYMER MICROSHELLS WITH TRACE GAS FILL.

\*Work performed under the auspices of the U. S. Department of Energy by the Lawrence Livermore National Laboratory under contract number W 7405 ENG 48.

## I. Simplified and Faster Shell Handling:

### A. Shell Dispersing Equipment

When the plastic microshells are produced in the drop tower they are collected in a 6 inch diameter petri dish. Features of a petri dish full of plastic shells are:

1. The shells have a very strong static charge which makes them difficult to move around and separate one from the other and from the petri dish.
2. They often are clumped together in large numbers and are difficult to separate due to the static charge.
3. They are often interspersed with microshells of a diameter other than the desired diameter. The shells of different diameters are often small enough to cause problems with PVA coating if they are processed along with the shells of the correct diameter.

To prepare the shells for PVA processing an acrylic plastic tube is placed over the petri dish. Some of the shells are blown out of the petri dish onto the walls of the plastic tube using a small diameter polyethylene hose and house air at a regulator pressure of less than 17 psi. The plastic tube is then placed onto a flat plate from which the shells are collected for processing. The shells are blown off the walls of the plastic tube onto the flat plate. This process allows the shells to be rapidly separated for processing without damaging them or introducing foreign matter on the surface of the shells.

### B. Pickup tool system (Figures 1 and 2)

The microshells are prepared for PVA coating by vacuuming them into glass capillaries (micropipettes) which are 5 inches (125 mm) long and (for 425 micron o.d. shells) have an i.d. of 570 microns. Characteristics of working with the micropipettes are:

1. They are rather fragile.
2. The operator must maintain the micropipette with a steady hand for extended periods of time (minimum of 30 minutes for 6 capillaries).

3. During this time the operator must be able to move the capillary diagonally 800 microns minimum (approximately 1,800 times for 6 capillaries) to keep from crushing shells or vacuuming up unwanted shells while moving to new locations on the shell collection dish.

A semi-automated system was developed for the shell pickup process. The system greatly reduces the tedium and strain previously associated with picking up shells; reduces waste; and, increases reliability and speed.

## II. Increased yields

When the microshells are injected into the drop tower for drying an interplay of events affects the yield per run (Fig. 3). Studies were made to characterize these events and increase the yield and reliability of the column. The events studied were:

1. Shroud location in injector.
2. Capillary location in shroud.
3. Speed of flow of shells out of capillary.
4. Cleanliness of shroud.
5. Dampness of saturator wick.
6. Flowmeter setting on stripping gas.
7. Temperature of PVA bath.
8. Flowmeter settings for column gas inflow and outflow.
9. Column temperatures.

Results: The column is now 100% reliable with a 5% increase in yield. The main feature is the 100% reliability. It is much easier to schedule a PVA run with confidence that there will be product from the run to meet programmatic needs.

## III. Versatility of the System

Changing target specifications required an expansion of the sizes of shells coated with PVA solution and changes in the quality of the PVA coatings.

- A. Coating shells of varying diameters:



1. The glass capillaries into which the shells are gathered were studied. Shell diameter to required micropipette diameter was characterized.
2. The procedure for handling the capillaries was modified to handle the various shell diameters.
3. The column characterization elements were studied and modified to accept the changes in shell diameter.

Results: 300-700 micron diameter shells are now processed.

#### B. Doping the PVA solution:

Trace amounts of LiCl were added to the PVA solution. The resultant solution was successfully coated on the polymer microshells. No major changes to equipment or procedure were required for this function.

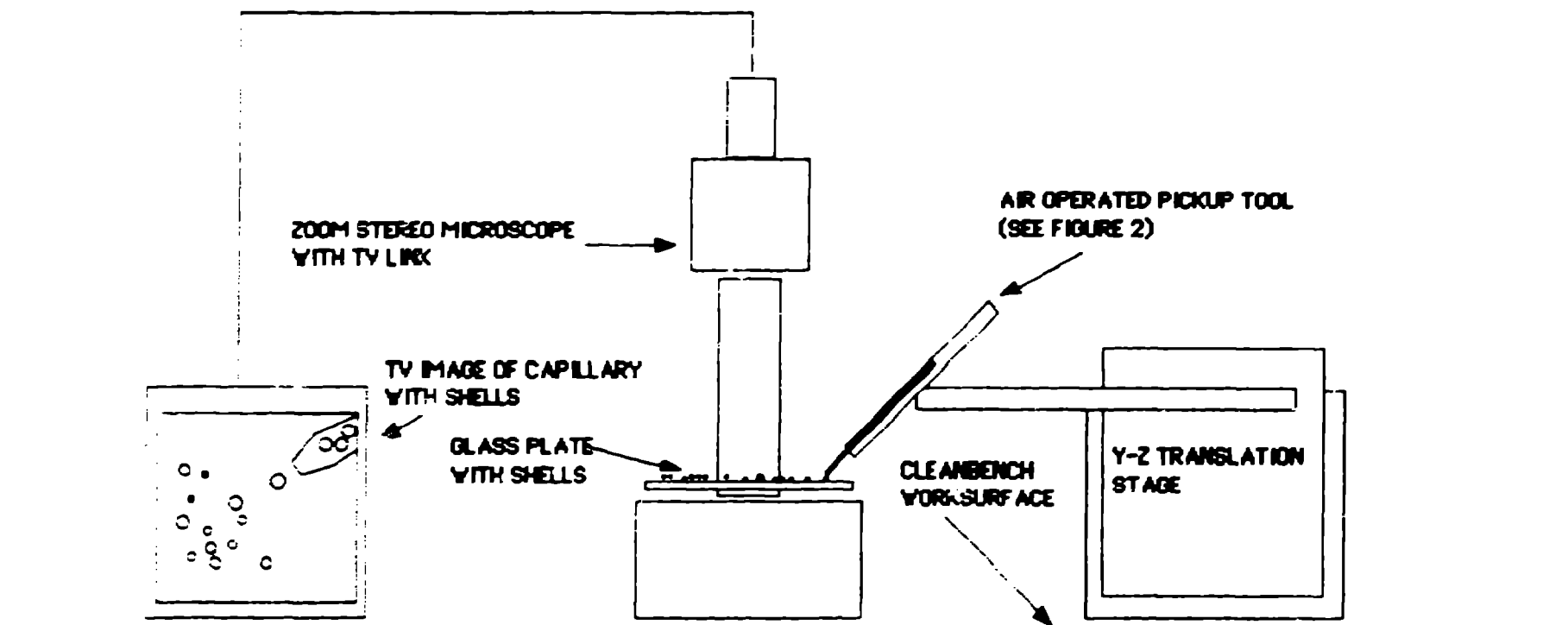
#### IV. Greater Accuracy of Trace Gases in the Coated Shells.

After the microshells are in the glass capillaries the shells are coated with PVA solution. Before the shells are coated atmospheric gases are evacuated and are replaced with precise amounts of trace gases (using a differential pressure gauge).

The key elements to this function are:

1. Without the PVA solution coating on the shells all gases diffuse through the polymer shells almost instantly.
2. Wet PVA solution appears to provide the barrier needed to stop the instantaneous diffusion of gases through the shells.

In order to control the gases that are inside the shells at the instant the shells are coated with PVA solution a vacuum coating chamber was designed (Fig. 4). The vacuum chamber is evacuated; the precise amount of trace gas is flowed into the chamber; to keep the PVA solution from boiling the chamber is filled to 3.00 psi below atmosphere with  $O_2$ ; and, the PVA solution is flowed into each capillary.



SHELL PICK-UP SYSTEM

Figure 1

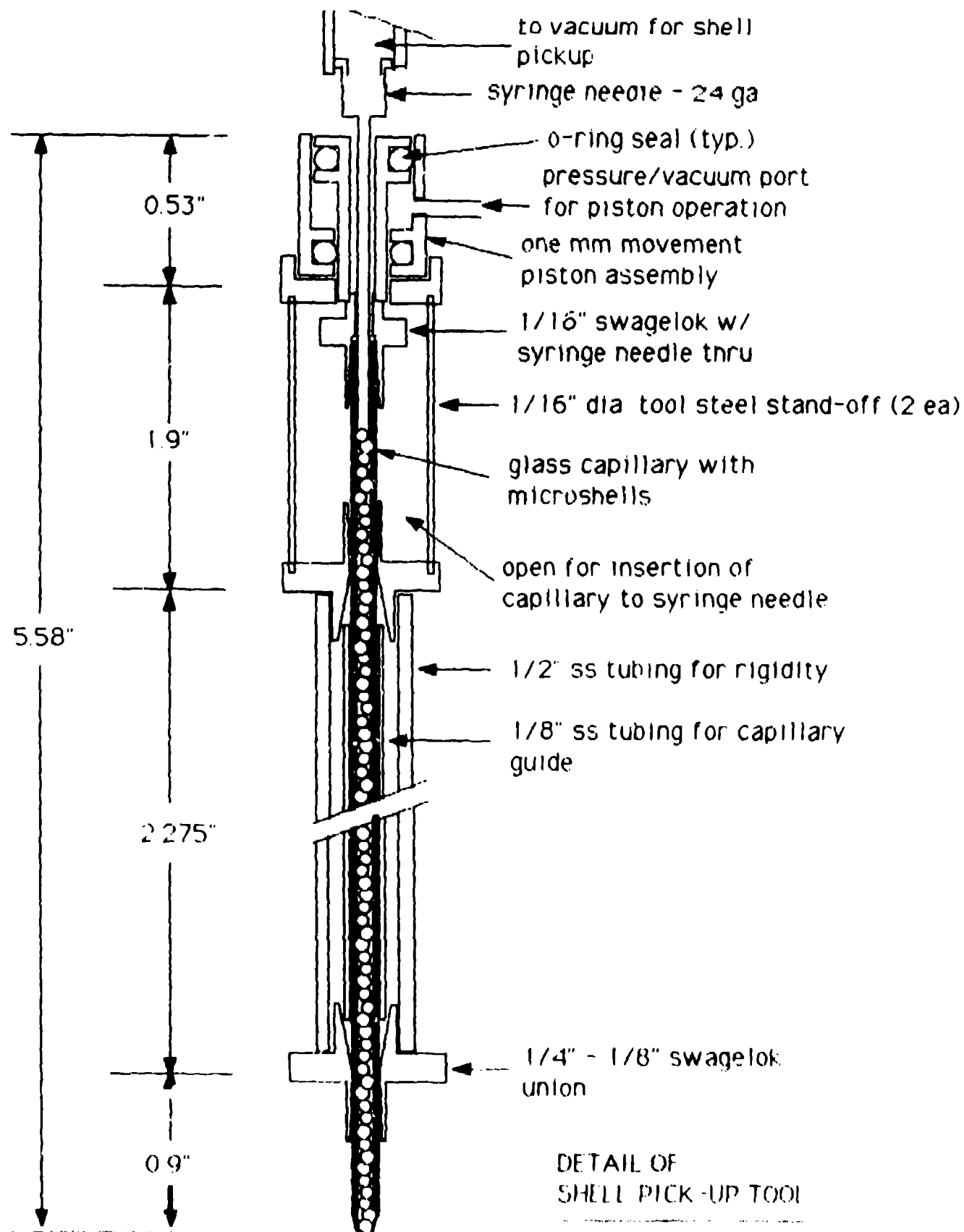
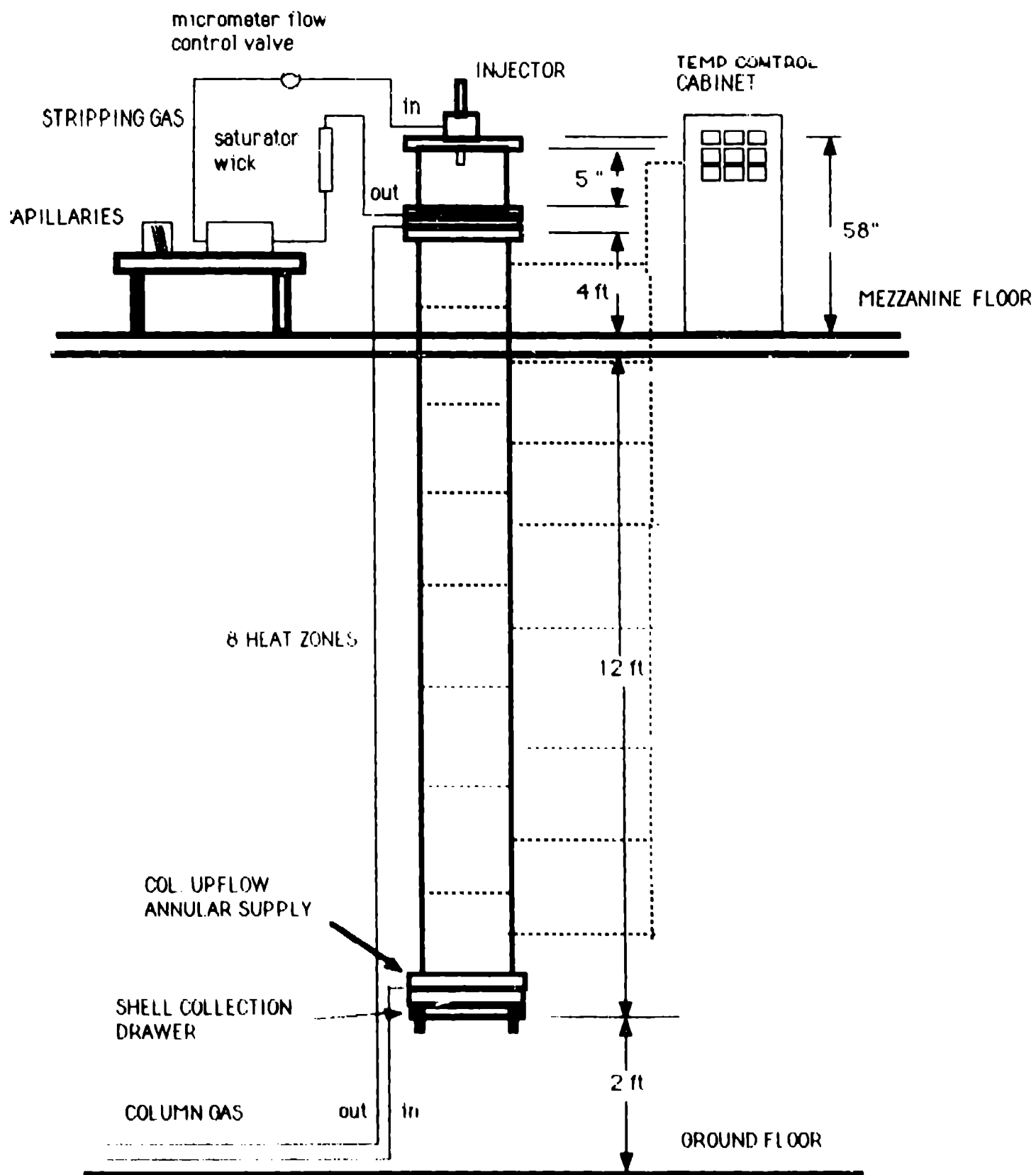


Figure .

(do not scale - all dims approx)

font = 12

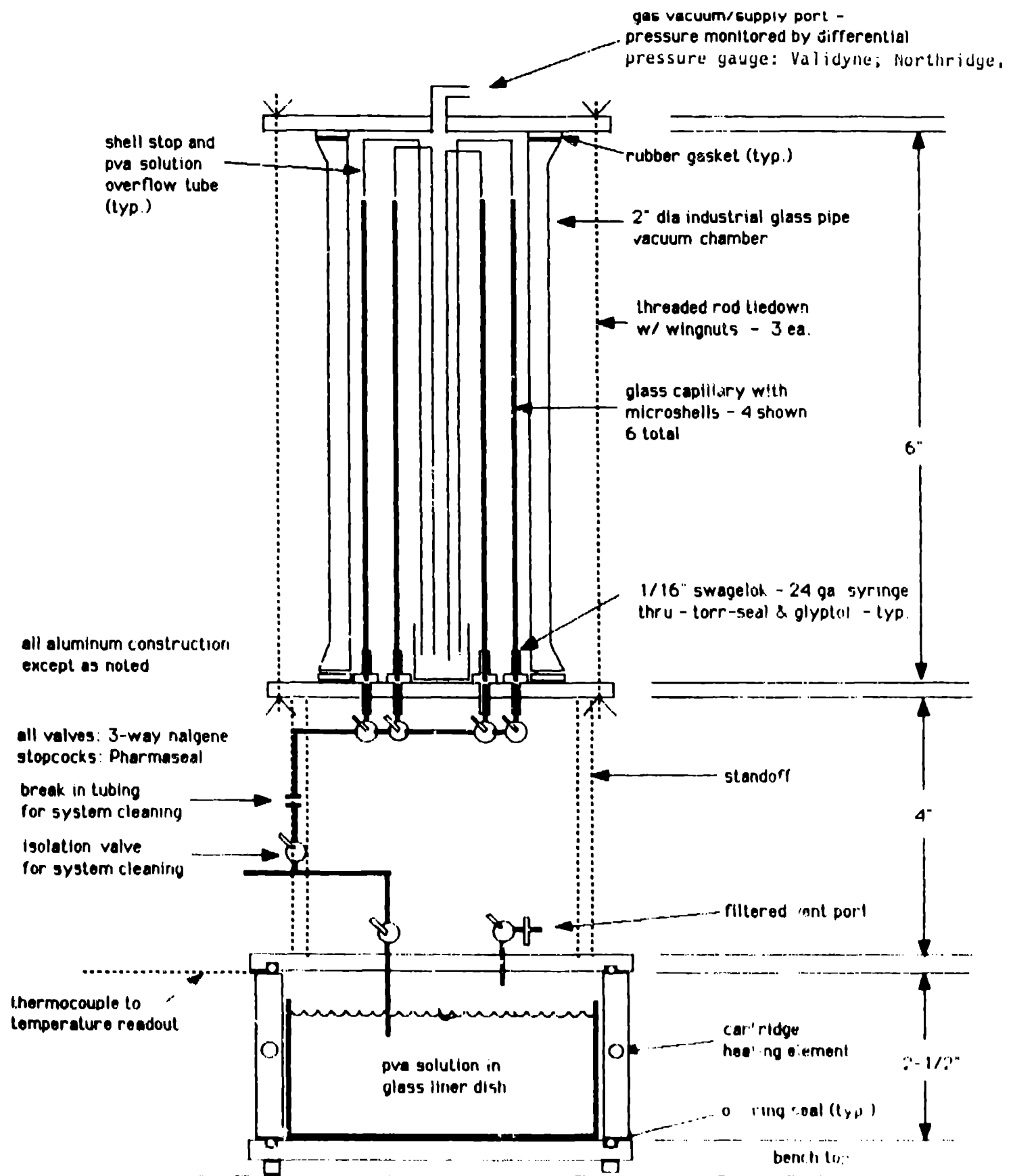


## DROP TOWER SYSTEM

FIGURE 3

font # 10

(do not scale) 1/1



PVA SOLUTION COATER

Figure 4

font size 9

(do not scale)

## METROLOGY ADVANCEMENTS IN TARGET ASSEMBLY\*

Marita Spragge, Daniel Donovan and Dean Harms

University of California  
Lawrence Livermore National Laboratory  
P. O. Box 5508, Livermore, CA 94550

The success of laser fusion experiments depends a great deal upon the degree to which assembly tolerances are achieved. Accurate means of measuring target components and their placement is therefore critical.

In the past, target measurements were accomplished by first calibrating a reticle in the microscope eyepiece to determine the number of microns per division on the reticle. The part to be measured was placed under the microscope and reticle divisions were counted. This worked reasonably well at high magnification where the number of microns per division was small, but was much more inaccurate on low magnification where one division could equal eighty microns. The first improvement to our metrology came with the acquisition of the Unitron measuring microscope (Fig. 1).

With the Unitron, targets or target parts were measured by manually moving the stage in the X and/or Y direction and reading the digital displays. It was not, however, designed to measure angles and, therefore was not able to complete the metrology required on many of the targets.

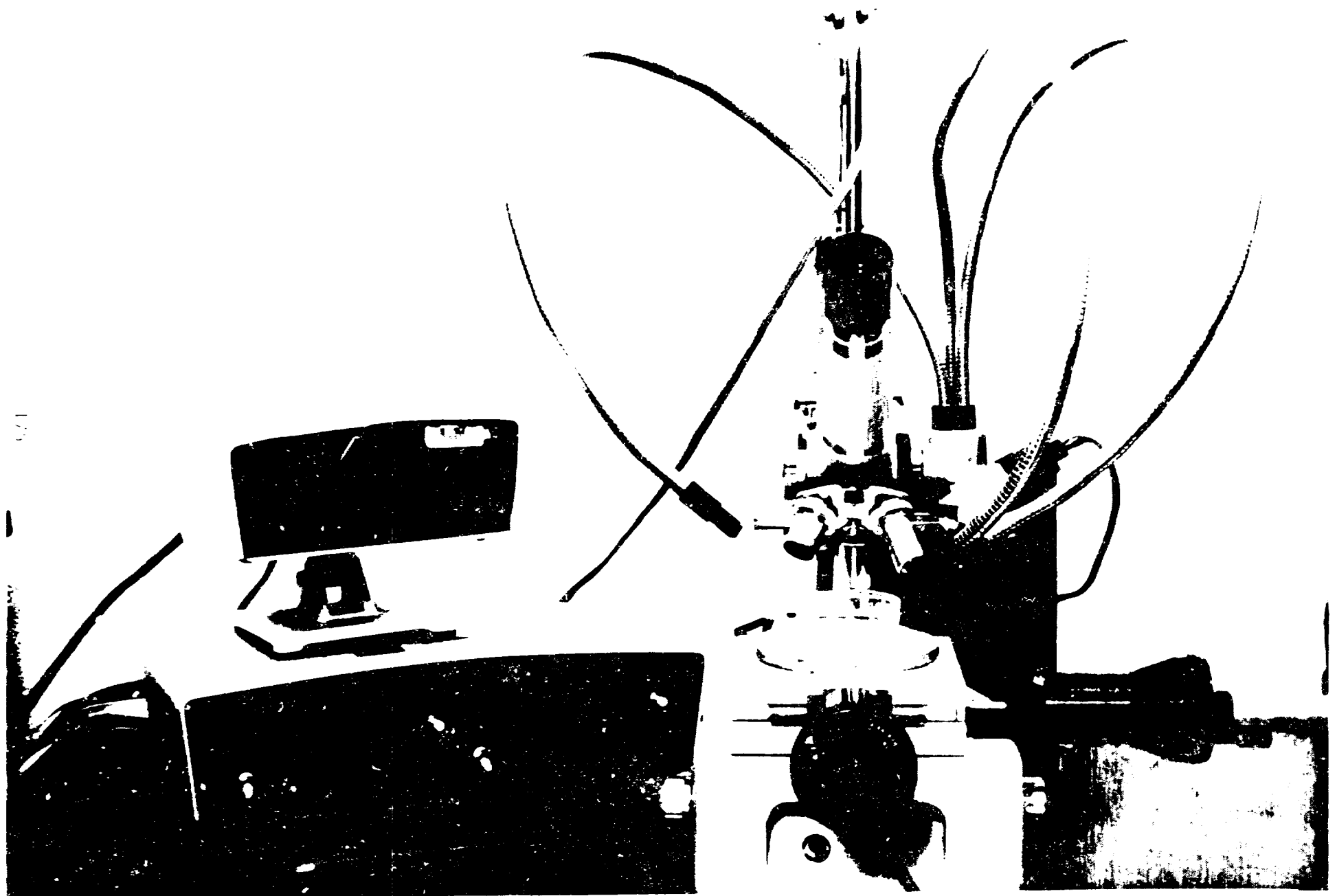
A Nikon optical comparator with digital displays (Fig. 2) was the next addition to our metrology tools. It had a vernier around the screen so that angular measurements could be taken. The stage was modified to allow a target, in its base, to be placed below the normal level of the stage in order to have enough travel in the Z direction. With this modification, measurement of all dimensions and angles was possible. However, because the Nikon is a shadowgraph there were problems defining features on the top surfaces of targets. The Nikon was the primary metrology tool in target assembly until arrival of the Powellscope (Fig. 3.).

\*Work performed under the auspices of the U.S. Department of Energy by the Lawrence Livermore National Laboratory under contract number W 7405 ENG 48.

The Powellscope was designed by Roy Powell of the Atomic Weapons Establishment (AWE) in Aldermaston, England. It was assembled in England and brought to Lawrence Livermore National Laboratory to aid the AWE personnel in the metrology of their targets which were being shot in Nova. The Powellscope system consists of Klinger components with pushbutton controls, digital displays and a motorized target base manipulator with X,Y,Z and rotational capabilities. Linear dimensions are measured to one micron accuracy. Angles are measured to a hundredth of a degree. The forty-five degree inspection scope has a manual focus, a manual zoom and camera back. This system allows the target to be viewed from the same perspectives as any of Nova's laser beams or target chamber diagnostics (Fig. 4). The Powellscope is the primary metrology tool in use at Livermore today.

3121d

Figure 1. Uniftron





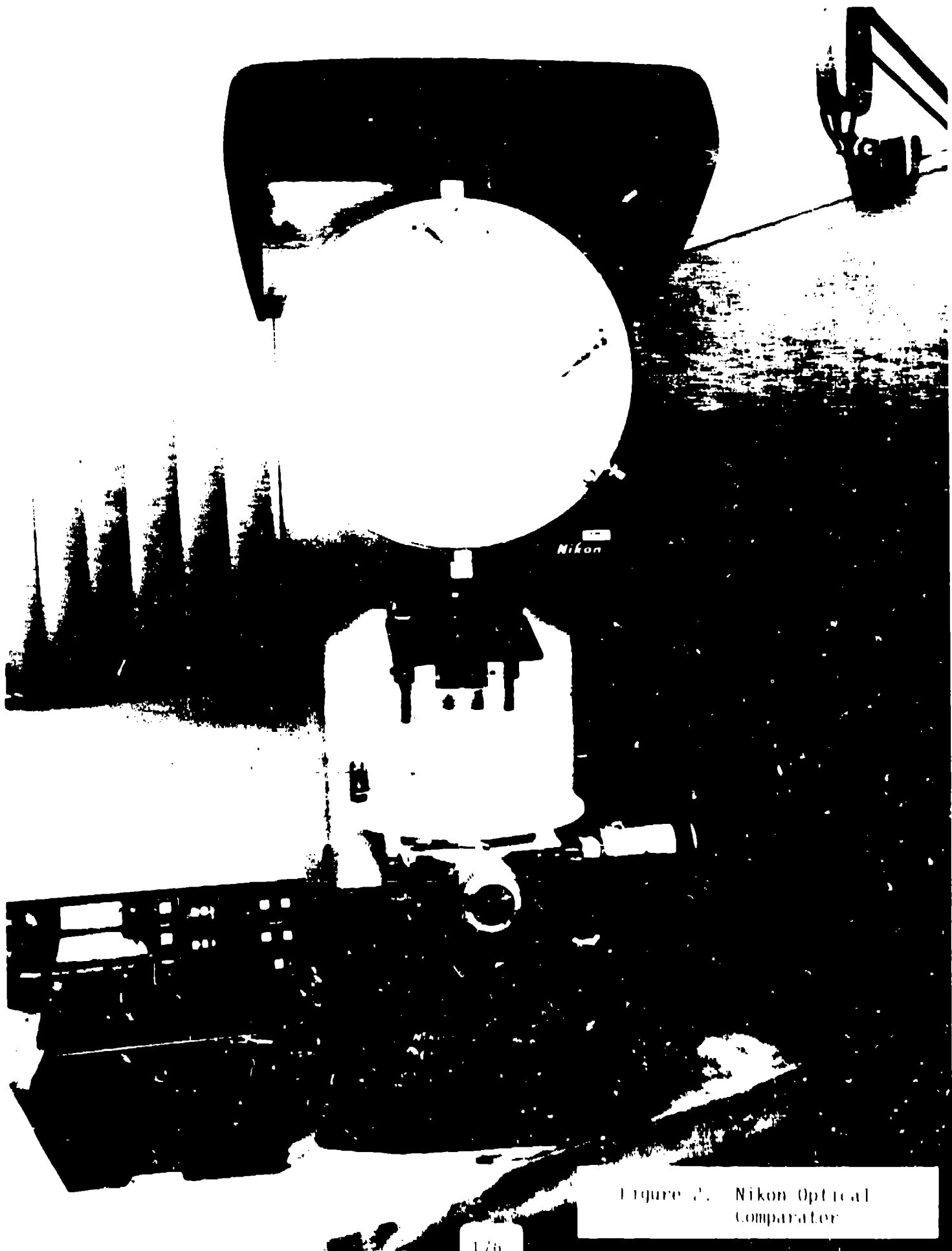


Figure 2. Nikon Optical  
Comparator

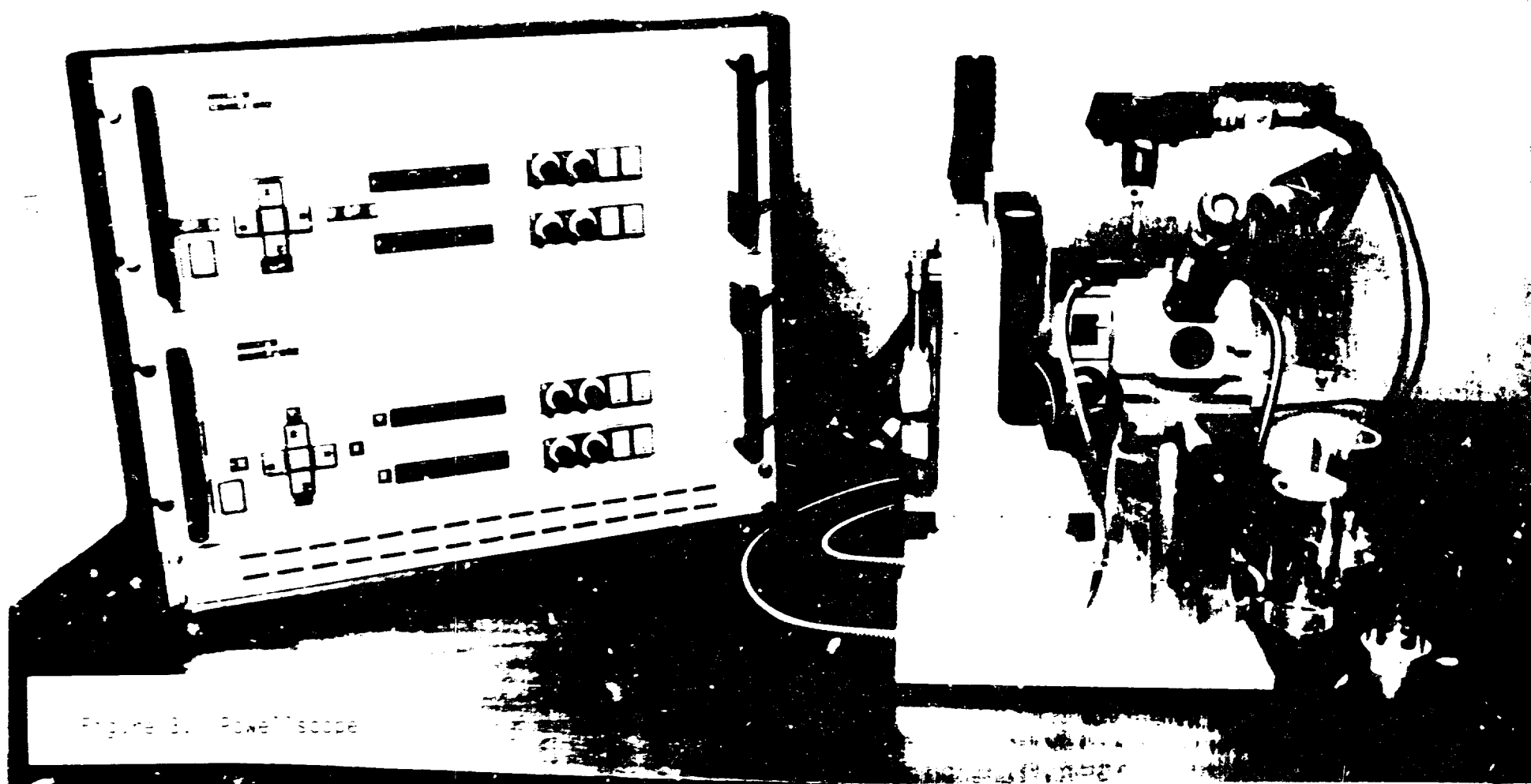
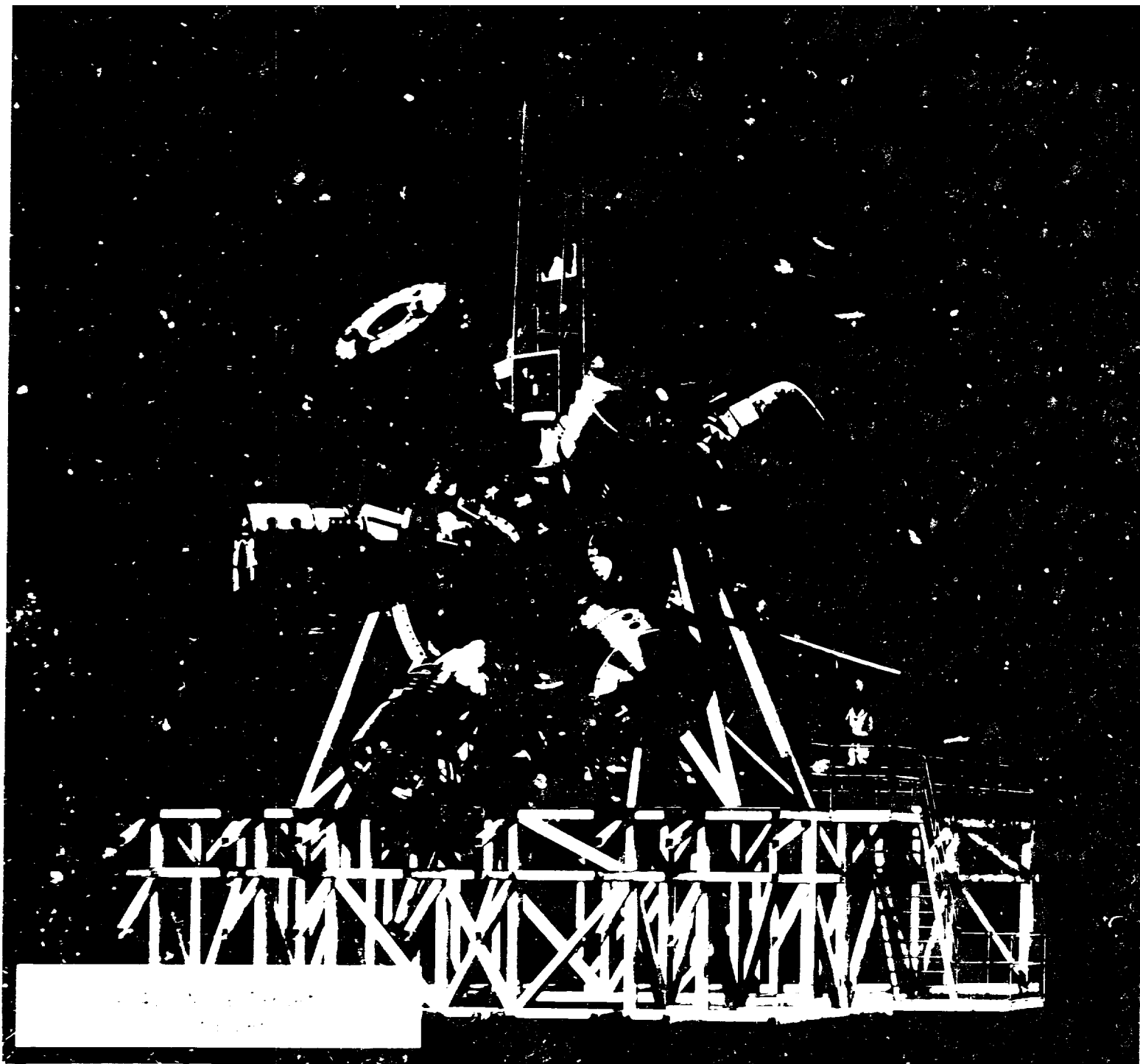


Figure 3. Powell scope



# **FORMATION OF SPHERICAL-SHELL $\text{SiO}_2$ AEROGEL PELLETS BY A SOL-GEL METHOD**

**BY**

**N. K. KIM, R. F. FALKNER, K. KIM, D. M. MILLAR, AND D. A. PAYNE  
FUSION TECHNOLOGY LABORATORY  
UNIVERSITY OF ILLINOIS  
URBANA, IL 61801**

**AND**

**R. S. UPADHYE  
LAWRENCE LIVERMORE NATIONAL LABORATORY  
LIVERMORE, CA 94550**

## **ABSTRACT**

**A SYSTEM WAS DESIGNED TO PRODUCE HOLLOW  $\text{SiO}_2$  SPHERES BY CONTROLLED HYDROLYSIS AND CONDENSATION REACTIONS OF TETRAETHYLOTHOSILICATE (TEOS). IN THIS SYSTEM, AN ACIDIC SOLUTION OF TEOS, WATER, ETHANOL (SOLVENT), AND NITRIC ACID (CATALYST) WAS ALLOWED TO FLOW THROUGH A TAPERED PYREX TUBE (OUTER NOZZLE) WHICH CONTAINED A COAXIALLY-MOUNTED HYPODERMIC NEEDLE (INNER NOZZLE). PASSAGE OF  $\text{N}_2/\text{NH}_3$  THROUGH THE INNER NOZZLE FORMED HOLLOW DROPS AT THE TIP OF THE PYREX TUBE. THE DROPS WERE LEVITATED IN A BASIC ATMOSPHERE AND CONSEQUENTLY CONDENSED TO FORM POROUS HOLLOW SPHERES.**

**WORK SUPPORTED BY THE UNITED STATES DEPARTMENT OF ENERGY  
UNDER LLNL SUBCONTRACT # 4180405**

## INTRODUCTION

A SYSTEM IS UNDER DEVELOPMENT FOR THE FABRICATION OF HOLLOW SILICA ( $\text{SiO}_2$ ) AEROGEL SPHERES BY HYDROLYSIS AND CONDENSATION REACTIONS OF TETRAETHYLOTHOSILICATE (TEOS). AN ALKOXIDE SOLUTION OF TEOS, WATER ( $\text{H}_2\text{O}$ ), ETHANOL ( $\text{EtOH}$ ), AND NITRIC ACID ( $\text{HNO}_3$ ) WAS ALLOWED TO FLOW THROUGH AN OUTER NOZZLE OF A DUAL-NOZZLE SYSTEM, AND A BASIC GAS MIXTURE (i.e.,  $\text{N}_2/\text{NH}_3$ ) WAS PASSED THROUGH A COAXIALLY-MOUNTED INNER NOZZLE TO FACILITATE GELATION AND SPHERICAL SHELL FORMATION, THUS PRODUCING A CONTINUOUS STREAM OF HOLLOW SPHERICAL DROPS.

IN THE PRESENT STUDY THE HOLLOW DROPS WERE LEVITATED IN A BASIC AMMONIA ATMOSPHERE BY COUNTER-BALANCING GRAVITY-FALL WITH A FORCED UPWARD GAS STREAM. THE BASIC ATMOSPHERE ACCELERATED THE CONDENSATION AND GELATION REACTIONS THEREBY REDUCING THE POSSIBILITY OF ANY DROP DEFORMATION THAT MIGHT OCCUR FROM CONTACT WITH FOREIGN OBJECTS WHILE THE DROPS WERE IN A NON-RIGID STATE.

SO AS TO INVESTIGATE THE EFFECT OF VARIOUS PARAMETERS ON THE GELATION PROCESS A DETAILED STUDY WAS CARRIED OUT ON THE DEPENDENCE OF TIME TO GELATION AS A FUNCTION OF COMPOSITION IN THE TEOS- $\text{EtOH}$ - $\text{H}_2\text{O}$  SYSTEM.

## OBJECTIVE

TO DEVELOP PROCESSING METHODS FOR THE FABRICATION OF HOLLOW  $\text{SiO}_2$  AEROGEL SPHERES, AND THE CONTROL OF THEIR PROPERTIES FOR ICF TARGET APPLICATIONS

## CHEMICAL REACTIONS

### HYDROLYSIS :

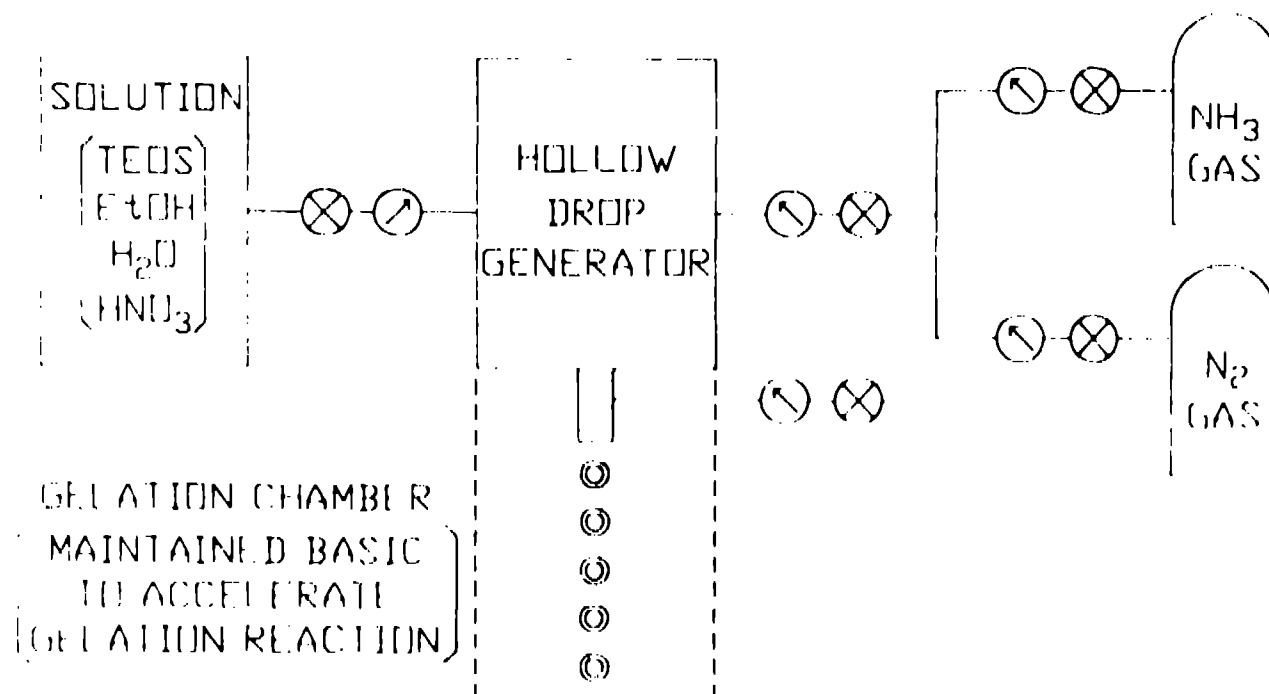


### CONDENSATION :

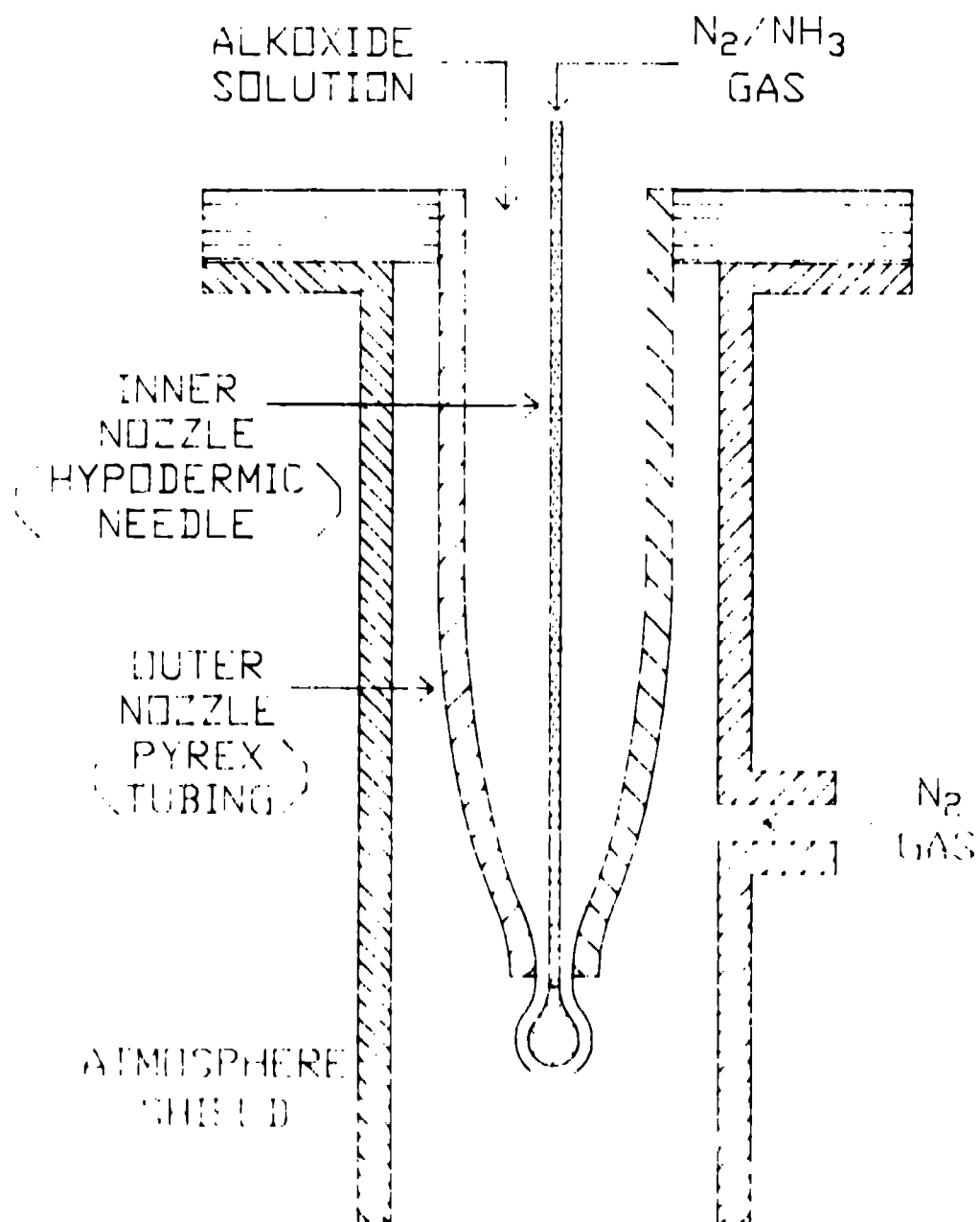


## APPARATUS

### SCHEMATIC DIAGRAM FOR THE GENERATION OF HOLLOW DROPS



## DETAILED SCHEMATIC OF THE DUAL-NOZZLE SYSTEM

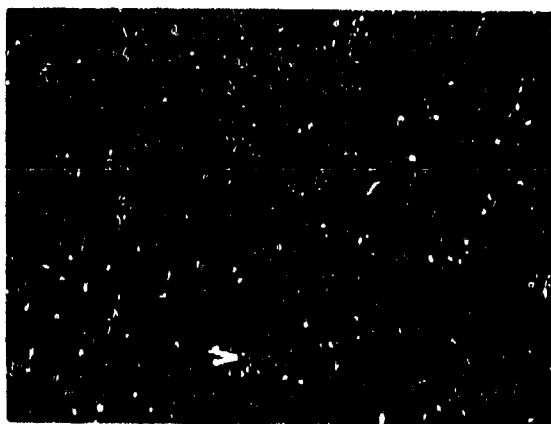
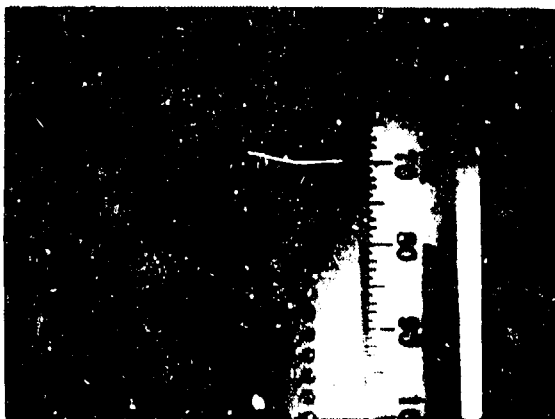


INSTANT CLOGGING AT THE NOZZLE TIP IN A BASIC ATMOSPHERE WAS PREVENTED BY A SHIELD OF NEUTRAL NITROGEN ATMOSPHERE.



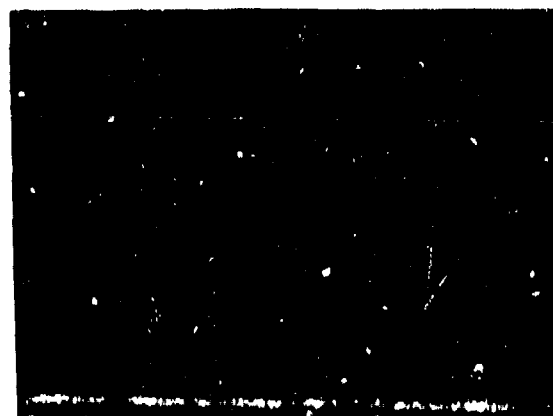
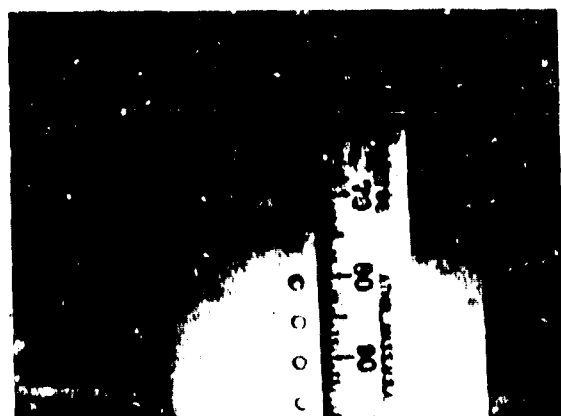
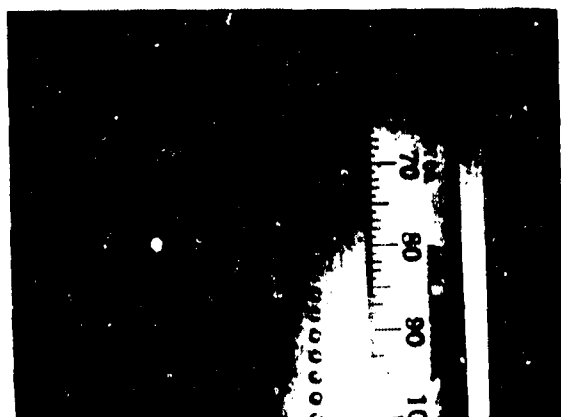
# RESULTS

## GENERATION OF HOLLOW DROPS

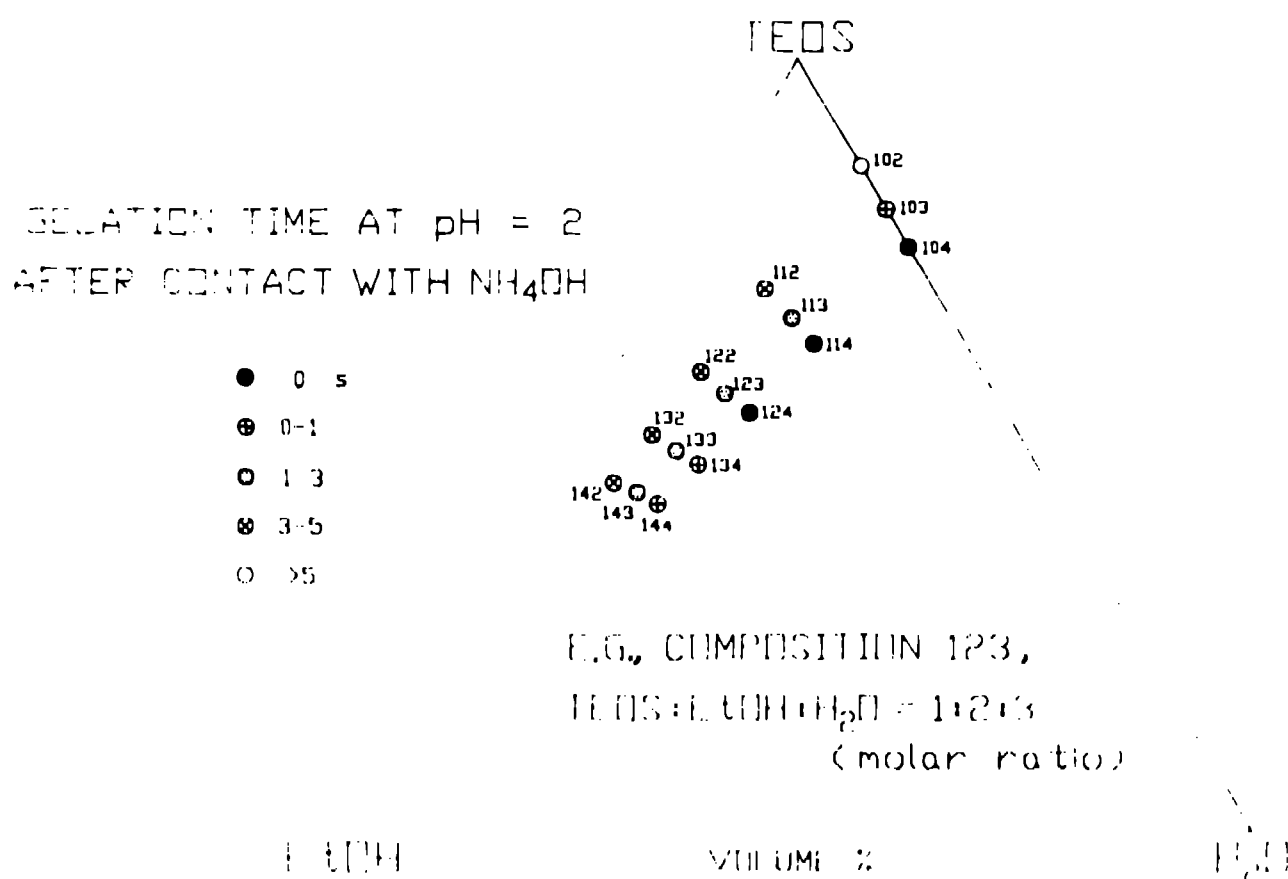


# RESULTS

## GENERATION OF HOLLOW DROPS



# TIME TO GELATION FOR SELECTED COMPOSITIONS IN THE TEOS-ETOH-H<sub>2</sub>O SYSTEM



SHORTEST TIME TO GELATION WAS ACHIEVED AT A  
COMPOSITION OF TEOS : ETOH : H<sub>2</sub>O = 1 : 0 : 4.  
NOTICE THAT ETOH WAS NOT REQUIRED IN THIS CASE.

## SUMMARY

- A CONTINUOUS STREAM OF UNIFORM HOLLOW DROPS OF TEOS SOLUTION WAS PREPARED USING A DUAL-NOZZLE SYSTEM.
- INSTANTANEOUS GELATION WAS ACHIEVED AT SEVERAL COMPOSITIONS. THE COMPOSITION FOR THE SHORTEST TIME TO GELATION WAS DETERMINED TO BE  $\text{TEOS} : \text{EtOH} : \text{H}_2\text{O} = 1 : 0 : 4$  AT  $\text{pH} = 2$ .
- HYDROLYSIS OF TEOS SOLUTION CAN OCCUR EVEN WITHOUT THE ADDITION OF EtOH (AS A MUTUAL SOLVENT FOR TEOS AND  $\text{H}_2\text{O}$ ), DUE TO THE SELF-GENERATED EtOH THAT IS A BY-PRODUCT OF THE REACTION.

## **WORK IN PROGRESS**

**INVESTIGATION AND OPTIMIZATION OF PROCESS PARAMETERS WHICH CONTROL THE PREPARATION AND PROPERTIES OF HOLLOW  $\text{SiO}_2$  AEROGEL SPHERES :**

- **SIZE OF THE INNER AND OUTER NOZZLES, AND THEIR RELATIVE POSITIONS**
- **COMPOSITION, TEMPERATURE, pH, AND VISCOSITY OF THE ALKOXIDE SOLUTION**
- **FLOW RATE OF THE ALKOXIDE SOLUTION AND THE BASIC GAS**
- **COMPOSITION OF THE FLOW GAS (e.g., RATIO BETWEEN  $\text{N}_2$  AND  $\text{NH}_3$ )**
- **TEMPERATURE OF THE GELATION CHAMBER**

## LOW-DENSITY CELLULOSE ACETATE FOAMS FOR DIRECT-DRIVE LASER ICF TARGETS\*(UNC)

Chuck Chen

University of California  
Lawrence Livermore National Laboratory  
P. O. Box 5508, Livermore, CA 94550

### INTRODUCTION

Cellulose acetate (CA) foams hold promise for direct-drive ICF targets because of their extremely small cell size, which appears to be in the range of 0.1-1  $\mu\text{m}$ . We began our development of CA foams in 1987 and are making good quality foams with densities of 40 to 50  $\text{mg}/\text{cm}^3$  and cell sizes less than 1 micron. The structure of the foam is determined by a phase separation technique. The foams are machinable, appear to be moldable, and wick liquid hydrogen. Gelling studies have been done to correlate the cooling rate and composition to the structure and strength of the dried foams. We have studied CA foams from gel concentrations of 2 to 15wt%. The compressive moduli of the foams are on the order of 0.3 MPa to 28 MPa for 3 to 15wt% gels respectively. The densities of the foams are predictable as a function of gel concentration.

### GEL PREPARATION

The foams are made by a phase separation technique, which is based on the solubility behavior of CA in benzyl alcohol. At temperatures greater than 45-50°C, CA has a very high solubility, but below 45°C the solubility drops off sharply. This allows the foams to be made in the following manner. The CA is dissolved in benzyl alcohol at 110°C and cooled to 30 to 45°C, where gelation takes place. The cooling is done in a water bath at programmed rates of 20-35°C/h. A series of solvent exchanges from benzyl alcohol to carbon dioxide is required to allow supercritical drying from

\*Work performed under the auspices of the U. S. Department of Energy by the Lawrence Livermore National Laboratory under contract number W-7405-ENG-48.

carbon dioxide. First, benzyl alcohol is exchanged for toluene, then the toluene is exchanged for liquid carbon dioxide, and finally the carbon dioxide is supercritically extracted. The entire process takes 5 to 7 days.

### PROPERTIES

The densities of the CA foams range from .28 to 225 mg/cm<sup>3</sup>, corresponding to gel concentrations of 2 to 15wt% respectively. The densities are higher than calculated due to some shrinkage resulting from the drying process. A scanning electron micrograph of the foam structure is shown in Fig. 1. It is very difficult to extract reliable structural information because the resolution is poor. An accurate assessment of foam structure will be made from a TEM study similar to the one done for RF foams. The X-ray radiograph shown in Fig. 2 shows that the material is very uniform. The compressive moduli of the foams range from 0.3 MPa for 3wt% gels to 28 MPa for 15wt% gels. BET surface area analysis yielded values of 600 to 800 m<sup>2</sup>/g. This is similar to the values for resorcinol-formaldehyde and silica xerogel. The coefficient of thermal expansion of the foams has been measured from 300 K to 20 K and was determined to be 0.6% contraction.

Tritium exposure and wicking tests are currently in progress.

### ALTERNATE CHEMISTRIES

Other cellulose esters were looked at to see if the mechanical properties would be improved. These have the basic cellulose structure, Fig. 3, but have different types of esterification of the hydroxyls of the ring. The materials used were cellulose triacetate (CTA) R, R' and R" = acetate, cellulose acetate butyrate (CAB) R = acetate, R' = butyrate, R" = hydrogen, and cellulose propionate (CP) R = propionate, R' and R" = hydrogen. All of these were prepared using the same method as the cellulose acetate and behaved similarly except for some differences in physical properties, mainly their solubility in benzyl alcohol. The CP dissolved in the benzyl alcohol, but did not separate out when cooled. The CTA and CAB dissolved and phase separation occurred when they were cooled. These gels were processed and dried to foams. A 3.8wt% gel of CTA yielded a foam with

a density of  $80 \text{ mg/cm}^3$  and a modulus of 0.56 MPa. The CTA foam seemed to be more rigid to the touch than CA foams due to a larger percentage crystallinity. CTA requires a higher temperature to dissolve than the other cellulose esters and is more difficult to get into solution. The processing of the CAB gel was the same as for CA and CTA through the solvent exchange steps, but when the CAB gels were pressurized in the super critical extractor with liquid carbon dioxide, the gels almost immediately collapsed, making CAB unsuitable for foams made by this process. We do not currently have an explanation for this behavior.

A solvent/non-solvent system is being investigated as an alternate method that uses a different solvent to dissolve the cellulose. The cellulose acetate is dissolved in a solvent and then the solution is placed in a permeable membrane container where the solvent is exchanged with a non-solvent. The solvent and non-solvent used were acetone and methanol, respectively. A gel is formed by precipitation as the solvent is exchanged with the non-solvent. The gel is then placed in methanol for a more thorough exchange of the acetone, and finally the methanol is exchanged with liquid carbon dioxide and the carbon dioxide is supercritically extracted. This approach is still being evaluated.

#### VISCOSITY MEASUREMENTS AND COOLING RATE EFFECTS

Viscosity and cooling rate studies were made to determine the gelation points of the CA/benzyl alcohol solution and to find an optimum cooling rate to control foam morphology to improve mechanical strength. Measurements were made of viscosity versus temperature as a function of time to determine the gel point of the CA solution. The viscosities were measured with a vibrating rod viscometer. Gels were prepared in 3 to 15wt% concentrations, placed in a jacketed reaction vessel, and cooled from 90 to 20°C during 3, 10, and 48 hour periods. Cooling rates were controlled by a refrigerated circulator bath and temperature programmer. Additional samples were placed in the bath to be cooled at the same time as the viscosity sample so that the gel point could be observed visually. Figure 4 shows that all the viscosities change at approximately the same rate, but have different values. The gelation point is seen as a sharp increase in viscosity at



temperatures ranging from 33 to 45°C depending on the gel concentration. The gel point increases with increasing concentration as expected. The rise in viscosity matches the observed gelation points of the solutions.

In Fig. 5, the densities of dried foams made from the gel samples are shown as a function of gel concentration. The densities are very reproducible and essentially independent of the cooling rate. There is a linear correlation between the densities and gel concentration. The 3wt% foams were submitted for X-ray crystallography analysis. The analysis indicated all the samples were amorphous, but we may need to use small angle x-ray scattering (SAXS) to observe any crystalline junctions. There were no observable differences in the structure of the 3wt% foams cooled at the different rates.

#### THERMAL ANALYSIS

A comparison of differential scanning calorimetry (DSC) scans for the CA starting materials and the dried foams showed no differences. This indicates that there is no chemical change in the CA during the foam-making process.

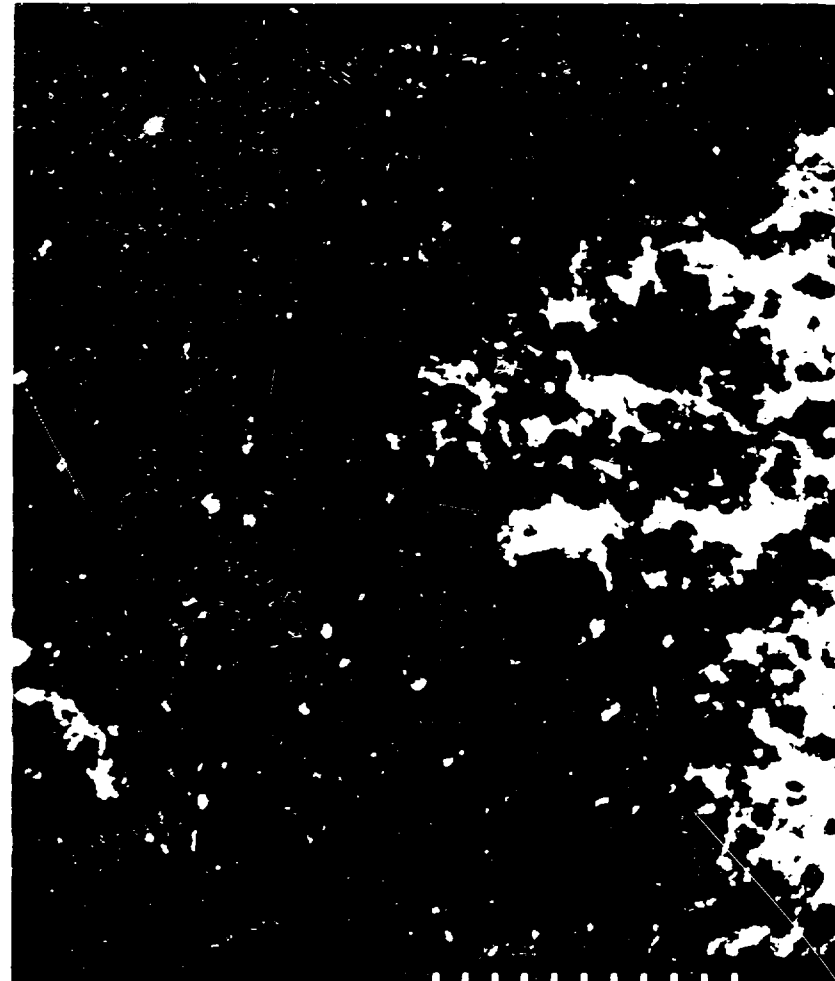
#### CONCLUSION

During our first year of making cellulose acetate foams we have produced a promising material. The properties measured thus far indicate that it could be a good candidate for a target foam. Work will continue on improving the formulation and processing methods and doing additional testing of foam properties.

# SEM of CA foam structure



Cellulose Acetate



6.0  $\mu\text{m}$

Figure 1

**Radiographs show that cellulose acetate foams have good uniformity characteristics**

---



0°

**Magnification 2X**



90°

02-32-0588-1209

**Figure 2**

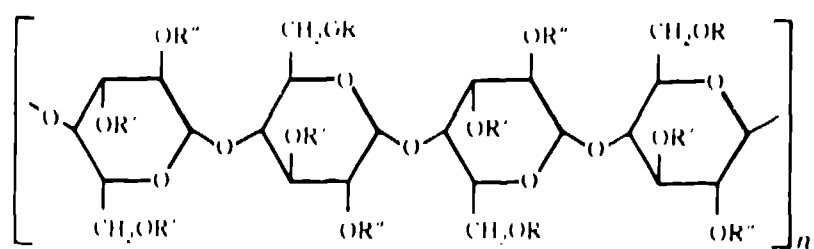
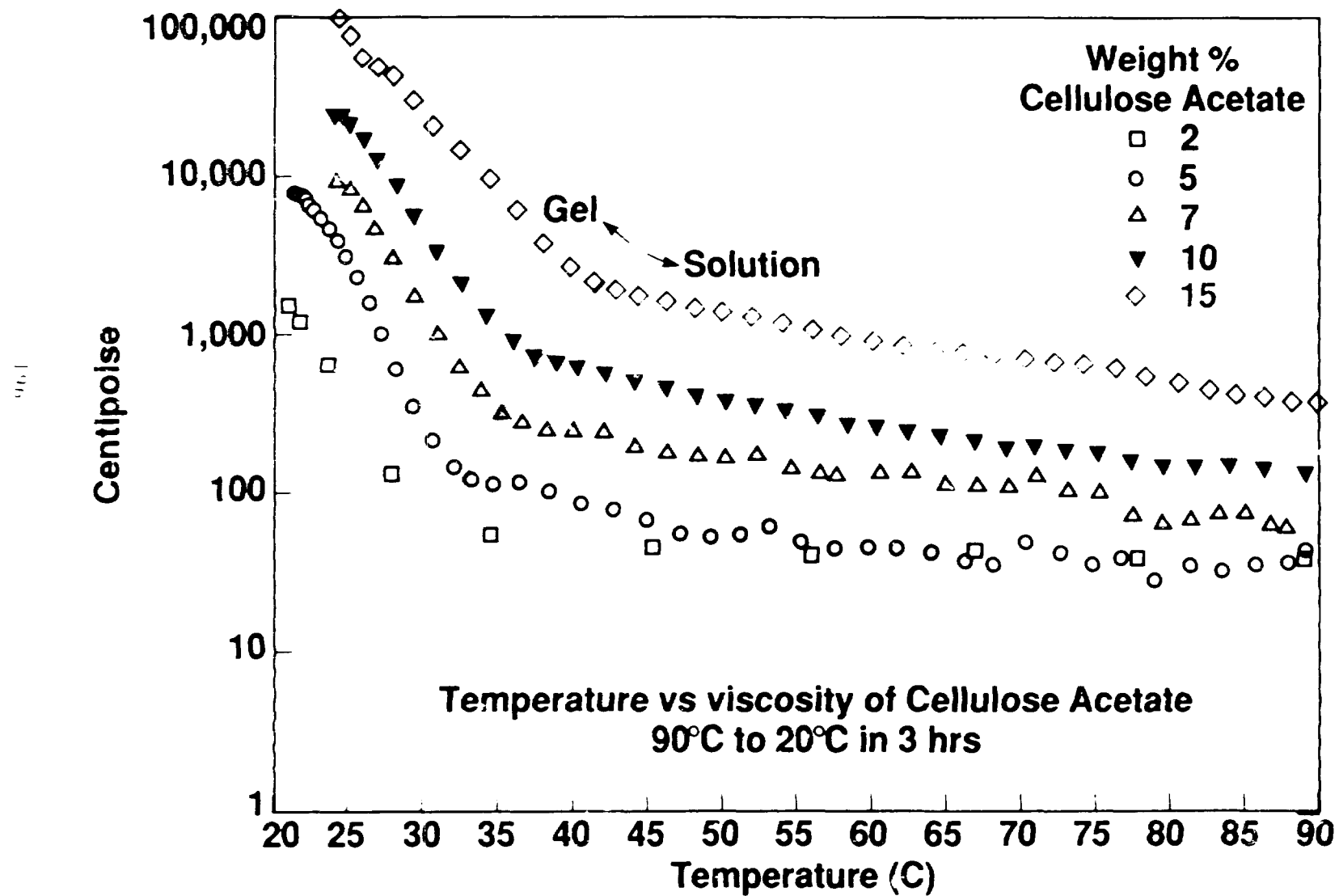


**Figure 3 - Chemical structure of cellulose acetates**

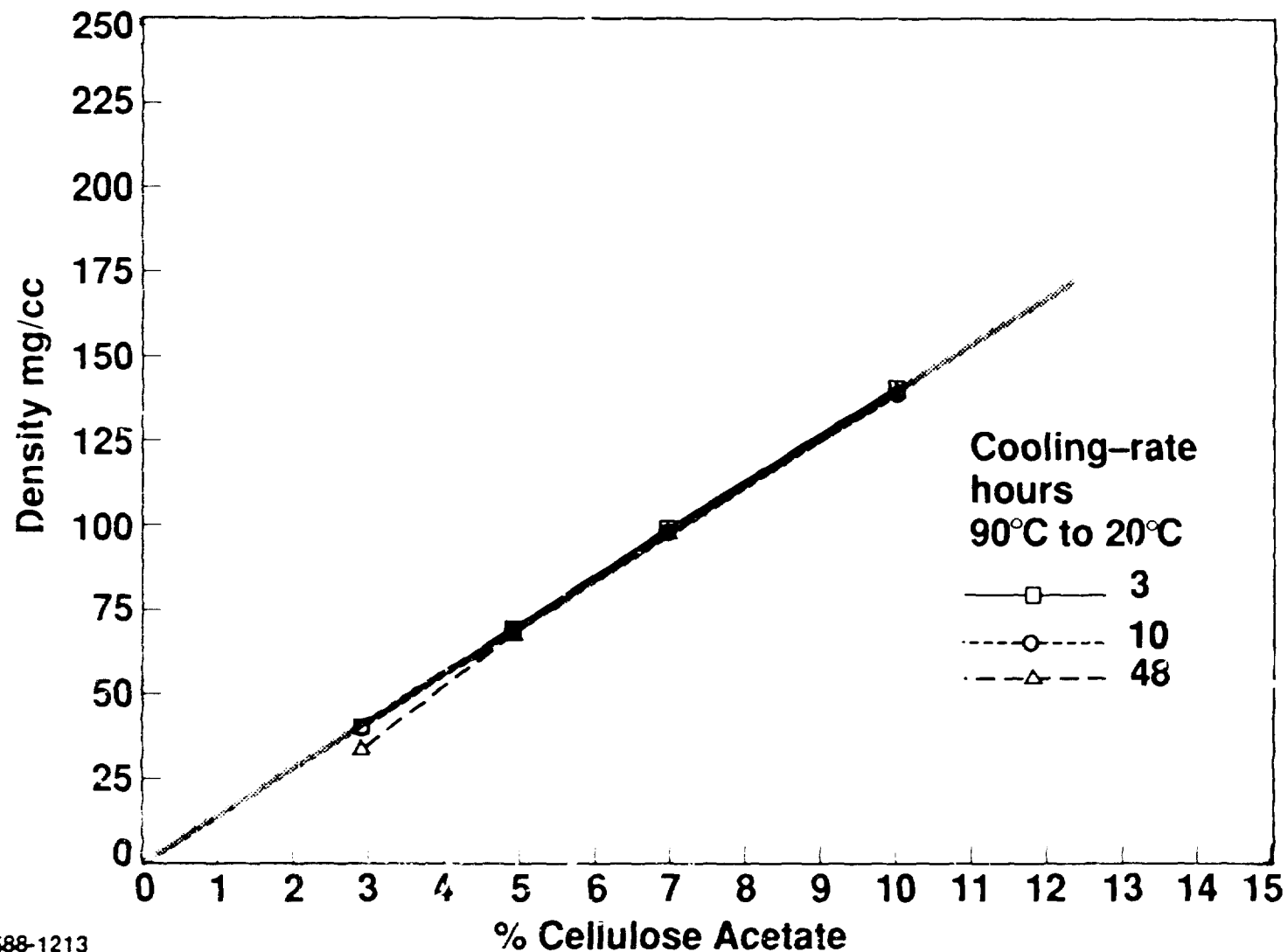
# Cellulose Acetate gel points are measured by viscometry



02-32-0588-1211  
PL 816-U-7253-02Rev

Figure 4

The density of CA foams can be controlled by adjusting the amount of CA in solution and is independent of the cooling rate



02-32-0588-1213  
FL 415-U-7253-01base

Figure 5

## THERMAL ANALYSIS OF LOW-DENSITY FOAMS FOR DIRECT-DRIVE LASER ICF TARGETS\*(UNC)

Steven R. Buckley

University of California  
Lawrence Livermore National Laboratory  
P. O. Box 5508, Livermore, CA 94550

### INTRODUCTION

Thermal analysis is an important tool in the development of low-density polymer foams for direct-drive Laser ICF targets.<sup>1</sup> In this preliminary study, we have assessed the thermal behavior of the foams and some of the starting materials and mixtures used to make them. We have investigated melting points and thermal decomposition. Ultimately we hope to correlate thermal behavior with other foam properties.

### BACKGROUND

We are investigating three candidate foam materials for use as targets: polystyrene (PS), resorcinol-formaldehyde (RF), and cellulose acetate (CA). PS foams are made from an inverse emulsion system using a syringe pump mixing device. After polymerization of the emulsion, the foams are dried in a vacuum oven. CA foams are made by a phase separation technique. The CA is dissolved in benzyl alcohol at 110°C and then allowed to cool to 30-45°C where gelation occurs. A series of solvent exchanges leading to supercritical drying from carbon dioxide is then carried out. RF foams are made from a condensation polymerization of resorcinol and formaldehyde at low weight percent in aqueous solution. Sodium carbonate is used to adjust the pH. After gel formation and curing, solvent exchanges and supercritical drying are performed to produce the foam. We are also studying carbonized RF foams (CRF), because carbonization at 1050°C dramatically improves the mechanical strength of RF foams. Further details on the preparation and properties of these foams may be found in Ref. 2 and Ref. 3.

\*Work performed under the auspices of the U. S. Department of Energy by the Lawrence Livermore National Laboratory under contract number W-7405-ENG-48.

## EXPERIMENTAL

The thermal techniques used in this study included thermogravimetric analysis (TGA) and differential scanning calorimetry (DSC). A Perkin-Elmer TGS-2 and a Perkin-Elmer DSC-4 were used. Data acquisition for TGA was through Perkin-Elmer Tadssoft, and Laboratory Microsystems software was used for the DSC work. The TGA experiments were done under argon at a flow rate of 20 cm<sup>3</sup>/min, while nitrogen at 5 cm<sup>3</sup>/min was used for DSC. Most samples were run in open pans made of platinum foil for the TGA studies, although in some cases they were sealed in stainless steel pans with pin holes in the lids. For the DSC work, stainless steel pans were weighed, baked in an oven, and reweighed before samples were inserted and the pans sealed. Typically samples were scanned at heating rates of 5.0–20.0°C/min, as this range was found to give good resolution of the weight loss onset temperatures in TGA. In DSC experiments, 10.0°C/min was found to give the best resolution of endothermic and exothermic peaks and onset temperatures.

Finished foam materials were scanned "as is". The starting materials tested were obtained in the highest purity available from the manufacturer and were used without further purification.

## RESULTS AND DISCUSSION

Thermograms were obtained for two of the starting materials used in making PS foams and are shown in Fig. 1. Sodium persulfate is used as the polymerization initiator. We investigated its thermal stability to determine how much of the material or its decomposition products would remain at 1050°C, since we would potentially like to be able to carbonize PS foams at that temperature. Figure 1a shows that approximately 38% of the original weight of the sample remains at 540°C, and the thermogram does not change above this temperature. This amount of material would therefore remain after any carbonization. Figure 1b shows the thermogram of Span 80, which is the surfactant used in making PS foams. The material begins to decompose at approximately 150°C and is completely gone at around 440°C. This thermogram corresponds well with one obtained from the manufacturer of the surfactant.



Figure 2 shows a thermogram for a low-density PS foam. Much of the early weight loss is ascribable to decomposition or loss of the surfactant, but at approximately 440°C, the rate of weight loss accelerates substantially, indicating that the polymer is decomposing as well. (The surfactant constitutes about 17wt% of the foam.)

In Fig. 3, a comparison is made between the cellulose acetate starting material and the low-density foam made from it. The thermograms are very similar up to about 440°C, but above this temperature the foam seems to have greater thermal stability. We do not currently have a good explanation for this.

A study of the effect of carbonization of RF foams on thermal behavior is shown in Fig. 4. As expected, the carbonized foam exhibits greater thermal stability, since the volatile components have already been removed. The sharp changes seen above 840°C are most likely artifacts introduced by violent outgassing of the samples, and new sample preparation techniques are being investigated.

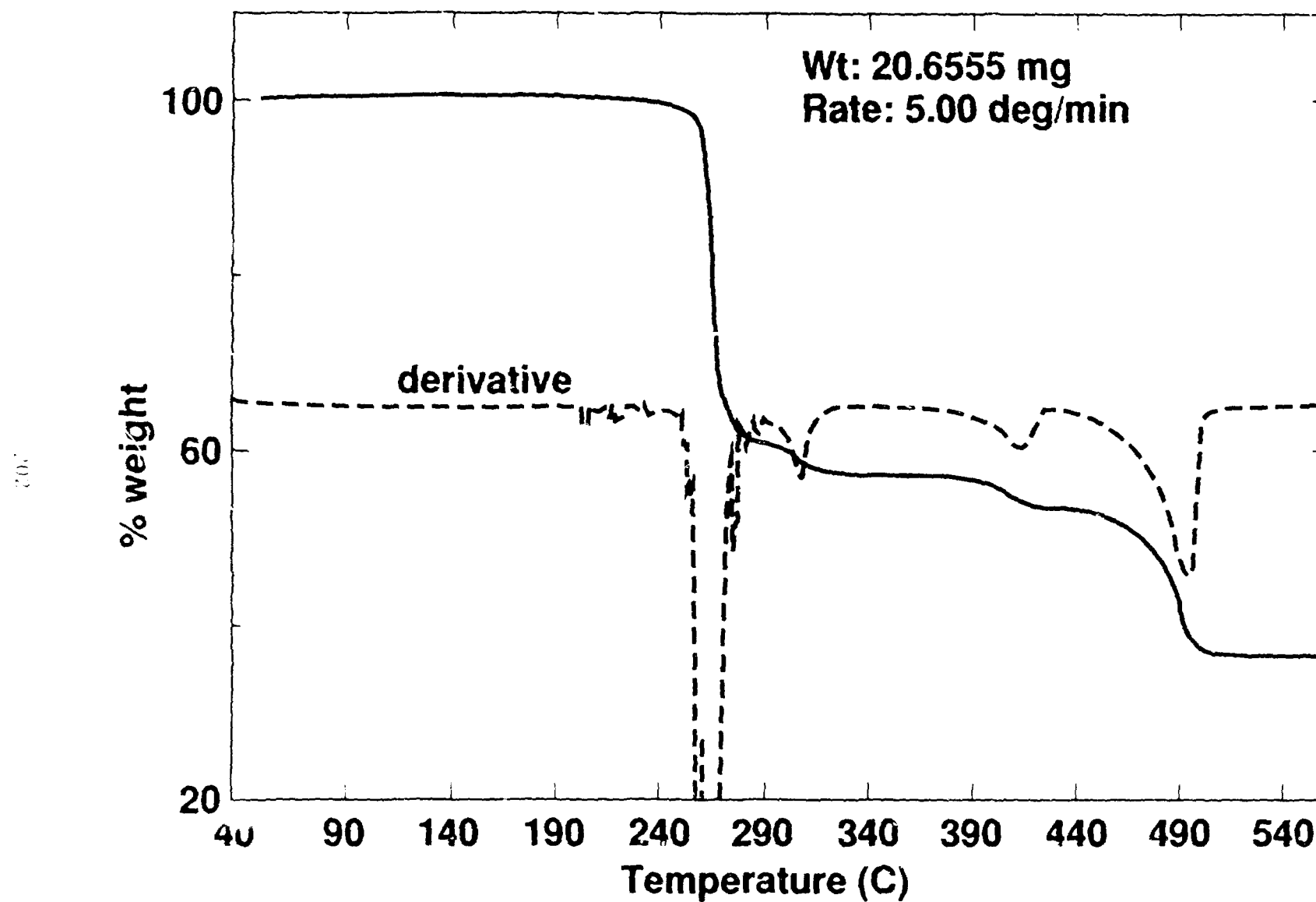
Finally, we used DSC to assess the extent of moisture content remaining in RF foams and the effect of curing on this moisture. Figure 5 shows the endotherm associated with water loss for three samples. Curve 1 shows a greater water content in a sample taken from the skin of an RF foam when compared to Curve 2, where the sample was taken from the core. In Curve 3, the effect of vacuum oven curing at 90°C is seen as a substantial reduction in the endotherm.

## CONCLUSION

Thermal analysis has proved to be a valuable tool in assessing the properties of low-density foams and their starting materials. We have obtained a considerable amount of information which now needs to be interpreted in terms of foam properties and structure. We will continue to use this technique to assess thermal stability, and we plan to interface the TGA with our gas chromatograph and Fourier Transform infrared spectrophotometer.

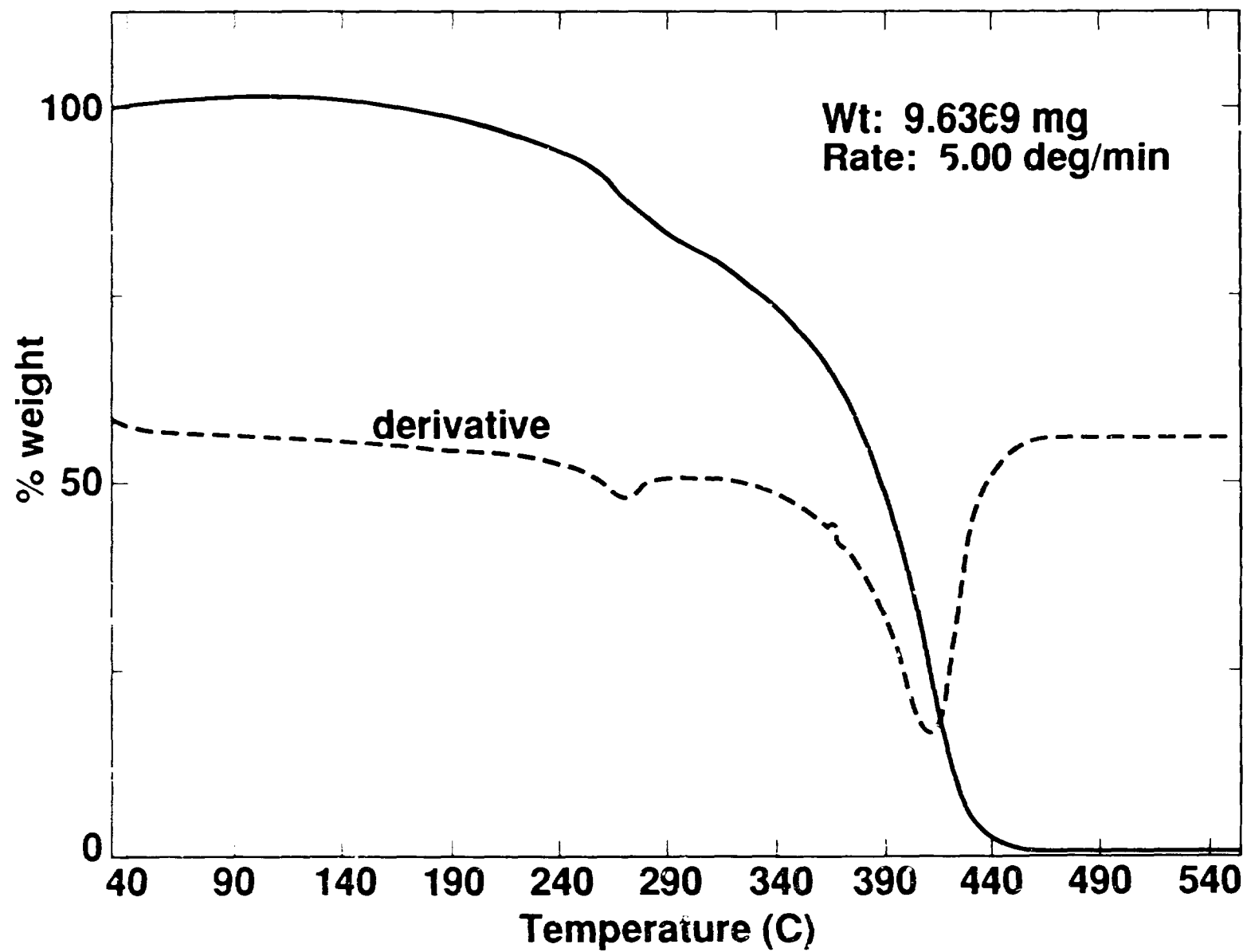
#### REFERENCES

1. R.A. Sacks and D.H. Darling, "Direct Drive Cryogenic ICF Capsules Employing DT Wetted Foam," Nucl. Fusion, 27(3),447,(1987).
2. Laser Program Annual Report 85, Lawrence Livermore National Laboratory, Livermore, Calif., UCRL-50021-85 (1986), pp.3-4 to 3-21.
3. Laser Program Annual Report 86, Lawrence Livermore National Laboratory, Livermore, Calif., UCRL-50021-86 (1987), pp.5-1 to 5-21.



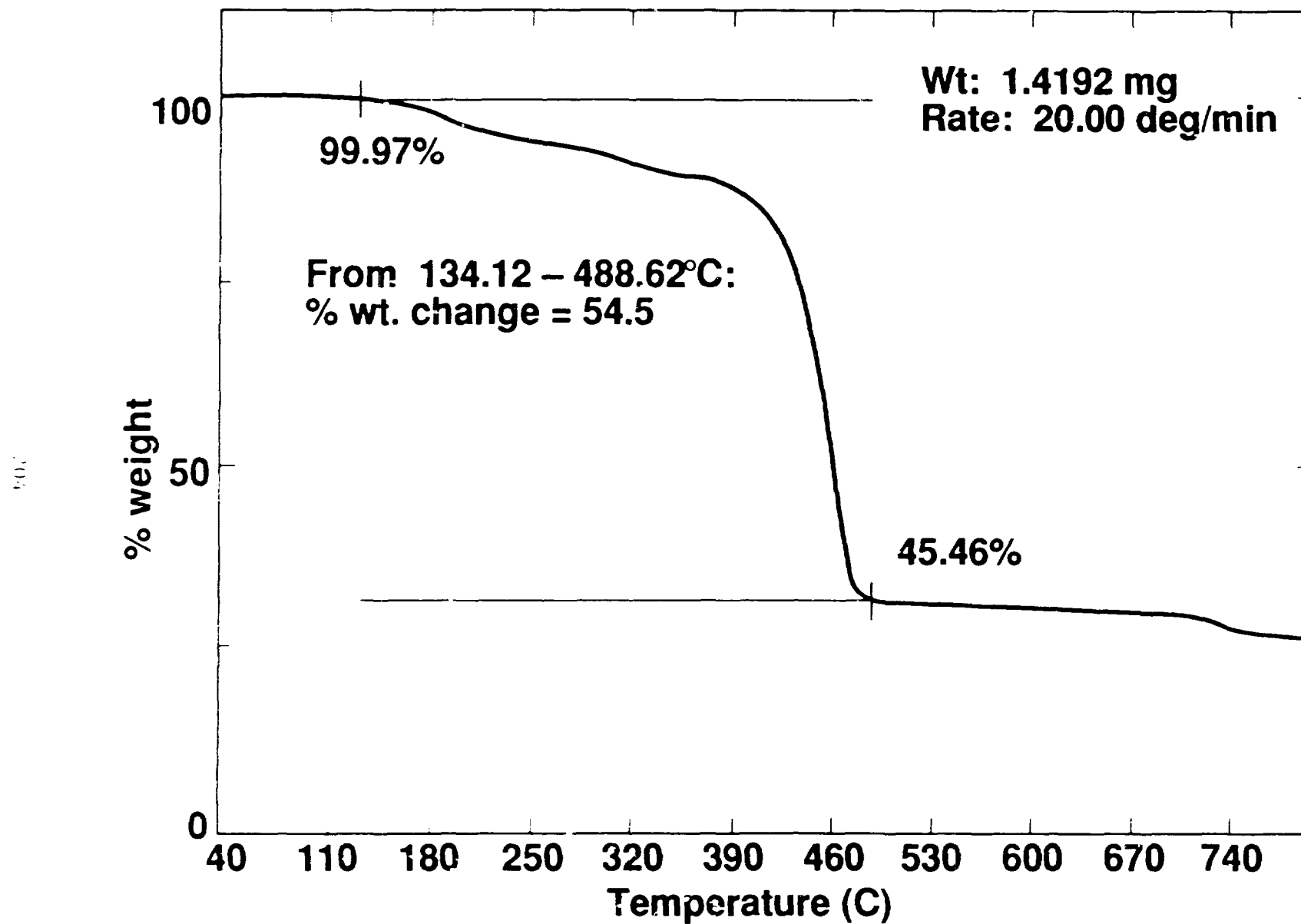
02-32-0588-1201  
MS-023-0-7225

Figure 1a - T6A scan of sodium persulfate showing that approximately 38% of the original weight remains after 540C.



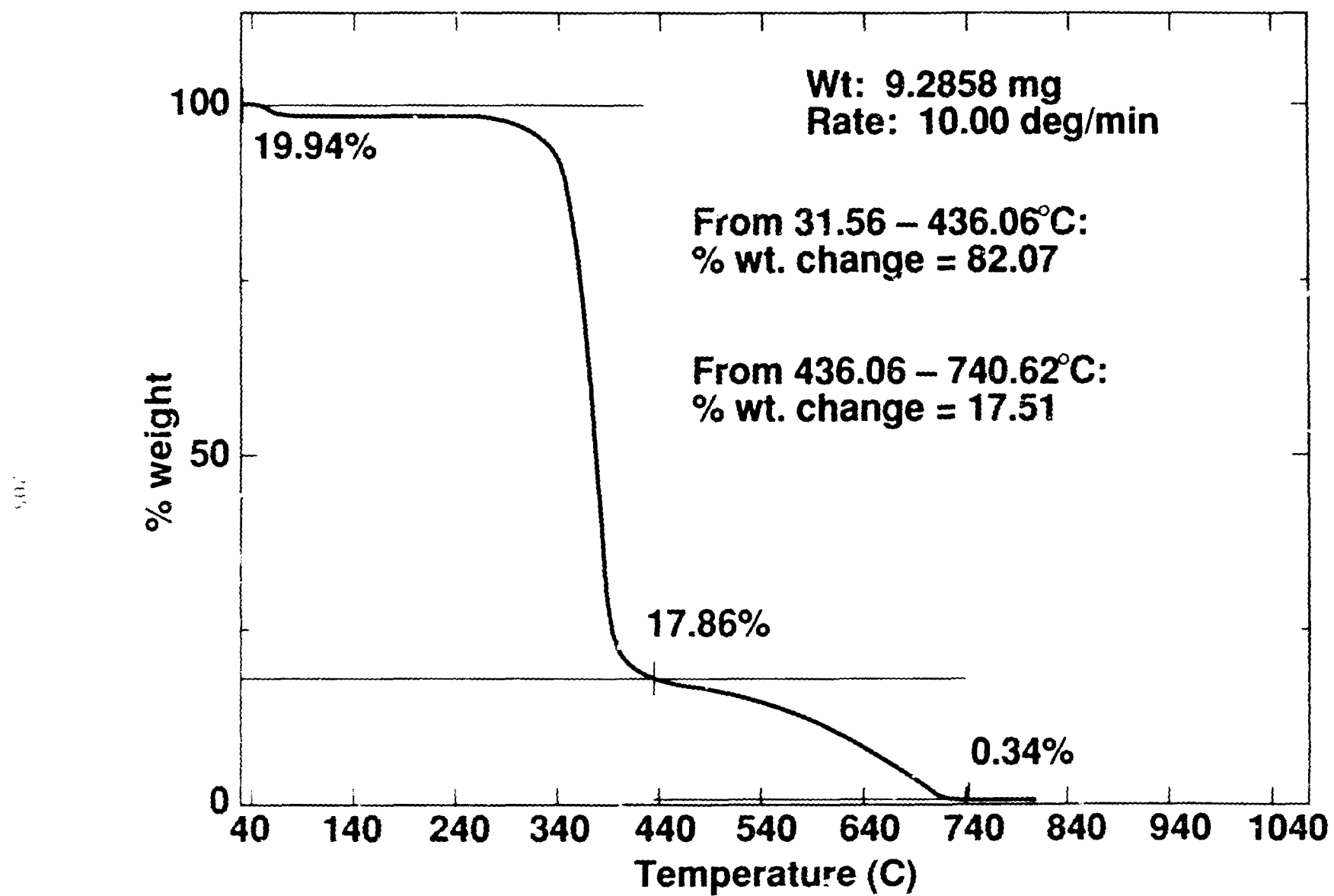
02-32-0588-1203  
TF-007-U-7225-G3a

Figure 1b - TGA scan of Span 80 completely decomposing at 440C.



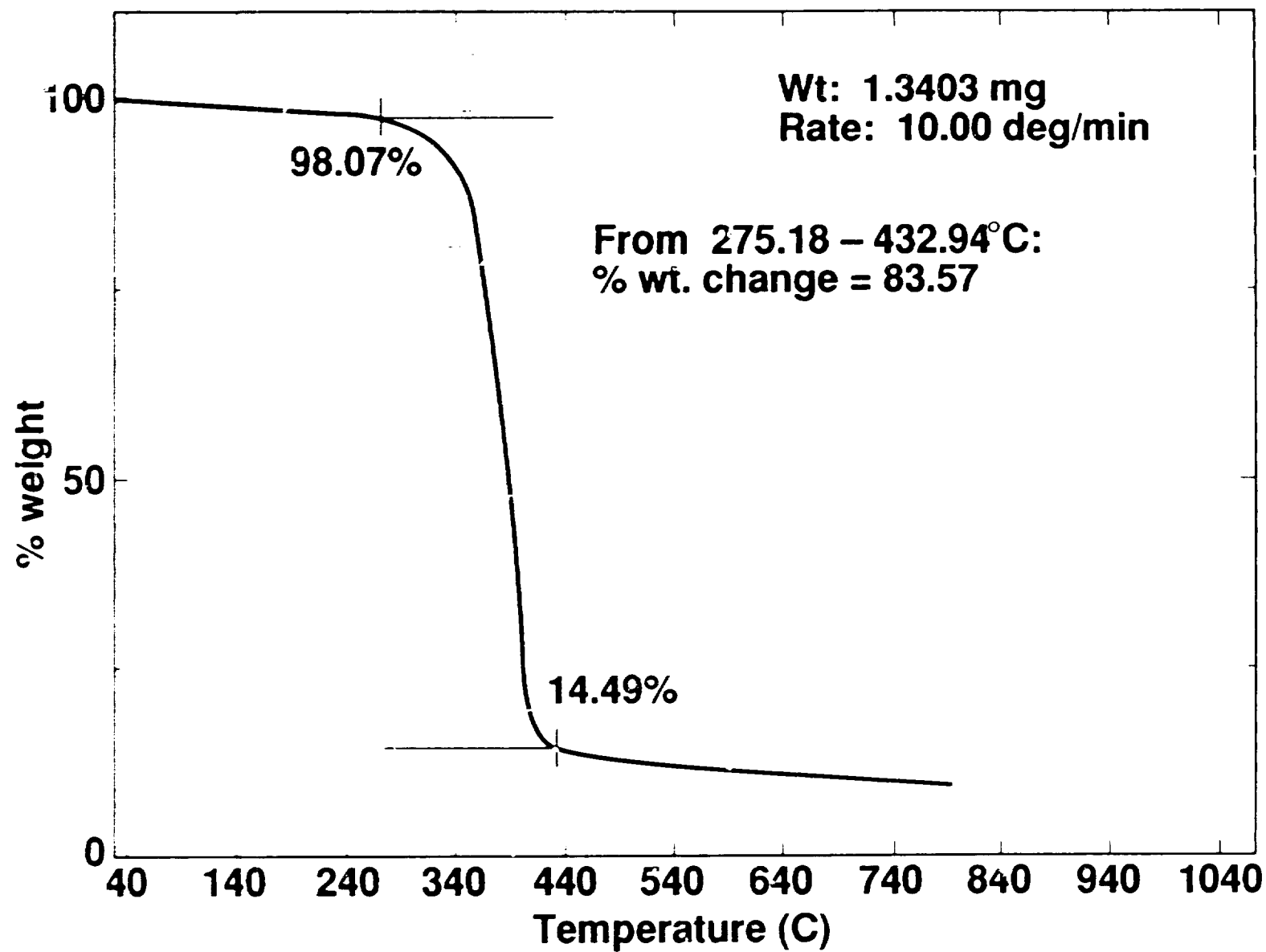
02-32-0588-1202  
TF 007-U-7225-04a

Figure 2 - T6A scan of PS foam showing accelerated weight loss at approximately 440C.



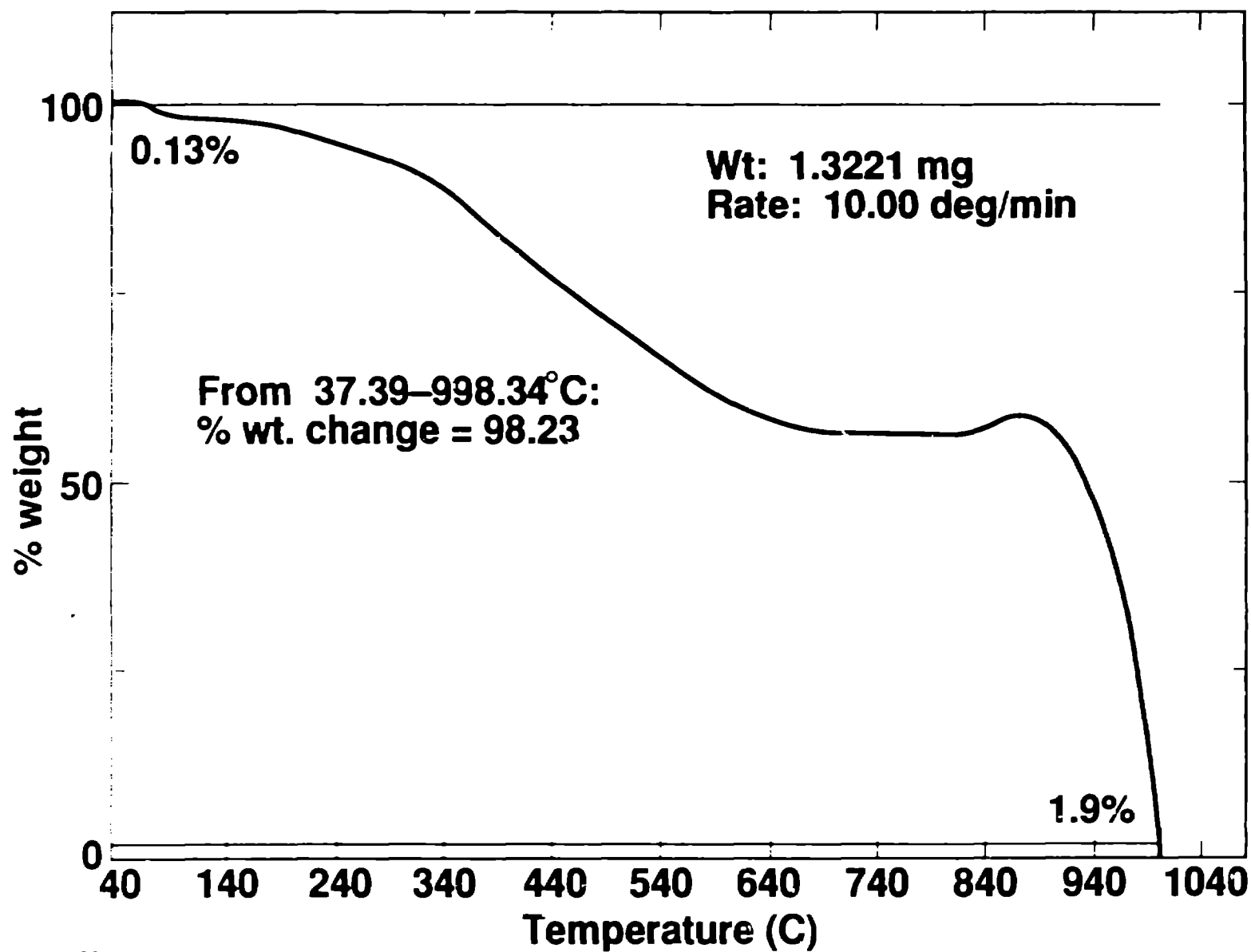
02-32-0588-1204  
TGA-001-01-0001-0001

Figure 3a - TGA scans of CA starting material



02-32-0588-1205  
TF-007-01-7225-01a

Figure 3b - T6A scans of CA foam



02-32-0588-1199  
T6A scan of uncarbonized R/F foam

Figure 4a - T6A scan of uncarbonized R/F foam.



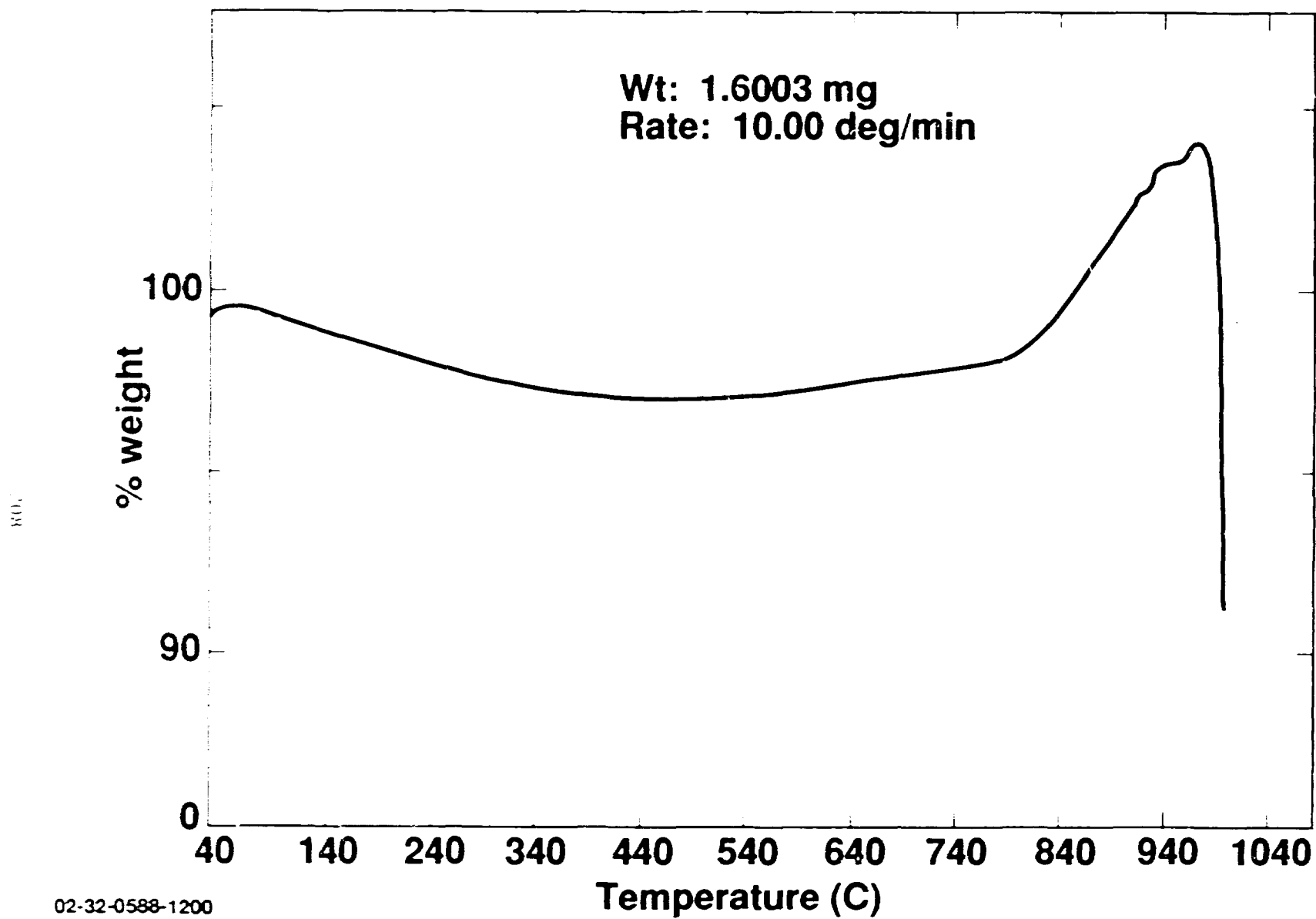
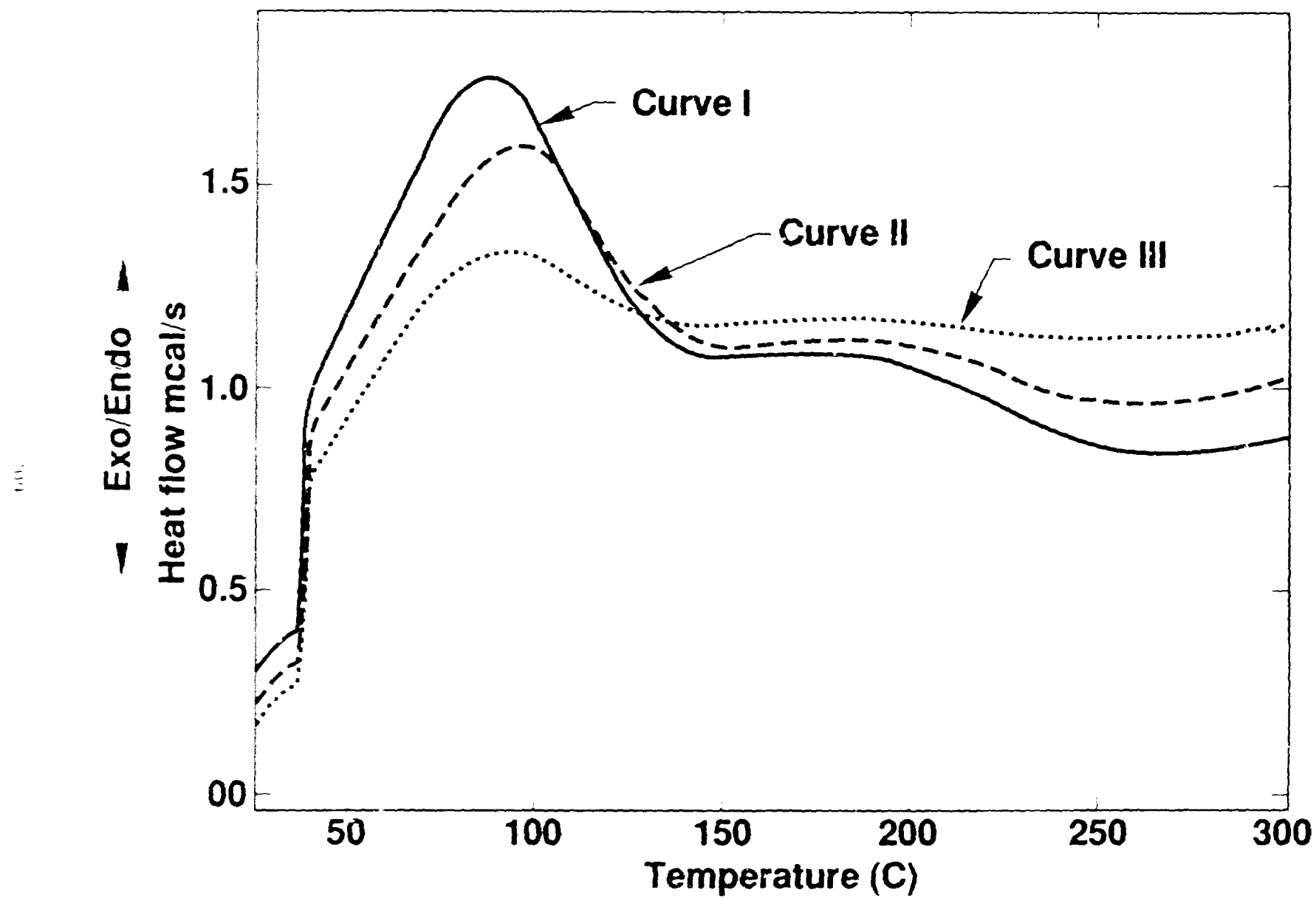


Figure 4b - T6A scan of carbonized R/F foam



02-32-0588-1197  
TF-001-00000000

Figure 5 - DSC scan used to assess the moisture content remaining in R/F foams.

## DEVELOPMENT OF A DIE SYSTEM FOR MOLDING TARGET PARTS FROM POLYSTYRENE\*

Harold D. Kramer and Ravindra S. Upadhye

University of California  
Lawrence Livermore National Laboratory  
P. O. Box 5508, Livermore, CA 94550

### INTRODUCTION

Polystyrene is one of the materials under consideration for the commercial ICF process. The required shot repetition rate for a commercial facility is estimated to be of the order of 10 Hz. If machining is selected to be the method of choice for making the hemishells, the number of spherical surfaces needed to be machined per day will be well over three million, which appears to be an impractical proposition. In this case, molding presents an acceptable alternative. Although molding will not eliminate the need for machining, the required machining will be limited to the flat surfaces that will be bonded.

### DEVELOPMENT OF APPARATUS

Molding of polystyrene foams for ICF targets imposes on us two apparently conflicting requirements:

- The material being molded should have low viscosity, so that it can be poured into the die without trapping air bubbles; and
- The emulsion being molded should be uniform, and have a small cell size. The way to satisfy this requirement is to mix the emulsion well, which increases its viscosity.

An immediate consequence of the above is that simple molding techniques, proven to be useful for many systems, do not work in this case. A low viscosity emulsion, which fills the die readily without any air bubbles on the surface, yields a high cell-size, nonuniform foam. A well formed

\*Work performed under the auspices of the U. S. Department of Energy by the Lawrence Livermore National Laboratory under contract number W-7405 Eng 48.

emulsion, having relatively high viscosity, almost always traps small air bubbles near the surface if one tries to fill the die with it; injection molding using flow-through dies is also difficult because the high viscosity of the emulsion requires pressure drops well beyond those capable of breaking, at least partially, the well-formed emulsion. Another, and more far-reaching, consequence of this dilemma is that any attempts to separate the issues of material processing (such as mixing the ingredients and forming a uniform, low cell-size, emulsion) and fabrication (such as filling the die while avoiding air bubbles) are not likely to be very rewarding.

This led us to the development of an integrated processing/molding scheme, wherein making and molding of the emulsion proceed simultaneously. In this technique, the syringes (used in the syringe pump described in more detail by Haendler et. al. earlier in this conference) are filled with the desired amounts of aqueous phase (comprising water and initiator), and organic phase (consisting of styrene, di-vinyl-benzene and surfactant), the die assembly and a specially designed mixing element (described later) are placed in between the syringes, and the mixing process is initiated. Figure 1 shows a picture of the syringe pump, the die, and the mixer assembly. The components of the die assembly are shown in Figure 2.

The original syringe mixer had to be modified for the molding application. As the various components of the system were being assembled, air invariably got trapped alongside the process liquids, leading to bulk and surface imperfections. To eliminate air bubbles, we modified our operating procedure, whereby the entire die-mixer-and-syringe assembly was made under water, and tested for leaks. We also modified the syringe supports so that the completely assembled system could be placed and secured inside them.

To cut down the pressure drop across the mixing orifice described in an earlier section, and thereby reduce the mixing time while still maintaining emulsion uniformity, we developed a new mixing element (shown in Figure 3) to replace the single orifice. This mixer initially contained a perforated plate with a number of holes half to one millimeter in diameter. Later on, we replaced the plate with commercially available perforated screens with nominal hole diameters of 200 microns. The number of holes per unit area

(and therefore the porosity) in these screens is quite high, which results in a relatively large cross sectional area for liquid flow, which in turn results in low pressure drop across the mixer. We have tried a variety of combinations of the number of screens and the separation between them. Our current design uses four screens separated by about one millimeter. The use of the new mixer has significantly reduced the required mixing time, and improved the emulsion uniformity.

The material of construction of the die imposes on us some special requirements. The ideal material should be:

- inert toward the emulsion (it should not chemically react with the emulsion components, and should not cause or aid emulsion breakup);
- easily machinable and capable of yielding a smooth surface; and
- strong (rigid) enough to obtain the design dimensions and maintain them during the molding operation.

Metals, while strong and capable of yielding a high quality surface finish, tend to interact with the emulsion. In the initial experiments, the part surfaces were invariably pitted, pointing to localized emulsion breakup near the die surfaces. Gold plating the die surfaces in contact with the emulsion proved to be only marginally useful. Teflon is an ideal material from the point of view of inertness, but is too flexible to maintain dimensional stability during machining and operation. One way around this problem is to use teflon rigidized by some impregnated materials, such as ceramic or graphite. We have successfully used both of these, however, our current material of choice is glass. It is chemically inert toward the emulsion, rigid, and capable of yielding a highly polished uniform surface.

The particle count of the ambient air has a major impact on the mold surface quality. Moving our mold assembling process to a clean bench showed major improvements in surface quality. Even better surface uniformity was obtained when the whole operation was carried out in a glove box wherein the air was continually circulated through filters.

## RESULTS

Figure 4 shows a hemispherical part made in the glass die, using the new mixer element and the modified syringe pump. Figure 5 presents the SEM

picture of another hemisphere to show foam uniformity and cell size.

Figure 4 shows that the surface of the part, although uniform in most places, has identifiable nonuniformities in a few places. Also, the surface is still not within the specified target finish of  $\pm 5$  microns. The surface finish of the die, being similar to that of the part, does appear to be the limiting factor here. In addition, localized breakdown of the emulsion may also cause larger surface defects.

#### FUTURE PLANS

The major problem in molding polystyrene parts at the present time appears to be surface finish. The following are some of the ways of improving surface quality:

- Continue to reduce the particle loading of the environment during the assembly of the die system. Similar precautions will be needed for all the chemicals used in the emulsion.

- Improve the die surface finish by techniques such as diamond machining, grinding, and lapping.

## Figure Captions

Figure 1: Syringe Pump/Die/Mixer Assembly

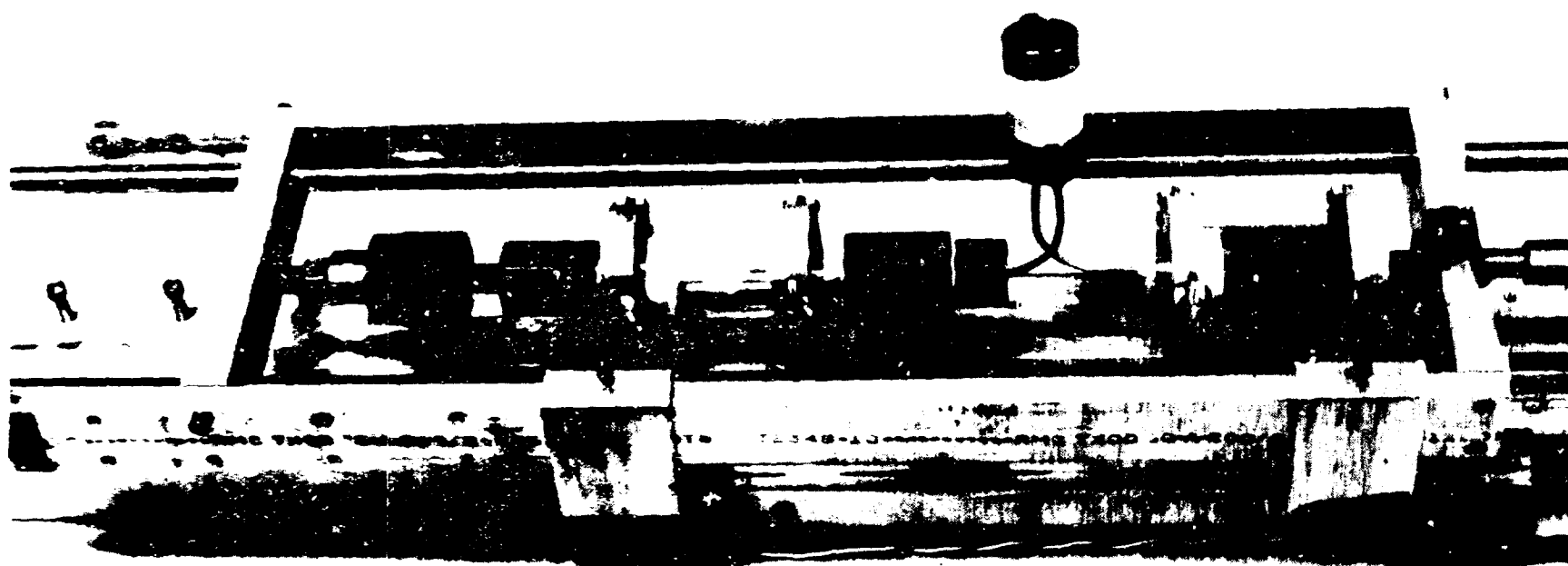
Figure 2: Details of the Die Design

Figure 3: Details of the Mixer Design

Figure 4: Molded Hemispherical Part

Figure 5: SEM Pictures of the Hemisphere Surface and Interior

## Modified syringe pump allows for easier assembly



02-32-0588-1287A

Figure 1



# Flow through molds prevent trapped air bubbles and allow complete filling

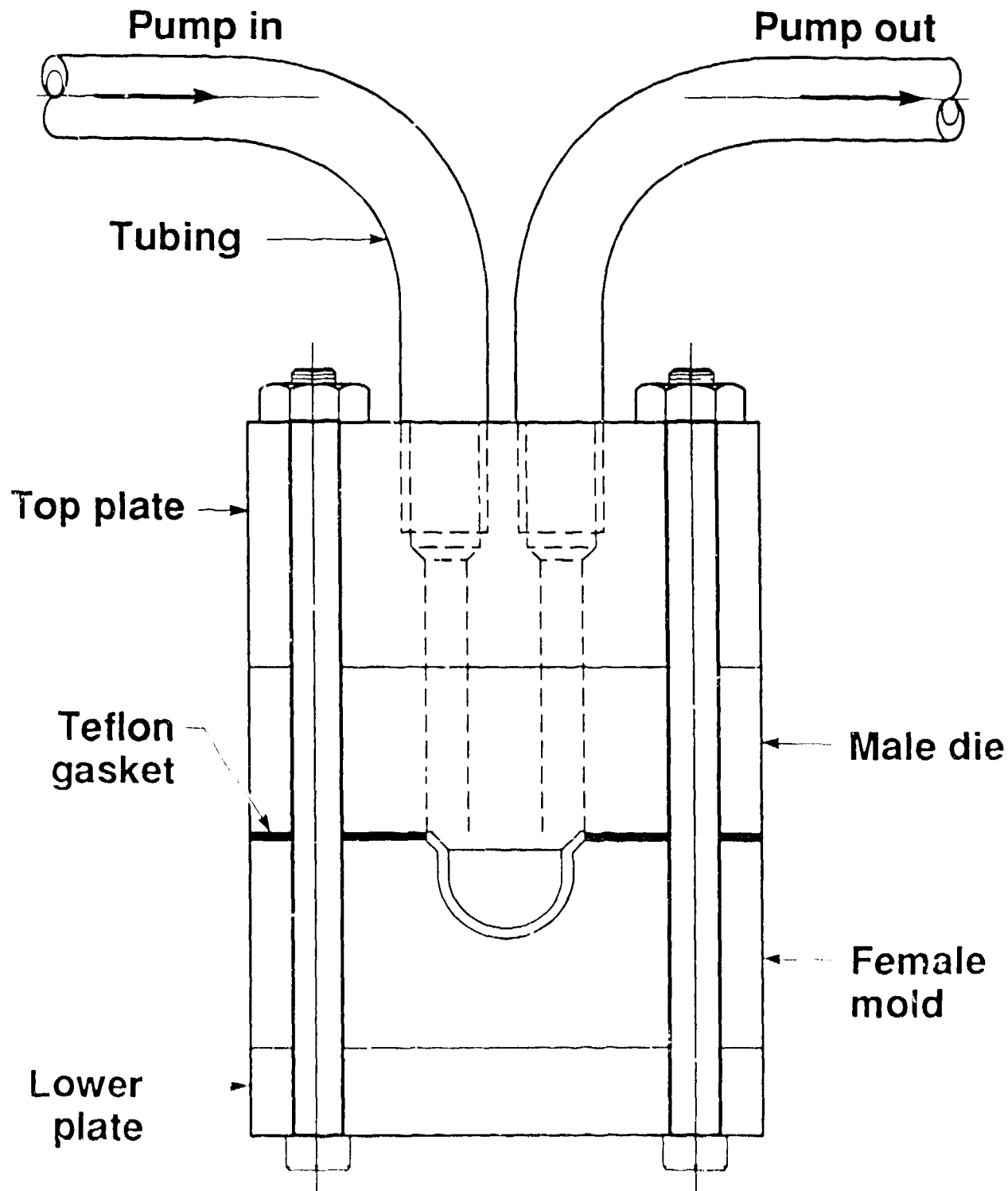


Figure 7-216

## New mixer design gives better mixing uniformity

---



FIG

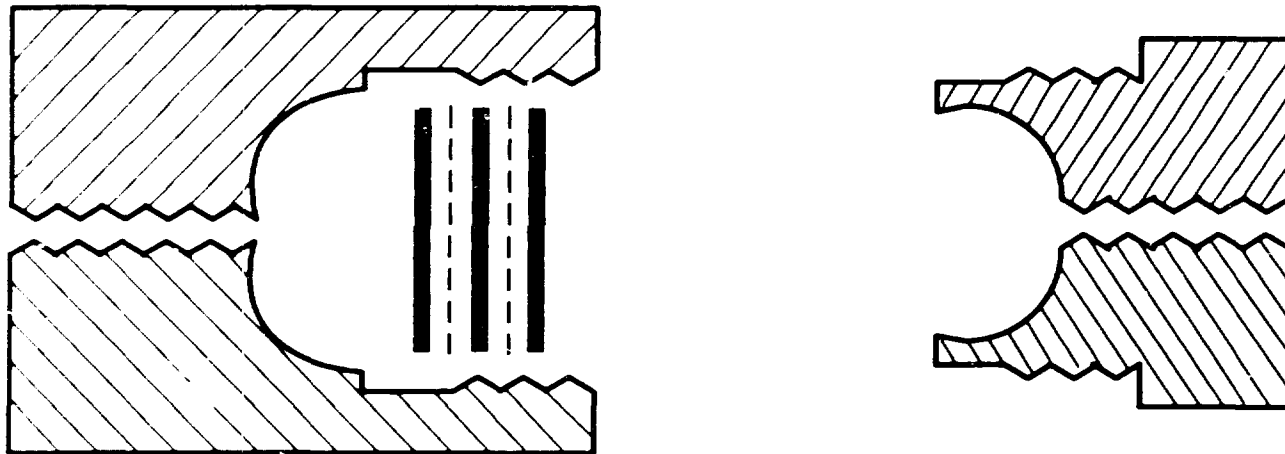
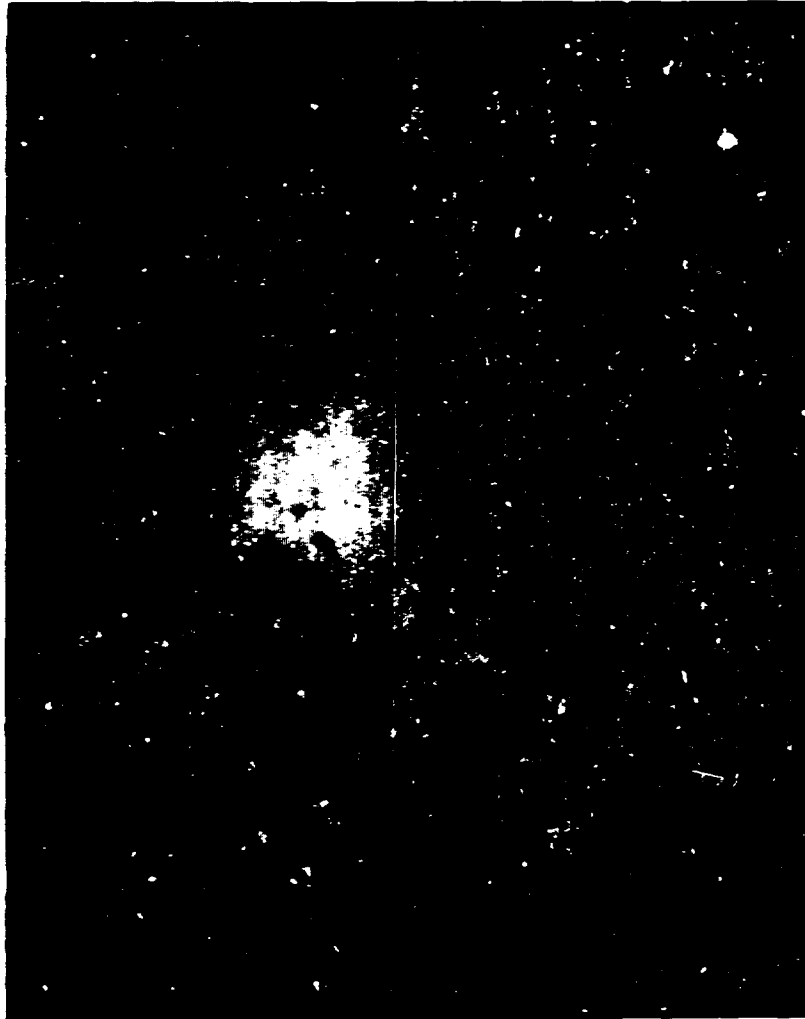


Figure 3

## Glass die improves surface quality



Outside



Inside

Figure 4

# Cell size uniformity is a key technical issue

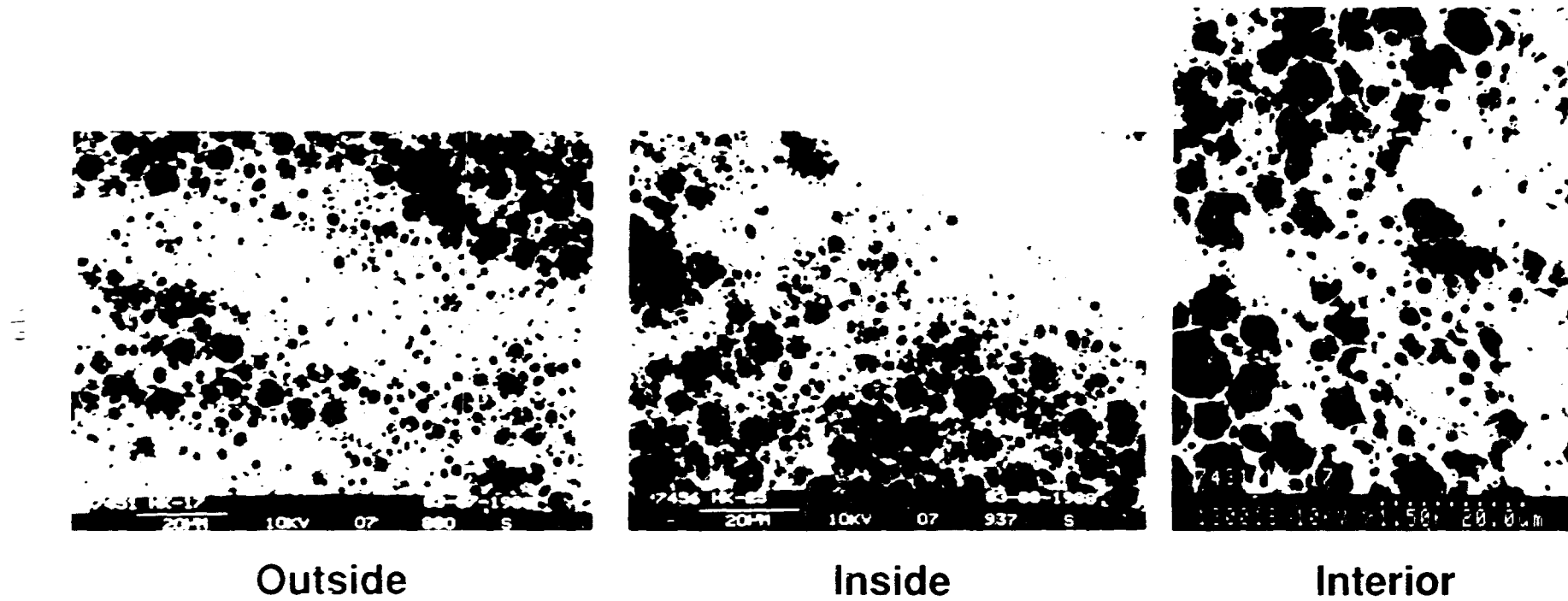


Figure 5